NEUTRAL PARTICLE TRANSPORT IN PLASMA EDGE USING TRANSMISSION/ESCAPE PROBABILITY (TEP) METHOD

A Dissertation
Presented to
The Academic Faculty

By

Dingkang Zhang

In Partial Fulfillment
of the Requirements for the Degree
Doctor of Philosophy
in
Nuclear and Radiological Engineering

School of Mechanical Engineering
Georgia Institute of Technology
May 2005

NEUTRAL PARTICLE TRANSPORT IN PLASMA EDGE USING TRANSMISSION/ESCAPE PROBABILITY (TEP) METHOD

Approved by:

Dr. Weston M. Stacey, Advisor
School of Mechanical Engineering
Georgia Institute of Technology

Dr. Farzad Rahnema
School of Mechanical Engineering
Georgia Institute of Technology

Dr. John Mandrekas
School of Mechanical Engineering
Georgia Institute of Technology

Dr. John L. Wood
School of Physics
Georgia Institute of Technology

Dr. Li You
School of Physics
Georgia Institute of Technology

Date Approved: April 12, 2005

ACKNOWLEDGMENT

I would like to thank my advisor, Dr. Weston M. Stacey. His ideas, support and guidance kept me focused and challenged me to always push to see what else can be accomplished. Without his true monitoring and insightful suggestion, I would not have been able to complete this work. I am also grateful to Dr. John Mandrekas for his valuable advice and useful discussions during the course of this work. I would like to thank Dr. Farzad Rahnema, Dr. John L. Wood and Dr. Li You for their willingness to serve on my thesis committee, and for all of their effort in reviewing my dissertation work.

Most importantly, I would like to thank all of my family members who supported me throughout the years especially my parents, but certainly not least, I would like to thank my wife, Li Wu, for everything she has sacrificed for me to make it this far in my career. For the past 10 years of friendship/marriage she has shown me extreme patience as well as offered unconditional love and support when I needed it most. She always offered me great advice and encouragement and still encourages me to pursue all of my interests.

TABLE OF CONTENTS

LIST OF TABLES

LIST OF FIGURES

SUMMARY

Neutral particles play an important role on the performance of tokamak plasmas. Transmission and Escape Probability (TEP) method has been demonstrated to be an efficient and accurate calculation for neutral transport in tokamak edges and divertor configurations. However, the comparisons with Monte Carlo have also shown that a number of approximations to simplify the TEP methodology limit the applications of the TEP method, especially for problems with very short or very large mean free path.

In this dissertation, the original TEP methodology, which assumed isotropic angular distributions in both the inward and outward hemispheres (DP_0), has been extended to take into account linearly (DP_1) and quadratically (DP_2) anisotropic distributions of angular fluxes for calculations of transmission probabilities. It has been confirmed by comparisons with Monte Carlo calculations that the DP_1 approximation significantly improves the accuracy of the TEP method, but there is no advantage to the implementation of the DP_2 approximation.

Three approaches, subdivision of optically thick regions, expansion of collision sources and the diffusion approximation, have been developed and implemented to correct effects of the preferential probability of collided neutrals escaping back across the incident surface. Solving the diffusion equation via the finite element method has been shown to be the most computationally efficient and accurate for a broader range of Δ/λ by comparisons with Monte Carlo simulations. To take into account spatial non-uniformities in angular fluxes along interfaces, a linear spatially dependent set of DP_N representation functions has been adopted. Benchmark simulations with Monte Carlo show that this approach significantly improves the accuracy of the simulations.

The average neutral energy (ANE) approximation, which assumes that the average neutral energy from a region is the weighted average of the energy of neutrals incident from contiguous regions and of the energy of neutrals resulting from charge-exchanged ions

within the region, has been developed and implemented into the GTNEUT code. The average neutral energy approximation has been demonstrated to be more accurate than the original local ion temperature approximation for optically thin regions. The simulations of the refined GTNEUT code agree excellently with the DEGAS predictions in DIII-D L-mode and H-mode discharges, and the results of both the codes are in good agreement with the experimental measurements.

CHAPTER 1

INTRODUCTION

Neutral atoms or molecules, resulting from neutral recycling or external injection for purpose of plasma heating or diagnosis, are always present in magnetically confined plasmas. The range of the neutral concentration in a typical tokamak varies from 10^{-5} in the core plasma region to more than 10% near the divertor.

The transport of neutral particles often plays a significant role not only in the local particle and energy balance, but also in the global behavior of thermonuclear plasmas. Low energy neutrals, reflected from material walls, may undergo ionization or charge-exchange scattering. The former process simply adds cold plasmas. However charge-exchange events, by which the newly created high-energy neutral particles can easily leak out of the confined region, result in consequent cooling of the plasma and the bombardment of the surrounding walls by energetic neutrals. In addition, through charge-exchange processes, neutral particles, due to their large diffusivity and the coupling with plasma transport, have a direct impact on the plasma ion momentum and the local heat balance in the edge and consequently modify the plasma density profile. Experiments [1] and theoretical simulations [2] demonstrate that neutral particles have a crucial influence on the global plasma performance and parameters. There is the strong evidence that neutral particles affect the total particle and energy confinement times , the H-L transition [3], the density limit [4] in the plasma edge and the formation of the edge pedestal [5]. For instance, high-resolution measurements of hydrogenic neutral properties in Alcator C-Mod [6] indicated that neutrals have an important impact on the evolution of the density pedestal found in H-modes, and it also was found that neutrals affect the characteristics of the pedestal through its width and height.

A detailed knowledge of the neutral particle distribution at the plasma edge is therefore

crucial to understanding the physics of tokamak edge plasmas, and the accurate prediction of the neutral density profile is very important for the interpretation of current fusion experimental results and for the prediction of the performance of next generation fusion reactors.

1.1 Characteristics of neutrals transport in the plasma edge

Neutral particles have no charge and therefore their trajectories are not affected by the strong electric and magnetic fields that exist in plasmas. Like the orbits of neutrons in a reactor medium, the orbits of neutrals in a plasma medium are straight lines between collisions, which are categorized into two types: 1) ionization, corresponding to absorption for neutron-matter interactions, and 2) charge exchange and neutral-ion scattering, corresponding to scattering for neutron-matter interactions.

The governing equation for neutral transport in edge plasmas is represented by the linearized version of the Boltzmann equation originally developed for the kinetic theory of gas and without taking into account the neutral-neutral collision. The steady-state intergro-differential neutral transport equation can be written as

$$\begin{aligned} & \boldsymbol{\Omega} \cdot \nabla \psi(\mathbf{r}, \boldsymbol{\Omega}, E) + \Sigma_t(\mathbf{r}, E)\, \psi(\mathbf{r}, \boldsymbol{\Omega}, E) \\ = & \int dE' \int_{4\pi} d\Omega' \Sigma_{cx}(\mathbf{r}, \boldsymbol{\Omega}' \rightarrow \boldsymbol{\Omega}, E' \rightarrow E)\, \psi(\mathbf{r}, \boldsymbol{\Omega}', E') + S_{ext}(\mathbf{r}, \boldsymbol{\Omega}, E), \end{aligned} \tag{1.1}$$

where $\psi(\mathbf{r}, \boldsymbol{\Omega}, E)$ is the neutral particle angular flux, $\Sigma_t(\mathbf{r}, E)$ is the total macroscopic cross section for neutrals with energy of E at point r, $\Sigma_{cx}(\mathbf{r}, \boldsymbol{\Omega}' \rightarrow \boldsymbol{\Omega}, E' \rightarrow E)$ is the double differential macroscopic charge-exchange cross section, and $S_{ext}(\mathbf{r}, \boldsymbol{\Omega}, E)$ represents all the volumetric sources resulting from creation processes such as ion-electron recombination.

The highest neutral concentration occurs at the plasma edge, where there are a strong gradient of background plasma properties and very complex geometric configurations with divertors, baffles and pumps. The mean free path of neutrals varies from millimeters at the core plasma regions to several meters in the vacuum regions. These facts, together with the large variety of physical processes taking place in plasma edge, make the successful

modeling of neutral transport in fusion plasmas very challenging.

Except for highly idealized problems, solving the neutral transport Eq. 1.1 is an almost impossible feat to perform analytically and difficult to achieve numerically. In general, a number of approximations such as isotropic scattering, local ion temperature or multi-group treatment of the neutral energies, and homogeneous plasma background in each computational region are employed to simplify Eq. 1.1 for numerical calculations. Initially, numerical methods from the neutron transport theories were directly adopted to simulate neutral transport in plasmas [7, 8]. These numerical methods can be categorized, according to the form of the Boltzmann transport equation, into three groups: stochastic methods, integro-differential methods and integral methods. However, it is realized that none of them was suitable for the coupled plasma-neutrals transport due to geometrical complexities, widely varying mean-free-path and the requirement of computational efficiency.

1.2 Existing methods

Currently the numerical methods for solving the neutral transport equation are the Monte Carlo method, the spherical harmonics or P_n method, the discrete ordinates or S_n method, the diffusion or Navier-Stokes fluid theory, the collision probability method and the interface current method.

1.2.1 Monte Carlo method

The basic concept of the Monte Carlo method [9, 10] is to perform statistical sampling experiments on a computer, so there is no need to explicitly write down the neutral transport equation. The Monte Carlo method obtains an answer by simulating a large but finite number of particle histories and recording some aspects of their average behavior.

The history of a particle is begun by sampling the source distribution to determine the initial energy, position and direction. Then, more pseudo random numbers are sampled to determine the subsequent events of the particle such as collision distance, reaction types, particle-wall interactions, etc. If it is ionized or vacuumed out of the device, the history is

terminated.

Because the Monte Carlo method can trace neutral particles propagating in the plasma edge and directly simulate the physical processes such as neutral-plasma and neutral-wall interactions in detail, the results of Monte Carlo method can be very accurate if the CPU time is not concerned. Nowadays the most sophisticated Monte Carlo codes for neutral transport in the edge plasma are DEGAS [11] and EIRENE [12]. Because of their high accuracy and capabilities of treating regions with realistic 3D geometries, widely varying mean free path and multi-species of neutrals, the Monte Carlo method is the most widely used methods in edge plasma neutral calculations. But, the limitations of the Monte Carlo method are also obvious: the Monte Carlo method is not efficient for some problems because of the significant computational effort required to achieve acceptably small uncertainty, especially for regions far away from sources. As a result, it is impractical to calculate the detailed spatial distribution in the whole device. Perhaps more crucial, because of its inherent statistical error, the Monte Carlo method is found to be ill-suited for coupled plasma-neutral simulations, where a large number of iterations are generally required. The stochastic characteristics of the Monte Carlo methodology makes iterative calculations extremely time-consuming and difficult to converge.

1.2.2 Differential transport methods

Starting from the differential transport equation, a lot of numerical methods have been developed either by a direct discretization of the transport operator or by an expansion of the angular flux in terms of a set of functions. Since the differential equation is based on a local particle balance it leads to sparse matrices, most of the elements of which are zero. Among those differential methods, the most widely used methods applied to neutral transport in the edge plasma are the diffusion theory, Navier-Stokes [13] and discrete ordinates [7]. However, differential methods are usually suitable for regular geometries such as slabs, rectangles and cylindrical annuli. In addition, for some plasma edge regions under study, the characteristic mean free path may not be small compared with plasma dimensions, and

under these conditions integro-differential transport methods are not justifiable.

1.2.3 Integral transport methods

The integral transport methods construct an expression for the angular flux at a given location by integrating over all external and scattering sources that could contribute, taking in account the probability of the source neutral reaching the given location without a collision. The collision probability method [14, 15, 16] result from partitioning the domain of the problem into a large number of finite size regions and formulating the equation to calculate the average value of the neutral flux in each region. Like the Monte Carlo method, the result of collision probability method can be very accurate. This method has been successfully implemented for neutral propagating in 3D rectangular grids [17]. Since the collision probability method is based on a global particle balance, the neutral flux at a given region is coupled to the neutral scalar flux of any other regions via collision probabilities which must be calculated by multi-dimensional numerical integration involving expensive evaluation of Bickley functions. Theoretically speaking, the ray-tracing method can be used to calculate collision probability coefficients for arbitrary geometries. But in practice, calculating these coefficients is a formidable task even for a high performance computer. However, the collision probability method is usually applied to periodic or regular geometries, where interpolation of collision probabilities and symmetric conditions can be exploited to improve efficiency. Since the neutral flux is coupled to all the regions via collision probabilities, we have to calculate the collision probability between any two regions no matter how far away they are. It is formidable requirements for a computer to calculate and store all these probabilities for any realistic tokamak and divertor.

1.2.4 IC and TEP methods

The Interface current (IC) method [18, 19, 20, 21] is also based on the integral transport equation, it assumes the distribution functions of the angular flux at each interface and the scalar flux within each region, and then a balance is performed relating the uncollided and

scattering (charge-exchange) currents across the surfaces bounding these regions. Therefore the outward partial current from a surface is only coupled to the scalar flux within that region and the inward fluxes at the interfaces bounding it, leading to very sparse transmission and escape probability matrices.

Because of the high charge-exchange fraction in most edge plasmas, a straightforward cell-by-cell iteration solving scalar fluxes within regions and partial currents on interfaces is computationally expensive. The Transmission and Escape Probability (TEP) method [22] [23] extends the IC method by treating charge-exchange sources analytically, eliminating the dependence on the scalar flux within regions. This leads to the benefit that the outgoing partial current from a region is coupled only to the incoming partial currents from all the adjacent regions.

Several advantages arise from the contiguous-region coupling of the partial currents. First, it results in very sparse probability matrices that must be numerically evaluated for solving the partial currents, in contrast to the full collision probability matrices that must be calculated for the collision probability method. Second, the local dependence of the interface currents allows the flexibility in choosing the level of approximations and the computational methods matching the physical properties of the regions of interest. For example, diffusion approximation may be used to calculate directional escape probabilities for optically thick regions; while the non-directional approximation may be a more reasonable choice for calculation of directionalities for a region with the long mean free path. Thus the TEP method can avoid the major difficulties of the other methods. These inherent advantages make the TEP method to be an ideal neutral particle transport method in realistic divertors and edge plasmas.

The TEP method has been successfully implemented into the Georgia Neutral Transport

code GTNEUT [24] for calculation of neutral transport at the edge of thermonuclear plasmas. Extensive comparisons [25, 26] with Monte Carlo simulations and experiment measurements have demonstrated its accuracy and computational efficiency. However, Benchmarking [27] with specially designed model problems also suggests that the assumptions made in the TEP methodology limit the ability of GTNEUT for extreme cases with very short or long mean free path.

1.3 Conclusions and introduction to thesis research

Neutral particle transport has an important effect on the behavior of thermonuclear plasmas. An efficient numerical method with the ability to simulating problems with complex geometries and widely varying mean free path is indispensable for plasma modeling.

The Monte Carlo method, differential methods and the collision probability method are limited either by the inefficiency to couple to iterative plasma fluid codes or by the difficulties to handle problems with geometric complexity and strong background plasma parameters. The TEP method has been demonstrated to be a promising candidate to model neutral transport at the plasma edge. Extensive comparisons and tests with Monte Carlo calculations also suggest that extensions in the following two areas would be useful: 1) taking anisotropy into account in the calculation of first-flight transmission probabilities when the neutral mean free path is much larger than the characteristic dimension of computational regions; 2) taking into account that the escape of charge-exchanged neutrals is preferentially across the incident surface when the mean free path is small compared to the characteristic dimension of the computational region.

Chapter 2 will review the TEP methodology and analyze its limitations. Chapter 3 will detail the DP_n approximation theory to take into account the anisotropy of the angular flux distribution at interfaces between regions. The validity of new assumptions will be investigated. In Chapter 4, three different approaches to address the effects of non-uniformly distributed charge-exchange sources will be discussed and compared. In addition, a new

function expansion to take into account the spatially dependent angular flux on interfaces will be introduced. The average neutral energy approximation will be developed in Chapter 5.

In Chapter 6 the accuracy of new extensions will be investigated by tests and comparisons with Monte Carlo calculations for realistic DIII-D problems and experimental measurements. Finally, Chapter 7 will draw conclusions from current work and point to areas that further research is needed.

CHAPTER 2

TRANSMISSION/ESCAPE PROBABILITY (TEP) METHOD

The TEP method is based on the the balance of the total partial currents crossing the surfaces bounding each computational region. Originally, a heuristic approach [22] was used to obtain the TEP balance equation. The total neutral partial current crossing an interface consists of three distinct contributions: uncollided neutrals, collided neutrals and external volumetric neutral sources together with their progenies. The uncollided flux is the sum of all the fluxes entering from the adjacent regions multiplied by surface-surface transmission probabilities. The secondary source in a intervening region is just the difference of the incoming currents and the outgoing uncollided currents crossing its bounding interfaces. The collided fluxes can be calculated through the total and directional escape probabilities. Then, approximations of the angular distribution of the flux at interfaces and the spatial distribution of the scalar flux within computational regions are made to calculate transmission, first-flight escape probabilities and directionalities. Based on the repeated application of the first-flight transport calculation of escape probabilities, the total escape probability is the sum of all generations charge-exchanged neutrals.

Alternatively, a stricter mathematical derivation starting from the integral transport equation can be proceeded to calculate the total partial current crossing an interface and the total collision rate within a region. After identifying the relations between the total collision rate within a region and all the incoming fluxes from the contiguous regions, the outgoing partial current from a region can be explicitly expressed in terms of all the incoming partial current from the adjacent regions via transmission and escape probabilities. Since it is easier to extend to the higher order approximation, the strict mathematical derivation of TEP equations will be presented in this chapter.

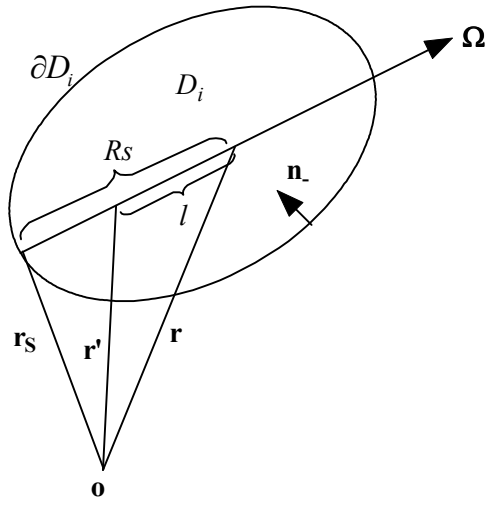

Figure 2.1. Schematic diagram for the integral transport equation

2.1 Integral transport equation

The one-speed steady-state integral transport equation [14] for a domain D_i with boundary ∂D_i, as shown in Figure 2.1, can be written as

$$\psi(\mathbf{r},\mathbf{\Omega}) = \psi_{in}(\mathbf{r_S},\mathbf{\Omega})\exp\left(-\tau(\mathbf{r},\mathbf{r_S})\right) + \int_0^{R_S} dl q(\mathbf{r}-l\mathbf{\Omega},\mathbf{\Omega})\exp\left(-\tau(\mathbf{r},\mathbf{r}-l\mathbf{\Omega})\right), \qquad (2.1)$$

where $\psi(\mathbf{r},\mathbf{\Omega})$ is the angular flux at point $\mathbf{r}$ in direction $\mathbf{\Omega}$ and $\mathbf{\Omega} = \frac{\mathbf{r}-\mathbf{r}_S}{|\mathbf{r}-\mathbf{r}_S|}$; $\psi_{in}(\mathbf{r}_S,\mathbf{\Omega})$ is the incoming flux at boundary; R is the distance between point $\mathbf{r}$ and the starting point $\mathbf{r}_S$ on the boundary and $R = |\mathbf{r}-\mathbf{r}_S|$; Σ_t is the total macroscopic cross section; Σ_{cx} is the macroscopic charge-exchange cross section; $\tau(\mathbf{r},\mathbf{r}')$ is the optical length between r and r' defined by the following expression,

$$\tau(\mathbf{r},\mathbf{r}') = \int_0^{|\mathbf{r}-\mathbf{r}'|} dl\Sigma_t\left(\mathbf{r}' + l\frac{\mathbf{r}-\mathbf{r}'}{|\mathbf{r}-\mathbf{r}'|}\right), \qquad (2.2)$$

and $q(\mathbf{r},\mathbf{\Omega})$ is the total volumetric source defined as

$$q(\mathbf{r},\mathbf{\Omega}) = \int_{4\pi} d\Omega'\Sigma_{cx}(\mathbf{r},\mathbf{\Omega}'\rightarrow\mathbf{\Omega})\psi(\mathbf{r},\mathbf{\Omega}') + S_{ext}(\mathbf{r},\mathbf{\Omega}), \qquad (2.3)$$

where $S_{ext}(\mathbf{r},\mathbf{\Omega})$ is external volumetric source.

With isotropic sources and charge-exchange scattering, the integral transport equation becomes

$$\psi(\mathbf{r},\mathbf{\Omega}) = \psi_{in}(\mathbf{r_S},\mathbf{\Omega})\exp\left(-\tau(\mathbf{r},\mathbf{r_S})\right) + \int_0^{R_S} dl\frac{q(\mathbf{r}-l\mathbf{\Omega})}{4\pi}\exp\left(-\tau(\mathbf{r},\mathbf{r}-l\mathbf{\Omega})\right). \qquad (2.4)$$

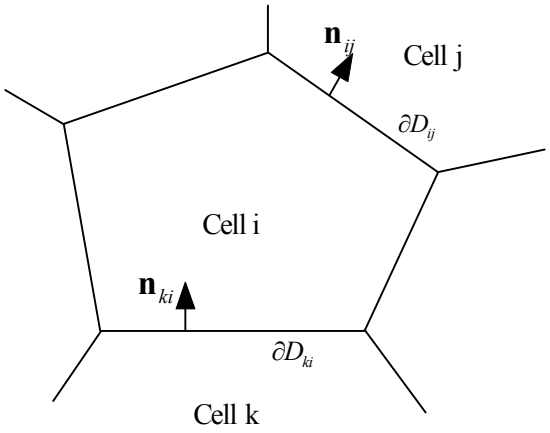

Figure 2.2. Schematic diagram for TEP methodology

Integrating over Ω over a 4π solid angle, we obtain scalar flux

$$\phi(\mathbf{r}) = \int_{D_i} d\mathbf{r}' \frac{q(\mathbf{r}')\exp(-\tau(\mathbf{r},\mathbf{r}'))}{4\pi|\mathbf{r}-\mathbf{r}'|^2} + \int_{\partial D_i} dS\,\psi_{in}(\mathbf{r}_S,\boldsymbol{\Omega})\frac{\exp(-\tau(\mathbf{r},\mathbf{r}_S))}{|\mathbf{r}-\mathbf{r}_S|^2}(\boldsymbol{\Omega}\cdot\mathbf{n}_-), \qquad (2.5)$$

where $\mathbf{n}_-$ is the inward normal unit vector at the boundary.

2.2 2D TEP equations

Starting from subdividing the region of interest into a number of convex polygons or cells, we calculate neutral transport within each single cell in which the background plasma properties can be treated as a constant. As shown in Figure 2.2, we consider an arbitrary cell i bounded by surface $\partial D_i = \sum_j \partial D_{ij}$, where ∂D_{ij} is the interface between cell i and the adjacent cell j.

First we define the total partial current from cell i into adjacent cell j, $\Gamma_{i,j}$ as

$$\Gamma_{i,j} = \int_{\partial D_{ij}} dS_{ij} \int_{\boldsymbol{\Omega}\cdot\mathbf{n}_{ij}>0} d\boldsymbol{\Omega}(\boldsymbol{\Omega}\cdot\mathbf{n}_{ij})\psi(\mathbf{r}_{ij},\boldsymbol{\Omega}), \qquad (2.6)$$

where $\mathbf{n}_{ij}$ is the outward normal (out of cell i) at interface ∂D_{ij}, and insert Eq. 2.4 into Eq.

2.6, we obtain

$$\begin{aligned}\Gamma_{i,j} &= \int_{\partial D_{ij}} dS_{ij} \int_{\mathbf{\Omega}\cdot\mathbf{n}_{ij}>0} d\mathbf{\Omega}(\mathbf{\Omega}\cdot\mathbf{n}_{ij})\Big[\psi_{in}(\mathbf{r}_S,\mathbf{\Omega})\exp\left(-\Sigma_t|\mathbf{r}_{ij}-\mathbf{r}_S|\right) \\ &\quad + \int_0^{R_b} dl \frac{q(\mathbf{r}_{ij}-l\mathbf{\Omega})}{4\pi}\exp\left(-\Sigma_t l\right)\Big] \\ &= \sum_k \int_{\partial D_{ij}} dS_{ij} \int_{\partial D_{ik}} dS_{ik}(\mathbf{\Omega}\cdot\mathbf{n}_{ij})\frac{(\mathbf{\Omega}\cdot\mathbf{n}_{ki})}{|\mathbf{r}_{ij}-\mathbf{r}_{ik}|^2}\psi(\mathbf{r}_{ik},\mathbf{\Omega})\exp\left(-\Sigma_t|\mathbf{r}_{ij}-\mathbf{r}_{ik}|\right) \\ &\quad + \int_{\partial D_{ij}} dS_{ij} \int_{D_i} dr \frac{q(r)}{4\pi|\mathbf{r}-\mathbf{r}_{ij}|^2}\exp\left(-\Sigma_t|\mathbf{r}-\mathbf{r}_{ij}|\right)(\mathbf{\Omega}\cdot\mathbf{n}_{ij}).\end{aligned} \tag{2.7}$$

Eq. 2.7 can be written in more concise form,

$$\Gamma_{i,j} = \sum_k \Gamma_{k,i} T^i_{k,j} + Q_i P_{0,i}\Lambda_{ij}. \tag{2.8}$$

where we define coefficients $T^i_{k,j}$,$P_{0,i}$,Λ_{ij} and the total volumetric source Q_i as

$$T^i_{k,j} = \frac{1}{\Gamma_{k,i}} \int_{\partial D_{ij}} dS_{ij} \int_{\partial D_{ik}} dS_{ik}(\mathbf{\Omega}\cdot\mathbf{n}_{ij})\frac{(\mathbf{\Omega}\cdot\mathbf{n}_{ki})}{|\mathbf{r}_{ij}-\mathbf{r}_{ik}|^2}\psi(\mathbf{r}_{ik},\mathbf{\Omega})\exp\left(-\Sigma_t|\mathbf{r}_{ij}-\mathbf{r}_{ik}|\right), \tag{2.9a}$$

$$P_{0,i} = \frac{1}{Q_i} \int_{\partial D_i} dS_i \int_{D_i} dr \frac{q(\mathbf{r})}{4\pi|\mathbf{r}-\mathbf{r}_i|^2}\exp\left(-\Sigma_t|\mathbf{r}-\mathbf{r}_i|\right)(\mathbf{\Omega}\cdot\mathbf{n}_+), \tag{2.9b}$$

$$\Lambda_{ij} = \frac{1}{Q_i P_{0,i}} \int_{\partial D_{ij}} dS_{ij} \int_{D_i} dr \frac{q(\mathbf{r})}{4\pi|\mathbf{r}-\mathbf{r}_{ij}|^2}\exp\left(-\Sigma_t|\mathbf{r}-\mathbf{r}_{ij}|\right)(\mathbf{\Omega}\cdot\mathbf{n}_{ij}), \tag{2.9c}$$

and

$$Q_i = \int_{D_i} d\mathbf{r} q(\mathbf{r}). \tag{2.10}$$

Apparently, the first term in the right hand side of Eq. 2.8 represents the uncollided flux from all the adjacent cells, the second term is the contribution from the volumetric source.

2.2.1 Transmission probability

A physical interpretation comes from Eq. 2.9a: $dS_{ik}\psi(\mathbf{r}_{ik},\mathbf{\Omega})(\mathbf{\Omega}\cdot\mathbf{n}_{ki})/\Gamma_{k,i}\cdot dS_{ij}(\mathbf{\Omega}\cdot\mathbf{n}_{ij})$ $/|\mathbf{r}_{ij}-\mathbf{r}_{ik}|^2 = dS_{ik}d\Omega\psi(\mathbf{r}_{ik},\mathbf{\Omega})(\mathbf{\Omega}\cdot\mathbf{n}_{ki})/\Gamma_{k,i}$ is the probability that neutrals entering from interface ∂D_{ik} will emit at $\mathbf{r}_{ik}$ about dS_{ik} and in direction $\mathbf{\Omega}$ about $d\mathbf{\Omega}$, $\exp\left(-\Sigma_t|\mathbf{r}_{ij}-\mathbf{r}_{ik}|\right)$ is the probability that neutral born at $\mathbf{r}_{ik}$ and in direction $\mathbf{\Omega}$ will transmit to $\mathbf{r}_{ij}$ without a

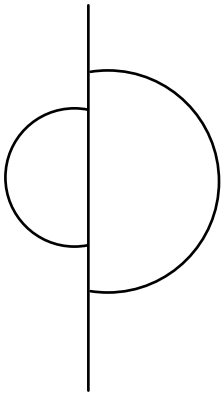

Figure 2.3. Schematic diagram for the DP_0 approximation

collision. Thus, the transmission probability $T^i_{k,j}$ defined in Eq. 2.9a is the probability for particles uncollidedly traveling from cell *k* to cell *j* through cell *i* without a collision.

In order to evaluate transmission probability $T^i_{k,j}$, we make the following assumptions: 1) the angular distribution of the flux at interface ∂D_{ik} is isotropic in the inward hemisphere; 2) the spatial distribution of the angular flux at interfaces is uniform. When we evaluate transmission probabilities for cell *k*, we again need to assume that the outward angular flux (actually it is inward direction for cell *k*) at interface ∂D_{ik} is isotropic, but it may the have different magnitude from the inward direction as shown in Figure 2.3. Thus the first assumption is usually called Double P_0 or DP_0 approximation. Now we denote $\psi(\mathbf{r}_{ik}, \mathbf{\Omega}) = \psi_0$, then $\Gamma_{k,i}$, the total incoming partial current at interface ∂D_{ik} is

$$\Gamma_{k,i} = \int_{\partial D_{ik}} dS_{ik} \int_{\mathbf{\Omega}\cdot\mathbf{n}_{ki}>0} d\mathbf{\Omega}(\mathbf{\Omega}\cdot\mathbf{n}_{ki})\psi(\mathbf{r}_{ik}, \mathbf{\Omega}) = \pi\psi_0 L_{ik}, \tag{2.11}$$

and transmission probability $T^i_{k,j}$ may be simplified as

$$\begin{aligned} T^i_{k,j} &= \frac{1}{\pi\psi_0 L_{ik}} \int_0^{L_{ik}} dx_{ik} \int_{\phi_{\min}(x_{ik})}^{\phi_{\max}(x_{ik})} d\phi \int_0^{\frac{\pi}{2}} d\theta \psi_0 \mathbf{\Omega}\cdot\mathbf{n}_{ki} \exp\left(-\frac{\Sigma_t l(x_{ik},\phi)}{\sin\theta}\right) \\ &= \frac{2}{\pi L_{ik}} \int_0^{L_{ik}} dx_{ik} \int_{\phi_{\min}(x_{ik})}^{\phi_{\max}(x_{ik})} d\phi \cos\phi Ki_3(\Sigma_t l(x_{ik},\phi)), \end{aligned} \tag{2.12}$$

where, as shown in Figure 2.4, L_{ik} is the length of interface ∂D_{ik}, $\phi_{\min}(x_{ik})$ and $\phi_{\max}(x_{ik})$ are the integral limits for the angular variable, and $l(\mathbf{r}_{ki}, \phi)$ is just the distance traveled by a

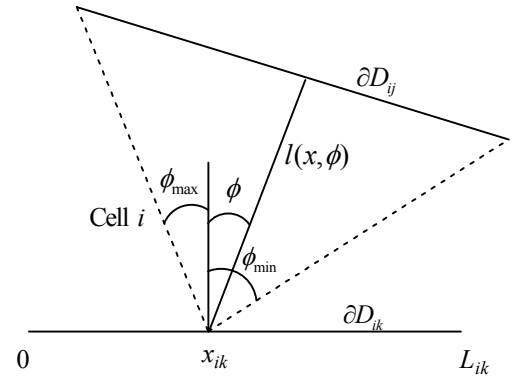

Figure 2.4. Planar projection of geometry for calculation of transmission probability in 2D

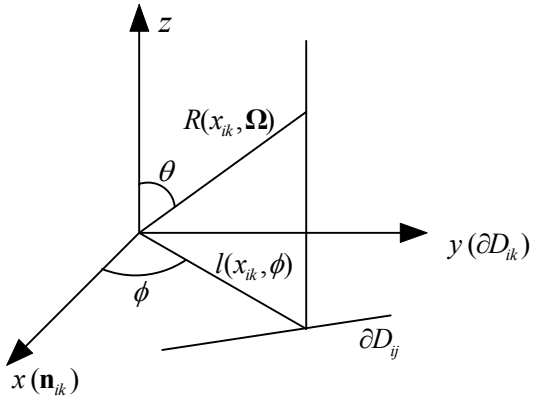

Figure 2.5. 3D geometry for calculation of transmission probability

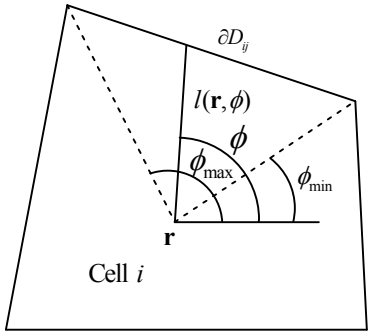

Figure 2.6. Geometry for calculate escape probability

neutral in the 2D plane and Ki_3 is the third order Bickley-Naylor function,

$$Ki_n(x) = \int_0^{\frac{\pi}{2}} d\theta \sin^{n-1}\theta \exp\left(-\frac{x}{\sin\theta}\right). \tag{2.13}$$

2.2.2 Escape probability

The coefficient defined in Eq. 2.9b also has a physical meaning: $q(\mathbf{r})d\mathbf{r}/Q_i \cdot dS_{ik}(\mathbf{\Omega} \cdot \mathbf{n}_{ki})/4\pi|\mathbf{r} - \mathbf{r}_{ik}|^2 = q(\mathbf{r})d\mathbf{r}/Q_i \cdot d\mathbf{\Omega}/4\pi$ is the probability that neutrals are born at $\mathbf{r}$ about $d\mathbf{r}$ in direction $\mathbf{\Omega}$ about $d\mathbf{\Omega}$; $\exp(-\Sigma_t|\mathbf{r} - \mathbf{r}_i|)$ is the probability that a neutral born at $\mathbf{r}_{ik}$ and in direction $\mathbf{\Omega}$ will escape to the adjacent regions without a collision. Thus $P_{0,i}$ is just the first-flight escape probability that neutrals born (volumetric sources) in cell i will escape from cell i without a collision with cell i. Similarly, the coefficient Λ_{ij} defined in Eq. 2.9c is the directional escape probability that a neutral born in and escaping from cell i will escape into the adjacent region j.

With the assumption that volumetric sources are uniformly distributed in cell i (flat flux assumption), we yield

$$\begin{aligned} P_{0,i} &= \frac{1}{4\pi S_i}\int_{D_i} d\mathbf{r}\int_{4\pi} d\mathbf{\Omega}\exp\left(-\frac{\Sigma_t l(\mathbf{r},\phi)}{\sin\theta}\right) \\ &= \frac{1}{4\pi S_i}\int_{D_i} d\mathbf{r}\int_0^{2\pi} d\phi\int_0^{\pi} d\theta\sin\theta\exp\left(-\frac{\Sigma_t l(\mathbf{r},\phi)}{\sin\theta}\right) \\ &= \frac{1}{2\pi S_i}\int_{D_i} d\mathbf{r}\int_{2\pi} d\phi Ki_2(\Sigma_t l(\mathbf{r},\phi)), \end{aligned} \tag{2.14}$$

and

$$\begin{aligned}\Lambda_{ij} &= \frac{1}{4\pi S_i P_{0,i}} \int_{D_i} d\mathbf{r} \int_{\phi^j_{\min}(\mathbf{r})}^{\phi^j_{\max}(\mathbf{r})} d\phi \int_0^{\pi} d\theta \sin\theta \exp\left(-\frac{\Sigma_t l(\mathbf{r},\phi)}{\sin\theta}\right) \\ &= \frac{1}{2\pi S_i P_{0,i}} \int_{D_i} d\mathbf{r} \int_{\phi^j_{\min}(\mathbf{r})}^{\phi^j_{\max}(\mathbf{r})} d\phi Ki_2\left(\Sigma_t l\left(\mathbf{r},\phi\right)\right).\end{aligned} \tag{2.15}$$

However, it is computationally expensive to calculate these first flight escape probabilities and the directional escape probabilities. Usually, a rational approximation for calculation of $P_{0,i}$ can achieve both high efficiency and accuracy.

$$P_{0,i} = \frac{1}{X}\left[1 - \left(1 + \frac{X}{n}\right)^{-n}\right], \tag{2.16}$$

where $X = 4S_i\Sigma_t/L_i$, S_i is the area of cell i and L_i is the perimeter of cell i and exponent $n = 2.09$ is resulted from comparisons with Monte Carlo calculations [27]. For the case of a cylinder, $n = 4.58$ is better. The directional escape probability is assumed to be proportional to L_{ij} , the length of interface ∂D_{ij}, i.e.

$$\Lambda_{ij} = \frac{L_{ij}}{L_i}. \tag{2.17}$$

2.2.3 Final forms of the TEP equations

However, the total volumetric source Q_i used in Eq. 2.8 is still unknown. In order to eliminate Q_i, we first need to determine its relation with S^i_{ext}, the total external volumetric source and $\{\Gamma_{k,i}, k = 1, ...\}$, the incoming total partial current from all the adjacent cells. Keep in mind that

$$q(\mathbf{r}) = \Sigma_{cx}\phi(\mathbf{r}) + S_{ext}(\mathbf{r}) = \Sigma_{cx}\phi(\mathbf{r}) + \frac{S^i_{ext}}{S_i}, \tag{2.18}$$

where S_i is the area of region i.

Inserting Eq. 2.5 into Eq. 2.18, we have

$$\begin{aligned} Q_i &= \int_{D_i} d\mathbf{r} q(\mathbf{r}) = \int_{D_i} d\mathbf{r} \left(\Sigma_{cx} \phi(\mathbf{r}) + \frac{S^i_{ext}}{S_i} \right) \\ &= S^i_{ext} + \int_{D_i} d\mathbf{r} \Sigma_{cx} \Big[\int_{D_i} d\mathbf{r}' \frac{q(\mathbf{r}') \exp\left(-\Sigma_t |\mathbf{r} - \mathbf{r}'|\right)}{4\pi |\mathbf{r} - \mathbf{r}'|^2} \\ &+ \int_{\partial D_i} dS \psi_{in}(\mathbf{r}_S, \mathbf{\Omega}) \frac{\exp\left(-\Sigma_t |\mathbf{r} - \mathbf{r}_S|\right)}{|\mathbf{r} - \mathbf{r}_S|^2} (\mathbf{\Omega} \cdot \mathbf{n}_-) \Big], \end{aligned} \tag{2.19}$$

using DP_0 and the flat flux assumption, it is possible to write the total volumetric source as

$$\begin{aligned} Q_i &= S^i_{ext} + Q_i \frac{\Sigma_{cx}}{\Sigma_t} \frac{\Sigma_t}{S_i} \int_{D_i} d\mathbf{r} \int_{D_i} d\mathbf{r}' \frac{\exp\left(-\Sigma_t |\mathbf{r} - \mathbf{r}'|\right)}{4\pi |\mathbf{r} - \mathbf{r}'|^2} \\ &+ \sum_k \Gamma_{k,i} \frac{\Sigma_{cx}}{\Sigma_t} \frac{\Sigma_t}{\pi L_{ki}} \int_{D_i} d\mathbf{r} \int_{\partial D_{ik}} dS_{ik} \frac{\exp\left(-\Sigma_t |\mathbf{r} - \mathbf{r}_{ik}|\right)}{|\mathbf{r} - \mathbf{r}_{ik}|^2} (\mathbf{\Omega} \cdot \mathbf{n}_{ki}) \\ &= S^i_{ext} + Q_i c_i P1_{ii} + \sum_k \Gamma_{k,i} c_i P2_{ki}, \end{aligned} \tag{2.20}$$

where coefficients $P1_{ii}$, $P2_{ki}$ and c_i are defined in the following equations.

$$P1_{ii} = \frac{\Sigma_t}{S_i} \int_{D_i} d\mathbf{r} \int_{D_i} d\mathbf{r}' \frac{\exp\left(-\Sigma_t |\mathbf{r} - \mathbf{r}'|\right)}{4\pi |\mathbf{r} - \mathbf{r}'|^2}, \tag{2.21a}$$

$$P2_{ki} = \frac{\Sigma_t}{\pi L_{ki}} \int_{D_i} d\mathbf{r} \int_{\partial D_{ik}} dS_{ik} \frac{\exp\left(-\Sigma_t |\mathbf{r} - \mathbf{r}_{ik}|\right)}{|\mathbf{r} - \mathbf{r}_{ik}|^2} (\mathbf{\Omega} \cdot \mathbf{n}_{ki}), \tag{2.21b}$$

$$c_i = \frac{\Sigma_{cx}}{\Sigma_t}. \tag{2.22}$$

Now we change dummy variables in the integral of Eq. 2.21a by $d\mathbf{r}' = R^2 dR d\mathbf{\Omega} =$

$(l/\sin\theta)^2 \cdot (dl/\sin\theta)d\mathbf{\Omega}$, then integrate along the neutral trajectory, we obtain

$$\begin{aligned}
P1_{ii} &= \frac{\Sigma_t}{4\pi S_i}\int\limits_{D_i} d\mathbf{r}\int\int\limits_{4\pi}\frac{dl}{\sin\theta}d\mathbf{\Omega}\exp\left(-\frac{\Sigma_t l}{\sin\theta}\right)\\
&= \frac{\Sigma_t}{2\pi S_i}\int\limits_{D_i} d\mathbf{r}\int\limits_{2\pi} d\phi\int dlKi_1\left(\Sigma_t l\right)\\
&= \frac{1}{2\pi S_i}\int\limits_{D_i} d\mathbf{r}\int\limits_{2\pi} d\phi\left(1-Ki_2\left(\Sigma_t l(\mathbf{r},\phi)\right)\right)\\
&= 1-\frac{1}{2\pi S_i}\int\limits_{D_i} d\mathbf{r}\int\limits_{2\pi} d\phi Ki_2\left(\Sigma_t l\left(\mathbf{r},\phi\right)\right)\\
&= 1-P_{0,i}.
\end{aligned} \tag{2.23}$$

During the derivation we used the differential property $dKi_n(x)/dx = -Ki_{n-1}(x)$ and $Ki_2(0) = 1$.

Similarly,

$$\begin{aligned}
P2_{ki} &= \frac{\Sigma_t}{\pi L_{ki}}\int\limits_{D_i} d\mathbf{r}\int\limits_{\partial D_{ik}} dS_{ik}\frac{\exp\left(-\Sigma_t\left|\mathbf{r}-\mathbf{r}_{ik}\right|\right)}{\left|\mathbf{r}-\mathbf{r}_{ik}\right|^2}\left(\mathbf{\Omega}\cdot\mathbf{n}_{ki}\right)\\
&= \frac{\Sigma_t}{\pi L_{ki}}\int\limits_{\partial D_{ik}} dS_{ik}\int\int\limits_{4\pi}\frac{dl}{\sin\theta}d\mathbf{\Omega}\exp\left(-\frac{\Sigma_t l}{\sin\theta}\right)\left(\mathbf{\Omega}\cdot\mathbf{n}_{ki}\right)\\
&= \frac{1}{\pi L_{ki}}\int\limits_{\partial D_{ik}} dS_{ik}\int\limits_{4\pi} d\mathbf{\Omega}\left[1-\exp\left(-\frac{\Sigma_t l(\mathbf{r}_{ki},\phi)}{\sin\theta}\right)\right]\left(\mathbf{\Omega}\cdot\mathbf{n}_{ki}\right)\\
&= 1-\frac{1}{\pi L_{ki}}\int\limits_{\partial D_{ik}} dS_{ik}\int\limits_{4\pi} d\mathbf{\Omega}\exp\left(-\frac{\Sigma_t l(\mathbf{r}_{ki},\phi)}{\sin\theta}\right)\left(\mathbf{\Omega}\cdot\mathbf{n}_{ki}\right)\\
&= 1-\frac{1}{\pi L_{ki}}\int\limits_{\partial D_{ik}} dS_{ik}\int\limits_{\partial D_i}\frac{dS_i\left(\mathbf{\Omega}\cdot\mathbf{n}_{+}\right)}{\left|\mathbf{r}_i-\mathbf{r}_{ik}\right|}\exp\left(-\Sigma_t\left|\mathbf{r}_i-\mathbf{r}_{ik}\right|\right)\left(\mathbf{\Omega}\cdot\mathbf{n}_{ki}\right)\\
&= 1-\sum_l\frac{1}{\pi L_{ki}}\int\limits_{\partial D_{ik}} dS_{ik}\int\limits_{\partial D_{il}}\frac{dS_{il}\left(\mathbf{\Omega}\cdot\mathbf{n}_{il}\right)}{\left|\mathbf{r}_{il}-\mathbf{r}_{ik}\right|}\exp\left(-\Sigma_t\left|\mathbf{r}_{il}-\mathbf{r}_{ik}\right|\right)\left(\mathbf{\Omega}\cdot\mathbf{n}_{ki}\right)\\
&= 1-\sum_l T^i_{k,l}.
\end{aligned} \tag{2.24}$$

Substitute Eqs. 2.23 and 2.24 into Eq. 2.20, we have

$$[1-c_i(1-P_{0,i})]Q_i = S^i_{ext}+\sum_k(1-\sum_l T^i_{k,l})c_i\Gamma_{k,i}, \tag{2.25}$$

or

$$Q_i = \frac{S^i_{ext} + \sum_k (1 - \sum_l T^i_{k,l}) c_i \Gamma_{k,i}}{1 - c_i(1 - P_{0,i})}. \tag{2.26}$$

Insert Q_i back into Eq. 2.8 and define the total escape probability,

$$P_i = \frac{P_{0,i}}{1 - c_i(1 - P_{0,i})}. \tag{2.27}$$

Finally, the TEP equations can be written as

$$\Gamma_{i,j} = \sum_k T^i_{k,j} \Gamma_{k,i} + \sum_k \Gamma_{k,i} \left(1 - \sum_l T^i_{k,l}\right) c_i P_i \Lambda_{ij} + S^i_{ext} P_i \Lambda_{ij}. \tag{2.28}$$

The first term of Eq. 2.28 represents the sum of the partial currents entering cell *i* from all the adjacent cells and being directly transmitted to region *j* without a collision with cell *i*. The second term is the sum of the partial current entering cell *i* from all the adjacent cells and having one or more charge-exchange scattering with cell *i* and finally exiting into cell *j*. The third term is the contribution of the external volumetric sources and their progenies.

The most salient feature of TEP method is that the exiting flux from a cell is only dependent on the incoming fluxes entering that cell from all the adjacent cells. Thus, the transmission coefficient matrix is sparse, with the number of nonzero elements growing linearly with the number of cells. Secondly, the shape of cells is arbitrary , so we can choose whatever shape in order to match the local geometry.

2.3 Boundary conditions

There are two kinds of boundary for neutral transport in tokamaks: wall and core plasma region. The former refers to the material surfaces surrounding the plasma. The latter is the part of plasma where neutrals get ionized or scattered back once they enter in, so it is computationally efficient to treat these core plasma regions as albedo boundary.

2.3.1 Wall boundary

When ions or neutrals hit the wall, the most important particle-surface interaction processes [28], which couple to the neutral transport as sources or sinks, are backscattering, desorption and absorption. In the first process, a neutral is recoiled back with a significant fraction

of the impact energy after suffering several elastic collisions with the target material. In the second process, neutral particles are implanted in the near surface, where they will reach thermal equilibrium with the wall material and subsequently be released as thermal molecules due to either direct particle-surface collisions or collisions of sputtered and backscattered particles. Absorption means the incident particles are permanently trapped inside the material wall. Usually the mean free path of the re-emitted thermal molecules is very small and they disassociate as Franck-Condon atoms with an energy of a few electron volts near the wall surface, so we may approximately treat these neutrals as a slow group of neutrals backscattered from the wall segments.

The particle and energy reflection coefficients R_N and R_E, which depend on the impact energy E_0, impact and substrate species, are two of the most important back-scattering data [29]. The particle reflection coefficient R_N is defined as to be the ratio of the number N of all reflected particles to the total number N_0 of incident particles,

$$R_N = \frac{N}{N_0}. \tag{2.29}$$

The energy reflection coefficient R_E is defined as to be the total energy of the reflected particles divided by the total energy of the incident particles, so the average energy of the back-scattered particles is

$$\overline{E} = \frac{R_E}{R_N} E_0. \tag{2.30}$$

The total reflection flux from the wall segment *kw* to the cell *i* can be written as

$$\Gamma_{kw,i} = \Gamma_{ext}^{kw} + R_N^{kw}\Gamma_{i,kw} + \left(1 - R_N^{kw}\right)\left(1 - f_{abs}^{kw}\right)\Gamma_{i,kw}, \tag{2.31}$$

where R_{kw} is the particle reflection coefficient for the wall segment *kw*, f_{abs}^{kw} is the fraction that particles are permanently trapped inside the wall material.

In Eq. 2.31, the first term is the external flux, the second term represents back-scattered flux with energy $\overline{E}$, and the last term represents the flux due to Franck-Condon atoms.

2.3.2 Albedo boundary

The mean free path of neutrals in core plasma regions is extremely small due to the large plasma densities, so these regions can be treated as a semi-infinite half-space. The reflected flux from a core plasma region can set be to equal to albedo, α, times the incident flux to the same region. Originally one-speed diffusion theory was exploited to calculate the albedo coefficient [30],

$$\alpha = \frac{1 - \frac{2}{\sqrt{3}}\sqrt{c_i^{-1} - 1}}{1 + \frac{2}{\sqrt{3}}\sqrt{c_i^{-1} - 1}}. \tag{2.32}$$

Eq. 2.32 has been found to be accurate if charge-exchange fraction c is greater that 0.9. However, the results of Eq.2.32 would be significant lower than the Monte Carlo calculations when c is smaller than 0.9, and even become negative when c is small than 0.57. The following fit to albedo coefficient based on data from Monte Carlo simulations is found to be very accurate for the entire range of charge-exchange fraction c as shown in Figure 2.6.

$$\alpha(c) = \frac{0.00059720174 + 0.2045041c - 0.3818644c^2 + 0.1769341c^3}{1 - 2.46848679c + 1.9744939c^2 - 0.505836c^3}. \tag{2.33}$$

2.4 The assumptions of TEP method and their limitation

The TEP method has been successfully implemented into the 2D neutral transport code GTNEUT [24]. The accuracy and performance of the TEP methodology and the GTNEUT code have been extensively investigated by comparison with Monte Carlo simulations for a variety of model problems and against realistic DIII-D experimental measurements [26]. These comparisons have demonstrated that the GTNEUT is an accurate and economic tool for simulation of neutral transport in realistic divertors and edge plamas. The sensitivity of the approximations made in the TEP methodology has been tested for a specially designed 9-region problems shown in Figure 2.8 over a wide range of the ratio Δ/λ, where Δ is the characteristic dimension of a computational region and λ is the mean free path of neutrals

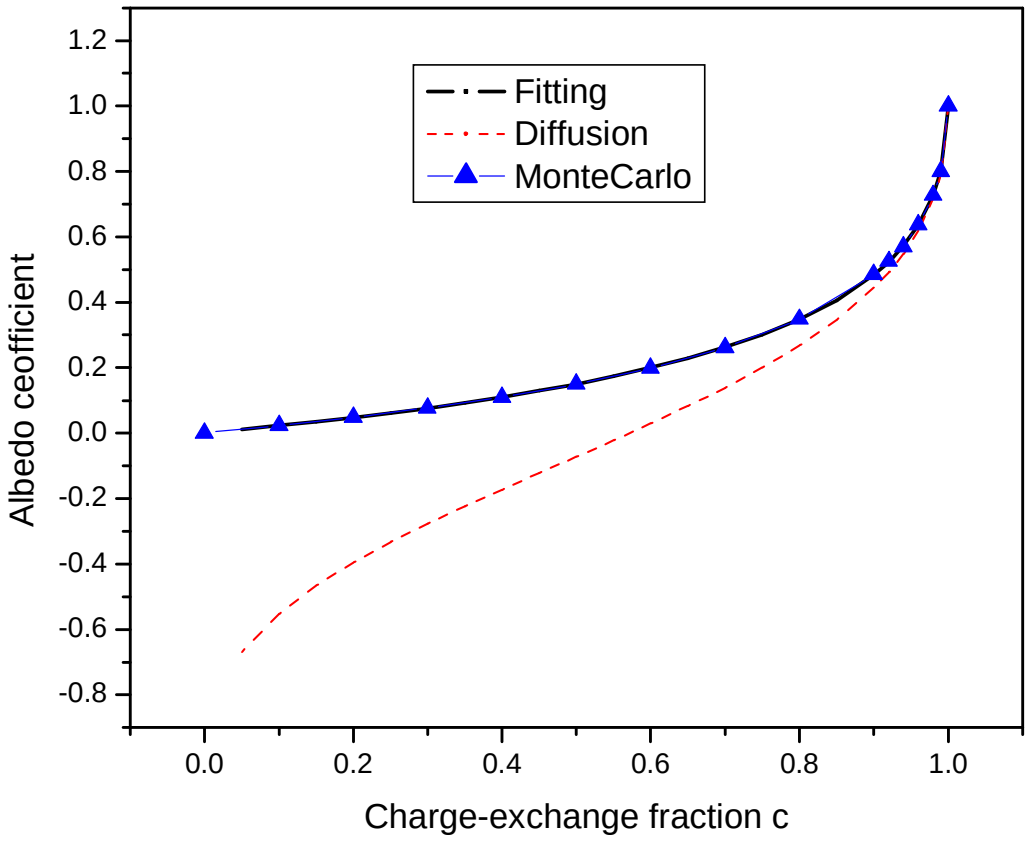

Figure 2.7. Comparison of albedo coefficients calculated by different methods

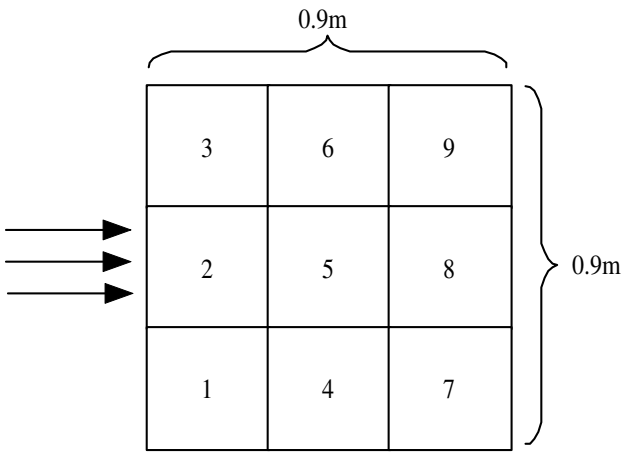

Figure 2.8. Nine uniform square regions model

in that region. The tests have shown that the predictions of the GTNEUT code agree very well with the calculations of the Monte Carlo code DEGAS as we can see from Figure 2.9, where $\Delta/\lambda = 1$. However the agreement deteriorates when $\Delta/\lambda < 1$, which drives the strong anisotropy of the angular fluxes, or when $\Delta/\lambda > 1$, which results in the strong gradient of the charge-exchanged neutral source.

TEP method is accurate, subject to the following approximations:(1) DP_0 approximation, which assumes that angular flux at each interface is isotropic in both the outward and inward hemispheres; (2) Flat collision source approximation, which assumes that scalar flux within each computational region is uniform. (3) Local ion temperature approximation, which assumes that neutral energy in each cell is equal to the local ion temperature.

The DP_0 assumption would be reasonable if the incident neutrals were dominantly composed of the collided neutrals from the previous computation cell because charge-exchange events tend to randomize neutrals' angular distribution. However, the anisotropy may be driven by the attenuation in a strongly ionizing medium or by the wall reflection and the presence of sources in optically thin regions. Consequently the TEP methodology underpredicts the uncollided neutral flux as shown in Figure 2.10.

The first flight escape probability calculated by the rational approximation is found to be very accurate for a wide range of conditions, but the non-directional escape assumption

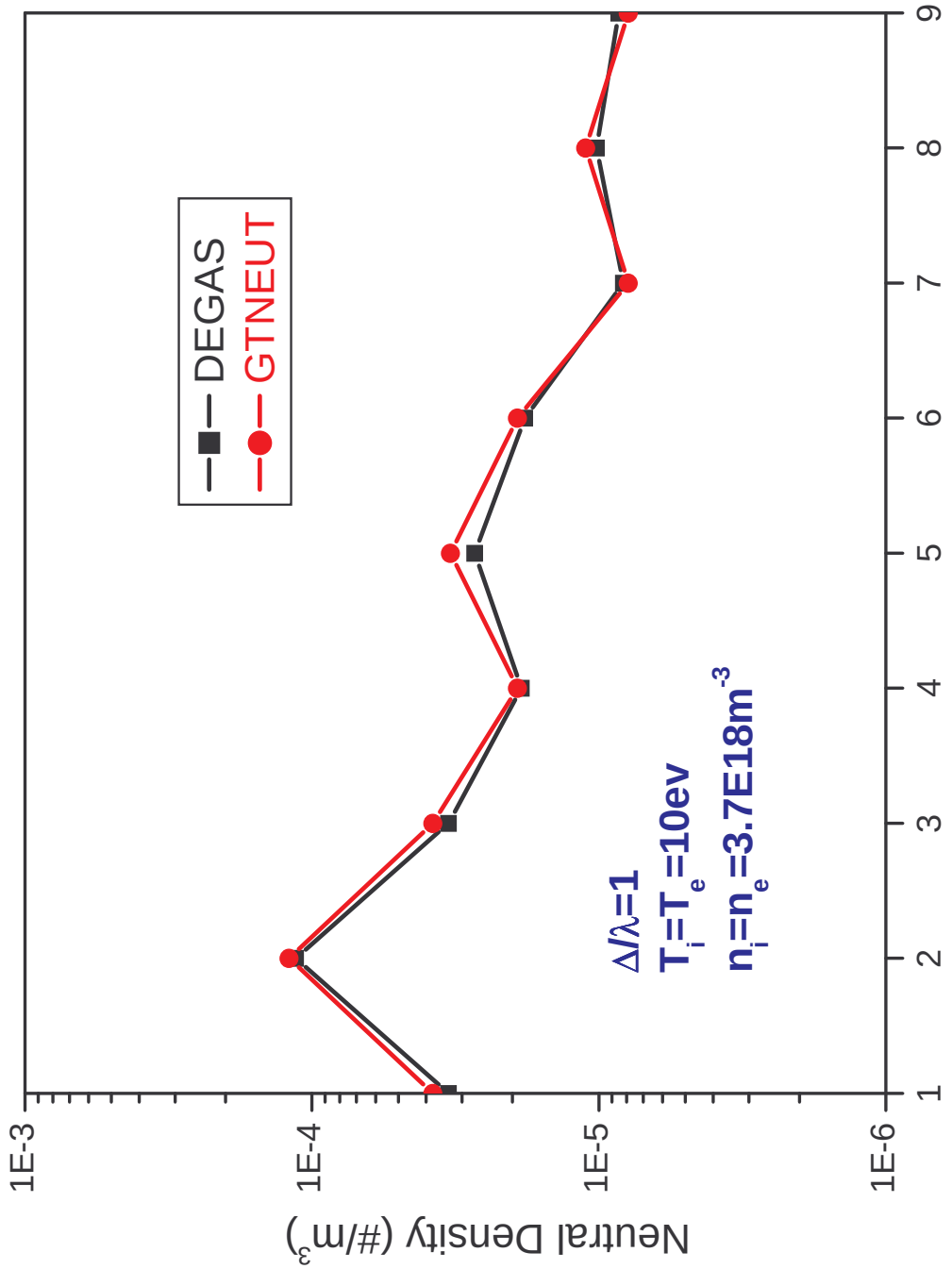

Figure 2.9. Good agreement of GTNEUT with DEGAS for a nine-region model with $\Delta/\lambda = 1$

is questionable when $\Delta/\lambda \gg 1$. In this case, the probability a collided neutral escapes back across the incident interface is larger than the probability that it escapes forward across the next interface. Due to failing to take this effect into account, Figure 2.11 shows the overestimation of the neutral penetration by the TEP method.

Extensive comparisons with Monte Carlo methods have shown the local ion temperature assumption is accurate if (1) the ion temperature varies slowly across many computational regions, or (2) most neutrals in a region have collided in that region. But if these conditions can not be satisfied, especially for the slow group of the reflected neutrals from the wall can penetrate very deep into the interested regions, a two-group or multi-group treatment is necessary.

The tests have also suggested that the refinements to the TEP methodology in the following two areas would improve its accuracy for the extreme conditions: (1) calculation of transmission probabilities based on the linearly anisotropic or the higher order approximation of the incident angular distribution when $\Delta/\lambda \ll 1$, and (2) calculation of the directional escape probabilities with taking into account that the charge-exchanged source is predominately distributed near the incident surface when $\Delta/\lambda \gg 1$.

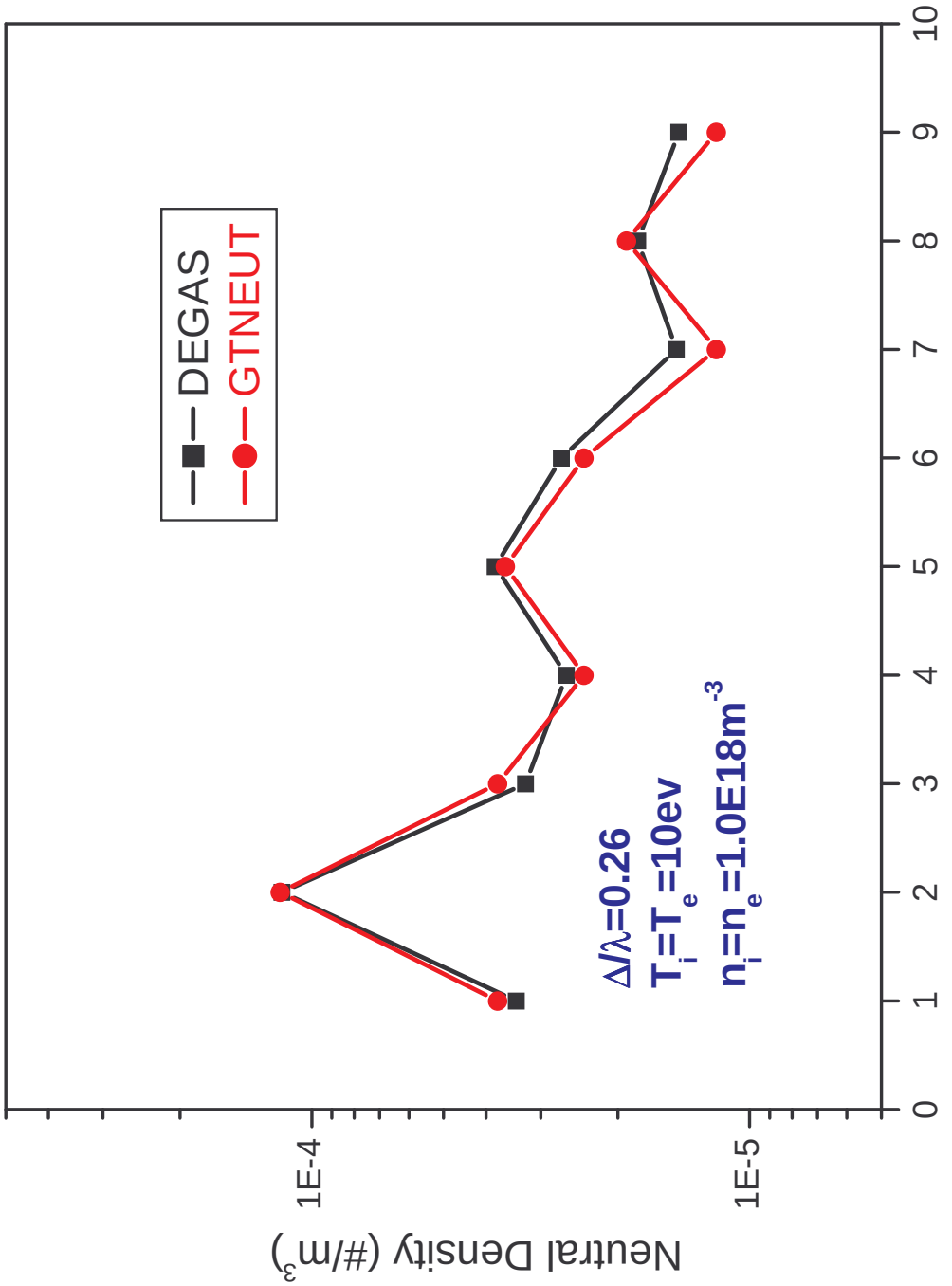

Figure 2.10. Under-prediction of GTNEUT for a nine-region model with $\Delta/\lambda = 0.26$

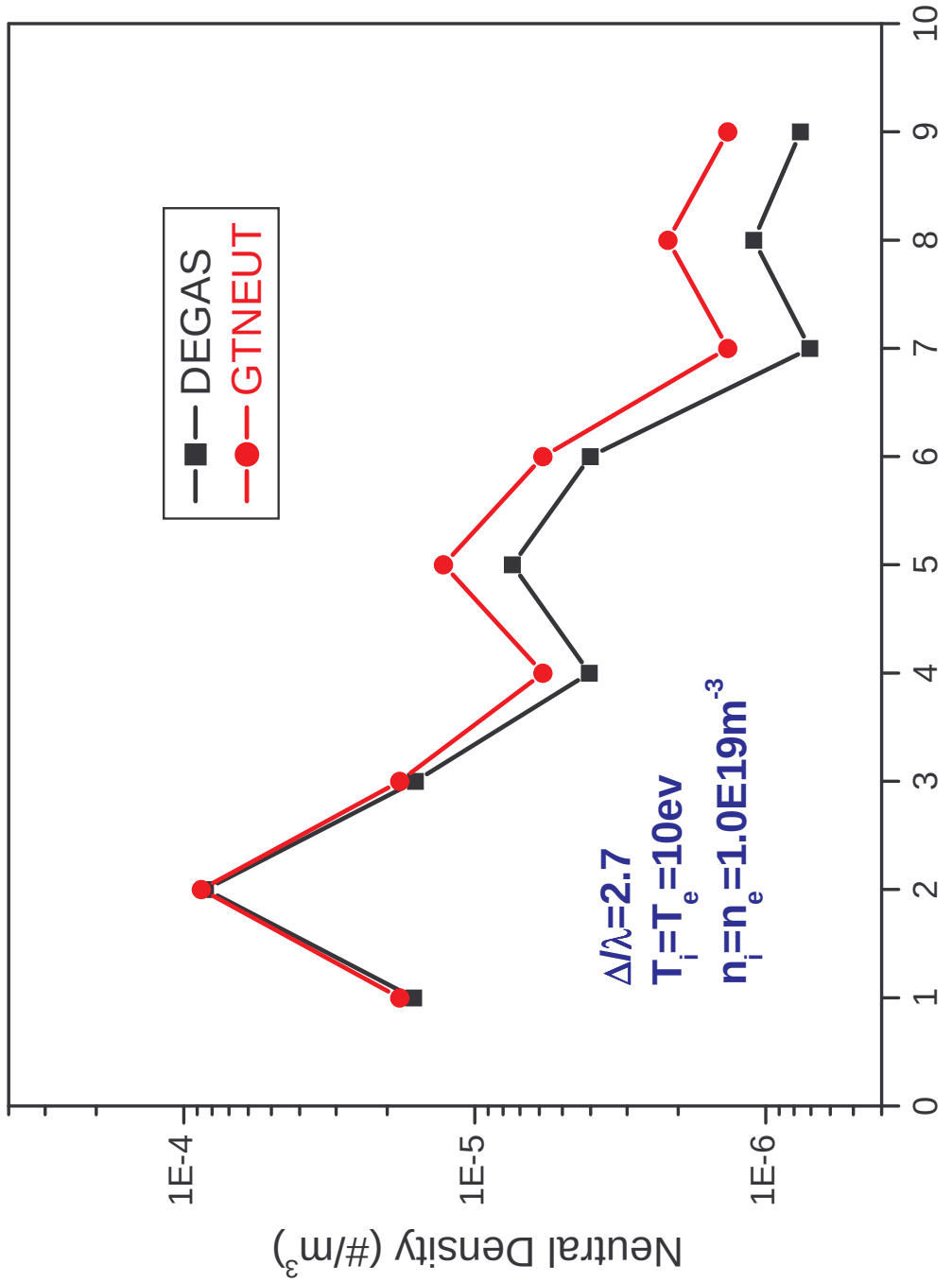

Figure 2.11. Over-prediction of GTNEUT for a nine-region model with $\Delta/\lambda = 2.7$

CHAPTER 3

ANISOTROPIC TRANSMISSION PROBABILITIES

3.1 Introduction

As mentioned in the previous chapter, if the neutral flux crossing an interface predominately consisted of the collided neutrals immediately from the previous computational region, the assumption of an isotropic angular distribution would be reasonable. However, anisotropies may be driven in regions with long mean free path, or in the presence of sources, strongly ionizing plasmas or boundaries.

Take the problem shown in Figure 3.1 as an example. An isotropic neutral flux is imposed from the left boundary and the neutral mean free path is longer than the grid size. The angular distribution at the next interface will be somewhat peaked in the forward direction due to greater attenuation of particles with a large angle than a smaller angle relative to the normal to the surfaces. The original TEP methodology [22] assumed an isotropic particle distribution in the forward half-space (DP_0 approximation) at each successive interface. In fact, particles with a large angle to the normal are preferentially attenuated, and the distribution at successive interfaces will become more forward peaked, as illustrated in Figure 3.1. The DP_0 approximation does not account for the preferential attenuation of particles moving at large angles relative to the normal and consequently over-estimates the attenuation between successive interfaces. Thus, the angular flux will become increasingly forward-peaked. As a result, the DP_0 approximation leads to significant under-prediction of neutrals' penetration. This effect has been observed for the specially designed model problems [27] to test the validity of the DP_0 assumption.

In order to improve the validity of the TEP methodology for long mean free path regions,in which the above problem is most important, an expansion of the angular flux at interfaces in terms of the linearly (DP_1) or quadratically (DP_2) anisotropic representation functions will be adopted in this chapter, then the balance equation for each partial current

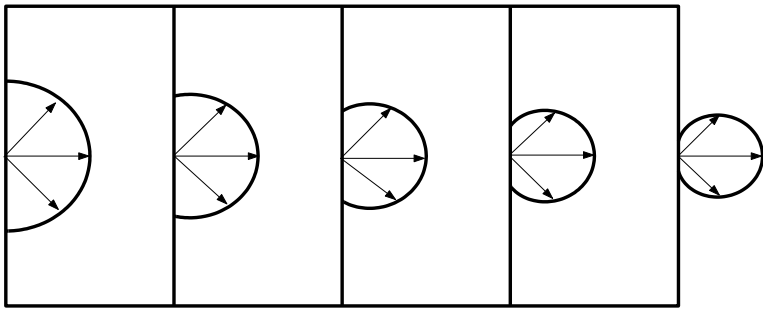

Figure 3.1. Anisotropy of angular flux in a 2D problem with long mean free path

moment associated with each expansion function will be developed. This is the standard technique [18, 19, 20] used to deal with the anisotropic neutron fluxes in fission reactors.

3.2 DP_N methodology

3.2.1 Basic equations

Taking the same approach as in the derivation of the original TEP methodology outlined in Chapter 2, we first subdivide the region of interest into relatively small cells, and then apply the integral transport equation to each cell. Again, our starting equations will be the integral forms of the angular flux at an interface and the scalar flux within cell D_i.

$$\psi(\mathbf{r},\mathbf{\Omega}) = \psi_{in}(\mathbf{r_S},\mathbf{\Omega})\exp\left(-\tau(\mathbf{r},\mathbf{r_S})\right) + \int_0^{R_S} dl \frac{q(\mathbf{r}-l\mathbf{\Omega})}{4\pi}\exp\left(-\tau(\mathbf{r},\mathbf{r}-l\mathbf{\Omega})\right), \qquad (3.1)$$

$$\phi(\mathbf{r}) = \int_{D_i} d\mathbf{r}' \frac{q(\mathbf{r}')\exp\left(-\tau(\mathbf{r},\mathbf{r}')\right)}{4\pi|\mathbf{r}-\mathbf{r}'|^2} + \int_{\partial D_i} dS\,\psi_{in}(\mathbf{r_S},\mathbf{\Omega})\frac{\exp\left(-\tau(\mathbf{r},\mathbf{r}_S)\right)}{|\mathbf{r}-\mathbf{r}_S|^2}(\mathbf{\Omega}\cdot\mathbf{n}_-), \qquad (3.2)$$

where $q(\mathbf{r},\mathbf{\Omega})$, $\mathbf{n}_-$ and τ have the same meaning as those defined in Chapter 2. The incoming flux $\psi_{in}(\mathbf{r},\mathbf{\Omega})$ is defined as

$$\psi_{in}(\mathbf{r}_s,\mathbf{\Omega}) = \psi_{i,j}(\mathbf{r}_s,\mathbf{\Omega}), \qquad \text{if } \mathbf{r}_s \in \partial D_{ij} \text{ and } \mathbf{\Omega}\cdot\mathbf{n}_{ij} < 0, \qquad (3.3)$$

where $\mathbf{n}_{ij}$ is the outward normal unit vector at interface ∂D_{ij}.

Assuming that the angular flux $\psi(\mathbf{r},\mathbf{\Omega})$ at an interface in the outward hemisphere can be expanded as a linear combination of a set of locally defined and orthonormal representation

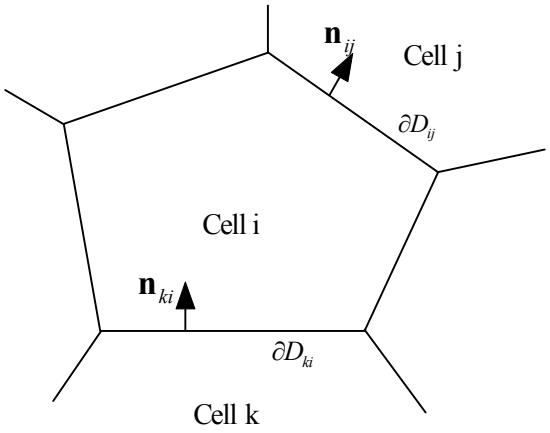

Figure 3.2. Schematic diagram for DP_N methodology

functions $\left\{\psi_{i,j}^{n}(\mathbf{r},\mathbf{\Omega})\,|n=0,1,\cdots;i=1,\cdots;j=\cdots\right\}$ [31, 32], we can write $\psi(\mathbf{r},\mathbf{\Omega})$ as

$$\psi(\mathbf{r},\mathbf{\Omega})=\sum_{n,i,j}\Gamma_{i,j}^{n}\psi_{i,j}^{n}(\mathbf{r},\mathbf{\Omega}). \tag{3.4}$$

The expansion functions $\psi_{i,j}^{n}(\mathbf{r},\mathbf{\Omega})$ are locally defined,

$$\psi_{i,j}^{n}(\mathbf{r},\mathbf{\Omega})=\begin{cases}\neq 0, & \text{if}\quad \mathbf{r}\in\partial D_{ij}\text{ and }\left(\mathbf{\Omega}\cdot\mathbf{n}_{ij}\right)>0;\\ =0, & \text{otherwise,}\end{cases} \tag{3.5}$$

and the expansion functions also satisfy the following orthogonal conditions,

$$\begin{aligned}\left\langle\psi_{i,j}^{n}(\mathbf{r},\mathbf{\Omega})\left|\psi_{i',j'}^{n'}(\mathbf{r},\mathbf{\Omega})\right.\right\rangle &= \int_{R^2}dS\int_{4\pi}d\mathbf{\Omega}\psi_{i,j}^{n}(\mathbf{r},\mathbf{\Omega})\,\psi_{i',j'}^{n'}(\mathbf{r},\mathbf{\Omega})\,|\mathbf{\Omega}\cdot\mathbf{n}_{+}|\\ &= \int_{\partial D_{ij}}dS_{ij}\int_{\mathbf{\Omega}\cdot\mathbf{n}_{i}j>0}d\mathbf{\Omega}\psi_{i,j}^{n}\left(\mathbf{r}_{ij},\mathbf{\Omega}\right)\psi_{i',j'}^{n'}\left(\mathbf{r}_{ij},\mathbf{\Omega}\right)\left(\mathbf{\Omega}\cdot\mathbf{n}_{ij}\right)\\ &= \frac{\delta_{nn'}\delta_{ii'}\delta_{jj'}}{\pi S_{ij}},\end{aligned} \tag{3.6}$$

where we define inner product for any two angular flux functions $\psi_1(\mathbf{r},\mathbf{\Omega})$ and $\psi_2(\mathbf{r},\mathbf{\Omega})$ as

$$\langle\psi_1(\mathbf{r},\mathbf{\Omega})\,|\psi_2(\mathbf{r},\mathbf{\Omega})\rangle=\int_{R^2}dS\int_{4\pi}d\mathbf{\Omega}\psi_1(\mathbf{r},\mathbf{\Omega})\,\psi_2(\mathbf{r},\mathbf{\Omega})\,|\mathbf{\Omega}\cdot\mathbf{n}_{+}|\,. \tag{3.7}$$

S_{ij} is the area of interface ∂D_{ij}, and $\delta_{nn'}$ is the Kroneker's delta.

$\Gamma_{i,j}^{n}$ is the n-th coefficient of the expansion. Taking the inner product with Eq. 3.4 and the representation function $\psi_{i,j}^{n}$ and making use of the orthonormal conditions, we can

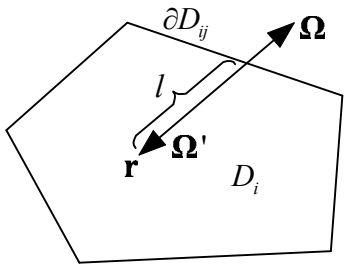

Figure 3.3. Optical paths used in DP_N approximation ray tracing

easily obtain

$$\begin{aligned}\left\langle \psi_{i,j}^{n} | \psi \right\rangle &= \left\langle \psi_{i,j}^{n} \left| \sum_{n',i',j'} \Gamma_{i',j'}^{n'} \psi_{i',j'}^{n'} \right. \right\rangle \\ &= \sum_{n',i',j'} \left\langle \psi_{i,j}^{n} \left| \Gamma_{i',j'}^{n'} \psi_{i',j'}^{n'} \right. \right\rangle \\ &= \sum_{n',i',j'} \Gamma_{i',j'}^{n'} \frac{\delta_{nn'}\delta_{nn'}\delta_{nn'}}{\pi S_{ij}} \\ &= \frac{\Gamma_{i,j}^{n}}{\pi S_{ij}}.\end{aligned} \tag{3.8}$$

So we have

$$\begin{aligned}\Gamma_{i,j}^{n} &= \pi S_{ij} \left\langle \psi_{i,j}^{n} | \psi \right\rangle \\ &= \pi S_{ij} \int_{\partial D_{ij}} dS_{ij} \int_{\mathbf{\Omega}\cdot\mathbf{n}_{ij}>0} d\mathbf{\Omega} \psi_{i,j}^{n}\left(\mathbf{r}_{ij}, \mathbf{\Omega}\right) \psi\left(\mathbf{r}_{ij}, \mathbf{\Omega}\right)\left(\mathbf{\Omega}\cdot\mathbf{n}_{ij}\right).\end{aligned} \tag{3.9}$$

If we want to expand the incoming flux $\psi_{i,j}(\mathbf{r}, \mathbf{\Omega})$ across interface ∂D_{ij}, which is nonzero only if $\mathbf{r} \in \partial D_{ij}$ and $\mathbf{\Omega} \cdot \mathbf{n}_{ij} > 0$, we have the simpler form,

$$\psi_{i,j}(\mathbf{r}, \mathbf{\Omega}) = \sum_{n} \Gamma_{i,j}^{n} \psi_{i,j}^{n}(\mathbf{r}, \mathbf{\Omega}). \tag{3.10}$$

The reason why orthogonal conditions 3.6 are chosen and the physical meaning of $\Gamma_{i,j}^{n}$ will be discussed in the next section.

Now substitute Eq. 3.1 into Eq. 3.9, and then change variable $\mathbf{\Omega}' = -\mathbf{\Omega}$ so that $\mathbf{\Omega}'$ is in the inward direction. Use $d\mathbf{\Omega}' = dS(\mathbf{\Omega}' \cdot \mathbf{n}_{+})/|\mathbf{r}_S - \mathbf{r}_{ij}|^2$ or $d\mathbf{r} = l^2 dl d\mathbf{\Omega}'$ and finally change

back $\mathbf{\Omega} = -\mathbf{\Omega}'$,

$$\begin{aligned}
\Gamma^n_{i,j} &= \pi S_{ij} \int\limits_{\partial D_{ij}} dS_{ij} \int\limits_{\mathbf{\Omega}\cdot\mathbf{n}_{ij}>0} d\mathbf{\Omega}\psi^n_{i,j}\left(\mathbf{r}_{ij},\mathbf{\Omega}\right)\psi_{in}(\mathbf{r_S},\mathbf{\Omega})\exp\left(-\tau(\mathbf{r_{ij}},\mathbf{r_S})\right)\left(\mathbf{\Omega}\cdot\mathbf{n}_{ij}\right) \\
&+ \pi S_{ij} \int\limits_{\partial D_{ij}} dS_{ij} \int\limits_{\mathbf{\Omega}\cdot\mathbf{n}_{ij}>0} d\mathbf{\Omega}\psi^n_{i,j}\left(\mathbf{r}_{ij},\mathbf{\Omega}\right)\int_0^{R_S} dl \frac{q(\mathbf{r_{ij}}-l\mathbf{\Omega})}{4\pi}\cdot \\
&\qquad \exp\left(-\tau(\mathbf{r_{ij}},\mathbf{r}_{ij}-l\mathbf{\Omega})\right)\left(\mathbf{\Omega}\cdot\mathbf{n}_{ij}\right) \\
&= \pi S_{ij} \int\limits_{\partial D_{ij}} dS_{ij} \int\limits_{\partial D_i} \frac{dS\,(\mathbf{\Omega}'\cdot\mathbf{n}_+)}{|\mathbf{r}_s-\mathbf{r}_{ij}|^2}\psi^n_{i,j}\left(\mathbf{r}_{ij},-\mathbf{\Omega}'\right)\psi_{in}(\mathbf{r_S},-\mathbf{\Omega}')\cdot \\
&\qquad \exp\left(-\tau(\mathbf{r_{ij}},\mathbf{r_S})\right)\left(-\mathbf{\Omega}'\cdot\mathbf{n}_{ij}\right) \\
&+ \pi S_{ij} \int\limits_{\partial D_{ij}} dS_{ij} \int\limits_{D_i} d\mathbf{r}\psi^n_{i,j}\left(\mathbf{r}_{ij},-\mathbf{\Omega}'\right)\frac{q(\mathbf{r})}{4\pi|\mathbf{r}-\mathbf{r}_{ij}|^2}\exp\left(-\tau(\mathbf{r_{ij}},\mathbf{r})\right)\left(-\mathbf{\Omega}'\cdot\mathbf{n}_{ij}\right).
\end{aligned}$$

Notice that $\partial D_i = \sum\limits_k \partial D_{ki}$, then

$$\begin{aligned}
\Gamma^n_{i,j} &= \pi S_{ij} \sum_k \int\limits_{\partial D_{ij}} dS_{ij} \int\limits_{\partial D_{ki}} dS_{ki}\psi^n_{i,j}\left(\mathbf{r}_{ij},\mathbf{\Omega}\right)\psi_{k,i}(\mathbf{r_{ki}},\mathbf{\Omega})\cdot \\
&\qquad \frac{\exp\left(-\tau(\mathbf{r_{ij}},\mathbf{r_{ki}})\right)}{|\mathbf{r}_{ki}-\mathbf{r}_{ij}|^2}\left(\mathbf{\Omega}\cdot\mathbf{n}_{ij}\right)\left(\mathbf{\Omega}\cdot\mathbf{n}_{ki}\right) \\
&+ \pi S_{ij} \int\limits_{\partial D_{ij}} dS_{ij} \int\limits_{D_i} d\mathbf{r}\psi^n_{i,j}\left(\mathbf{r}_{ij},\mathbf{\Omega}\right)\frac{q(\mathbf{r})}{4\pi|\mathbf{r}-\mathbf{r}_{ij}|^2}\exp\left(-\tau(\mathbf{r_{ij}},\mathbf{r})\right)\left(\mathbf{\Omega}\cdot\mathbf{n}_{ij}\right).
\end{aligned} \tag{3.11}$$

Making use of Eq. 3.10 to expand $\psi_{k,i}(\mathbf{r},\Omega)$, we have

$$\begin{aligned}
\Gamma^n_{i,j} &= \pi S_{ij} \sum_{k,n'} \Gamma^{n'}_{k,i} \int\limits_{\partial D_{ij}} dS_{ij} \int\limits_{\partial D_{ki}} dS_{ki}\psi^n_{i,j}\left(\mathbf{r}_{ij},\mathbf{\Omega}\right)\psi^{n'}_{k,i}(\mathbf{r_{ki}},\mathbf{\Omega})\cdot \\
&\qquad \frac{\exp\left(-\tau(\mathbf{r_{ij}},\mathbf{r_{ki}})\right)}{|\mathbf{r}_{ki}-\mathbf{r}_{ij}|^2}\left(\mathbf{\Omega}\cdot\mathbf{n}_{ij}\right)\left(\mathbf{\Omega}\cdot\mathbf{n}_{ki}\right) \\
&+ \pi S_{ij} \int\limits_{\partial D_{ij}} dS_{ij} \int\limits_{D_i} d\mathbf{r}\psi^n_{i,j}\left(\mathbf{r}_{ij},\mathbf{\Omega}\right)\frac{q(\mathbf{r})}{4\pi|\mathbf{r}-\mathbf{r}_{ij}|^2}\exp\left(-\tau(\mathbf{r_{ij}},\mathbf{r})\right)\left(\mathbf{\Omega}\cdot\mathbf{n}_{ij}\right) \\
&= \sum_{k,n'} \Gamma^{n'}_{k,i} T^{n'\to n}_{i,k\to j} + Q_i P_{0,i}\Lambda^n_{i,j},
\end{aligned} \tag{3.12}$$

where we define coefficients $T^{n'\to n}_{i,k\to j}$, $P_{0,i}$ and $\Lambda^n_{i,j}$ as

$$T^{n'\to n}_{i,k\to j} = \pi S_{ij} \int\limits_{\partial D_{ij}} dS_{ij} \int\limits_{\partial D_{ki}} dS_{ki}\psi^n_{i,j}\left(\mathbf{r}_{ij},\mathbf{\Omega}\right)\psi^{n'}_{k,i}(\mathbf{r_{ki}},\mathbf{\Omega}) \tag{3.13a}$$

$$\frac{\exp\left(-\tau(\mathbf{r_{ij}},\mathbf{r_{ki}})\right)}{|\mathbf{r}_{ki}-\mathbf{r}_{ij}|^2}\left(\mathbf{\Omega}\cdot\mathbf{n}_{ij}\right)(\mathbf{\Omega}\cdot\mathbf{n}_{ki}),$$

$$P_{0,i}=\frac{\pi}{Q_i}\sum_j S_{ij}\int_{\partial D_{ij}}dS_{ij}\int_{D_i}d\mathbf{r}\psi^0_{i,j}\left(\mathbf{r}_{ij},\mathbf{\Omega}\right)q(\mathbf{r})\frac{\exp\left(-\tau(\mathbf{r_{ij}},\mathbf{r})\right)}{4\pi|\mathbf{r}-\mathbf{r}_{ij}|^2}\left(\mathbf{\Omega}\cdot\mathbf{n}_{ij}\right), \tag{3.13b}$$

$$\Lambda^n_{i,j}=\frac{\pi S_{ij}}{Q_iP_{0,i}}\int_{\partial D_{ij}}dS_{ij}\int_{D_i}d\mathbf{r}\psi^n_{i,j}\left(\mathbf{r}_{ij},\mathbf{\Omega}\right)q(\mathbf{r})\frac{\exp\left(-\tau(\mathbf{r_{ij}},\mathbf{r})\right)}{4\pi|\mathbf{r}-\mathbf{r}_{ij}|^2}\left(\mathbf{\Omega}\cdot\mathbf{n}_{ij}\right), \tag{3.13c}$$

and the total volumetric source Q_i

$$Q_i=\int_{D_i}d\mathbf{r}q(\mathbf{r}). \tag{3.14}$$

By convention, we choose the 0-th representation function to be a constant. To satisfy the orthogonal conditions we choose $\psi^0_{i,j}=1/\pi S_{ij}$. Comparing with Eq. 2.9 we will find $P_{0,i}$ defined in Eq. 3.13b is exactly the first-flight escape probability. $T^{n'\to n}_{i,k\to j}$ is the generalized transmission probability; $\Lambda^n_{i,j}$ is the generalized directional escape probability. The 0-th moment has the same value and physical meaning as the transmission and directional escape probabilities defined in Chapter 2.

Until now, Eq. 3.12 is exact and no approximation was made. In order to evaluate the first-flight and directional escape probabilities, we must make an assumption of the spatial distribution of charge-exchanged neutral sources. If the flat collision source assumption is made again, then the total and directional escape probabilities may be written as

$$P_{0,i}=\frac{\pi}{V_i}\sum_j S_{ij}\int_{\partial D_{ij}}dS_{ij}\int_{D_i}d\mathbf{r}\psi^0_{i,j}\left(\mathbf{r}_{ij},\mathbf{\Omega}\right)\frac{\exp\left(-\tau(\mathbf{r_{ij}},\mathbf{r})\right)}{4\pi|\mathbf{r}-\mathbf{r}_{ij}|^2}\left(\mathbf{\Omega}\cdot\mathbf{n}_{ij}\right), \tag{3.15}$$

$$\Lambda^n_{i,j}=\frac{\pi S_{ij}}{V_iP_{0,i}}\int_{\partial D_{ij}}dS_{ij}\int_{D_i}d\mathbf{r}\psi^n_{i,j}\left(\mathbf{r}_{ij},\mathbf{\Omega}\right)\frac{\exp\left(-\tau(\mathbf{r_{ij}},\mathbf{r})\right)}{4\pi|\mathbf{r}-\mathbf{r}_{ij}|^2}\left(\mathbf{\Omega}\cdot\mathbf{n}_{ij}\right). \tag{3.16}$$

3.2.2 Total volumetric source

The total volumetric source Q_i is still unknown. Apparently, the total volumetric source depends on the incoming fluxes at the bounding interfaces and the external volumetric

source. Two approaches generally can be used to deal with Q_i. In the first approach, we begin with making a guess of Q_i, then we can solve the linear system 3.12. In the next step, we use Eq. 3.2 and Eq. 3.14 to calculate the volumetric source Q_i. Then we can solve for the angular flux using the updated Q_i and repeat these steps until the result is converged. The iterative procedure is straightforward, but it is not efficient for regions with a high charge-exchange fraction. The alternative way is to identify the relation between the total volumetric source Q_i, the incoming flux ψ_{in} and the external volumetric source S^i_{ext}.

Starting from Eq. 3.14, we obtain the total volumetric source in cell i,

$$\begin{aligned} Q_i &= \int_{D_i} d\mathbf{r} q(\mathbf{r}) = \int_{D_i} d\mathbf{r} \left(\Sigma_s \phi(\mathbf{r}) + \frac{S^i_{ext}}{V_i} \right) \\ &= S^i_{ext} + \int_{D_i} d\mathbf{r} \Sigma_s \Big[\int_{D_i} d\mathbf{r}' \frac{q(\mathbf{r}') \exp\left(-\Sigma_t |\mathbf{r} - \mathbf{r}'|\right)}{4\pi |\mathbf{r} - \mathbf{r}'|^2} \\ &\quad + \int_{\partial D_i} dS \psi_{in}(\mathbf{r}_S, \mathbf{\Omega}) \frac{\exp\left(-\Sigma_t |\mathbf{r} - \mathbf{r}_S|\right)}{|\mathbf{r} - \mathbf{r}_S|^2} (\mathbf{\Omega} \cdot \mathbf{n}_-) \Big]. \end{aligned} \tag{3.17}$$

Expanding ψ_{in} and making use of the flat collision source assumption, the total volumetric source can be written as

$$\begin{aligned} Q_i &= S^i_{ext} + Q_i \frac{\Sigma_s}{\Sigma_t} \frac{\Sigma_t}{S_i} \int_{D_i} d\mathbf{r} \int_{D_i} d\mathbf{r}' \frac{\exp\left(-\Sigma_t |\mathbf{r} - \mathbf{r}'|\right)}{4\pi |\mathbf{r} - \mathbf{r}'|^2} \\ &\quad + \sum_{k,n'} \Gamma^{n'}_{k,i} \frac{\Sigma_s}{\Sigma_t} \Sigma_t \int_{D_i} d\mathbf{r} \int_{\partial D_{ki}} dS_{ki} \psi^{n'}_{k,i}(\mathbf{r}_k i, \mathbf{\Omega}) \frac{\exp\left(-\Sigma_t |\mathbf{r} - \mathbf{r}_{ki}|\right)}{|\mathbf{r} - \mathbf{r}_{ki}|^2} (\mathbf{\Omega} \cdot \mathbf{n}_{ki}) \\ &= S^i_{ext} + Q_i c_i P1_{ii} + \sum_{k,n'} \Gamma_{k,i} c_i P2^{n'}_{ki} \\ &= S^i_{ext} + Q_i c_i (1 - P_{0,i}) + \sum_{k,n'} \Gamma_{k,i} c_i P2^{n'}_{ki}, \end{aligned} \tag{3.18}$$

where $P1_{ii}$ and c_i are the same as those defined in Eq. 2.21a and 2.22. The coefficient $P2^{n'}_{ki}$ is

$$P2^{n'}_{ki} = \Sigma_t \int_{D_i} d\mathbf{r} \int_{\partial D_{ki}} dS_{ki} \psi^{n'}_{k,i}(\mathbf{r}_{ki}, \mathbf{\Omega}) \frac{\exp\left(-\Sigma_t |\mathbf{r} - \mathbf{r}_{ki}|\right)}{|\mathbf{r} - \mathbf{r}_{ki}|^2} (\mathbf{\Omega} \cdot \mathbf{n}_{ki}). \tag{3.19}$$

Exchange the order of the integrals in Eq. 3.19, then change variables $d\mathbf{r} = R^2 dR d\mathbf{\Omega}$,

so we can find the integrals parallel to the neutral path can be performed analytically,

$$
\begin{aligned}
P2_{ki}^{n'} &= \Sigma_t \int_{D_i} d\mathbf{r} \int_{\partial D_{ki}} dS_{ki} \psi_{k,i}^{n'}(\mathbf{r}_{ki}, \mathbf{\Omega}) \frac{\exp\left(-\Sigma_t \left|\mathbf{r}-\mathbf{r}_{ki}\right|\right)}{\left|\mathbf{r}-\mathbf{r}_{ki}\right|^2} \left(\mathbf{\Omega}\cdot\mathbf{n}_{ki}\right) \\
&= \Sigma_t \int_{\partial D_{ki}} dS_{ki} \int \int_{4\pi} \frac{dl}{\sin\theta} d\mathbf{\Omega} \psi_{k,i}^{n'}(\mathbf{r}_{ki}, \mathbf{\Omega}) \exp\left(-\frac{\Sigma_t l}{\sin\theta}\right) \left(\mathbf{\Omega}\cdot\mathbf{n}_{ki}\right) \\
&= \int_{\partial D_{ki}} dS_{ki} \int_{4\pi} d\mathbf{\Omega} \psi_{k,i}^{n'}(\mathbf{r}_{ki}, \mathbf{\Omega}) \left[1 - \exp\left(-\frac{\Sigma_t l(\mathbf{r}_{ki}, \phi)}{\sin\theta}\right)\right] \left(\mathbf{\Omega}\cdot\mathbf{n}_{ki}\right) \\
&= \pi S_{ki} \left\langle \psi_{k,i}^{n'}(\mathbf{r}_{ki}, \mathbf{\Omega}) | \psi_{k,i}^{0}(\mathbf{r}_{ki}, \mathbf{\Omega}) \right\rangle \\
&- \sum_l \int_{\partial D_{ki}} dS_{ki} \int_{\partial D_{il}} \frac{dS_{il}\left(\mathbf{\Omega}\cdot\mathbf{n}_{il}\right)}{\left|\mathbf{r}_{il}-\mathbf{r}_{ki}\right|} \psi_{k,i}^{n'}(\mathbf{r}_{ki}, \mathbf{\Omega}) \exp\left(-\Sigma_t \left|\mathbf{r}_{il}-\mathbf{r}_{ki}\right|\right) \left(\mathbf{\Omega}\cdot\mathbf{n}_{ki}\right) \\
&= \delta_{n'0} - \sum_l T_{i,k\to l}^{n'\to 0}
\end{aligned}
\tag{3.20}
$$

Substitute Eq.3.20 into Eq. 3.18, Q_i can then be written as

$$
Q_i = \frac{S_{ext}^{i} + \sum_{k,n'} (\delta_{n'0} - \sum_l T_{i,k\to l}^{n'\to 0}) c_i \Gamma_{k,i}^{n'}}{1 - c_i(1 - P_{0,i})}. \tag{3.21}
$$

To better understand the physical meaning of Eq. 3.21, we expand the factor $\frac{1}{1-c_i(1-p_{0,i})}$ as $1 + c_i(1-p_{0,i}) + [c_i(1-p_{0,i})]^2 + \cdots$. The first term of Eq. 3.21 is the sum of the external volumetric source and its progenies. Realizing that $\sum_{k,n'} (\delta_{n'0} - \sum_l T_{i,k\to l}^{n'\to 0}) c_i \Gamma_{k,i}^{n'}$ is the difference of the total incoming partial currents and the total outgoing uncollided partial currents crossing all the bounding surfaces, the second term turns out to be the sum of the first collision source, the second collision source and so on.

3.2.3 Final balance equations

Inserting Q_i from Eq. 3.21 into Eq. 3.12, finally we end with the final balance equations,

$$
\Gamma_{i,j}^{n} = \sum_k \sum_{n'} T_{i,k\to j}^{n'\to n} \Gamma_{k,i}^{n'} + \sum_k \sum_{n'} \left(\delta_{n'0} - \sum_l T_{i,k\to l}^{n'\to 0}\right) \Gamma_{k,i}^{n'} c_i P_i \Lambda_{i,j}^{n} + S_{ext}^{i} P_i \Lambda_{i,j}^{n}. \tag{3.22}
$$

As in the original TEP equations, Eq. 3.22 states that the n-th moment of the partial current from region i to region j, $\Gamma_{i,j}^{n}$, is the sum of three contributions:

1. The sum of the n'-th moment of the total partial current from all the adjacent regions k into region i, times the probability $T_{i,k\to j}^{n'\to n}$ that a neutral emitted from region k in moment n' is transmitted across region i to region j in moment n without a collision within region i.

2. The sum of the collided neutrals from all the adjacent regions k, $\sum_{n'}\left(\delta_{n'0}-\sum_{l}T_{i,k\to l}^{n'\to 0}\right)$, times the fraction c_i that the collision is a charge-exchange scattering, times the probability $P_i\Lambda_{i,j}^{n}$ that a neutral produced uniformly and isotropically in region i escapes from region i into region j in moment n.

3. The sum of the external neutrals born in region i times the probability that these neutrals or their progenies escape into region j in moment n.

Also as in the original TEP equations, an outgoing partial current moment from a region is coupled only to all the incoming partial current moments from its contiguous regions.

3.3 Properties of the orthogonal conditions

The orthogonal conditions 3.6 and the inner product defined in Eq. 3.7 appear unfamiliar, however, they have the following properties.

1. The 0-th moment of the angular flux $\Gamma_{i,j}^{0}$ is the exact total partial current from region i to region j;

2. The orthogonal conditions 3.6 guarantee the particle conservation at each interface;

3. The coefficients defined in Eq. 3.9 ensure the expansion 3.10 to be the best approximation.

The first property is quite obvious. Insert $\psi_{i,j}^{0}=1/\pi S_{ij}$ into Eq. 3.9, then

$$\begin{aligned}\Gamma_{i,j}^{0}&=\pi S_{ij}\int_{\partial D_{ij}}dS_{ij}\int_{\mathbf{\Omega}\cdot\mathbf{n}_{ij}>0}d\mathbf{\Omega}\frac{1}{\pi S_{ij}}\psi\left(\mathbf{r}_{ij},\mathbf{\Omega}\right)\left(\mathbf{\Omega}\cdot\mathbf{n}_{ij}\right)\\&=\int_{\partial D_{ij}}dS_{ij}\int_{\mathbf{\Omega}\cdot\mathbf{n}_{ij}>0}d\mathbf{\Omega}\psi\left(\mathbf{r}_{ij},\mathbf{\Omega}\right)\left(\mathbf{\Omega}\cdot\mathbf{n}_{ij}\right).\end{aligned}\tag{3.23}$$

Compared with Eq. 3.11, it can be seen that the 0-th moment of the angular flux is the total partial current from region i to region j.

Actually, the particle conservation relations have already been derived in the previous section. Rewrite the 0-th moment of Eq. 3.22, Eq. 2.23 and Eq. 3.20 as following,

$$\Gamma_{k,j}^{0}=\sum_{k}\sum_{n'}T_{i,k\to j}^{n'\to 0}\Gamma_{k,i}^{n'}+\sum_{k}\sum_{n'}\left(\delta_{n'0}-\sum_{l}T_{i,k\to l}^{n'\to 0}\right)\Gamma_{k,i}^{n'}c_{i}P_{i}\Lambda_{i,j}^{0}+S_{ext}^{i}P_{i}\Lambda_{i,j}^{0}, \tag{3.24}$$

$$P1_{ii}+P_{0,i}=1, \tag{3.25}$$

$$P2_{ki}^{n}+\sum_{l}T_{i,k\to j}^{n\to 0}=\delta_{n0}. \tag{3.26}$$

Eq. 3.24 is the particle balance equation over interface ∂D_{ij}; Eq. 3.25 states that the sum of the volume-volume collision probabilities and the volume-surface escape probabilities is equal to 1; Eq. 3.26 represents that the sum of the transmission probabilities (equivalently the surface-surface escape probabilities) and the surface-volume collision probabilities is equal to the total particles entering through a given interface, which is 1 for the 0-th moment or 0 otherwise.

The third property means that, for all possible expansions in subspace $\Psi_N=\{\psi_{i,j}^{n}|n=0,\cdots,N\}$, the expansion 3.10 is the best one. It is equivalent to

$$\begin{aligned}&\left\langle\psi_{i,j}(\mathbf{r},\mathbf{\Omega})-\sum_{n=0}^{N}\Gamma_{i,j}^{n}\psi_{i,j}^{n}(\mathbf{r},\mathbf{\Omega})\middle|\psi_{i,j}(\mathbf{r},\mathbf{\Omega})-\sum_{n=0}^{N}\Gamma_{i,j}^{n}\psi_{i,j}^{n}(\mathbf{r},\mathbf{\Omega})\right\rangle\\&\le\left\langle\psi_{i,j}(\mathbf{r},\mathbf{\Omega})-\sum_{n=0}^{N}\chi_{i,j}^{n}\psi_{i,j}^{n}(\mathbf{r},\mathbf{\Omega})\middle|\psi_{i,j}(\mathbf{r},\mathbf{\Omega})-\sum_{n=0}^{N}\chi_{i,j}^{n}\psi_{i,j}^{n}(\mathbf{r},\mathbf{\Omega})\right\rangle,\quad\text{for }\chi_{i,j}^{n}\in R.\end{aligned} \tag{3.27}$$

The proof is quite simple: we begin with defining the norm between the original angular flux and the expansion approximation as

$$d_N=\sqrt{\left\langle\psi_{i,j}(\mathbf{r},\mathbf{\Omega})-\sum_{n=0}^{N}\Gamma_{i,j}^{n}\psi_{i,j}^{n}(\mathbf{r},\mathbf{\Omega})\middle|\psi_{i,j}(\mathbf{r},\mathbf{\Omega})-\sum_{n=0}^{N}\Gamma_{i,j}^{n}\psi_{i,j}^{n}(\mathbf{r},\mathbf{\Omega})\right\rangle}. \tag{3.28}$$

Apparently,

$$d_N^2=\left\langle\psi_{i,j}|\psi_{i,j}\right\rangle-2\sum_{n=0}^{N}\Gamma_{i,j}^{n}\left\langle\psi_{i,j}^{n}|\psi_{i,j}\right\rangle+\sum_{n=0}^{N}\frac{(\Gamma_{i,j}^{n})^2}{\pi S_{ij}}. \tag{3.29}$$

In order to make d_N is the minimum, it must have

$$\frac{\partial d_N^2}{\partial \Gamma_{i,j}^n} = 0, \qquad n = 0, \cdots, N. \tag{3.30}$$

So we can easily have

$$\begin{aligned} \Gamma_{i,j}^n &= \pi S_{ij} \left\langle \psi_{i,j}^n | \psi_{i,j} \right\rangle \\ &= \pi S_{ij} \int_{\partial D_{ij}} dS_{ij} \int_{\mathbf{\Omega}\cdot\mathbf{n}_{ij}>0} d\mathbf{\Omega} \psi_{i,j}^n \left(\mathbf{r}_{ij}, \mathbf{\Omega}\right) \psi \left(\mathbf{r}_{ij}, \mathbf{\Omega}\right) \left(\mathbf{\Omega} \cdot \mathbf{n}_{ij}\right). \end{aligned} \tag{3.31}$$

This means that, if we choose expansion coefficients as defined in Eq. 3.31, the expansion 3.10 is the best approximation in subspace Ψ_N. The higher order an expansion, the better the approximation. It should be mentioned that the norm d_N is defined as the integral over the entire interface ∂D_{ij} and the whole 2π solid angle. As a result, d_N is a parameter describing the global behavior of expansions. In slab geometries, transmission probabilities are also an integral over the 2π solid angle. So the higher the expansion, the more accurate the DP_N approximation. However, the 2D transmission probabilities defined by Eq. 3.13a are an integral over a part of the 2π solid angle. Thus, for the transmission probability between a given pair of interfaces, the error may oscillate as the order of the expansion increases. But eventually, it will diminish if the order of the expansion is sufficiently high.

3.4 DP_1 and DP_2 approximations

Until now, the only approximation made is the flat collision source assumption. So, if each computational cell is sufficiently small compared to the neutral mean free path, calculations of the new TEP method approach to the exact solutions. However, for practical reasons, we cannot use an infinite number of representation functions and must truncate the series at a finite number N. The choice of the representation functions is almost arbitrary except subject to the orthogonal conditions. The simplest approximation for angular fluxes is to assume that they are isotropic over the inward hemisphere and uniform on the entire interface as was done in the original TEP method. This has been proven to be inaccurate for some cases. To overcome this limitation, the more sophisticated angular representation

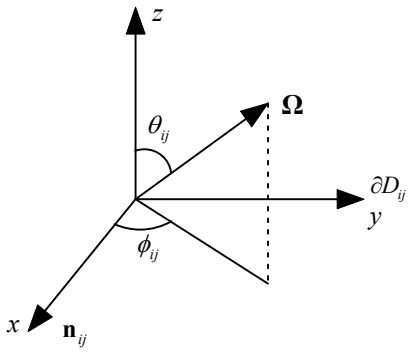

Figure 3.4. Geometry for angular representation functions

functions will be presented in this chapter. Alternatively, subdividing the 2π solid angle into small cones and piecewise-linearly interpolating is also possible.

3.4.1 Construction of the DP_1 and DP_2 representation functions

Naturally, we first consider an isotropic (constant) representation function, then linear and quadratic functions. So the 0-th representation function can be set as $\Psi_0 = 1$. if θ_{ij} is the angle between vector $\mathbf{\Omega}$ and the z axis, ϕ_{ij} is the angle between the interface normal $\mathbf{n}_{ij}$ and the projection of $\mathbf{\Omega}$ onto the $x - y$ plane, as shown in Figure 3.3. A linear function dependent on $\mathbf{\Omega}$ would be like the following form,

$$f(\mathbf{\Omega}) = a_1 \sin\theta_{ij} \sin\phi_{ij} + a_2 \sin\theta_{ij} \cos\phi_{ij} + a_3 \cos\theta_{ij}. \tag{3.32}$$

Since the function $\cos\theta_{ij}$ violates the symmetry in the z direction, which requires that $f(\pi - \theta_{ij}, \phi_{ij})$ has the same value as $f(\theta_{ij}, \phi_{ij})$, its expansion coefficient must be zero. Therefore $\Psi_1 = \sin\theta_{ij} \sin\phi_{ij}$ and $\Psi_2 = \sin\theta_{ij} \cos\phi_{ij}$.

Similarly, a quadratic function dependent on $\mathbf{\Omega}$ can be written as

$$\begin{aligned} f(\mathbf{\Omega}) = \mathbf{\Omega}^T \mathbf{A} \mathbf{\Omega} = {} & a_1 \sin^2\theta_{ij} \sin^2\phi_{ij} + a_2 \sin^2\theta_{ij} \cos^2\phi_{ij} + a_3 \cos^2\theta_{ij} \\ & + a_4 \sin^2\theta_{ij} \sin\phi_{ij} \cos\phi_{ij} + a_5 \sin\theta_{ij} \cos\theta_{ij} \sin\phi_{ij} + a_6 \sin\theta_{ij} \cos\theta_{ij} \cos\phi_{ij}. \end{aligned} \tag{3.33}$$

Since the sum of the three diagonal terms is equal to 1, only two of them are independent. The terms $\sin\theta_{ij} \cos\theta_{ij} \sin\phi_{ij}$ and $\sin\theta_{ij} \cos\theta_{ij} \cos\phi_{ij}$ also violate the symmetry in the z direction. So the acceptable quadratic representation functions are $\Psi_4 = \cos^2\theta_{ij}$, $\Psi_5 = \sin^2\theta_{ij} \sin^2\phi_{ij}$ and $\Psi_6 = \sin^2\theta_{ij} \sin\phi_{ij} \cos\phi_{ij}$.

However, these representation functions are not orthogonal. We use the following strategy to obtain the orthogonal representation functions.

1. If Ψ_n is not normalized, we set $\psi^n_{i,j} = 1/\sqrt{\langle\Psi_n|\Psi_n\rangle/\pi S_{ij}}\Psi_n$.

2. If Ψ_n is not orthogonal to $\{\psi^{n'}_{i,j}|n' = 0, \cdots, n-1\}$, we set

$$\psi^n_{i,j} = \Psi_n - \sum_{n'=0}^{n-1} \pi S_{ij} \langle\psi^{n'}_{i,j}|\Psi_n\rangle. \tag{3.34}$$

Following the above procedures, we obtain the orthogonal representation functions,

$$\psi^0_{i,j}(\mathbf{r}_{ij}, \mathbf{\Omega}) = \frac{1}{\pi S_{ij}}, \tag{3.35a}$$

$$\psi^1_{i,j}(\mathbf{r}_{ij}, \mathbf{\Omega}) = \frac{2}{\pi S_{ij}} \sin\theta_{ij} \sin\phi_{ij}, \tag{3.35b}$$

$$\psi^2_{i,j}(\mathbf{r}_{ij}, \mathbf{\Omega}) = \frac{3\sqrt{2}}{\pi S_{ij}} \sin\theta_{ij} \cos\phi_{ij} - 2\sqrt{2}\psi^0_{i,j}(\mathbf{r}_{ij}, \mathbf{\Omega}), \tag{3.35c}$$

$$\psi^3_{i,j}(\mathbf{r}_{ij}, \mathbf{\Omega}) = \frac{20}{\sqrt{17}\pi S_{ij}} \sin^2\theta_{ij} - \frac{2\sqrt{2}}{\sqrt{17}}\psi^2_{i,j}(\mathbf{r}_{ij}, \mathbf{\Omega}) - \frac{15}{\sqrt{17}}\psi^0_{i,j}(\mathbf{r}_{ij}, \mathbf{\Omega}), \tag{3.35d}$$

$$\begin{aligned}\psi^4_{i,j}(\mathbf{r}_{ij}, \mathbf{\Omega}) = {} & \frac{3\sqrt{34}}{\pi S_{ij}} \sin^2\theta_{ij} \sin^2\phi_{ij} - \frac{49}{10\sqrt{2}}\psi^3_{i,j}(\mathbf{r}_{ij}, \mathbf{\Omega}) \\ & + \frac{3\sqrt{17}}{5}\psi^2_{i,j}(\mathbf{r}_{ij}, \mathbf{\Omega}) - \frac{3\sqrt{34}}{4}\psi^0_{i,j}(\mathbf{r}_{ij}, \mathbf{\Omega}),\end{aligned} \tag{3.35e}$$

$$\psi^5_{i,j}(\mathbf{r}_{ij}, \mathbf{\Omega}) = \frac{30}{\sqrt{11}\pi S_{ij}} \sin^2\theta_{ij} \sin\phi_{ij} \cos\phi_{ij} - \frac{8}{\sqrt{11}}\psi^1_{i,j}(\mathbf{r}_{ij}, \mathbf{\Omega}). \tag{3.35f}$$

Representation function $\psi^0_{i,j}(\theta, \phi)$ is the isotropic term (DP_0); Functions $\psi^1_{i,j}(\theta, \phi)$ and $\psi^2_{i,j}(\theta, \phi)$ represent the linear terms (DP_1); Functions $\psi^3_{i,j}(\theta, \phi)$, $\psi^4_{i,j}(\theta, \phi)$ and $\psi^5_{i,j}(\theta, \phi)$ are the quadratically anisotropic functions (DP_2). It also should be noticed that this choice implies the angular flux is uniformly distributed over each interface because these representation functions are independent on $\mathbf{r}_{ij}$.

3.4.2 Transmission probabilities

A direct numerical integration of the transmission probabilities in Eq. 3.13a is very time-consuming. Moreover, the singularity at $\mathbf{r}_{ij} = \mathbf{r}_{ki}$, if the interfaces ∂D_{ij} and ∂D_{ki} are adjacent, will incur extra troubles. The best way to overcome this difficulty is to change

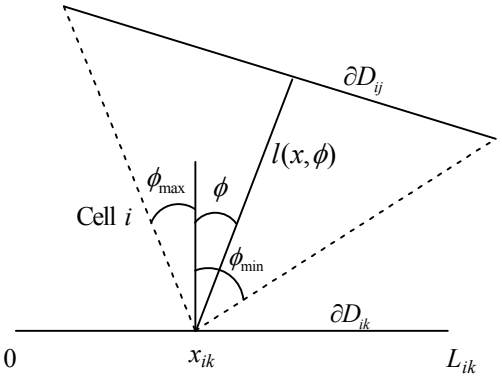

Figure 3.5. Geometry for calculation of transmission probabilities

variables $d\mathbf{\Omega} = dS_{ij}(\mathbf{\Omega} \cdot \mathbf{n}_{ij})/|\mathbf{r}_{ij} - \mathbf{r}_{ij}|^2$, so $|\mathbf{r}_{ij} - \mathbf{r}_{ij}|^2$ appears in both the numerator and denominator and can be canceled out. The transmission probabilities can be rewritten as

$$T_{i,k\to j}^{0\to 0} = \frac{2}{\pi L_{ki}} \int_0^{L_{ki}} dx_{ki} \int_{\varphi_{\min}}^{\varphi_{\max}} \cos\varphi_{ki} \cdot Ki_3\left(\Sigma_t l(x_{ki},\varphi_{ki})\right) d\varphi_{ki}, \tag{3.36a}$$

$$T_{i,k\to j}^{0\to 1} = \frac{4}{\pi L_{ki}} \int_0^{L_{ki}} dx_{ki} \int_{\varphi_{\min}}^{\varphi_{\max}} \sin\varphi_{ij}\cos\varphi_{ki} \cdot Ki_4\left(\Sigma_t l(x_{ki},\varphi_{ki})\right) d\varphi_{ki}, \tag{3.36b}$$

$$T_{i,k\to j}^{0\to 2} = \frac{6\sqrt{2}}{\pi L_{ki}} \int_0^{L_{ki}} dx_{ki} \int_{\varphi_{\min}}^{\varphi_{\max}} \cos\varphi_{ki}\cos\varphi_{ij} \cdot Ki_4\left(\Sigma_t l(x_{ki},\varphi_{ki})\right) d\varphi_{ki} - 2\sqrt{2}T_{i,k\to j}^{0\to 0}, \tag{3.36c}$$

$$T_{i,k\to j}^{1\to 0} = \frac{4}{\pi L_{ki}} \int_0^{L_{ki}} dx_{ki} \int_{\varphi_{\min}}^{\varphi_{\max}} \sin\varphi_{ki}\cos\varphi_{ki} \cdot Ki_4\left(\Sigma_t l(x_{ki},\varphi_{ki})\right) d\varphi_{ki}, \tag{3.36d}$$

$$T_{i,k\to j}^{1\to 1} = \frac{8}{\pi L_{ki}} \int_0^{L_{ki}} dx_{ki} \int_{\varphi_{\min}}^{\varphi_{\max}} \sin\varphi_{ij}\sin\varphi_{ki}\cos\varphi_{ki} \cdot Ki_5\left(\Sigma_t l(x_{ki},\varphi_{ki})\right) d\varphi_{ki}, \tag{3.36e}$$

$$T_{i,k\to j}^{1\to 2} = \frac{12\sqrt{2}}{\pi L_{ki}} \int_0^{L_{ki}} dx_{ki} \int_{\varphi_{\min}}^{\varphi_{\max}} \cos\varphi_{ij}\sin\varphi_{ki}\cos\varphi_{ki} \cdot Ki_5\left(\Sigma_t l(x_{ki},\varphi_{ki})\right) d\varphi_{ki} - 2\sqrt{2}T_{i,k\to j}^{1\to 0}, \tag{3.36f}$$

$$T_{i,k\to j}^{2\to 0} = \frac{6\sqrt{2}}{\pi L_{ki}} \int_0^{L_{ki}} dx_{ki} \int_{\varphi_{\min}}^{\varphi_{\max}} \cos^2\varphi_{ki} \cdot Ki_4\left(\Sigma_t l(x_{ki},\varphi_{ki})\right) d\varphi_{ki} - 2\sqrt{2}T_{i,k\to j}^{0\to 0}, \tag{3.36g}$$

$$T_{i,k\to j}^{2\to 1} = \frac{12\sqrt{2}}{\pi L_{ki}} \int_0^{L_{ki}} dx_{ki} \int_{\varphi_{\min}}^{\varphi_{\max}} \sin\varphi_{ij}\cos^2\varphi_{ki} \cdot Ki_5\left(\Sigma_t l(x_{ki},\varphi_{ki})\right) d\varphi_{ki} - 2\sqrt{2}T_{i,k\to j}^{0\to 1}, \tag{3.36h}$$

$$T_{i,k\to j}^{2\to 2} = \frac{36}{\pi L_{ki}} \int_0^{L_{ki}} dx_{ki} \int_{\varphi_{\min}}^{\varphi_{\max}} \cos\varphi_{ij} \cos^2\varphi_{ki} \cdot Ki_5\left(\Sigma_t l(x_{ki}, \varphi_{ki})\right) d\varphi_{ki} \tag{3.36i}$$
$$- 2\sqrt{2} T_{i,k\to j}^{2\to 0} - 2\sqrt{2} T_{i,k\to j}^{0\to 2} - 8 T_{i,k\to j}^{0\to 0},$$

where L_{ij} is the length of the interface ∂D_{ij}, l, ϕ_{min} and ϕ_{max} are defined in Figure 3.5.

All the transmission probabilities are expressed in terms of the Bickley-Naylor functions. For the DP_0 approximation,the number of transmission probabilities which must be numerically calculated for each pair interfaces is only 1; while for the DP_1 or DP_2 approximation, this number becomes 9 and 36, respectively. Though the higher order approximations generally enhance the accuracy of the TEP method, the order of the approximation higher than 2 is rarely used for 2D geometries, because the number of transmission probabilities significantly increases as the order of the approximation increases.

3.5 Boundary conditions

3.5.1 Vacuum boundary

For vacuum boundaries, neutrals will not be reflected back, so the reflected flux at the interface ∂D_{kwi}

$$\psi_{kw,i}(\mathbf{r}, \mathbf{\Omega}) = 0, \qquad \mathbf{\Omega} \cdot \mathbf{n}_{kw,i} > 0, \tag{3.37}$$

where $\mathbf{n}_{kw,i}$ is the inward normal at the boundary.

Since the flux expansion, in the DP_N approximation, is made only in a half-space, we easily obtain

$$\Gamma_{kw,i}^n = \pi S_{kw,i} \left\langle \psi_{kw,i}^n(\mathbf{r}, \mathbf{\Omega}) | \psi_{kw,i}(\mathbf{r}, \mathbf{\Omega}) \right\rangle = 0, \qquad n = 0, \cdots, N. \tag{3.38}$$

3.5.2 Albedo boundary

Since neutrals emerging from an albedo boundary is almost isotropic, the angular flux at this boundary is

$$\psi_{pl,i}(\mathbf{r}, \mathbf{\Omega}) = \frac{\alpha_{pl} \int_{\mathbf{\Omega}' \cdot \mathbf{n}_{\mathbf{i,pl}} > 0} d\mathbf{\Omega}' (\mathbf{\Omega}' \cdot \mathbf{n}_{\mathbf{i,pl}}) \psi_{i,pl}(\mathbf{r}, \mathbf{\Omega}')}{\pi}, \tag{3.39}$$

where α_{pl} is the albedo coefficient, $\mathbf{n}_{i,pl}$ and $\mathbf{n}_{pl,i}$ are the outward and inward normals at the albedo boundary, respectively. So

$$\Gamma^n_{pl,i} = \pi S\, pl, i \left\langle \psi^n_{pl,i} \middle| \psi_{pl,i} \right\rangle = \begin{cases} \alpha_{pl}\Gamma^0_{i,pl}, & n = 0; \\ 0, & n > 0. \end{cases} \tag{3.40}$$

3.5.3 Wall boundary

As mentioned in Chapter 2, neutrals reflected from the material wall segment are composed of two components: fast and slow neutrals. Both of them are isotropic in the inward hemisphere. Like the albedo boundary, the reflected neutral angular flux can be expressed as:

$$\psi_{kw,i}(\mathbf{r}, \mathbf{\Omega}) = \frac{\left[R_{kw} + (1 - R_{kw}) f^{kw}_{abs}\right] \int\limits_{\mathbf{\Omega}' \cdot \mathbf{n_{i,kw}} > 0} d\mathbf{\Omega}' (\mathbf{\Omega}' \cdot \mathbf{n_{i,kw}}) \psi_{i,kw}(\mathbf{r}, \mathbf{\Omega}')}{\pi}, \tag{3.41}$$

where R_{kw} is the particle reflection coefficient, f^{kw}_{abs} is the fraction that particles are permanently trapped inside the wall material, $\mathbf{n}_{i,kw}$ and $\mathbf{n}_{kw,i}$ are the outward and inward normal at the albedo boundary, respectively. So

$$\Gamma^n_{kw,i} = \pi S_{kw,i} \left\langle \psi^n_{kw,i} \middle| \psi_{kw,i} \right\rangle = \begin{cases} \left[R_{kw} + (1 - R_{kw}) f^{kw}_{abs}\right] \Gamma^0_{i,kw}, & n = 0; \\ 0, & n > 0. \end{cases} \tag{3.42}$$

3.5.4 Mirror boundary

The mirror boundary means that neutrals are reflected at the specular angle. Actually, the mirror boundary doesn't exist for the neutral transport in the plasma edge. However, for some problems with perfect symmetry, there exists an interface, on which the outgoing angular flux at a given angle has the same magnitude as the incoming angular flux at the specular angle. So for these cases, we just need to deal with half of the system by treating the interface as a mirror boundary.

For a mirror boundary, the reflected angular flux is

$$\psi_{kw,i}(\mathbf{r}, \mathbf{\Omega}_r) = \psi_{i,kw}(\mathbf{r}, \mathbf{\Omega}), \tag{3.43}$$

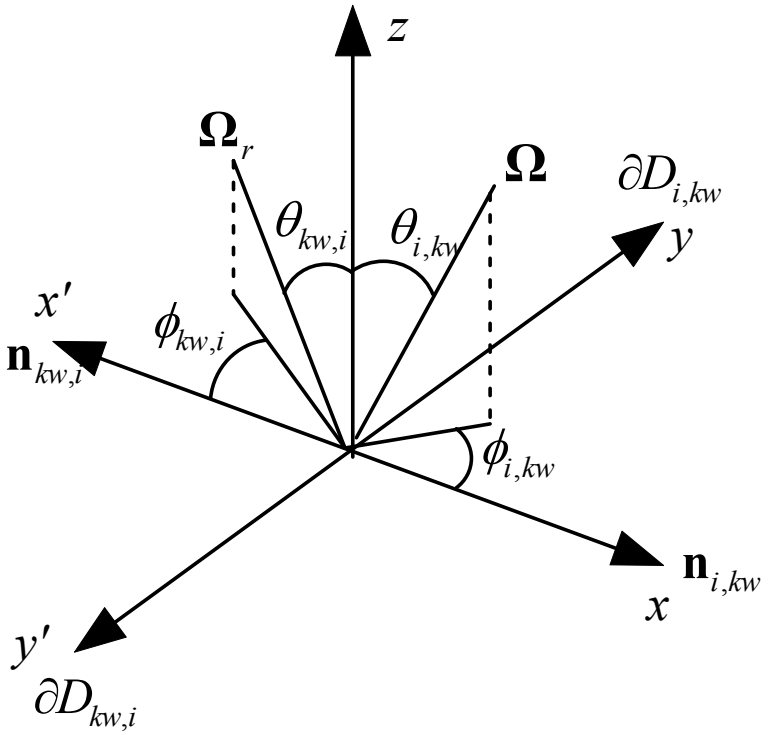

Figure 3.6. Geometric relations between Ω and Ω_r

where

$$\mathbf{\Omega}_r = \mathbf{\Omega} - 2(\mathbf{\Omega} \cdot \mathbf{n}_{i,kw})\mathbf{n}_{i,kw}. \tag{3.44}$$

Assuming the representation of Ω in the ($x(\mathbf{n}_{i,kw})$, $y(\partial D_{i,kw})$,z) coordinate system is ($\theta_{i,kw}$, $\phi_{i,kw}$), so

$$\mathbf{\Omega} = \sin\theta_{i,kw}\cos\phi_{i,kw}\mathbf{e}_x + \sin\theta_{i,kw}\sin\phi_{i,kw}\mathbf{e}_y + \cos\theta_{i,kw}\mathbf{e}_z, \tag{3.45}$$

and

$$\mathbf{\Omega}_r = -\sin\theta_{i,kw}\cos\phi_{i,kw}\mathbf{e}_x + \sin\theta_{i,kw}\sin\phi_{i,kw}\mathbf{e}_y + \cos\theta_{i,kw}\mathbf{e}_z. \tag{3.46}$$

So the representation of Ω_r in the ($x(\mathbf{n}_{i,kw})$, $y(\partial D_{i,kw})$,z) coordinate system is ($\theta_{i,kw}$, $\pi - \phi_{i,kw}$). However, the reflected flux $\psi_{kw,i}(\mathbf{r}, \mathbf{\Omega})$ is expanded in the ($x'(\mathbf{n}_{kw,i})$, $y'(\partial D_{kw,i})$,z) coordinate system,

$$\mathbf{\Omega}_r = \sin\theta_{i,kw}\cos\phi_{i,kw}\mathbf{e}_{x'} - \sin\theta_{i,kw}\sin\phi_{i,kw}\mathbf{e}_{y'} + \cos\theta_{i,kw}\mathbf{e}_z. \tag{3.47}$$

Assuming the representation of $\mathbf{\Omega}_r$ in the ($x'(\mathbf{n}_{kw,i})$, $y'(\partial D_{kw,i})$,z) coordinate system is ($\theta_{kw,i}, \phi_{kw,i}$), then

$$\theta_{kw,i} = \theta_{i,kw}, \tag{3.48a}$$

$$\phi_{kw,i} = -\phi_{i,kw}. \tag{3.48b}$$

Inserting Eq. 3.48 into representation functions 3.35, we will find out

$$\psi^n_{kw,i}(\mathbf{r}_{kw,i}, \mathbf{\Omega}_r) = \begin{cases} \psi^n_{i,kw}(\mathbf{r}_{i,kw}, \mathbf{\Omega}), & n = 0, 2, 3, 4 \quad \text{even moments;} \\ -\psi^n_{i,kw}(\mathbf{r}_{i,kw}, \mathbf{\Omega}), & n = 1, 5 \quad \text{odd moments.} \end{cases} \tag{3.49}$$

Combining Eqs. 3.43 and 3.49, we immediately draw the conclusion that

$$\Gamma^n_{kw,i} = \begin{cases} \Gamma^n_{i,kw}, & n = 0, 2, 3, 4 \quad \text{even moments;} \\ -\Gamma^n_{i,kw}, & n = 1, 5 \quad \text{odd moments.} \end{cases} \tag{3.50}$$

3.6 Symmetry properties

Due to the fact that transmission and escape probabilities are multi-dimensional numerical integrals, the evaluation of these probabilities is computationally expensive. Symmetry relations may be employed to substantially reduce the amount of calculations need to evaluate these probabilities. There are two kinds of symmetry relations: reciprocity relations and conservation relations. The reciprocity relations result from the symmetry of the optical length, $\tau(\mathbf{r}, \mathbf{r}') = \tau(\mathbf{r}', \mathbf{r})$, and the inherent symmetries of the representation functions, $\psi^n_{i,j}(\mathbf{r}, \mathbf{\Omega}) = \psi^n_{j,i}(\mathbf{r}, -\mathbf{\Omega})$. The conservation relations are associated with the general properties of the Boltzmann's linear equation.

In general, the reciprocity of the Green's function can be used to derive the reciprocity relations between all kinds of probabilities, and the particle balance equations usually can be employed to obtain the conservation relations.

We should keep in mind that the representation functions are defined in the local coordinate systems. Assuming the coordinates of $\mathbf{\Omega}$ in the outward half-space is (θ_{ij}, ϕ_{ij})

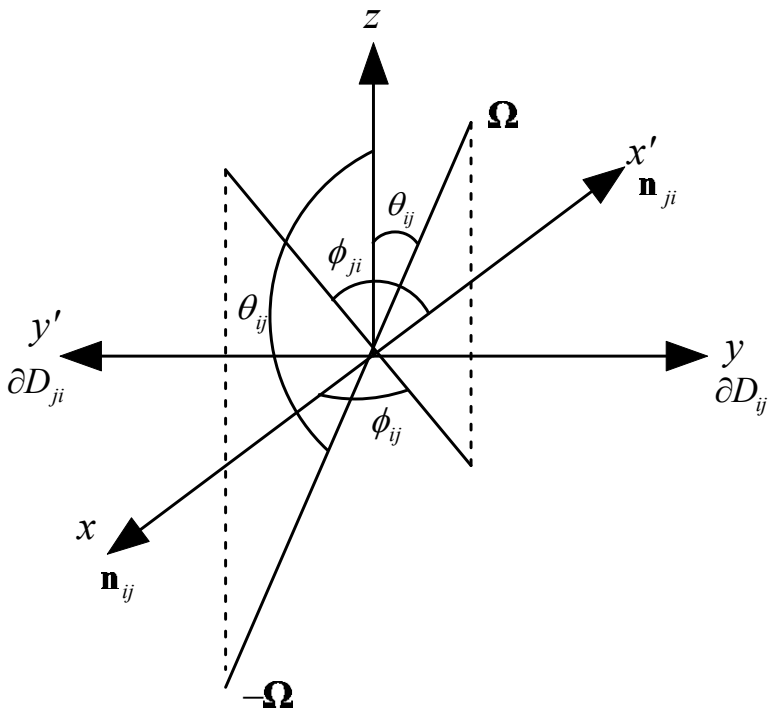

Figure 3.7. Geometry for symmetry between representation functions

and the coordinates of $-\mathbf{\Omega}$ in the inward half-space is (θ_{ji}, ϕ_{ji}), then, from Figure 3.7 we immediately have the following relations,

$$\theta_{ji} = \pi - \theta_{ij}, \tag{3.51a}$$

$$\phi_{ji} = \phi_{ij}. \tag{3.51b}$$

Substituting the previous equations into the angular representation functions, we obtain the following symmetry relations,

$$\psi^n_{i,j}(\mathbf{r}, \mathbf{\Omega}) = \psi^n_{j,i}(\mathbf{r}, -\mathbf{\Omega}) \qquad n = 0, \cdots . \tag{3.52}$$

3.6.1 Reciprocity relations

Noting the symmetry of the optical length, $\tau(\mathbf{r}, \mathbf{r}') = \tau(\mathbf{r}', \mathbf{r})$, which means the attenuation of a neutron traveling from $\mathbf{r}$ to $\mathbf{r}'$ is the same as the attenuation of a neutron traveling from $\mathbf{r}'$ to $\mathbf{r}$, it is easier to obtain the reciprocity by a direct comparison.

$$T^{n' \to n}_{i,k \to j} = \pi S_{ij} \int_{\partial D_{ij}} dS_{ij} \int_{\partial D_{ki}} dS_{ki} \psi^n_{i,j}\left(\mathbf{r}_{ij}, \mathbf{\Omega}\right) \psi^{n'}_{k,i}(\mathbf{r_{ki}}, \mathbf{\Omega}) \cdot \tag{3.53a}$$

$$\frac{\exp\left(-\tau(\mathbf{r_{ij}},\mathbf{r_{ki}})\right)}{|\mathbf{r}_{ki}-\mathbf{r}_{ij}|^2}\left(\boldsymbol{\Omega}\cdot\mathbf{n}_{ij}\right)(\boldsymbol{\Omega}\cdot\mathbf{n}_{ki}),$$

$$T^{n\to n'}_{i,j\to k} = \pi S_{ik}\int\limits_{\partial D_{ik}} dS_{ik}\int\limits_{\partial D_{ji}} dS_{ji}\psi^{n'}_{i,k}(\mathbf{r}_{ik},\boldsymbol{\Omega}')\,\psi^{n}_{j,i}(\mathbf{r_{ji}},\boldsymbol{\Omega}')\cdot \tag{3.53b}$$

$$\frac{\exp\left(-\tau(\mathbf{r_{ik}},\mathbf{r_{ji}})\right)}{|\mathbf{r}_{ji}-\mathbf{r}_{ik}|^2}(\boldsymbol{\Omega}'\cdot\mathbf{n}_{ik})(\boldsymbol{\Omega}'\cdot\mathbf{n}_{ji}).$$

Recall that $\boldsymbol{\Omega}$ is the direction from $\mathbf{r}'$ to $\mathbf{r}$ and that $\boldsymbol{\Omega}'$ is the direction from $\mathbf{r}$ to $\mathbf{r}'$, so $\boldsymbol{\Omega}' = -\boldsymbol{\Omega}$. Changing dummy variables and using the symmetry relations 3.52, we obtain the reciprocity relations,

$$S_{ik}T^{n'\to n}_{i,k\to j} = S_{ij}T^{n\to n'}_{i,j\to k}. \tag{3.54}$$

3.6.2 Conservation relations

Starting from Eq. 3.16, we rewrite

$$P_{0,i}\Lambda^{n}_{i,j} = \frac{\pi S_{ij}}{V_i}\int\limits_{\partial D_{ij}} dS_{ij}\int\limits_{D_i} d\mathbf{r}\psi^{n}_{i,j}\left(\mathbf{r}_{ij},\boldsymbol{\Omega}\right)\frac{\exp\left(-\tau(\mathbf{r_{ij}},\mathbf{r})\right)}{4\pi|\mathbf{r}-\mathbf{r}_{ij}|^2}\left(\boldsymbol{\Omega}\cdot\mathbf{n}_{ij}\right). \tag{3.55}$$

To integrate along the path of neutrals traveling, we change variables $d\mathbf{r} = R^2 dR d\boldsymbol{\Omega}'$. It yields

$$\begin{aligned} P_{0,i}\Lambda^{n}_{i,j} &= \frac{\pi S_{ij}}{V_i}\int\limits_{\partial D_{ij}} dS_{ij}\int\limits_{2\pi} d\boldsymbol{\Omega}'\int_0^{R_{max}} dRR^2\psi^{n}_{i,j}\left(\mathbf{r}_{ij},\boldsymbol{\Omega}\right)\frac{\exp\left(-\Sigma_t R\right)}{4\pi R^2}\left(\boldsymbol{\Omega}\cdot\mathbf{n}_{ij}\right) \\ &= \frac{S_{ij}}{4V_i\Sigma_t}\int\limits_{\partial D_{ij}} dS_{ij}\int\limits_{2\pi} d\boldsymbol{\Omega}'\psi^{n}_{i,j}\left(\mathbf{r}_{ij},-\boldsymbol{\Omega}'\right)\left[1-\exp\left(-\Sigma_t R_{max}\right)\right]\left(\boldsymbol{\Omega}'\cdot\mathbf{n}_{ji}\right), \end{aligned} \tag{3.56}$$

then changing variables $d\mathbf{\Omega}' = dS_i(\mathbf{\Omega}' \cdot \mathbf{n}_+)/|\mathbf{r}_i - \mathbf{r}_{ij}|^2$, we have

$$
\begin{aligned}
P_{0,i}\Lambda^n_{i,j} &= \frac{S_{ij}}{4V_i\Sigma_t}\int_{\partial D_{ji}} dS_{ji}\int_{2\pi} d\mathbf{\Omega}'\psi^n_{j,i}\left(\mathbf{r}_{ji},\mathbf{\Omega}'\right)\left(\mathbf{\Omega}'\cdot\mathbf{n}_{ji}\right)\\
&\quad - \frac{S_{ij}}{4V_i\Sigma_t}\int_{\partial D_{ji}} dS_{ji}\int_{\partial D_i} \frac{dS_i(\mathbf{\Omega}'\cdot\mathbf{n}_+)}{|\mathbf{r}_i-\mathbf{r}_{ji}|^2}\psi^n_{j,i}\left(\mathbf{r}_{ji},\mathbf{\Omega}'\right)\exp\left(-\Sigma_t|\mathbf{r}_i-\mathbf{r}_{ji}|\right)\left(\mathbf{\Omega}'\cdot\mathbf{n}_{ji}\right)\\
&= \frac{S_{ij}}{4V_i\Sigma_t}\Bigg[\delta_{n0} - \sum_k \pi S_{ik}\int_{\partial D_{ji}} dS_{ji}\int_{\partial D_{ik}} dS_{ik}(\mathbf{\Omega}'\cdot\mathbf{n}_{ik}) \\
&\qquad \cdot\psi^n_{j,i}\left(\mathbf{r}_{ji},\mathbf{\Omega}'\right)\psi^0_{i,k}\left(\mathbf{r}_{ik},\mathbf{\Omega}'\right)\frac{\exp\left(-\Sigma_t|\mathbf{r}_{ik}-\mathbf{r}_{ji}|\right)}{|\mathbf{r}_{ik}-\mathbf{r}_{ji}|^2}\left(\mathbf{\Omega}'\cdot\mathbf{n}_{ji}\right)\Bigg]\\
&= \frac{S_{ij}}{4V_i\Sigma_t}\left[\delta_{n0} - \sum_k T^{n\to 0}_{i,j\to k}\right].
\end{aligned}
\tag{3.57}
$$

Multiplying Eq. 3.57 with a factor $4V_i\Sigma_t/S_{ij}$ makes its physical meaning more obvious: the sum of the escaped particles and the collided particles is equal to the total incident particles.

Either for the one-speed or multi-group TEP method, these reciprocity and conservation relations can greatly increase the computational efficiency. However, for the current version of the TEP method, where we make the so called local ion temperature approximation (i.e. the neutral energy is equal to the local ion temperature), neutrals entering from different interfaces have different mean free paths because of their different energy. Therefore, these symmetry relations cannot directly be exploited.

3.7 Further simplifications

Since the evaluation of escape probabilities are still expensive for the TEP method with the local ion temperature assumption, additional approximations can be made to achieve computational efficiency. Assuming the angular flux at an interface due to the volumetric sources is isotropic, we can ignore the anisotropic flux such as the second and third terms of Eq. 3.22,

$$
\Gamma^n_{k,j} = \sum_k\sum_{n'} T^{n'\to n}_{i,k\to j}\Gamma^{n'}_{k,i} + \sum_k\sum_{n'}\left(\delta_{n'0} - \sum_l T^{n'\to 0}_{i,k\to l}\right)\Gamma^{n'}_{k,i}c_iP_i\Lambda^0_{i,j}\delta_{n0} + S^i_{ext}P_i\Lambda^0_{i,j}\delta_{n0}. \tag{3.58}
$$

Actually, this assumption is reasonable for optically thick regions, because the charge-exchange scattering tends to isotropize the angular distribution of neutrals. This fact can be proved by the conservation relations,

$$\Sigma_t \Delta \gg 1 \qquad \Longrightarrow \qquad T \ll 1.$$

So

$$\left| \frac{P_{0,i}\Lambda^n_{i,j}}{P_{0,i}\Lambda^0_{i,j}} \right| = \left| \frac{-\sum_k T^{n\to 0}_{i,j\to k}}{1-\sum_k T^{0\to 0}_{i,j\to k}} \right| \qquad \text{if } n > 1$$

$$\approx T \ll 1.$$

The maximum ratio of the anisotropic flux to the isotropic flux, due to the volumetric source in a rectangular region, varying with Δ/λ is illustrated in Figure 3.8. The angular flux is almost isotropic for optically thick regions, while the fraction of the anisotropic flux increases to 20% for optically thin regions where, however, the total angular flux is dominantly composed of the uncollided flux. Therefore the error resulting from ignoring the anisotropic contribution from the volumetric sources has almost no impact on the total angular flux. The validity of this assumption will be tested with the full version of the DP_N method in the next section.

3.8 Testing the validity of the DP_N approximation

During the implementation of the DP_N approximation, in addition to the flat collision source assumption, it was assumed: 1) the angular flux distribution at the interfaces can be expanded in terms of the linearly (DP_1) or quadratically (DP_2) angular representation functions in each half space; 2) the angular flux at the interfaces is uniformly distributed; 3) the angular flux at the interfaces resulting from the volumetric sources is isotropic for the simplified DP_N method. The purpose of this section is to test the accuracy of the DP_1, DP_2 approximations and their simplified forms.

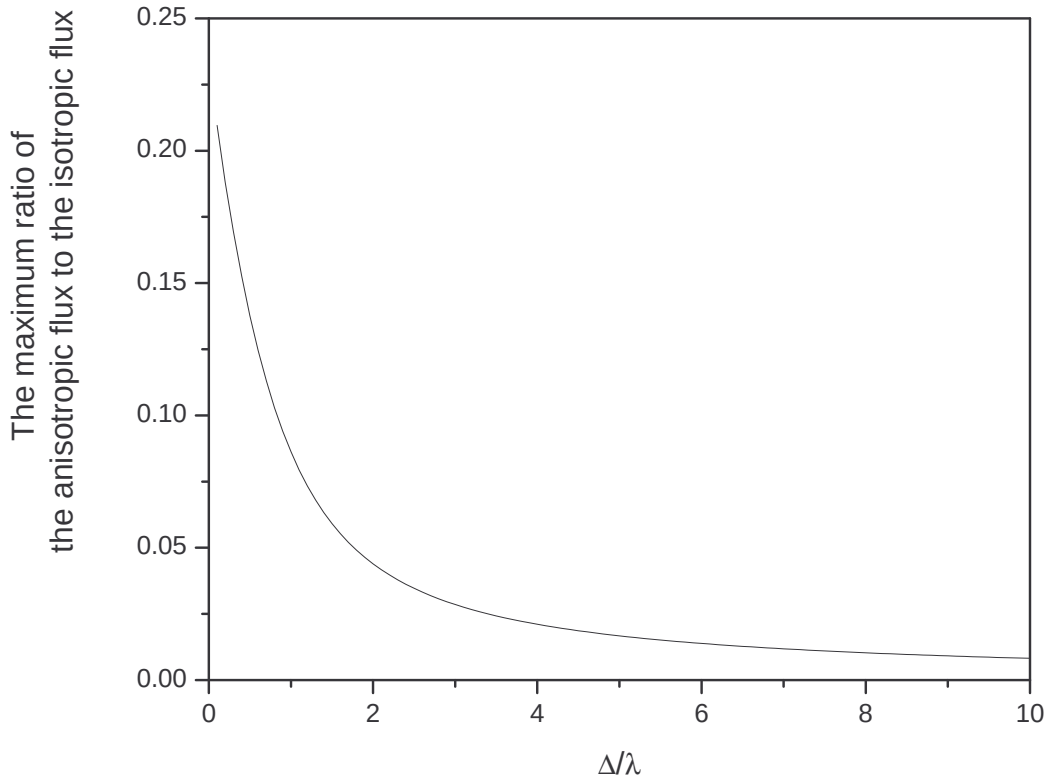

Figure 3.8. The maximum ratio of anisotropic flux to isotropic flux, due to volumetric source in a rectangular region, verses Δ/λ

3.8.1 Test of the DP_N methodology in a slab geometry

3.8.1.1 A slab geometry in a purely ionized medium

In order to test the accuracy of transmission probabilities and exclude any other discrepancy such as those associated with the flat collision source approximation for the calculation of escape probabilities, we have considered the neutral transport in a purely ionizing medium. Similarly, to avoid effects introduced by the reflection model, only vacuum boundary conditions are imposed.

The problem shown in Figure 3.9 is a slab composed of seven identical regions. The width of each regions is $\Delta = 0.3m$. The model has a uniform background plasma. Vacuum boundary conditions are imposed on the either side of the slab. An isotropic and uniform flux of neutral particles with the total partial current of 1 $m^{-2} \cdot s^{-1}$ is injected from the left boundary ($x = 0$). The neutral particles released from the boundary have an energy of 10eV. There are no volumetric sources within the slab.

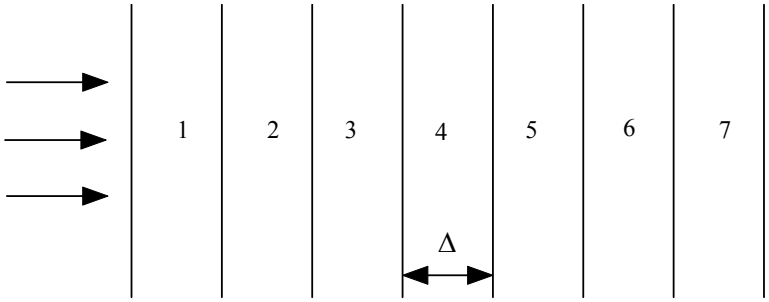

Figure 3.9. A seven-region slab with purely ionizing medium and vacuum boundary

After neutrals travel to the next interface, the original isotropic angular flux becomes peaked in the forward direction. Because it is assumed that more particles are emitted at the large angles, the DP_0 assumption has two effects: (1) over-prediction of the neutral density in the same region; (2) under-prediction of the angular flux or the partial current at the next interface. The first effect results from an over-prediction of the neutral flight time in that region, however this effect can generally be ignored for optically thick regions, in which the neutral flight time is determined by the mean free path rather than by the width of the region. The second effect results from an over-prediction of the neutral attenuation because these neutrals at larger angles have to travel a longer distant to escape to the next interface. This fact was demonstrated in a test with $\Delta/\lambda = 0.27 < 1$. The four different curves in Figure 3.10 correspond to the Monte Carlo (DEGAS), the original GTNEUT code (DP_0) and the GTNEUT code with the DP_1 and DP_2 approximations. The flux distribution at each interface for the different approximations is illustrated in Figure 3.11. It can be seen that GTNEUT with the DP_0 approximation slightly over-predicts the neutral densities in regions 2,3,4 because the first effect is dominant, and then slightly under-predicts the neutral densities in regions 6,7 because of the over-estimation of attenuation. While the GTNEUT simulations with the DP_1 and DP_2 approximations are almost identical as the Monte Carlo calculations throughout the entire region because of the more reasonable assumption of the angular distribution at each interface.

In the second case, we adjust the neutral background plasma properties so that $\Delta/\lambda = 1$. When the neutral mean free path become smaller, the effect of over-predicting the neutral

attenuation becomes dominant. This causes the neutral densities predicted by the DP_0 approximation to be significantly lower than those predicted by the Monte Carlo code, DEGAS, in the cells away from the source (i.e., cells 3,4,5,6,7). This result can be observed in Figure 3.12. Again, GTNEUT with the DP_1 or DP_2 approximation predicts the neutral densities very well for all the cells compared to Monte Carlo. The neutral angular distribution predicted by the different approximations and its exact value is shown in Figure 3.13. It can be observed that the angular flux becomes increasingly forward-peaked while traversing regions, and that the DP_1 and DP_2 approximations predict this change quite well.

In the third case, we set $\Delta/\lambda = 2$. The results of the neutral density and the angular flux profiles are illustrated in Figure 3.14 and 3.15,respectively. Since the neutral flux becomes extremely peaked in the forward direction, the DP_0 approximation is expected to significantly under-predict the neutral densities. The calculations of the DP_2 approximation are in the excellent agreement with the simulations of DEGAS, because a quadratic expansion can represent the anisotropy of the angular flux very well. The neutral densities calculated by the DP_1 approximation are only slightly lower than those calculated by the Monte Carlo code despite that a linear expansion function cannot sufficiently represent the strong anisotropy at the interfaces away from the incident surface.

3.8.1.2 A slab with a realistic background plasma

The purely absorbing background plasma is highly unlikely to occur in realistic situations. Actually, the charge-exchange fraction in edge plasmas varies from 0.7 to almost 1. To test the DP_N approximation for the cases with a realistic background plasma, a series of problems with charge-exchanged sources and different Δ/λ ratios have been investigated.

The geometry of the problems is the same as that presented in section 3.7.1.1. The only difference between the two is that the problems in this section have charge-exchanged sources. The total partial current of the injected isotropic flux remains $1\#/m^2 \cdot s$. The ion temperature is 10eV throughout the entire slab. Vacuum boundary conditions exist on either side of the slab.

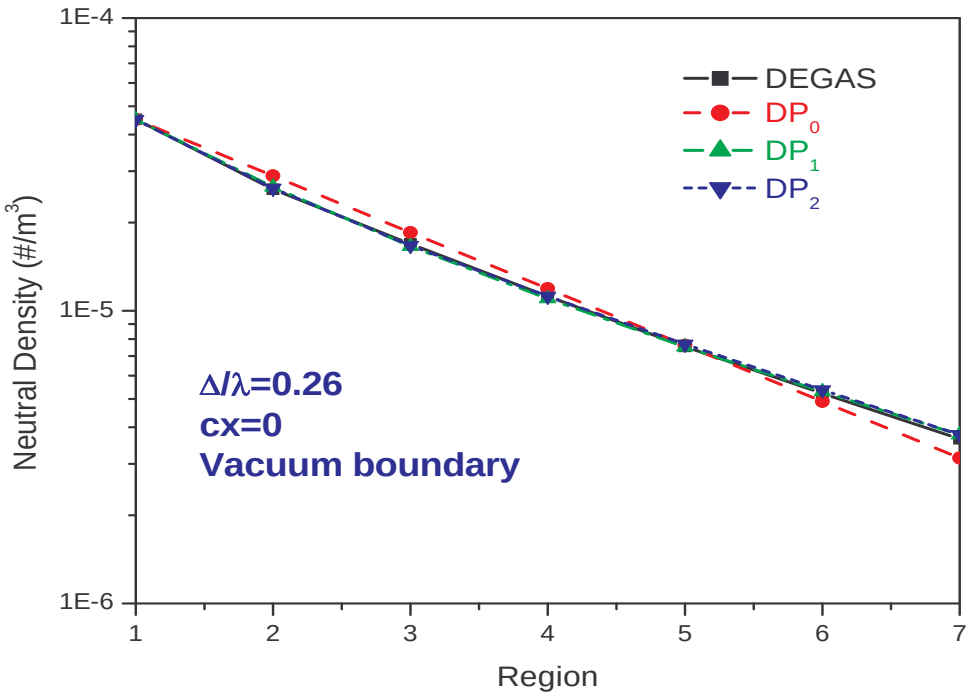

Figure 3.10. Comparison of neutral density for a seven-region slab with purely ionizing medium and

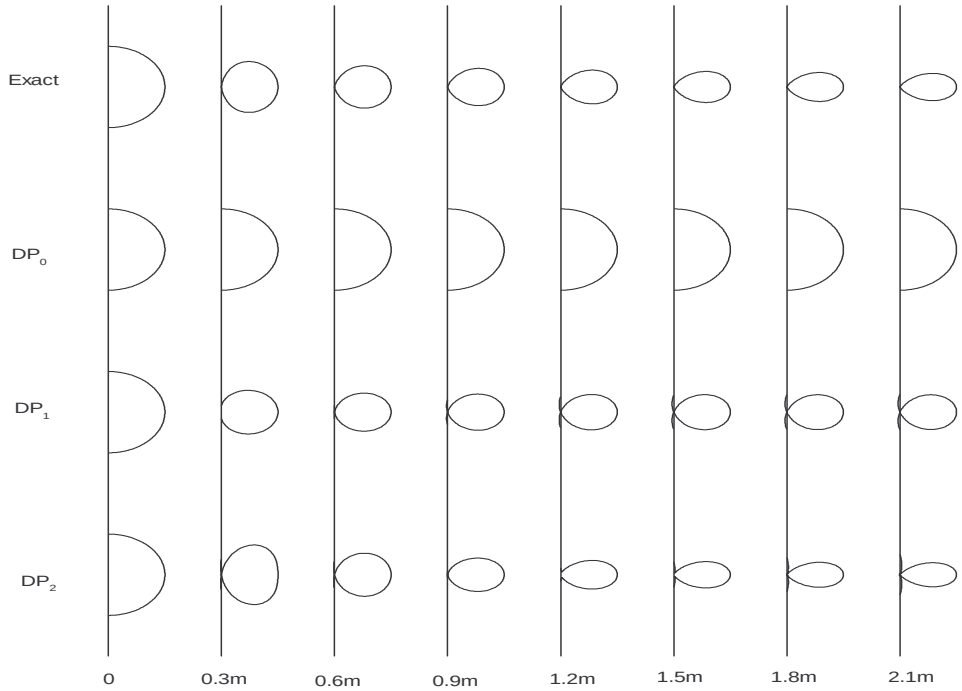

Figure 3.11. Angular distributions of different methods for a seven-region slab with purely ionizing medium and $\Delta/\lambda = 0.26$

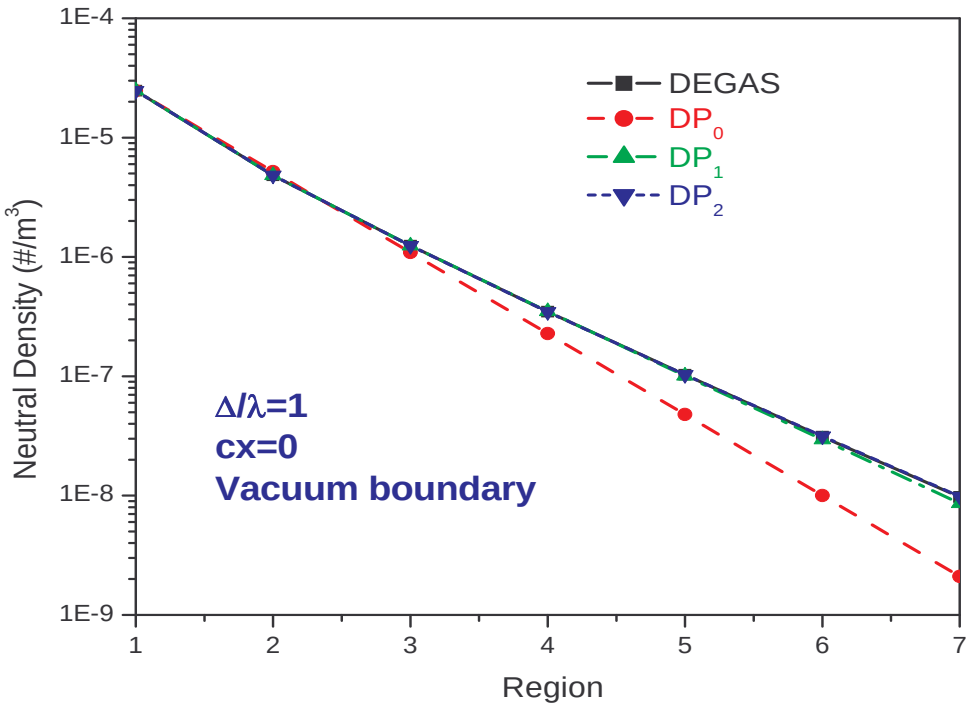

Figure 3.12. Comparison of neutral density for a seven-region slab with purely ionizing medium and

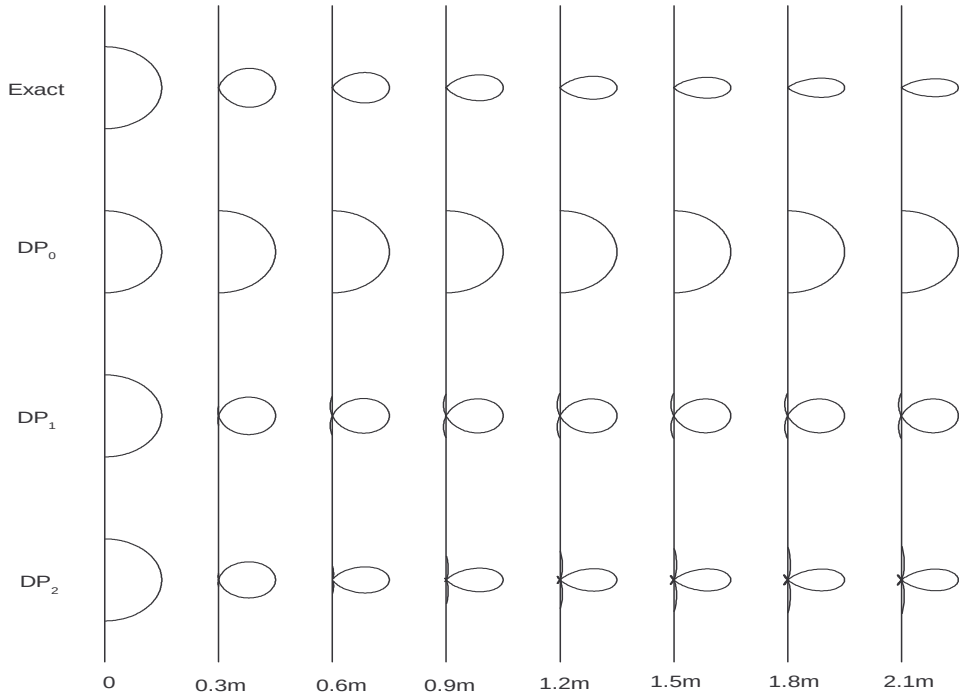

Figure 3.13. Angular distributions of different methods for a seven-region slab with purely ionizing medium and $\Delta/\lambda = 1$

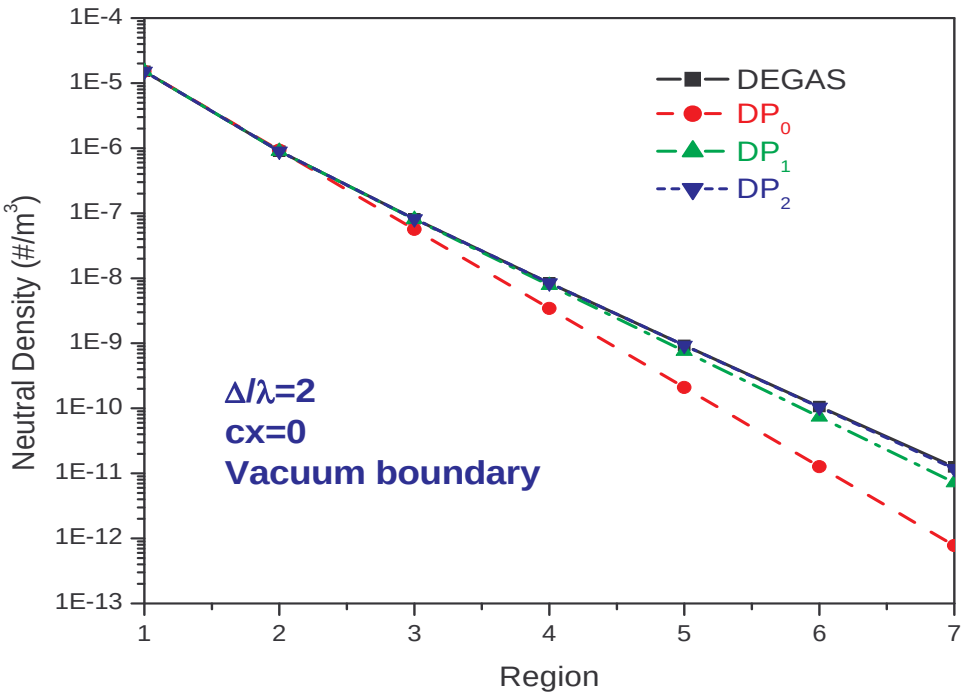

Figure 3.14. Comparison of neutral density for a seven-region slab with purely ionizing medium and

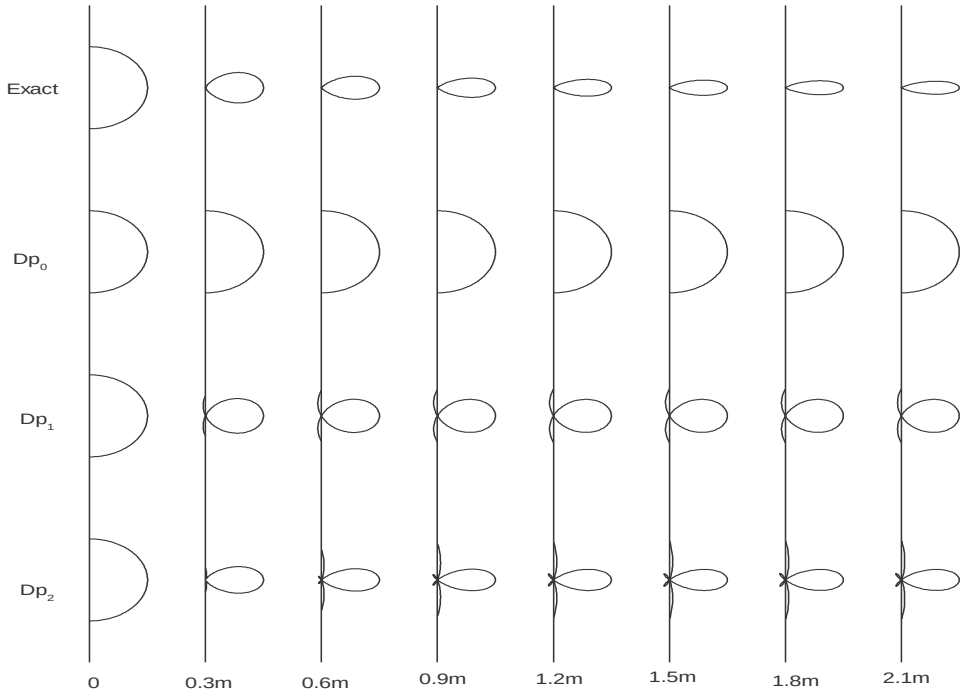

Figure 3.15. Angular distributions of different methods for a seven-region slab with purely ionizing medium and $\Delta/\lambda = 2$

Again, there are three regimes of particular interest: $\Delta/\lambda > 1$, $\Delta/\lambda < 1$, and $\Delta/\lambda \approx 1$. The neutral densities calculated by the different level approximations for the case with $\Delta/\lambda = 0.26$ are shown in Figure 3.16. The calculations of the TEP method with the DP_0, DP_1 or DP_2 approximation are in the excellent agreement with the simulations of DEGAS. The good agreement is expected as the result of mitigating the anisotropy of the angular flux by the randomization of charge-exchange events. The comparisons of the angular flux distributions at each interface for the different level approximations with the Monte Carlo calculations are presented in Figure 3.17.

If the neutral mean free path is comparable to or smaller than the characteristic dimension of the interested regions, the angular flux at each interface is almost isotropic because for this situation the neutral particle flux at a given interface is dominated by the collided particles from the previous computational region. The fact was demonstrated by two runs with $\Delta/\lambda = 1$ and $\Delta/\lambda = 2$, respectively. The angular flux distributions for the different approximations are compared in Figures 3.19 and 3.21, from which it is evident that strong charge-exchange scattering events isotropize the neutral angular distribution. It implies that the neutral densities calculated by the TEP method with the different level approximations will converge to the same results. This fact is obvious from the Figures 3.18 and 3.20, which show the comparisons of the neutral densities calculated by GTNEUT with the simulations of DEGAS. However, because the flat flux breaks down for these regions, the TEP method apparently over-predicts the neutral densities for the cells away from the incident surface. This issue will be addressed by the correction to directionalities associated with non-uniform collided neutral sources in the next chapter.

3.8.2 Test of the DP_N methodology in 2D multi-region problems

As stated in Chapter 2, anisotropies of angular fluxes are driven mainly by the attenuation of a purely absorbing medium in 1D geometry, while for 2D problems anisotropies are also driven by the presence of sources with a finite dimension or asymmetric boundary conditions. The accuracy of the TEP method with the different level approximations have

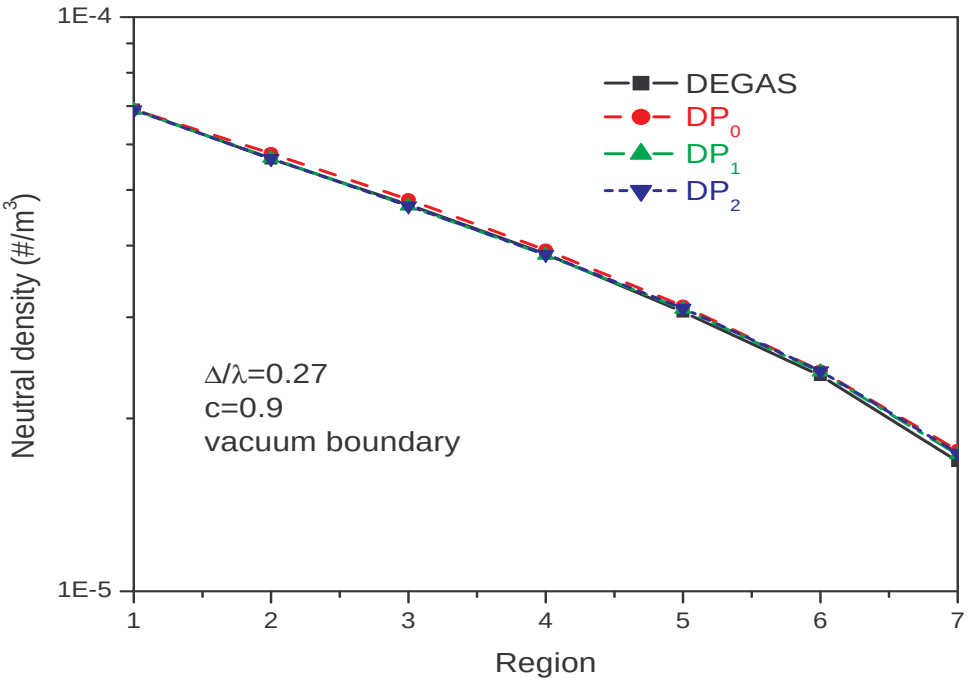

Figure 3.16. Comparison of neutral density for a seven-region slab with c=0.9 and $\Delta/\lambda = 0.26$

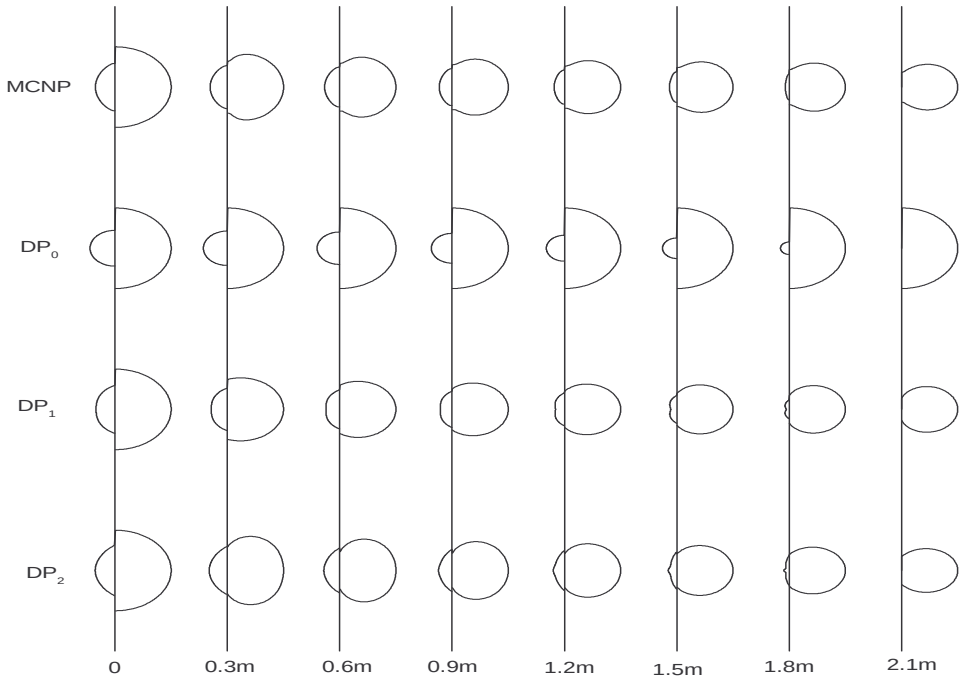

Figure 3.17. Angular distributions of different methods for a seven-region slab with c=0.9 and $\Delta/\lambda = 0.26$

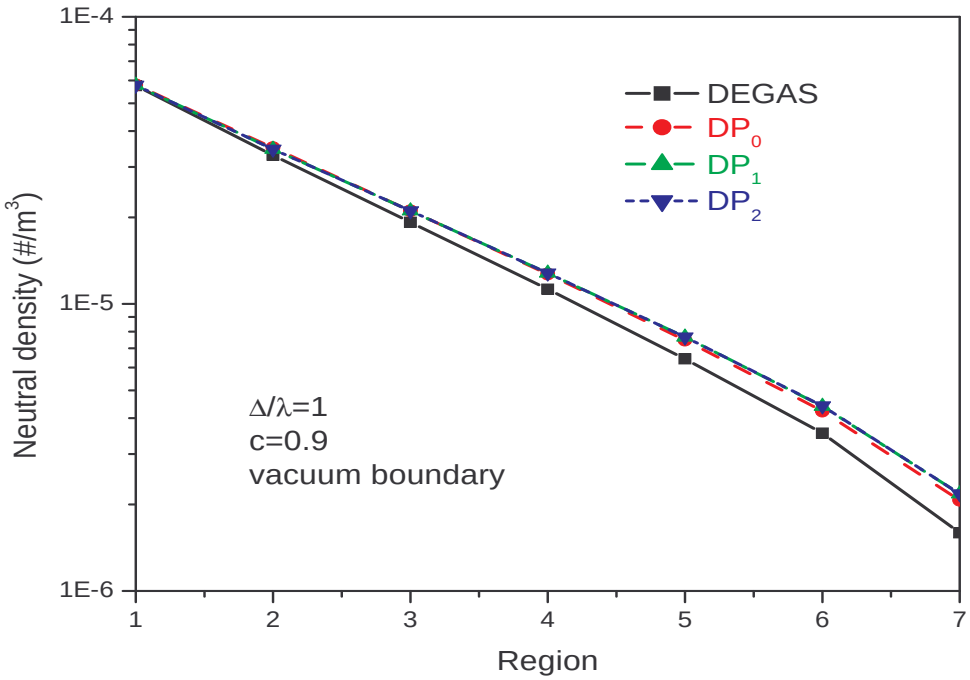

Figure 3.18. Comparison of neutral density for a seven-region slab with c=0.9 and $\Delta/\lambda = 1$

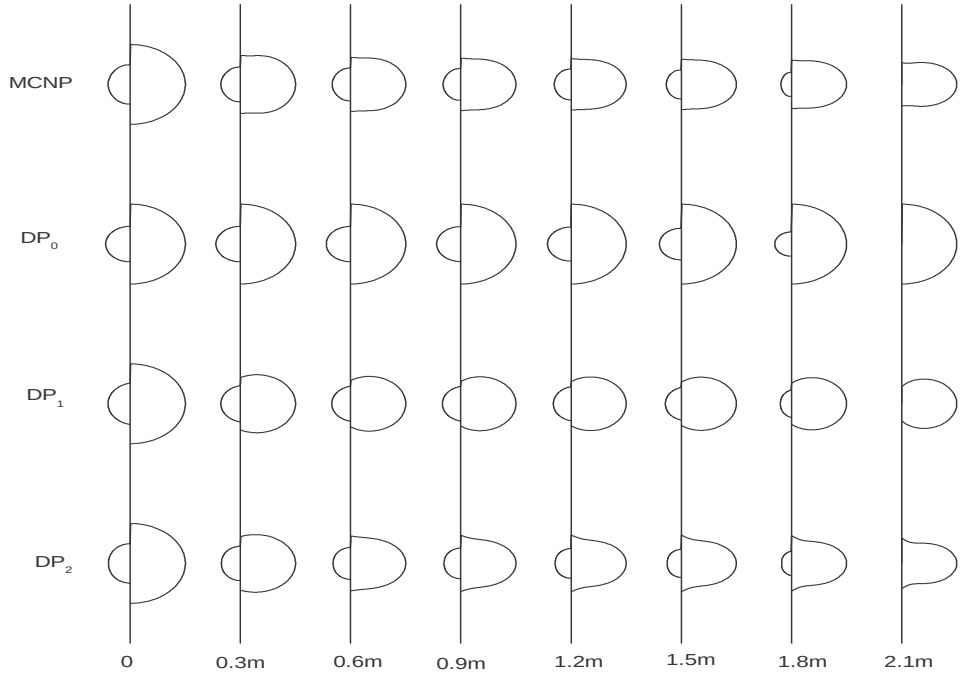

Figure 3.19. Angular distributions of different methods for a seven-region slab with c=0.9 and $\Delta/\lambda = 1$

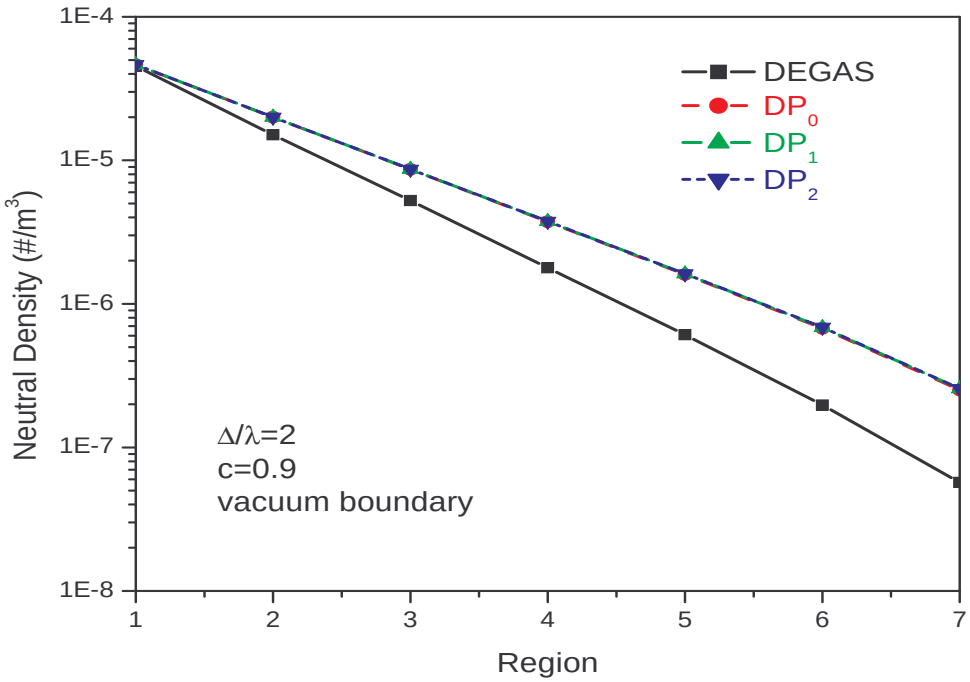

Figure 3.20. Comparison of neutral density for a seven-region slab with c=0.9 and $\Delta/\lambda = 2$

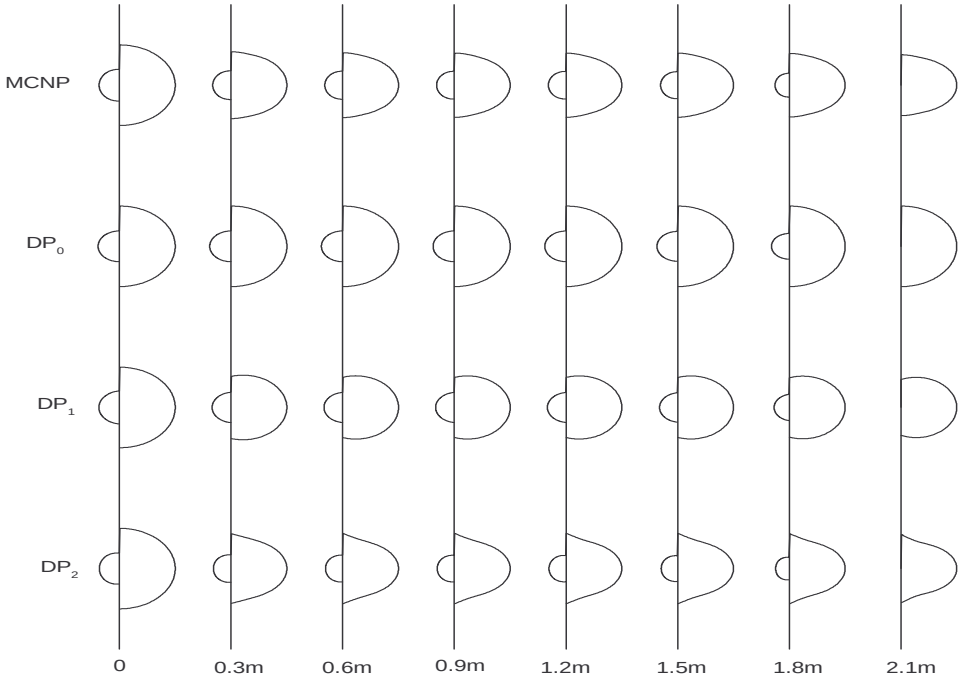

Figure 3.21. Angular distributions of different methods for a seven-region slab with c=0.9 and $\Delta/\lambda = 2$

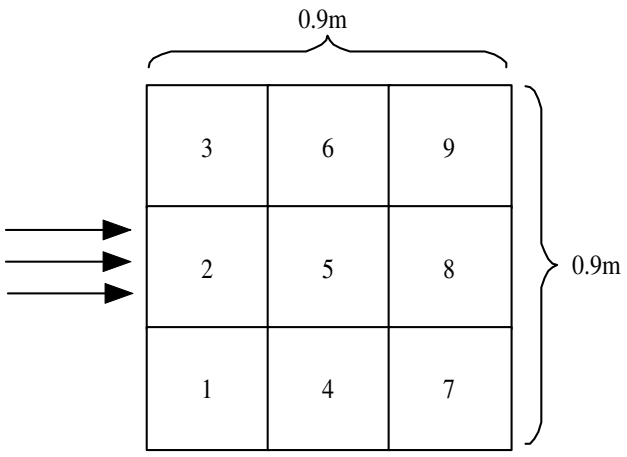

Figure 3.22. Nine uniform square regions model

been evaluated for one-dimensional geometries. The purpose of this section is to test the accuracy of the DP_N approximation for problems with strong 2D effects.

3.8.2.1 A uniform nine-region problem with a purely ionizing medium

The model considered is a 0.9 m × 0.9 m square region composed of nine identical cells. The arrangement of cells is shown in Figure 3.22. As in the previous section, a homogeneous and purely ionizing background plasma is assumed to exclude effects introduced by the flat collision source assumption. To avoid the effects of the reflection model, vacuum boundary conditions are assumed on the four surfaces of the box. The characteristic dimension of each cell is Δ=0.3 m. an isotropic and uniform flux of unit strength is imposed on the left boundary of the second cell. Both the injected neutral energy and the plasmas (ion and electron) temperatures are 10eV.

In the first case considered, the mean free path of neutral particles is set to 1.17 m by adjusting the densities of the background plasma. Unlike in a slab geometry, the angular fluxes become strongly anisotropic once they enter into the next regions though the attenuation is not very strong in this case. For example, at interface between regions 5 and 6, neutral particles must be in the northwest direction. Figure 3.23 shows the neutral densities calculated by the different methods versus the region index. Since the DP_0 assumption fails to take the anisotropy into account, it leads to the under-prediction of the uncollided

flux for the regions (cells 4, 6-9) away from the incident flux. The over-prediction of the density in region 5 by the DP_0 approximation results from the over-estimation of the neutral flight time in this region. Both the DP_1 and DP_2 approximations agree very well with the calculations of DEGAS because of the more reasonable angular flux approximations. However it should be mentioned that the accuracy of the DP_2 is a bit worse than that of the DP_1 approximation compared to the results of the Mont Carlo, unlike for a 1D slab, where the higher order approximation always agrees better with DEGAS than the lower order approximation. this counterintuitive effect can, as stated earlier, be explained by the fact that 2D transmission probabilities are the integrals over a part of the 2π solid angle, while the DP_N approximation is optimized over the whole 2π solid angle.

In the second case, the neutral mean free path is set to 0.3m, so $\Delta/\lambda = 1$. The comparisons of the TEP method (the DP_0 or DP_1 approximation) with DEGAS are presented in Figure 3.24. The neutral flight time in region 5 is mainly determined by the collision distance, so the over-prediction of the flight time by the DP_0 approximation is not important. It can be seen from Figure 3.26 that the neutral density predicted by the DP_0 in region 5 is in good agreement with the Monte Carlo. For regions 4, 6-9 which are away from the incident source, the DP_0 approximation predicts less penetration than DEGAS. The DP_1 and DP_2 approximations result in good agreement between the GTNEUT and DEGAS calculations for the entire region, since they take the anisotropy into account for the calculation of transmission probabilities.

In the third case, the mean free path is 0.15 m, which is smaller than the characteristic dimension of each cell. Figure 3.25 is the graphical output of the neutral densities calculated by the various approximations and DEGAS. It shows that both the DP_1 and DP_2 do a good job for the entire region except cells 4 and 6, while the DP_0 predicts less penetration of the uncollided flux for cells 7-9 than the Monte Carlo code. The discrepancy between the DP_N approximations and DEGAS in cells 4 and 6 is related to the DP_N representation functions. Recalling from section 3.3 that all the DP_N representation functions are

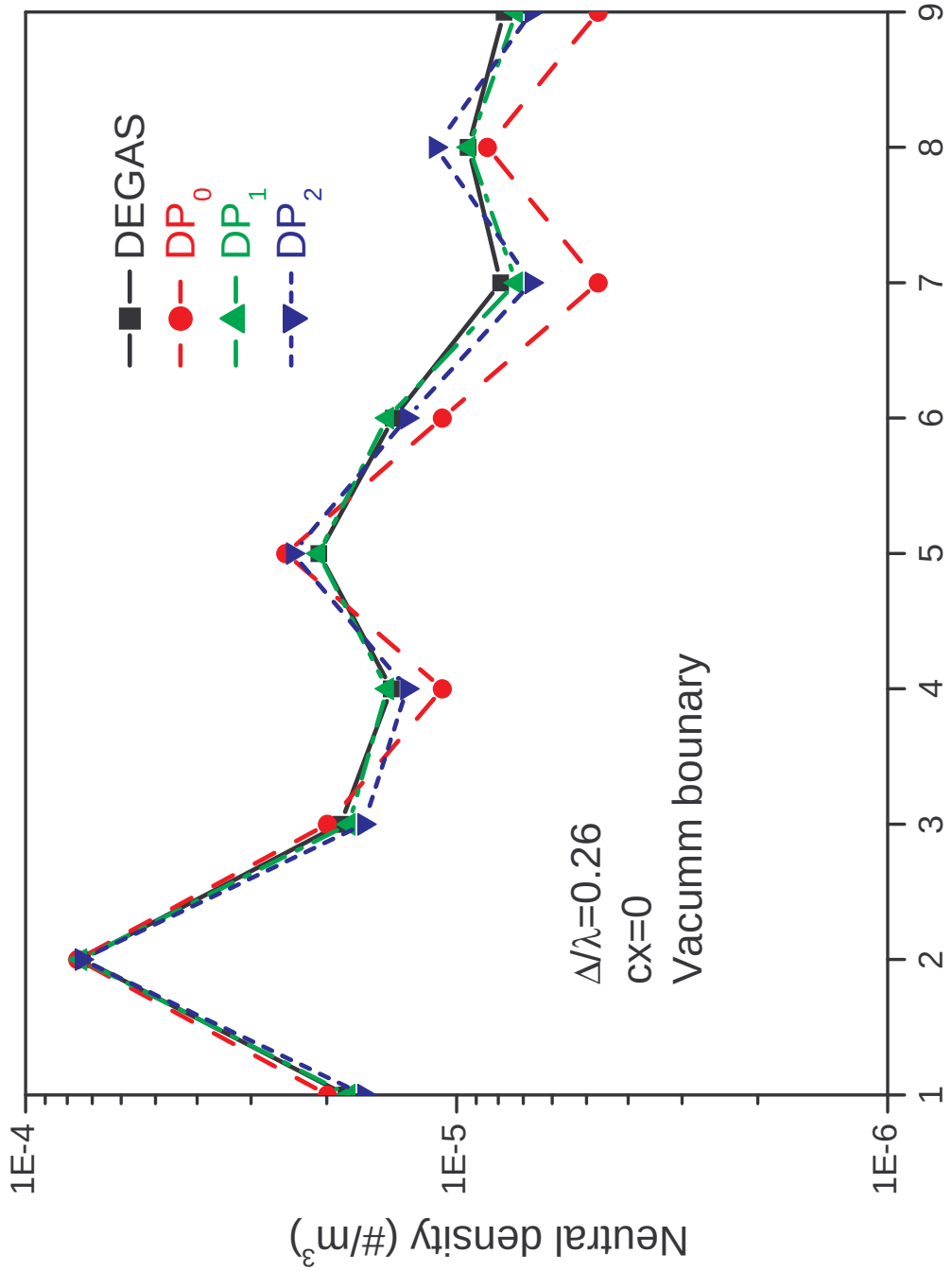

Figure 3.23. Comparison of neutral density for a nine-region model with purely ionizing medium and $\Delta/\lambda = 0.26$

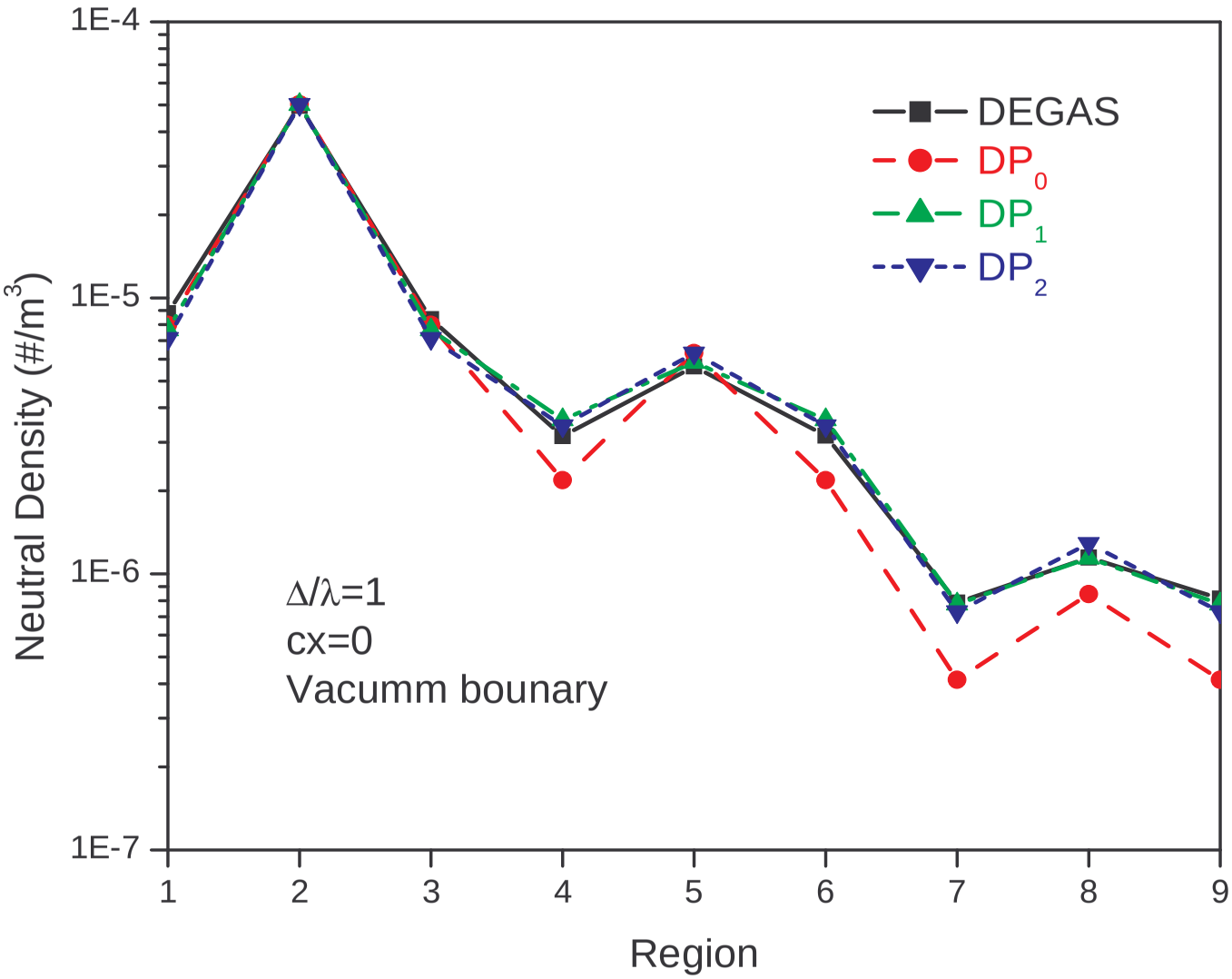

Figure 3.24. Comparison of neutral density for a nine-region model with purely ionizing medium and $\Delta/\lambda = 1$

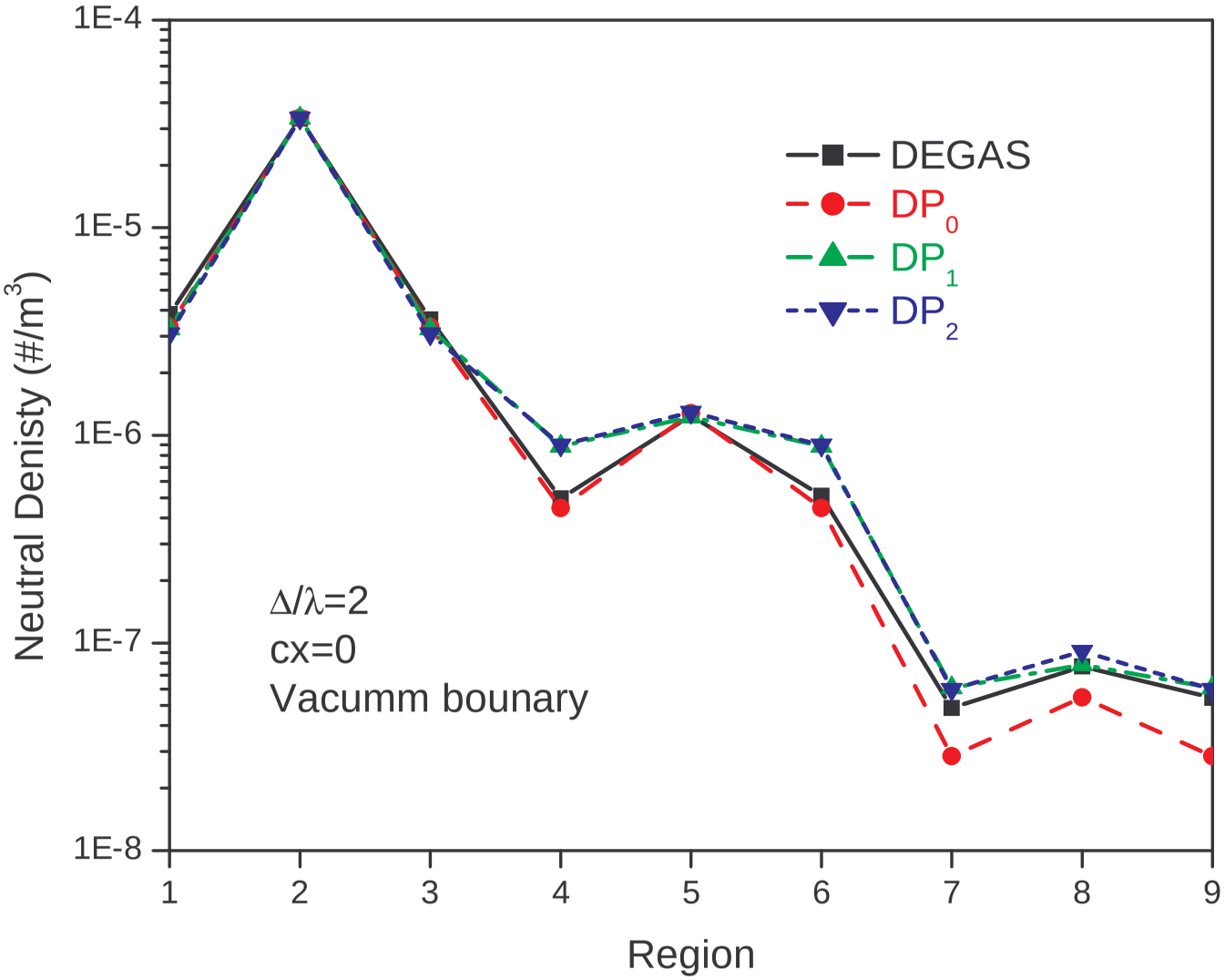

Figure 3.25. Comparison of neutral density for a nine-region model with purely ionizing medium and $\Delta/\lambda = 2$

spatially independent, it assumes that the angular flux is uniformly distributed over each interface. In fact, the strength of the flux at an interface strongly depends on the spatial variables for short mean free path cases. Taking the interface between cells 2 and 3 as an example, the flux at the right end is much smaller than the flux at the left end. Obviously, the neutral particles emitted from the right end have higher probability to be transmitted to cell 6 than those emitted from the other end. As a result, the assumption of the spatially uniform flux leads to the DP_N over-predicting the uncollided flux from cell 3 to cell 6. A similar explanation can be applied to cell 4. For the DP_0 approximation, the error produced by the uniform flux assumption tends to balance with the under-prediction introduced by the isotropic assumption, consequently the agreement between the DP_0 approximation and DEGAS can be seen clearly in cells 4 and 6.

3.8.2.2 A uniform nine-region problem with realistic background plasmas

In order to test the accuracy of the DP_N approximations for 2D geometries with realistic background plasmas, the same geometry as in the previous section is used. The only difference is that in the problems of this section the charge-exchange fraction is set to 0.9. Vacuum boundary conditions are imposed on the four surfaces of the box. An isotropic and uniform flux with unit strength is injected from the left boundary of cell 2. The energy of the incident neutrals and the plasma temperature are 10eV. Again, three cases with $\Delta/\lambda = 0.26$, $\Delta/\lambda = 1$ and $\Delta/\lambda = 2$ are tested.

The comparisons are presented in Figures 3.26-3.28, respectively. For the case with long mean free path, similar results are obtained as those with a purely absorbing medium because of the domination of the directly transmitted flux. In the case of $\Delta/\lambda = 1$, the DP_0 approximation actually agrees the best with Monte Carlo. This is due to the fact that for this situation the errors of the isotropization and the directional escape probabilities almost cancel with each other. However, the cancelation is broken for the DP_1 or DP_2 methodology because of its higher order approximation.

For the case of $\Delta/\lambda = 2$, as a result of the isotropization of charge-exchange events, the

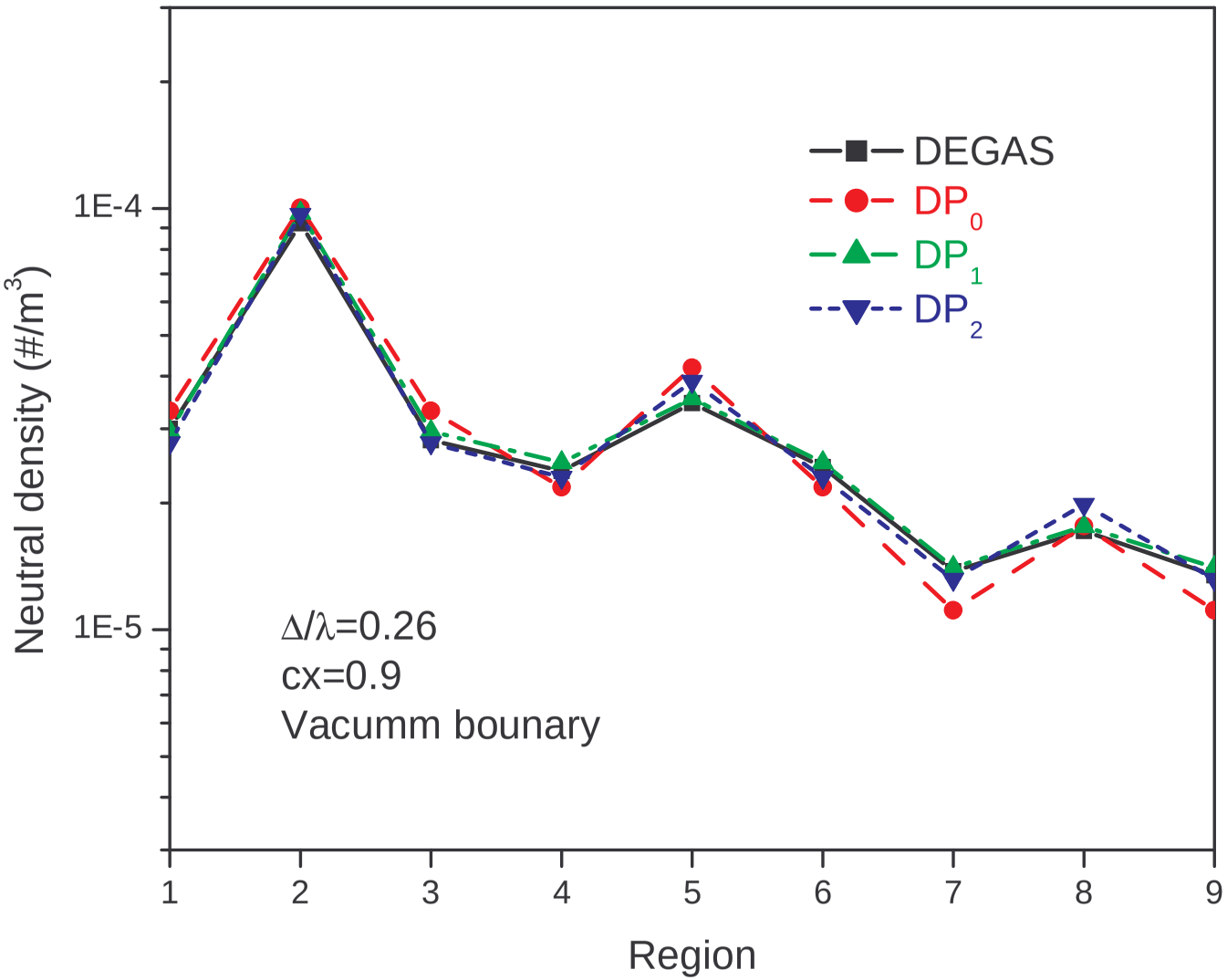

Figure 3.26. Comparison of neutral density for a nine-region model with c=0.9 and $\Delta/\lambda = 0.26$

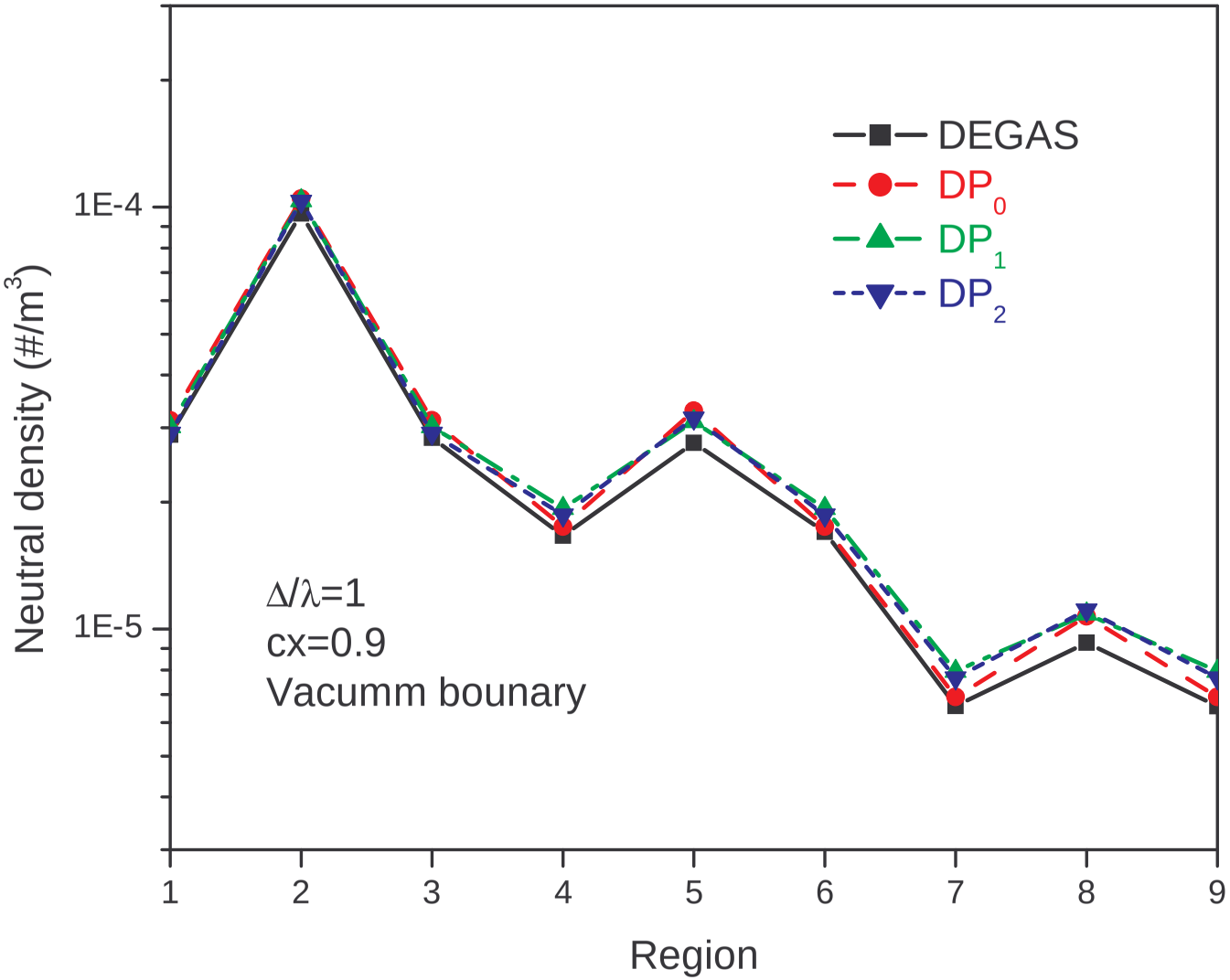

Figure 3.27. Comparison of neutral density for a nine-region model with c=0.9 and $\Delta/\lambda = 1$

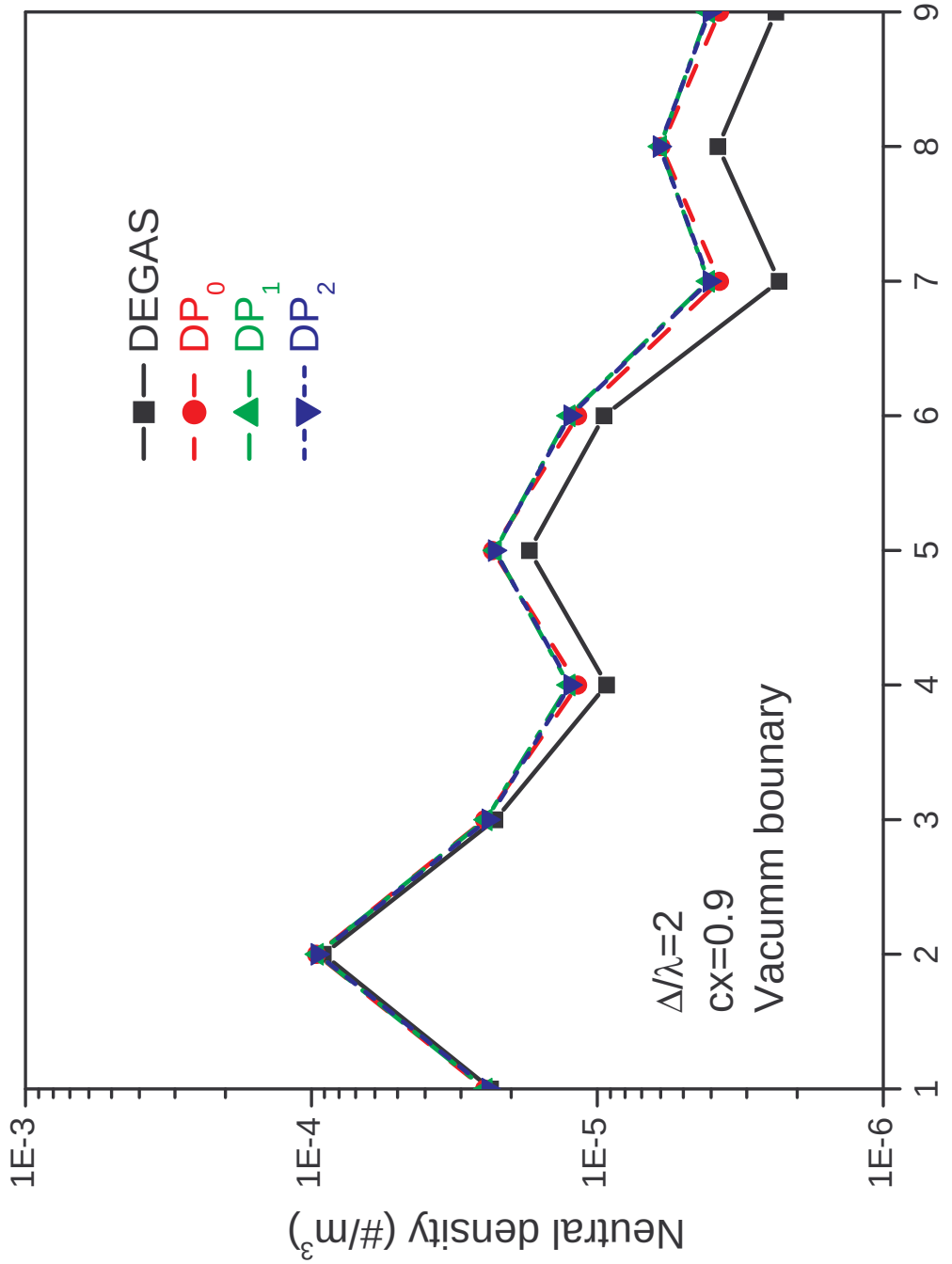

Figure 3.28. Comparison of neutral density for a nine-region model with c=0.9 and $\Delta/\lambda = 2$

calculations of the TEP method with the different level approximations approach the same results. However, all of them over-predict the collided flux because of the flat collision source assumption.

3.8.3 Test of the simplified DP_1 methodology

In Section 3.7, a simplified version of the DP_N approximation was proposed. Essentially it is assumed the collided neutral flux at an interface is isotropically distributed. In order to test this approximation, the nine-region problem shown in Figure 3.22 is used to compare the calculations of the full and simplified DP_1 approximations. The model problem has a uniform background plasma and vacuum boundary conditions at the four external surfaces. The plasma ion temperature is set to 10eV, the charge-exchange fraction is adjusted to be 0.9. An isotropic and uniform flux with unit intensity is injected from the right boundary of region 2.

In the first case, the mean free path for neutrals is λ=1.17 m, resulting in $\Delta/\lambda = 0.26$. In Figure 3.29, the comparison of the predictions of the full and simplified DP_1 approximations is presented. Since the mean free path is much longer the characteristic dimension of the regions of interest, the flux at each interface is predominantly composed of the uncollided neutrals. The discrepancy between the full and simplified approximations is expected to be negligible as shown in Figure 3.29. In the second case, the mean free path for neutral is λ=0.15 m, resulting in $\Delta/\lambda = 2$. For optically thick regions, the collided neutrals play a more important role. However, charge-exchange events tend to isotropize the neutral distribution function. As a result the simplified DP_1 approximation should not introduce any extra significant errors. As we can see from Figure 3.30, the results of the simplified approximation are almost the same as those of the full DP_1 approximation. In the last case the ratio Δ/λ is set to equal 1. The comparison is presented in Figure 3.31. As in the previous two cases, the simplified DP_1 approximation is sufficient to represent the angular distribution of neutrals crossing interfaces.

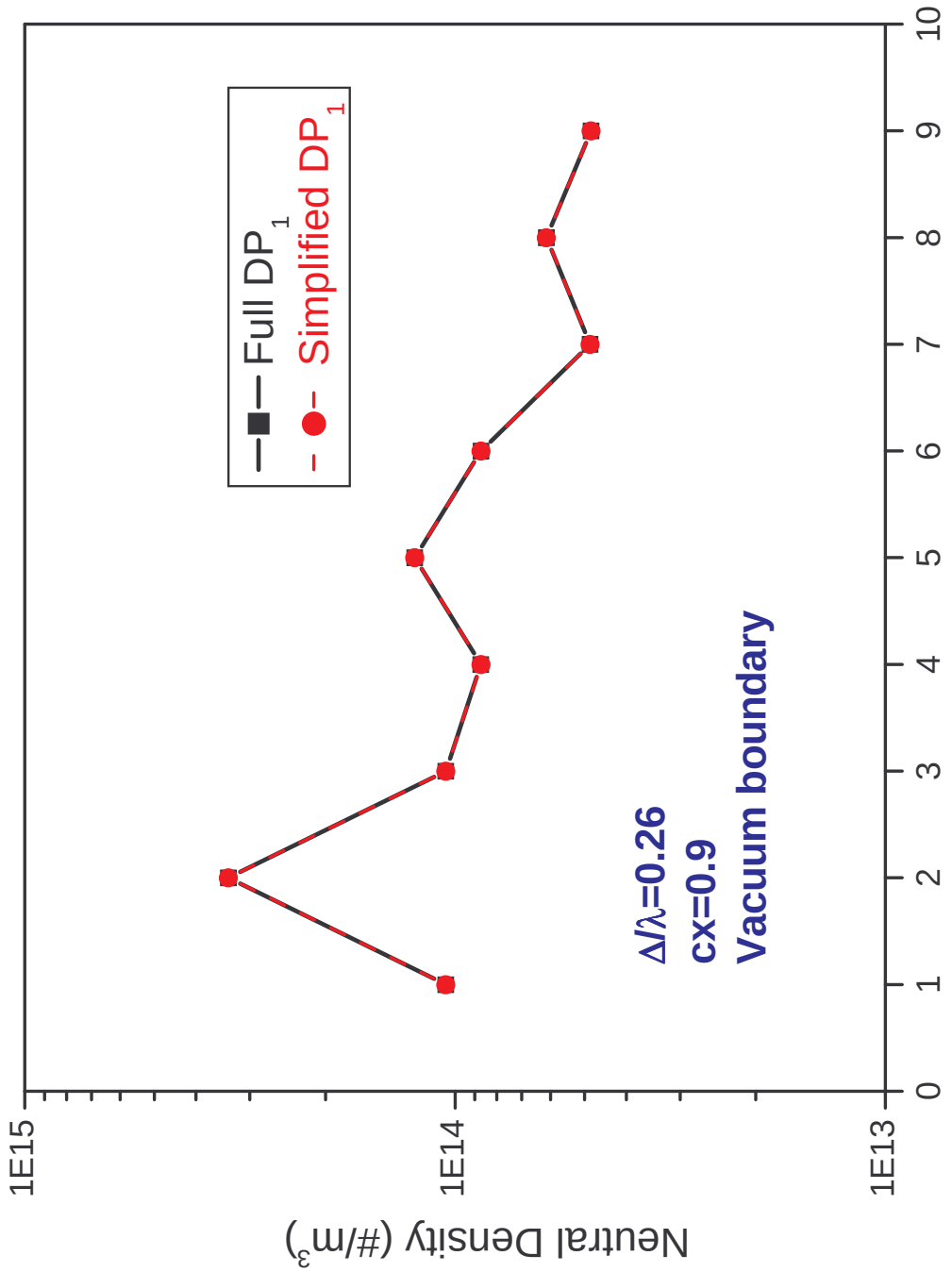

Figure 3.29. Test of the simplified DP_1 for a nine-region model with c=0.9 and $\Delta/\lambda = 0.26$

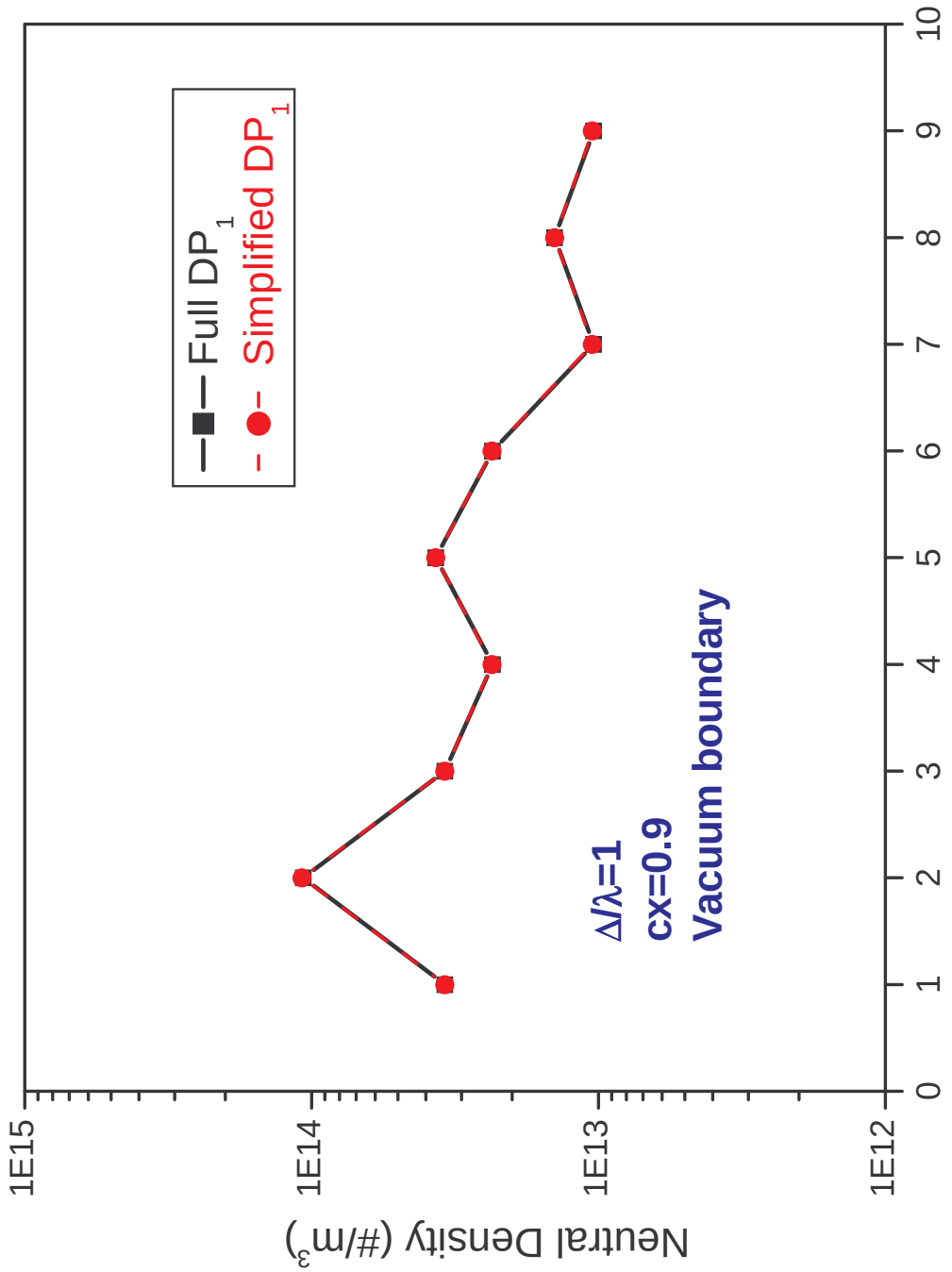

Figure 3.30. Test of the simplified DP_1 for a nine-region model with c=0.9 and $\Delta/\lambda = 1$

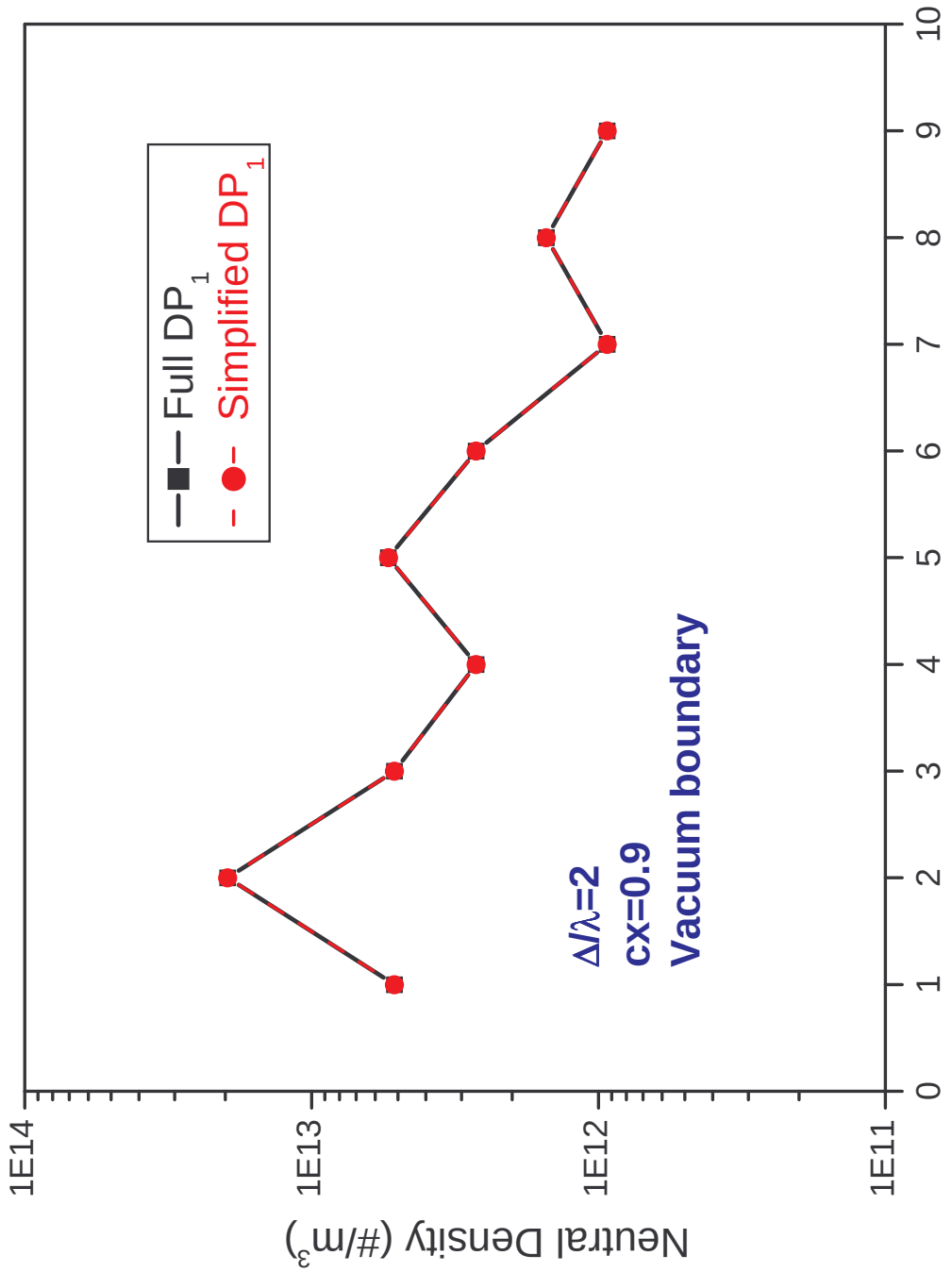

Figure 3.31. Test of the simplified DP_1 for a nine-region model with c=0.9 and $\Delta/\lambda = 2$

3.9 Conclusions

The DP_1 and DP_2 approximations have been derived and implemented to take into account the anisotropy of the angular flux at each interface, driven by the presence of sources, boundaries or attenuation. The angular flux crossing each interface is assumed to be linearly or quadratically distributed over both the inward and outward hemispheres, respectively, in these approximations. The moment of the exiting partial current crossing each interface is coupled to all the moments of the incident currents from the adjacent regions via transmission and escape probabilities. To improve the computational efficiency, an additional assumption that the collided flux is isotropically distributed at each interface was made to further simplify the DP_N method.

In order to exclude the discrepancies introduced by the assumption of the uniform charge-exchanged sources and the reflection model, a number of specially designed model problems with artificial purely ionizing background plasmas and vacuum boundaries are exploited to test the accuracy of the DP_1 and DP_2 approximations. This study has indicated that the DP_1 approximation significantly improves the agreement with the Monte Carlo simulations, while there is little advantage to further extend to the DP_2 approximation.

The comparisons of the full and simplified DP_N approximations have revealed that the assumption of the isotropic collided flux is a reasonable approximation for all the range of Δ/λ ratios considered.

Finally, though the angular distribution of neutral flux crossing each interface can be adequately represented by the DP_N expansion functions, the error produced by the assumption of the uniform charge-exchanged sources leads to an over-prediction of the collided neutrals, due to the failure to take into account the predominant escape of particles back across the incident surface for optically thick regions. The approaches to address the effect of non-uniform collided neutral sources will be presented in the next chapter.

CHAPTER 4

CORRECTIONS TO DIRECTIONALITIES

4.1 Introduction

The flat collision source approximation assumes that charge-exchanged or elastic scattered sources, which are responsible for the collided term in the balance equations of partial current moments, are uniformly distributed in each computational cell. Detailed comparisons with Monte Carlo indicate that the flat collision source assumption is a good approximation for optically thin regions, where attenuation can be neglected. However, if neutrals can penetrate into the inner plasma region, whose characteristic dimension is much larger than neutral mean free path, the charge-exchanged or elastic scattering sources are preferentially located near the incident surface. In this case the flat collision source approximation leads to an over-prediction of collided neutrals in the forward direction.

Since the TEP method is based on a particle balance over each computational cell, the problem of interest can be broken into a number of smaller problems, in which the collided neutral particle current distribution leaving each cell is determined as a function of the neutral partial current entering the cell. With each small problem solved, total and directional escape probabilities are determined, then a global calculation can be carried out to obtain the partial current moments at each interface. With the partial current moments known, a local calculation can proceed to determine the neutral densities or ionization rates. A variety of techniques such as the discrete ordinance, the collision probability method, the diffusion theory and the Monte Carlo method can be utilized in evaluating escape probability matrices. The choice of methods depends on the physics of the problems under consideration and the level of approximations.

In this chapter, the following three approaches will be proposed and tested: (1) subdividing optically thick cells; (2) expansion of collision sources; and (3) diffusion approximation.

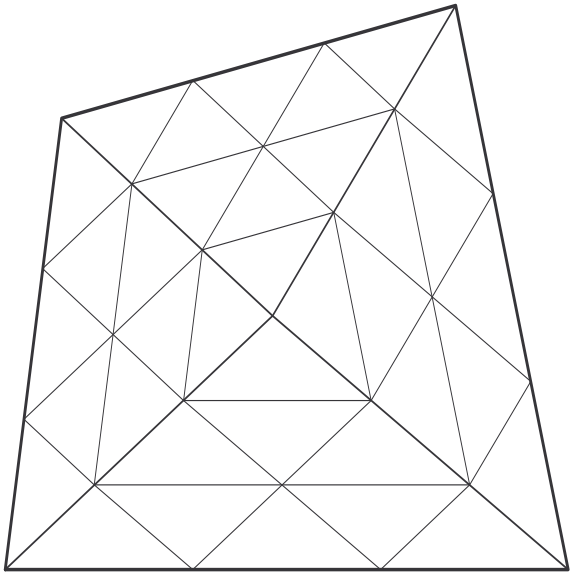

Figure 4.1. Schematic diagram of subdivision of an optically thick region

4.2 Approach I: Subdividing optically thick cells

The easiest and most straightforward way to address effects of the non-uniformity of collided neutrals is to subdivide an optically thick region into sufficiently small cells, within which the charge-exchange sources can be approximated to be uniformly distributed. The following strategy of dividing an optically thick region shown in Figure 4.1 can significantly improve computational efficiency. First, any polygon with m sides can be divided into m triangles. Each triangle can then be sub-divided into identical smaller triangles as illustrated in Figure 4.1. Finally, TEP balance equations for partial current moments are applied to each smaller triangle.

$$\Gamma^{n}_{k,j} = \sum_{k}\sum_{n'} T^{n'\to n}_{i,k\to j}\Gamma^{n'}_{k,i} + \sum_{k}\sum_{n'}\left(\delta_{n'0} - \sum_{l} T^{n'\to 0}_{i,k\to l}\right)\Gamma^{n'}_{k,i}c_i P_i \Lambda^{0}_{i,j}\delta_{n0} + S^{i}_{ext}P_i\Lambda^{0}_{i,j}\delta_{n0}. \quad (4.1)$$

Since all the small triangles within a large triangle are identical, the problem of interest is subdivided into a large number of cells–but only m cell types. If the plasma properties are uniform, only one transmission and escape probability matrix is required to be evaluated for each cell type. Therefore, the computational effort to numerically evaluate transmission and escape probability matrices is substantially reduced. However, this technique usually results in a large matrix for the final linear system. For example, in order to make the flat

collision source assumption valid for a computational region with $\Delta/\lambda = 3$, it is required to subdivide this region into more than 100 subregions with $\Delta/\lambda = 0.3$. Furthermore, as stated in the previous chapter, the finer the grid, the higher order the DP_N approximation needed. The number of transmission probabilities for each pair interfaces increases as N^4 as the order N of an approximation increases. The requirement to use higher order DP_N approximations makes it unattractive to implement this method for a realistic tokamak plasma configuration.

To overcome the difficulties in evaluating expensive high order transmission probabilities, an alternative way is to apply the collision probability method to subregions within each optically thick region, so partial current moments are be used to link the solutions in the cells of an optically thick medium. This method is called as the multi-cell interface current method in neutron transport theory. However, the multi-cell interface current method results in a dense collision probability matrix within each optically thick region.

4.3 Approach II: Linear expansion of collision sources

4.3.1 Balance equations

To formulate TEP balance equations with an expansion of collided neutral sources we begin with the two equations relating the angular flux leaving a cell, $\psi(\mathbf{r}, \mathbf{\Omega})$, and the scalar flux inside the cell, $\phi(\mathbf{r})$,

$$\psi(\mathbf{r}, \mathbf{\Omega}) = \psi_{in}(\mathbf{r_S}, \mathbf{\Omega}) \exp\left(-\tau(\mathbf{r}, \mathbf{r_S})\right) + \int_0^{R_S} dl \frac{q(\mathbf{r} - l\mathbf{\Omega})}{4\pi} \exp\left(-\tau(\mathbf{r}, \mathbf{r} - l\mathbf{\Omega})\right), \tag{4.2}$$

$$\phi(\mathbf{r}) = \int_{D_i} d\mathbf{r}' \frac{q(\mathbf{r}') \exp\left(-\tau(\mathbf{r}, \mathbf{r}')\right)}{4\pi|\mathbf{r} - \mathbf{r}'|^2} + \int_{\partial D_i} dS \psi_{in}(\mathbf{r_S}, \mathbf{\Omega}) \frac{\exp\left(-\tau(\mathbf{r}, \mathbf{r}_S)\right)}{|\mathbf{r} - \mathbf{r}_S|^2} (\mathbf{\Omega} \cdot \mathbf{n}_-). \tag{4.3}$$

To solve the above system of equations, we expand the incoming and outgoing angular fluxes at each interface and the scalar flux within each computational cell. We write

$$\psi(\mathbf{r}, \mathbf{\Omega}) = \sum_{i,j,n} \Gamma^n_{i,j} \psi^n_{i,j}(\mathbf{r}, \mathbf{\Omega}), \tag{4.4}$$

$$\phi(\mathbf{r}) = \sum_{i,\alpha} \Phi^\alpha_i \phi^\alpha_i(\mathbf{r}), \tag{4.5}$$

where $\psi^n_{i,j}(\mathbf{r},\mathbf{\Omega})$ and $\phi^n_i(\mathbf{r})$ are the locally defined angular and scalar flux representation functions, $\Gamma^n_{i,j}$ and Φ^n_i are the expansion coefficients associated with these representation functions. The expansion functions satisfy the following orthogonality conditions,

$$\left\langle \psi^n_{i,j}(\mathbf{r},\mathbf{\Omega}) \middle| \psi^{n'}_{i',j'}(\mathbf{r},\mathbf{\Omega}) \right\rangle = \frac{\delta_{nn'}\delta_{ii'}\delta_{jj'}}{\pi S_{ij}}, \tag{4.6}$$

$$\left(\phi^\alpha_i(\mathbf{r}), \psi^{\alpha'}_{i'}(\mathbf{r})\right) = \frac{\delta_{\alpha\alpha'}\delta_{ii'}}{V_i}, \tag{4.7}$$

where S_{ij} is the area of interface between cells i and j, V_i is the volume of cell i, and the inner products are defined as

$$\langle \psi_1(\mathbf{r},\mathbf{\Omega}) | \psi_2(\mathbf{r},\mathbf{\Omega}) \rangle = \int_{R^2} dS \int_{4\pi} d\mathbf{\Omega} \psi_1(\mathbf{r},\mathbf{\Omega}) \psi_2(\mathbf{r},\mathbf{\Omega}) |\mathbf{\Omega}\cdot\mathbf{n}_+|, \tag{4.8}$$

$$(\phi_1(\mathbf{r}), \psi_2(\mathbf{r})) = \int_{R^3} d\mathbf{r}\phi_1(\mathbf{r})\phi_2(\mathbf{r}). \tag{4.9}$$

Making use of the orthogonality conditions 4.6 and 4.7, expansion coefficients of the angular and scalar fluxes can be expressed as

$$\Gamma^n_{i,j} = \pi S_{ij} \left\langle \psi^n_{i,j}(\mathbf{r},\mathbf{\Omega}) | \psi(\mathbf{r},\mathbf{\Omega}) \right\rangle, \tag{4.10}$$

$$\Phi^\alpha_i = V_i (\phi^\alpha_i(\mathbf{r}), \phi(\mathbf{r})). \tag{4.11}$$

If we choose the zeroth representation functions to be a constant, $\Gamma^0_{i,j}$ is the total partial current from i to region j, and Φ^0_i is the total scalar flux in region i.

To obtain the n-th moment of the angular flux from region i to region j, we multiply both the sides of Eq. 4.2 by a factor $\pi S_{ij}\psi^n_{i,j}(\mathbf{r}_{ij},\mathbf{\Omega})(\mathbf{\Omega}\cdot\mathbf{n_{ij}})$ and expand ψ_{in} and the volumetric source $q(\mathbf{r})$, then integrate the equation over the interface ∂D_{ij} and the solid angle 2π. The result is

$$\Gamma^n_{i,j} = \sum_{k,n'} \Gamma^{n'}_{k,i} T^{n'\to n}_{i,k\to j} + \sum_\alpha PE^{n\alpha}_{ji} Q^\alpha_i, \tag{4.12}$$

where $T^{n'\to n}_{i,k\to j}$ is the generalized transmission probability defined in Eq. 3.13a, $PE^{n\alpha}_{ji}$ is the generalized escape probability, which is the probability that neutral particles emitted in

region i and in mode α will escape into region j in mode n without a collision within region i.

$$PE_{ji}^{n\alpha} = \pi S_{ij} \int_{\partial D_{ij}} dS_{ij} \int_{D_i} d\mathbf{r} \psi_{i,j}^{n}\left(\mathbf{r}_{ij}, \mathbf{\Omega}\right) \phi_i^{\alpha}(\mathbf{r}) \frac{\exp\left(-\tau(\mathbf{r_{ij}}, \mathbf{r})\right)}{4\pi|\mathbf{r} - \mathbf{r}_{ij}|^2} \left(\mathbf{\Omega} \cdot \mathbf{n}_{ij}\right), \tag{4.13}$$

and Q_i^{α} is the n-th moment of the total volumetric source, so

$$\begin{aligned} Q_i^{\alpha} &= V_i\left(\left(\phi_i^{\alpha}(\mathbf{r}), q(\mathbf{r})\right)\right) \\ &= \Sigma_{cx} \Phi_i^{\alpha} + S_i^{\alpha}, \end{aligned} \tag{4.14}$$

where we expand the external volumetric source S_i^{ext}.

$$S_i^{\alpha} = V_i\left(\phi_i^{\alpha}(\mathbf{r}), S_i^{ext}(\mathbf{r})\right). \tag{4.15}$$

Substituting Eq. 4.3 into Eq. 4.11 yields

$$\begin{aligned} \Phi_i^{\alpha} &= V_i\left(\phi_i^{\alpha}(\mathbf{r}), \phi(\mathbf{r})\right) \\ &= V_i \int_{D_i} d\mathbf{r} \int_{D_i} d\mathbf{r}' \phi_i^{\alpha}(\mathbf{r}) \frac{q(\mathbf{r}') \exp\left(-\tau(\mathbf{r}, \mathbf{r}')\right)}{4\pi|\mathbf{r} - \mathbf{r}'|^2} \\ &\quad + V_i \int_{D_i} d\mathbf{r} \int_{\partial D_i} dS\, \phi_i^{\alpha}(\mathbf{r}) \psi_{in}(\mathbf{r_S}, \mathbf{\Omega}) \frac{\exp\left(-\tau(\mathbf{r}, \mathbf{r}_S)\right)}{|\mathbf{r} - \mathbf{r}_S|^2} (\mathbf{\Omega} \cdot \mathbf{n}_{-}). \end{aligned} \tag{4.16}$$

Expanding $q(\mathbf{r}')$ and $\psi_{in}(\mathbf{r_S}, \mathbf{\Omega})$ in the above equation, we have

$$\begin{aligned} \Phi_i^{\alpha} &= V_i\left(\phi_i^{\alpha}(\mathbf{r}), \phi(\mathbf{r})\right) \\ &= V_i \sum_{\alpha'} Q_i^{\alpha'} \int_{D_i} d\mathbf{r} \int_{D_i} d\mathbf{r}' \phi_i^{\alpha}(\mathbf{r}) \phi_i^{\alpha'}(\mathbf{r}') \frac{\exp\left(-\tau(\mathbf{r}, \mathbf{r}')\right)}{4\pi|\mathbf{r} - \mathbf{r}'|^2} \\ &\quad + V_i \sum_{k,m} \Gamma_{k,i}^{m} \int_{D_{ij}} d\mathbf{r} \int_{\partial D_{ik}} dS_{ik} \phi_i^{\alpha}(\mathbf{r}) \psi_{k,i}^{m}(\mathbf{r_{ik}}, \mathbf{\Omega}) \frac{\exp\left(-\tau(\mathbf{r}, \mathbf{r}_{ik})\right)}{|\mathbf{r} - \mathbf{r}_{ik}|^2} (\mathbf{\Omega} \cdot \mathbf{n_{ki}}). \end{aligned} \tag{4.17}$$

Define

$$P1_i^{\alpha\alpha'} = V_i \int_{D_i} d\mathbf{r} \int_{D_i} d\mathbf{r}' \Sigma_t \phi_i^{\alpha}(\mathbf{r}) \phi_i^{\alpha'}(\mathbf{r}') \frac{\exp\left(-\tau(\mathbf{r}, \mathbf{r}')\right)}{4\pi|\mathbf{r} - \mathbf{r}'|^2}, \tag{4.18}$$

and

$$P2_{ik}^{\alpha m} = V_i \int_{D_{ij}} d\mathbf{r} \int_{\partial D_{ik}} dS_{ik} \Sigma_t \phi_i^{\alpha}(\mathbf{r}) \psi_{k,i}^{m}(\mathbf{r_{ik}}, \mathbf{\Omega}) \frac{\exp\left(-\tau(\mathbf{r}, \mathbf{r}_{ik})\right)}{|\mathbf{r} - \mathbf{r}_{ik}|^2} (\mathbf{\Omega} \cdot \mathbf{n_{ki}}). \tag{4.19}$$

$\mathbf{P1}_i$ is the generalized volume-volume collision probability matrix, $\mathbf{P2}_{ik}$ is the generalized surface-volume collision probability matrix. The higher moments of these matrices have no direct physical meaning, but $P1_i^{00}$ is the probability that neutrals emitted isotropically and uniformly in region i will make their first collision within region i, and similarly $P2_{ik}^{00}$ is the probability that neutrals injected isotropically and uniformly from the interface ∂D_{ik} will make their first collision within region i.

Then Eq. 4.17 can be written in a more concise form,

$$\Sigma_{cx}\Phi_i^{\alpha} = \sum_{\alpha'} c_i P1_i^{\alpha\alpha'} Q_i^{\alpha'} + \sum_{k,m} c_i P2_{ik}^{\alpha m}\Gamma_{k,i}^{m}. \tag{4.20}$$

Noting that the moment of the volumetric flux is also related to the emission density, then inserting Eq. 4.14 into the above equation, we obtain, after some algebra,

$$\sum_{\alpha'} \left(\mathbf{I} - c_i\mathbf{P1}_i\right)_{\alpha\alpha'} \Sigma_{cx}\Phi_i^{\alpha'} = \sum_{\alpha'} c_i P1_i^{\alpha\alpha'} S_i^{\alpha'} + \sum_{k,m} c_i P2_{ik}^{\alpha m}\Gamma_{k,i}^{m}, \tag{4.21}$$

where $\mathbf{I}$ is an identity matrix with elements

$$I_{\alpha\alpha'} = \delta_{\alpha\alpha'}. \tag{4.22}$$

Solving the collision rate from Eq. 4.21, then substituting into Eq. 4.12, we obtain the balance equation,

$$\begin{aligned}\Gamma_{i,j}^{n} = &\sum_{k,n'} \Gamma_{k,i}^{n'} T_{i,k\to j}^{n'\to n} + \sum_{\alpha,\alpha',k,n'} c_i PE_{ji}^{n\alpha'} \left[\left(\mathbf{I} - c_i\mathbf{P1}_i\right)^{-1}\right]_{\alpha'\alpha} P2_{ik}^{\alpha' n'}\Gamma_{k,i}^{n'} \\ &+ \sum_{\alpha,\alpha'} PE_{ji}^{n\alpha'} \left[\left(\mathbf{I} - c_i\mathbf{P1}_i\right)^{-1}\right]_{\alpha'\alpha} S_i^{\alpha}.\end{aligned} \tag{4.23}$$

where $\left(\mathbf{I} - c_i\mathbf{P1}_i\right)^{-1}$ is the inverse matrix of $\mathbf{I} - c_i\mathbf{P1}_i$, and we made use of the following identity.

$$\mathbf{I} + \left(\mathbf{I} - c_i\mathbf{P1}_i\right)^{-1} c_i\mathbf{P1}_i = \left(\mathbf{I} - c_i\mathbf{P1}_i\right)^{-1}. \tag{4.24}$$

By eliminating the collision rate from the particle balance equation, the outgoing flux moment from a given region is explicitly expressed in terms of external volumetric sources

and all the incoming flux moments from all the contiguous regions via generalized transmission probabilities, escape probabilities, volume-volume and surface-volume collision probabilities.

The right hand side of Eq. 4.23 consists of three terms. The first term is the uncollided flux directly transmitted from all the adjacent regions. The second term represents all the neutrals entering from the adjacent regions with one or more collision within region *i* and then exiting into region *j*. The third term corresponds to the contribution from the external volumetric sources.

Since expansion representation functions are locally defined, all probability matrices for this section, like those in the DP_N balance equations, are sparse. However, within each region, surface-volume and volume-volume collision probability matrices are dense because of full coupling between the different moments of collision rates. The numerical steps to solve Eq. 4.23 are:

1. Define representation functions of angular and scalar fluxes.

2. Evaluate all transmission probabilities, escape probabilities, surface-volume and volume-volume collision probabilities.

3. Invert the collision probability matrix for each region.

4. Solve the linear system and calculate the average neutral density using the particle balance equation.

4.3.2 Evaluation of transmission, escape and collision probabilities

The construction of angular flux representation functions and the numerical evaluation of transmission probabilities have already been discussed in chapter 3. Since the magnitude of collision rates (proportional to scalar fluxes) exponentially decrease away from the incident surface, it seems reasonable to construct exponential-like functions as representation functions. However, noting that the volume-volume collision probabilities in Eq. 4.18 are 5D

numerical integrals, tremendous computational effort is required to numerically evaluate the collision probabilities. For reasons of computational efficiency, scalar flux representation functions must be chosen to ensure that some of the integrals in Eq. 4.18 can be carried out analytically. Realizing that in 2D geometries Eq. 4.18 can be written in terms of the Bickley-Naylor functions, the integrability conditions requires that scalar flux representation functions be a polynomial.

A function linearly dependent on spatial variables can be written as

$$f(x,y) = a_0 + a_1 x + a_2 y. \tag{4.25}$$

So the linear representation functions are $\varphi_i^0 = 1$, $\varphi_i^1 = x$ and $\varphi_i^2 = y$. Following the steps in section 3.3.1, we obtain orthogonal linear representation functions,

$$\phi_i^0(\mathbf{r}) = \frac{1}{V_i}, \tag{4.26a}$$

$$\phi_i^1(\mathbf{r}) = \frac{(x - \bar{x})}{V_i \sqrt{\overline{x^2} - \bar{x}^2}}, \tag{4.26b}$$

$$\begin{aligned}\phi_i^2(\mathbf{r}) = &\frac{\sqrt{\overline{x^2} - \bar{x}^2}(y - \bar{y})}{V_i \sqrt{(\overline{x^2} - \bar{x}^2)(\overline{y^2} - \bar{y}^2) - (\overline{xy} - \overline{xy})^2}} \\ &- \frac{\overline{xy} - \overline{xy}}{V_i \sqrt{(\overline{x^2} - \bar{x}^2)(\overline{y^2} - \bar{y}^2) - (\overline{xy} - \overline{xy})^2}} \phi_i^1(\mathbf{r}),\end{aligned} \tag{4.26c}$$

where

$$\bar{x} = \frac{\int_{D_i} x d\mathbf{r}}{V_i}, \tag{4.27}$$

$$\overline{x^2} = \frac{\int_{D_i} x^2 d\mathbf{r}}{V_i}, \tag{4.28}$$

$$\bar{y} = \frac{\int_{D_i} y d\mathbf{r}}{V_i}, \tag{4.29}$$

$$\overline{y^2} = \frac{\int_{D_i} y^2 d\mathbf{r}}{V_i}, \tag{4.30}$$

$$\overline{xy} = \frac{\int_{D_i} xy d\mathbf{r}}{V_i}. \tag{4.31}$$

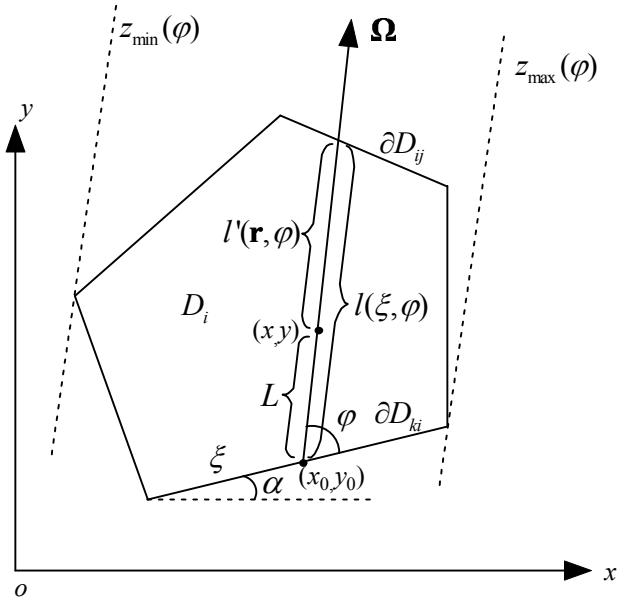

Figure 4.2. Coordinates used in evaluation of volume-volume collision probabilities

To perform the integration of Eq. 4.18 we start by changing variables $d\mathbf{r}' = \Delta r^2 d\Delta r d\boldsymbol{\Omega}$,

$$\begin{aligned}
P1_i^{\alpha'\alpha} &= V_i\Sigma_t \int_{D_i} d\mathbf{r} \int_{D_i} d\mathbf{r}' \phi_i^{\alpha}(\mathbf{r})\phi_i^{\alpha'}(\mathbf{r}') \frac{\exp(-\Sigma_t \Delta r)}{4\pi\Delta r^2} \\
&= \frac{V_i\Sigma_t}{4\pi} \int_{D_i} d\mathbf{r} \int_{D_i} d\Delta r \Delta r^2 d\boldsymbol{\Omega} \phi_i^{\alpha}(\mathbf{r})\phi_i^{\alpha'}(\mathbf{r}') \frac{\exp(-\Sigma_t \Delta r)}{\Delta r^2} \\
&= \frac{V_i\Sigma_t}{4\pi} \int_{D_i} d\mathbf{r} \int_0^{l'} dl'' \int_{2\pi} d\varphi \int_0^{\pi} d\theta \phi_i^{\alpha}(\mathbf{r})\phi_i^{\alpha'}(\mathbf{r} + l''\boldsymbol{\Omega}) \exp\left(-\frac{\Sigma_t l''}{\sin\theta}\right) \\
&= \frac{V_i\Sigma_t}{2\pi} \int_{D_i} d\mathbf{r} \int_0^{l'} dl'' \int_{2\pi} d\varphi \phi_i^{\alpha}(x,y)\phi_i^{\alpha'}(x + l''\cos(\alpha+\varphi), y + l''\sin(\alpha+\varphi)) Ki_1(\Sigma_t l'').
\end{aligned} \tag{4.32}$$

Noting that linear scalar flux representation functions have the following property,

$$\begin{aligned}
\phi_i^{\alpha'}(x + l''\cos(\alpha+\varphi), y + l''\sin(\alpha+\varphi)) &= \phi_i^{\alpha'}(x,y) \\
&+ l''\left[\phi_i^{\alpha'}(\cos(\alpha+\varphi), \sin(\alpha+\varphi)) - \phi_i^{\alpha'}(0,0)\right].
\end{aligned} \tag{4.33}$$

Making use of the following identity,

$$\int xKi_n(x)\,dx = -xKi_{n+1}(x) - Ki_{n+2}(x), \tag{4.34}$$

and integrating over the path parallel to neutral trajectories, the volume-volume collision probabilities can be written as

$$\begin{aligned} P1_i^{\alpha'\alpha} = \frac{V_i}{2\pi}\int_{2\pi} d\varphi \int_{D_i} d\mathbf{r}\phi_i^{\alpha}(x,y)\Big(\phi_i^{\alpha'}(x,y)\left[1-Ki_2(\Sigma_t l')\right] \\ + \left[\phi_i^{\alpha'}(\cos(\alpha+\varphi),\sin(\alpha+\varphi)) - \phi_i^{\alpha'}(0,0)\right] \\ \cdot \frac{1}{\Sigma_t}\left[\frac{\pi}{4} - \Sigma_t l' Ki_2(\Sigma_t l') - Ki_3(\Sigma_t l')\right]\Big). \end{aligned} \tag{4.35}$$

The above equation is a 3D integral and a part of the integration can be performed if we change dummy variables as follows,

$$\begin{aligned} \int_0^{2\pi} d\varphi \int_{D_i} d\mathbf{r} f &= \int_0^{2\pi} d\varphi \int_{z_{min}}^{z_{max}} dz \int_0^{l} dL f \\ &= \left[\int_0^{\pi} d\varphi \int_{z_{min}}^{z_{max}} dz + \int_0^{\pi} d\varphi \int_{z_{max}}^{z_{min}} dz\right] \int_0^{l} dL f \\ &= \oint_{\partial D_i} d\xi \int_o^{\pi} d\varphi \int_0^{l} dl' f \\ &= \sum_k \int_0^{L_{ki}} d\xi \sum_j \int_{\varphi_{min}(\varphi)}^{\varphi_{max}(\varphi)} d\varphi \int_0^{l} dl' f. \end{aligned} \tag{4.36}$$

It yields

$$\begin{aligned} P1_i^{\alpha'\alpha} = \frac{V_i}{2\pi}\sum_{k,j}\int_0^{L_{ki}} d\xi \int_{\varphi_{min}(\varphi)}^{\varphi_{max}(\varphi)} d\varphi \int_0^{l} dl' \phi_i^{\alpha}(x,y) \\ \Big(\phi_i^{\alpha'}(x,y)\left[1-Ki_2(\Sigma_t l')\right] + \left[\phi_i^{\alpha'}(\cos(\alpha+\varphi),\sin(\alpha+\varphi)) - \phi_i^{\alpha'}(0,0)\right] \\ \cdot \frac{1}{\Sigma_t}\left[\frac{\pi}{4} - \Sigma_t l' Ki_2(\Sigma_t l') - Ki_3(\Sigma_t l')\right]\Big). \end{aligned} \tag{4.37}$$

Since

$$\begin{cases} x = x_0 + (l-l')\cos(\alpha+\varphi), \\ y = y_0 + (l-l')\sin(\alpha+\varphi), \end{cases} \tag{4.38}$$

we define

$$\begin{cases} A_\alpha = \phi_i^{\alpha}(x_0,y_0); \\ B_\alpha = \phi_i^{\alpha}(\cos(\alpha+\varphi),\sin(\alpha+\varphi)) - \phi_i^{\alpha}(0,0). \end{cases} \tag{4.39}$$

Eq. 4.37 becomes

$$P1_i^{\alpha'\alpha} = \frac{V_i}{2\pi}\sum_{k,j}\int_0^{L_{ki}} d\xi \int_{\varphi_{min}(\varphi)}^{\varphi_{max}(\varphi)} d\varphi \int_0^l dl' \left[A_\alpha + B_\alpha(l-l')\right] \Bigg(\left[A_{\alpha'} + B_{\alpha'}(l-l')\right]\left[1 - Ki_2(\Sigma_t l')\right] + \cdot \frac{B_{\alpha'}}{\Sigma_t}\left[\frac{\pi}{4} - \Sigma_t l' Ki_2(\Sigma_t l') - Ki_3(\Sigma_t l')\right]\Bigg). \tag{4.40}$$

Integrating over l', we finally end with

$$\begin{aligned} P1_i^{\alpha'\alpha} = \frac{V_i}{2\pi}\sum_{k,j}\int_0^{L_{ki}} d\xi \int_{\varphi_{min}(\varphi)}^{\varphi_{max}(\varphi)} d\varphi \Bigg\{ & \frac{B_{\alpha\alpha' l^3}}{3} + \left[A_\alpha A_{\alpha'} + \frac{\pi B_{\alpha'}}{4\Sigma_t}(A_\alpha + A_\alpha l)\right] l \\ & + \frac{1}{2}\left[A_\alpha B_{\alpha'} + A_{\alpha'} B_\alpha - \frac{\pi B_\alpha B_{\alpha'}}{\Sigma_t}\right] l^2 - \frac{B_{\alpha'}}{\Sigma_t^2}(A_\alpha + B_\alpha l)\left[Ki_4(0) - Ki_4(l)\right] \\ & - \frac{1}{\Sigma_t}(A_\alpha + B_\alpha l)(A_{\alpha'} + B_{\alpha'} l)\left[\frac{\pi}{4} - Ki_3(\Sigma_t l)\right] \\ & + \frac{B_\alpha}{\Sigma_t^2}(A_{\alpha'} + B_{\alpha'} l)\left[Ki_4(0) - \Sigma_t l Ki_3(\Sigma_t l) - Ki_4(l)\right] \\ & + \frac{B_\alpha B_{\alpha'}}{\Sigma_t}\left[Ki_5(0) - \Sigma_t l Ki_4(\Sigma_t l) - Ki_5(l)\right]\Bigg\}, \end{aligned} \tag{4.41}$$

or the more simple form

$$P1_i^{\alpha'\alpha} = \sum_{j,k,p} TE_{i,kj}^{p,\alpha'\alpha}, \tag{4.42}$$

where $TE_{i,kj}^{p,\alpha'\alpha}$ are the effective transmission probabilities. Take $P1_i^{11}$ as an example, the effective transmission probabilities are

$$TE_{i,kj}^{1,11} = \frac{1}{2\pi\Sigma_t V_i\sqrt{\overline{x^2} - \overline{x}^2}}\int_0^{L_{ki}} d\xi \int_{\varphi_{\min}(\xi)}^{\varphi_{\max}(\xi)} d\varphi x_0 \left[\frac{\pi}{4} - Ki_3\left(\Sigma_t l\right)\right], \tag{4.43a}$$

$$TE_{i,kj}^{2,11} = \frac{1}{\pi\Sigma_t V_i\sqrt{\overline{x^2} - \overline{x}^2}}\int_0^{L_{ki}} d\xi \int_{\varphi_{\min}(\xi)}^{\varphi_{\max}(\xi)} d\varphi x_0 \sin\varphi \left[\frac{2}{3} - Ki_4\left(\Sigma_t l\right)\right], \tag{4.43b}$$

$$TE_{i,kj}^{3,11} = \frac{3}{\pi\Sigma_t V_i\sqrt{\overline{x^2} - \overline{x}^2}}\int_0^{L_{ki}} d\xi \int_{\varphi_{\min}(\xi)}^{\varphi_{\max}(\xi)} d\varphi x_0 \cos\varphi \left[\frac{2}{3} - Ki_4\left(\Sigma_t l\right)\right], \tag{4.43c}$$

$$TE_{i,kj}^{4,11} = \frac{1}{2\pi\Sigma_t^2 V_i\sqrt{\overline{x^2} - \overline{x}^2}}\int_0^{L_{ki}} d\xi \int_{\varphi_{\min}(\xi)}^{\varphi_{\max}(\xi)} d\varphi \cos\left(\alpha + \varphi + \frac{\pi}{2}\right) \left[\frac{2}{3} - \Sigma_t l Ki_3\left(\Sigma_t l\right) - Ki_4\left(\Sigma_t l\right)\right], \tag{4.43d}$$

$$TE_{i,kj}^{5,11} = \frac{1}{\pi\Sigma_t^2 V_i\sqrt{\overline{x^2} - \overline{x}^2}}\int_0^{L_{ki}} d\xi \int_{\varphi_{\min}(\xi)}^{\varphi_{\max}(\xi)} d\varphi \sin\varphi\cos\left(\alpha + \varphi + \frac{\pi}{2}\right) \tag{4.43e}$$

$$\left[\frac{3\pi}{16} - \Sigma_t l K i_4(\Sigma_t l) - K i_5(\Sigma_t l)\right],$$

$$TE^{6,11}_{i,kj} = \frac{3}{\pi\Sigma_t^2 V_i \sqrt{\overline{x^2} - \overline{x}^2}} \int_0^{L_{ki}} d\xi \int_{\varphi_{\min}(\xi)}^{\varphi_{\max}(\xi)} d\varphi \cos\varphi \cos\left(\alpha + \varphi + \frac{\pi}{2}\right) \tag{4.43f}$$

$$\left[\frac{3\pi}{16} - \Sigma_t l K i_4(\Sigma_t l) - K i_5(\Sigma_t l)\right].$$

These effective transmission probabilities have no direct physical meaning. Similarly, other elements of volume-volume collision matrix, escape and surface-volume collision probabilities can be simplified as the sum of a number of effective transmission probabilities, which are 2D integrals. However, together with the real transmission probabilities, we have to evaluate 72 probabilities for each pair interfaces.

4.4 Approach III: Diffusion approximation

As mentioned in Chapters 2 and 3, the effects of non-uniformly distributed charge-exchanged sources are important only for optically thick regions, where the diffusion theory is a good approximation by noticing that charge-exchange fractions are quite high in edge plasmas. In this section, diffusion theory will be employed to calculate total and directional escape probabilities.

4.4.1 Diffusion equation

The diffusion approximation is simply the lowest-order spherical-harmonics approximation (P_1). Because of the linearity of the neutral transport equation, the problems of interest can be separated into several relatively simpler problems with a flux injected only from one side. Taking region i shown in Figure 4.3 as an example, it is assumed that an external flux is injected from the interface ∂D_{ji}. Since only escape probabilities are concerned, the diffusion equation for this problem is

$$-\nabla \cdot D(\mathbf{r})\nabla\,\phi(\mathbf{r}) + \Sigma_a \phi(\mathbf{r}) = S^0_{j,i}(\mathbf{r}), \tag{4.44}$$

where the diffusion coefficient $D(\mathbf{r})$ and the transport cross section Σ_{tr} are defined by

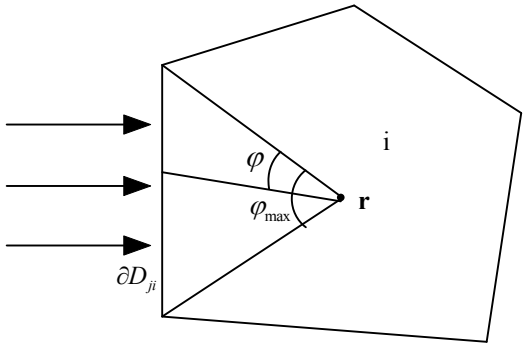

Figure 4.3. Diagram for calculating the first collision source

$$D = \frac{1}{3(\Sigma_t - \bar{\mu}\Sigma_{cx})} = \frac{1}{3\Sigma_{tr}}, \tag{4.45}$$

where μ is the average cosine of scattering angles, $\Sigma_a = \Sigma_t - \Sigma_{cx}$, $S^0_{j,i}(\mathbf{r})$ is the first collision source associated with a flux injected from the interface ∂D_{ji}. If the flux from the interface ∂D_{ji} is assumed to be uniform and isotropic and with a unit strength, then

$$S^0_{j,i}(\mathbf{r}) = \frac{\Sigma_{cx}(\mathbf{r})}{\pi} \int_{\varphi_{min}(\mathbf{r})}^{\varphi_{max}(\mathbf{r})} d\varphi Ki_2(\Sigma_t l(\mathbf{r}, \varphi)). \tag{4.46}$$

The exact boundary condition is

$$\psi(\mathbf{r}, \mathbf{\Omega}) = 0, \qquad \mathbf{r} \in \partial D_{ji} \text{ and } \Omega \cdot \mathbf{n}_{ji} > 0, \tag{4.47}$$

where $\mathbf{n}_{ji}$ is the inward normal to the interface ∂D_{ji}. However, the diffusion theory gives only an approximate representation of ψ:

$$\psi(\mathbf{r}) = \frac{1}{4\pi}\phi(\mathbf{r}) + \frac{3}{4\pi}\mathbf{\Omega} \cdot \mathbf{J}(\mathbf{r}). \tag{4.48}$$

With such an approximation it is impossible to satisfy Eq. 4.47 exactly. An approximate choice is to conserve the total number of particles crossing into the interface, so

$$\begin{aligned} J_- &= \int_{\mathbf{\Omega}\cdot\mathbf{n}_{ji}>0} d\Omega(\mathbf{\Omega} \cdot \mathbf{n}_{ji})\psi(\mathbf{r}, \mathbf{\Omega}) \\ &= \int_{\mathbf{\Omega}\cdot\mathbf{n}_{ji}>0} d\Omega(\mathbf{\Omega} \cdot \mathbf{n}_{ji}) \left[\frac{1}{4\pi}\phi(\mathbf{r}) + \frac{3}{4\pi}\mathbf{\Omega} \cdot \mathbf{J}(\mathbf{r})\right] \\ &= \frac{\phi(\mathbf{r})}{4} + \frac{\mathbf{n}_{ji} \cdot \mathbf{J}(\mathbf{r})}{2} \\ &= \frac{\phi(\mathbf{r})}{4} - \frac{\mathbf{n}_{ij} \cdot \mathbf{J}(\mathbf{r})}{2} = 0. \end{aligned} \tag{4.49}$$

Alternatively, we can solve the diffusion equation without volumetric sources and with the boundary condition $J_- = 1$. However in this case the solution to the diffusion equation would include the contribution of uncollided fluxes. It should be noticed that Eq. 4.44 reduces the original 2-group problem to a one-speed problem. Initially, neutrals entering from the adjacent regions may have different energies. After charge-exchange scattering, the energy of all neutrals can be set as the local ion temperature.

An analytical solution to Eq. 4.44 can only be found for very idealized cases with regular geometries and homogeneous background plasmas. However, such cases rarely exist in realistic plasmas, where numerical evaluation is generally necessary. Among possible numerical methods of solving Eq. 4.44 with boundary conditions Eq. 4.49, the finite element method [33, 34] is the most suitable for problems with geometric complexity and can be easily updated to the higher order approximations.

4.4.2 Finite element method

The finite element method, based on the classical Ritz procedure [34] for solving the variational form of a differential equation, has been widely used for the neutron transport [21, 33, 34]. Although a weak solution to the diffusion equation 4.44 can be obtained by the Galerkin projection, we take the following functional as the starting point,

$$F[\phi] = \int_{D_i} d\mathbf{r} \left\{ D(\nabla\phi)^2 + \Sigma_a \phi^2 - 2\phi S^0_{j,i} \right\} + \frac{1}{2} \oint_{\partial D_i} \phi^2 dS_i. \tag{4.50}$$

Now we take a small variation of $\delta\phi$ form the reference function ϕ_0,

$$\phi = \phi_0 + \delta\phi. \tag{4.51}$$

Suppose that $F[\phi]$ can expanded as the sum of series as follows:

$$F[\phi] = F[\phi_0] + \delta F[\phi] + \delta^2 F[\phi] \tag{4.52}$$

Substituting the above two equations into the original functional, we obtain

$$\begin{aligned} F[\phi_0]+\delta F[\phi]+\delta^2 F[\phi] &= \int_{D_i} d\mathbf{r}\left\{D[\nabla(\phi_0+\delta\phi)]^2+\Sigma_a(\phi_0+\delta\phi)^2-2(\phi_0+\delta\phi)S^0_{j,i}\right\} \\ &+\frac{1}{2}\oint_{\partial D_i}(\phi_0+\delta\phi)^2 dS_i \\ &=\int_{D_i} d\mathbf{r}\left\{D(\nabla\phi_0)^2+\Sigma_a\phi_0^2-2\phi_0 S^0_{j,i}\right\}+\frac{1}{2}\oint_{\partial D_i}\phi_0^2 dS_i \\ &+2\int_{D_i} d\mathbf{r}\left[D\nabla\phi_0\cdot\nabla\delta\phi+\Sigma_a\phi_0\delta\phi-\delta\phi S^0_{j,i}\right]+\oint_{\partial D_i} dS\,\phi_0\delta\phi \\ &+\int_{D_i} d\mathbf{r}\left\{D(\nabla\delta\phi)^2+\Sigma_a(\delta\phi)^2-2\delta\phi S^0_{j,i}\right\}+\frac{1}{2}\oint_{\partial D_i}(\delta\phi)^2 dS_i. \end{aligned} \tag{4.53}$$

Separating orders, we have,

The zeroth order:

$$F[\phi_0]=\int_{D_i} d\mathbf{r}\left\{D(\nabla\phi_0)^2+\Sigma_a\phi_0^2-2\phi_0 S^0_{j,i}\right\}+\frac{1}{2}\oint_{\partial D_i}\phi_0^2 dS_i. \tag{4.54}$$

The first order:

$$\delta F[\phi]=2\int_{D_i} d\mathbf{r}\left[D\nabla\phi_0\cdot\nabla\delta\phi+\Sigma_a\phi_0\delta\phi-\delta\phi S^0_{j,i}\right]+\oint_{\partial D_i} dS\,\phi_0\delta\phi. \tag{4.55}$$

and the second order:

$$\delta^2 F[\phi]=\int_{D_i} d\mathbf{r}\left\{D(\nabla\delta\phi)^2+\Sigma_a(\delta\phi)^2-2\delta\phi S^0_{j,i}\right\}+\frac{1}{2}\oint_{\partial D_i}(\delta\phi)^2 dS_i. \tag{4.56}$$

Noting the identity

$$\nabla\cdot(\delta\phi D\nabla\phi_0)=D\nabla\phi_0\cdot\nabla\delta\phi+\delta\phi\nabla\cdot D\nabla\phi_0. \tag{4.57}$$

Integrating both the sides of the above equation over D_i, then applying the divergence theorem to the left hand side yields

$$\begin{aligned} \int_{D_i} d\mathbf{r}D\nabla\phi_0\cdot\nabla\delta\phi &= -\int_{D_i} d\mathbf{r}\delta\phi\nabla\cdot D\nabla\phi_0+\int_{D_i} d\mathbf{r}\nabla\cdot(\delta\phi D\nabla\phi_0) \\ &= -\int_{D_i} d\mathbf{r}\delta\phi\nabla\cdot D\nabla\phi_0+\oint_{\partial D_i} dS\,\delta\phi(\mathbf{n}_+\cdot D\nabla\phi_0). \end{aligned} \tag{4.58}$$

Then substituting the above equation into Eq. 4.55, the first order variation may be written as

$$\delta F[\phi] = 2\int_{D_i} d\mathbf{r}\delta\phi\left[-\nabla\cdot D\nabla\phi_0 + \Sigma_a\phi_0 - S^0_{j,i}\right] - 2\oint_{\partial D_i} dS\,\delta\phi\left[\mathbf{n}_-\cdot D\nabla\phi_0 - \frac{1}{2}\phi_0\right]. \quad (4.59)$$

Suppose that the variation functional $F[\phi]$ is stationary at ϕ_0, then it is required that the first order variation vanish. Since $\delta\phi$ is an arbitrary function, it leads to

$$\begin{aligned} -\nabla\cdot D(\mathbf{r})\nabla\,\phi(\mathbf{r}) + \Sigma_a\phi(\mathbf{r}) &= S^0_{j,i}(\mathbf{r}), \qquad \mathbf{r}\in D_i, \\ \frac{\phi(\mathbf{r})}{2} - \mathbf{n}_-\cdot D(\mathbf{r})\mathbf{J}(\mathbf{r}) &= 0, \qquad\qquad \mathbf{r}\in\partial D_i. \end{aligned} \quad (4.60)$$

The stationary condition implies that a small perturbation of $\delta\phi$ from the reference function ϕ_0 will, to the first order in this variation, have no effect on the value of the functional. Noting that $\delta^2F[\phi]$ is positive-definite, the functional has the minimum value at ϕ_0. Actually, the finite element equations can be directly derived by the least-square method. The treatment of boundary conditions are automatically incorporated into the variation functional, therefore they are usually called natural boundary conditions.

Because of its equivalence to the original diffusion equation with associated boundary conditions, requiring the first variation of the functional Eq. 4.50 to vanish leads to very powerful and versatile numerical approximations to the originial differential equation. To look for an approximate solution to the diffusion equation, it is assumed that the trial function belongs to a finite dimensional subspace Φ_N.

$$\phi \approx \sum_{n=1}^{N}\phi_n h_n(\mathbf{r}), \quad (4.61)$$

where $\{h_n(\mathbf{r})|n = 1,\cdots,N\}$ is a set of basis functions of the subspace Φ_N, and ϕ_n are the expansion coefficients. Then we choose coefficients ϕ_n such that the first variation vanishes when the approximate solution is substituted into the variational functional, or equivalently, we look for coefficients such that the linear combination in Eq. 4.61 is the best approximation available in the subspace Φ_N.

To write finite element functions in a more concise form, we first define ϕ_n and h_n as component of the vectors $\mathbf{\Phi}$ and $\mathbf{H}$ respectively,

$$\mathbf{\Phi}^T = \{\phi_1, \phi_2, \cdots, \phi_N\}, \tag{4.62}$$

and

$$\mathbf{H}^T = \{h_1, h_2, \cdots, h_N\}. \tag{4.63}$$

Then ϕ can be written as a dot product of the above two vectors,

$$\phi = \mathbf{\Phi}^T\mathbf{H} = \mathbf{H}^T\mathbf{\Phi}. \tag{4.64}$$

Substituting it into Eq. 4.50, we have

$$\begin{aligned} F(\mathbf{\Phi}) &= \int_{D_i} d\mathbf{r}\left\{D(\nabla\mathbf{\Phi}^T\mathbf{H})^2 + \Sigma_a(\mathbf{\Phi}^T\mathbf{H})^2 - 2\mathbf{\Phi}^T\mathbf{H}S^0_{j,i}\right\} + \frac{1}{2}\oint_{\partial D_i}(\mathbf{\Phi}^T\mathbf{H})^2 dS_i \\ &= \mathbf{\Phi}^T\left\{\int_{D_i} d\mathbf{r}D\nabla\mathbf{H}\cdot\nabla\mathbf{H}^T + \Sigma_a\mathbf{\Phi}\mathbf{\Phi}^T + \frac{1}{2}\oint_{\partial D_i}\mathbf{H}\mathbf{H}^T dS_i\right\}\mathbf{\Phi} - 2\mathbf{\Phi}^T\int_{D_i} d\mathbf{r}\mathbf{H}S^0_{j,i} \\ &= \mathbf{\Phi}^T\mathbf{A}\mathbf{\Phi} - 2\mathbf{\Phi}^T\mathbf{S}, \end{aligned} \tag{4.65}$$

where we define coefficient matrix $\mathbf{A}$ as

$$\mathbf{A} = \int_{D_i} d\mathbf{r}\left[D\nabla\mathbf{H}\cdot\nabla\mathbf{H}^T + \Sigma_a\mathbf{H}\mathbf{H}^T\right] + \frac{1}{2}\oint_{\partial D_i}\mathbf{H}\mathbf{H}^T dS_i, \tag{4.66}$$

and the source vector

$$\mathbf{S} = \int_{D_i} d\mathbf{r}\mathbf{H}S^0_{j,i}. \tag{4.67}$$

It is obvious matrix A is a $N \times N$ symmetric matrix. To vanish the first variation of functional $F[\phi]$ or equivalently to minimize function $F(\mathbf{\Phi})$, we require

$$\frac{\partial F(\mathbf{\Phi})}{\partial \phi_i} = 0, \qquad i = 1, 2, \cdots, N. \tag{4.68}$$

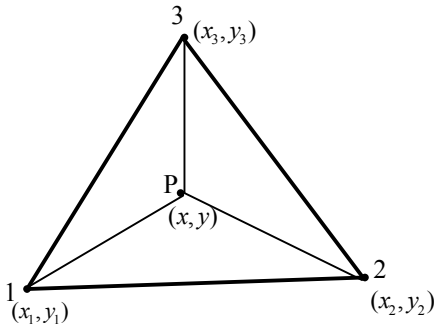

Figure 4.4. Area coordinates u_1, u_2, u_3

Substituting $F(\mathbf{\Phi})$ into the above equation we have

$$\begin{aligned}\frac{\partial F(\mathbf{\Phi})}{\partial \phi_i} &= \frac{\partial \left[\sum\limits_{m,n} A_{mn}\phi_m\phi_n - 2\sum\limits_{m} S_m\phi_m\right]}{\partial \phi_i} \\ &= \sum_{m,n} A_{mn}\left[\frac{\partial \phi_m}{\partial \phi_i}\phi_m + \frac{\partial \phi_n}{\partial \phi_i}\phi_n\right] - 2\sum_{m} S_m\frac{\partial \phi_m}{\phi_i} \qquad i = 1, 2, \cdots, N \\ &= 2\sum_{m} A_{i,m}\phi_m - 2S_i = 0,\end{aligned} \tag{4.69}$$

or

$$\mathbf{A\Phi} = \mathbf{S}. \tag{4.70}$$

4.4.3 Triangular finite elements

To construct finite element equations we first have to partition each optically thick cell into small regions, in which the neutral scalar flux could be represented adequately by linear or low-order polynomials. These small regions are called finite elements. Rectangular elements with bi-linear trial functions have been widely used in the neutron transport theory, but here triangular subdivisions as shown in Figure 4.1 are considered because of their computational efficiency.

Take the triangle shown in Figure 4.4 as an example, we assume that the three vertices are represented in the counterclockwise order by $(x_1, y_1), (x_2, y_2)$ and (x_3, y_3). We define area coordinates (u_1, u_2, u_3) for point P at (x, y) as the ratios of the areas of triangles.

$$u_1 = \frac{\triangle_{P23}}{\triangle_{123}} \tag{4.71a}$$

$$u_2 = \frac{\triangle_{P31}}{\triangle_{123}} \tag{4.71b}$$

$$u_3 = \frac{\triangle_{P12}}{\triangle_{123}} \tag{4.71c}$$

where $\triangle_{ijk}$ is the area of a triangle with vertices $(x_i, y_i), (x_j, y_j)$ and (x_k, y_k), and

$$\Delta_{ijk} = \frac{1}{2}\begin{vmatrix} 1 & x_i & y_i \\ 1 & x_j & y_j \\ 1 & x_k & y_k \end{vmatrix}. \tag{4.72}$$

It is easily seen that

$$u_l(\mathbf{r}_{l'}) = \delta_{ll'}. \tag{4.73}$$

It is assumed that the scalar flux can be approximated by a piecewise linear function, which is essentially expanded in terms of the three linear Lagrange interpolation functions,

$$\phi(\mathbf{r}) = \sum_l h_l(\mathbf{r})\phi_l. \tag{4.74}$$

The linear Lagrange interpolation function associated with vertex (x_1, y_1) has the following properties;

$$\begin{aligned} h_{1m}(\mathbf{r}) &= d_{11}u_1 + d_{12}u_2 + d_{13}u_3 \\ &= a_{1m} + b_{1m}x + c_{1m}y, \end{aligned} \tag{4.75}$$

and

$$h_{lm}(\mathbf{r}_{l'}) = \delta_{ll'}. \tag{4.76}$$

Comparing the above equation with Eq. 4.73, we have

$$h_{lm}(\mathbf{r}) = u_l. \tag{4.77}$$

Combining Eqs. 4.71, 4.72 and 4.77 with Eq. 4.75, we obtain the coefficients a_{1i}, b_{1i}, and c_{1m}:

$$a_{1m} = \frac{1}{2\triangle_{123}}(x_2y_3 - x_3y_2), \tag{4.78a}$$

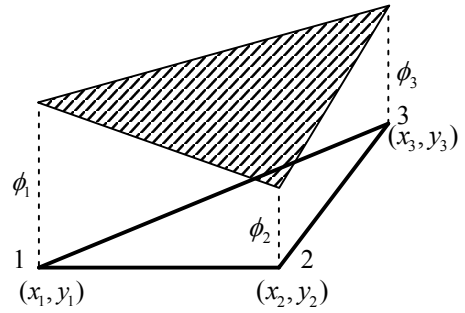

Element function

Shape functions

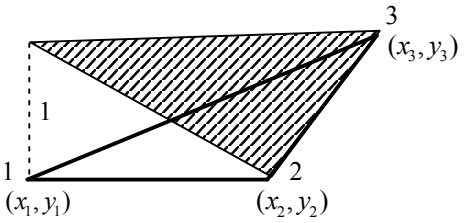

h_1

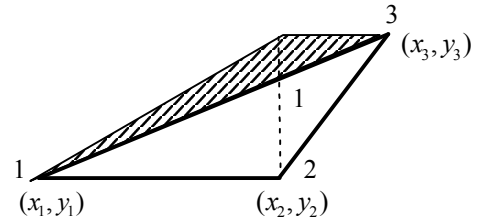

h_2

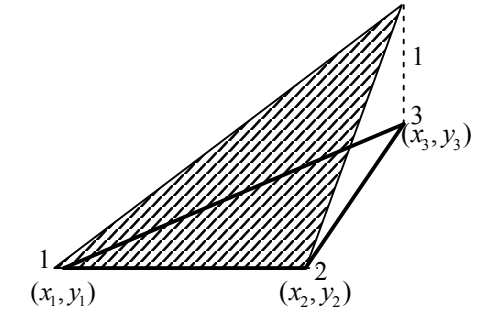

h_3

Figure 4.5. Element and shape functions for a linear triangular element

$$b_{1m} = \frac{1}{2\triangle_{123}}(y_2 - y_3), \tag{4.78b}$$

$$c_{1m} = \frac{1}{2\triangle_{123}}(x_3 - x_2). \tag{4.78c}$$

Inserting these coefficients into Eq. 4.75, we have

$$h_{1m}(\mathbf{r}) = \frac{1}{2\triangle_{123}}[x_2y_3 - x_3y_2 + (y_2 - y_3)x + (x_3 - x_2)y]. \tag{4.79}$$

Similarly, we can obtain the linear Lagrange interpolation functions $h_{2m}(\mathbf{r})$ and $h_3(\mathbf{r})$.

$$h_{2m}(\mathbf{r}) = \frac{1}{2\triangle_{123}}[x_3y_1 - x_1y_3 + (y_3 - y_1)x + (x_1 - x_3)y], \tag{4.80}$$

$$h_{3m}(\mathbf{r}) = \frac{1}{2\triangle_{123}}[x_1y_2 - x_2y_1 + (y_1 - y_2)x + (x_2 - x_1)y]. \tag{4.81}$$

Because $h_{lm}(\mathbf{r})$ is zero outside triangle m, it is discontinuous along sides 12 and 13. The discontinuity along interfaces between triangles may exist though an expansion of the solution in terms of such functions will be continuous within each triangle. However, the sum of all the expansion functions with the common vertex m will result in a continuous expansion for the whole region of interest.

$$h_l(\mathbf{r}) = \sum_m h_{lm}(\mathbf{r}) \tag{4.82}$$

or equivalently

$$h_l(\mathbf{r}) = \begin{cases} h_{lm}(\mathbf{r}) & \text{if l is a vertex of } \Delta\text{m and } \mathbf{r} \in \Delta m \\ 0 & \text{otherwise} \end{cases} \tag{4.83}$$

4.4.4 Finite element equations

With the linear triangular element representation functions, we are able to approximate the solution function as a linear combination of these representation functions. Taking a polygon with N_1 side as an example, we first divide it into N_1 triangles. In order that a piecewise linear approximation is sufficiently accurate, each triangle is further divided into N_2^2 identical small triangles as shown in Figure 4.1. Therefor, the total number of grid points is $N = 1 + \frac{N_1N_2(N_2+1)}{2}$ and the total number of divisions is $N_1N_2^2$.

Assuming that the scalar flux at vertex n is ϕ_n for $n = 1, \cdots, N$, the scalar flux within the whole region can be expressed in terms of the linear Lagrange interpolation functions $h_n(\mathbf{r})$.

$$\phi(\mathbf{r}) = \sum_{n=1}^{N} \phi_n h_n(\mathbf{r}) \tag{4.84}$$

Inserting $\mathbf{H}^T = \{h_1(\mathbf{r}), \cdots, h_N(\mathbf{r})\}$ into Eqn. 4.50, we obtain the reduced functional:

$$\begin{aligned} F[\mathbf{\Phi}] &= \int_{D_i} d\mathbf{r} \left\{ D(\nabla \mathbf{\Phi}^T \mathbf{H})^2 + \Sigma_a (\mathbf{\Phi}^T \mathbf{H})^2 - 2\mathbf{\Phi}^T \mathbf{H} S^0_{j,i} \right\} + \frac{1}{2} \oint_{\partial D_i} (\mathbf{\Phi}^T \mathbf{H})^2 dS_i \\ &= \mathbf{\Phi}^T \mathbf{A} \mathbf{\Phi} - 2\mathbf{\Phi}^T \mathbf{S}, \end{aligned} \tag{4.85}$$

where

$$\mathbf{A} = \int_{D_i} d\mathbf{r} \left[D \nabla \mathbf{H} \cdot \nabla \mathbf{H}^T + \Sigma_a \mathbf{H} \mathbf{H}^T \right] + \frac{1}{2} \oint_{\partial D_i} \mathbf{H} \mathbf{H}^T dS_i, \tag{4.86}$$

and

$$\mathbf{S} = \int_{D_i} d\mathbf{r} \mathbf{H} S^0_{j,i}. \tag{4.87}$$

Assume that $\mathbf{S0}_n = S^0_{j,i}(\mathbf{r}_n), n = 1, \cdots, N$, where $\mathbf{r}_n$ is the grid point n, we approximate the first collision source $s^0_{j,i}$ in terms of the linear Lagrange interpolation functions.

$$s^0_{j,i}(\mathbf{r}) = \sum_{n=1}^{N} S0_n h_n(\mathbf{r}) = \mathbf{H}^T \mathbf{S0}. \tag{4.88}$$

So it leads

$$\mathbf{S} = \int_{D_i} d\mathbf{r} \mathbf{H} \mathbf{H}^T \mathbf{S0} = \mathbf{B} \mathbf{S0}, \tag{4.89}$$

where we define

$$\mathbf{B} = \int_{D_i} d\mathbf{r} \mathbf{H} \mathbf{H}^T. \tag{4.90}$$

If we now require the reduced variation functional, Eq. 4.85, to be stationary with respect to the variation in vector $\mathbf{\Phi}$, we obtain a set of linear equations,

$$\begin{bmatrix} A_{11} & A_{12} & \cdots & A_{1N} \\ A_{21} & A_{22} & \cdots & A_{2N} \\ \vdots & \vdots & \vdots & \vdots \\ A_{N1} & A_{N2} & \cdots & A_{NN} \end{bmatrix} \begin{bmatrix} \phi_1 \\ \phi_2 \\ \vdots \\ \phi_N \end{bmatrix} = \begin{bmatrix} S_1 \\ S_2 \\ \vdots \\ S_N \end{bmatrix}. \tag{4.91}$$

Substituting $h_i(\mathbf{r})$ and $h_j(\mathbf{r})$ into Eqn. 4.86, we obtain

$$\begin{aligned} A_{mn} &= \int_{D_i} d\mathbf{r}\,[D\nabla h_m(\mathbf{r})\cdot\nabla h_n(\mathbf{r}) + \Sigma_a h_m(\mathbf{r})h_n(\mathbf{r})] + \frac{1}{2}\oint_{D_i} dS_i h_m(\mathbf{r})h_n(\mathbf{r}) \\ &= \sum_{\mathbf{r}_m,\mathbf{r}_n\in\Delta_l}\int_{\Delta_l} d\mathbf{r}\,[D\nabla h_{ml}(\mathbf{r})\cdot\nabla h_{nl}(\mathbf{r}) + \Sigma_a h_m(\mathbf{r})h_n(\mathbf{r})] \\ &+ \frac{1}{2}\sum_{L_{mn}\subset\partial D_i}^{L_{mn}\subset\Delta_l}\int_{L_{mn}} dL h_{ml}(\mathbf{r})h_{nl}(\mathbf{r}). \end{aligned} \tag{4.92}$$

Inserting triangular representation functions into the above equation, we may integrate these elements analytically.

$$\begin{aligned} A_{mn} = \sum_{\mathbf{r}_m,\mathbf{r}_n\in\Delta_l}\Delta_l\Big\{ & D(b_{ml}b_{nl}+c_{ml}c_{nl}) + \Sigma_a[a_{ml}a_{nl} + (a_{ml}b_{nl}+a_{nl}b_{ml})\overline{x_l^A} \\ & + (a_{ml}c_{nl}+a_{nl}c_{ml})\overline{y_l^A} + (b_{ml}c_{nl}+b_{nl}c_{ml})\overline{xy_l^A} \\ & + b_{ml}b_{nl}\overline{xx_l^A} + b_{ml}b_{nl}\overline{yy_l^A}]\Big\} + \frac{1}{2}\sum_{L_{mn}\subset\partial D_i}^{L_{mn}\subset\Delta_l} L_{mn}[a_{ml}a_{nl} \\ & + b_{ml}b_{nl}\overline{xx_{mn}^L} + c_{ml}c_{nl}\overline{yy_{mn}^L} + (a_{ml}b_{nl}+a_{nl}b_{ml})\overline{x_{mn}^L} \\ & + (a_{ml}c_{nl}+a_{nl}c_{ml})\overline{y_{mn}^L} + (b_{ml}c_{nl}+b_{nl}c_{ml})\overline{xy_{mn}^L}], \end{aligned} \tag{4.93}$$

and

$$\begin{aligned} B_{mn} = \sum_{\mathbf{r}_m,\mathbf{r}_n\in\Delta_l}\Delta_l\Sigma_a[a_{ml}a_{nl} + (a_{ml}b_{nl}+a_{nl}b_{ml})\overline{x_l^A} + (a_{ml}c_{nl}+a_{nl}c_{ml})\overline{y_l^A} \\ + (b_{ml}c_{nl}+b_{nl}c_{ml})\overline{xy_l^A} + b_{ml}b_{nl}\overline{xx_l^A} + b_{ml}b_{nl}\overline{yy_l^A}] \end{aligned} \tag{4.94}$$

where area Δ_l and average qualities are defined as follows:

$$\Delta_l = \int_{\Delta_l} d\mathbf{r}, \tag{4.95}$$

$$\overline{x_l^A} = \frac{1}{\Delta_l}\int_{\Delta_l}, d\mathbf{r}x \tag{4.96}$$

$$\overline{y_l^A} = \frac{1}{\Delta_l}\int_{\Delta_l}, d\mathbf{r}y \tag{4.97}$$

$$\overline{xx_l^A} = \frac{1}{\Delta_l}\int_{\Delta_l}, d\mathbf{r}x^2 \tag{4.98}$$

$$\overline{yy_l^A} = \frac{1}{\Delta_l}\int_{\Delta_l}, d\mathbf{r}y^2 \tag{4.99}$$

$$\overline{xy_l^A} = \frac{1}{\Delta_l}\int_{\Delta_l}, d\mathbf{r}xy \tag{4.100}$$

$$\overline{x_{mn}^L} = \frac{1}{L_{mn}}\int_{L_{mn}} dLx, \tag{4.101}$$

$$\overline{y_{mn}^L} = \frac{1}{L_{mn}}\int_{L_{mn}} dLy, \tag{4.102}$$

$$\overline{xx_{mn}^L} = \frac{1}{L_{mn}}\int_{L_{mn}} dLx^2, \tag{4.103}$$

$$\overline{yy_{mn}^L} = \frac{1}{L_{mn}}\int_{L_{mn}} dLy^2, \tag{4.104}$$

$$\overline{xy_{mn}^L} = \frac{1}{L_{mn}}\int_{L_{mn}} dLxy. \tag{4.105}$$

Assuming the coordinates for the tree vertices of triangle Δ_l are (x_1, y_1), (x_2, y_2) and (x_3, y_3) respectively, we may write the above equations as

$$\Delta_l = \frac{1}{2}[(x_1y_2 - x_2y_1) + (x_2y_3 - x_3y_2) + (x_3y_1 - x_1y_3)], \tag{4.106}$$

$$\overline{x_l^A} = \frac{1}{3}(x_1 + x_2 + x_3), \tag{4.107}$$

$$\overline{y_l^A} = \frac{1}{3}(y_1 + y_2 + y_3), \tag{4.108}$$

$$\overline{xx_l^A} = \frac{1}{6}(x_1^2 + x_2^2 + x_3^2 + x_1x_2 + x_1x_3 + x_2x_3), \tag{4.109}$$

$$\overline{y_l^A} = \frac{1}{6}(y_1^2 + y_2^2 + y_3^2 + y_1y_2 + y_1y_3 + y_2y_3), \tag{4.110}$$

$$\overline{xy_l^A} = \frac{1}{12}[2(x_1y_1 + x_2y_2 + x_3y_3) + x_1y_2 + x_2y_1 + x_1y_3 + x_3y_1 + x_2y_3 + x_3y_2], \tag{4.111}$$

$$\overline{x_{mn}^L} = \frac{1}{2}(x_m + x_n), \tag{4.112}$$

$$\overline{y_{mn}^L} = \frac{1}{2}(y_m + y_n), \tag{4.113}$$

$$\overline{xx_{mn}^L} = \frac{1}{3}(x_m^2 + x_n^2 + x_mx_n), \tag{4.114}$$

$$\overline{yy^L_{mn}} = \frac{1}{3}(y_m^2 + y_n^2 + y_m y_n), \tag{4.115}$$

$$\overline{xy^L_{mn}} = \frac{1}{6}(2x_m y_m + 2x_n y_n + x_m y_n + x_n y_m). \tag{4.116}$$

Once matrices **A** and **B** are calculated, we can use a linear solver to solve Eq.4.91. Before proceeding to treatments of total and directional escape probabilities,it is instructive to mention a number of very important properties regarding the finite element matrices **A**, **B** and linear systems.

1. Matrices **A** and **B** are symmetric. It can be easily proved, starting from Eqs. 4.86 and 4.90 respectively, that $A_{mn} = A_{nm}$ and $B_{mn} = B_{nm}$.

2. **A** is a sparse matrix. The representation functions $h_m(\mathbf{r})$ are locally defined, in another word, they are nonzero only for the triangles, one of whose vertices is grid point m. Therefore A_{mn} is nonzero only if grid points m and n are two of the vertices of a same triangle.

3. The parameters defined in 4.95-4.116 depend only on a single cell. There are only N_1 different types of triangles as we can see from the subdivisions illustrated in Figure 4.1, because all the smaller triangles within a larger triangle are identical. As a result, the geometric parameters are needed to calculate and to store only for N_1 triangles, no matter how many subdivisions we actually make.

4. Matrices **A** and **B** depend only on the geometry and background plasma properties. Keep in mind that the solution to the diffusion equation 4.44 is the scalar flux associated with the collision sources due to a unit current injected from region j, in order to evaluate escape probabilities associated with currents entering from other adjacent regions, we may have to repeat the same process. However, matrices **A** and **B** need to be evaluated only once because of their independence on source distribution. And more importantly, LU decomposition, which is responsible for a significant portion of effort to solve a linear system, is needed to be carried out only once. Therefore we

just need to recalculate the first collision source at each grid point when evaluating probabilities associated with currents entering from other adjacent regions.

4.4.5 TEP balance equations

Once the diffusion equation is solved, we can easily calculate total and directional escape probabilities using the following equations.

$$P_i^j = \frac{\oint_{\partial D_i} dS_i(\mathbf{n}_+ \cdot \mathbf{J}_+(\mathbf{r}))}{\int_{D_i} S^0_{j,i}(\mathbf{r}) d\mathbf{r}}, \tag{4.117}$$

and

$$\Lambda_{ik}^j = \frac{\int_{\partial D_{ik}} dS_{ik}(\mathbf{n}_+ \cdot \mathbf{J}_+(\mathbf{r}))}{\oint_{\partial D_i} dS_i(\mathbf{n}_+ \cdot \mathbf{J}_+(\mathbf{r}))}, \tag{4.118}$$

where the total escape probability P_i^j is the probability that the first charge-exchanged neutrals, originally entering region i from region j, have zero or more collision within region i and finally escape from region i. The directional escape probability Λ_{ik}^j is the probability that neutrals escaping from region i, associated with the neutrals originally entering region i from region j, escape into region k.

As discussed in sections 3.1.3 and 4.3.1, for each interface between two adjacent cells, a moment of the total partial current can be explicitly expressed in terms of all the incident moments from contiguous regions via transmission and escape probabilities. Taking the n-th moment of the total partial current from region i to region j, $\Gamma_{i,j}^n$, as an example, it consists of three distinct contributions:

1. The n-th moment of uncollided neutrals

   It is the sum of neutrals entering into region i from all contiguous regions k in moment n' will be directly transmitted into region j in moment n without an interaction withing region i. The n-th moment of uncollided neutrals can be written in the usual

form,

$$\Gamma_{i,j}^{n,u} = \sum_{k,n'} T_{i,k\to j}^{n'\to n}\Gamma_{k,i}^{n'}. \tag{4.119}$$

2. The n-th moment of collided neutrals

   The n-th collided moment is the sum of neutrals entering into region *i* from all the contiguous regions *k* in moment n' will undergo one or more charge-exchange scattering within region *i* and finally exit into region *j* in moment *n*. Since the collided flux is almost isotropic, the n-th moment of the collided flux, according to the definition of total and directional escape probabilities, can be expressed as

$$\Gamma_{i,j}^{n,c} = \sum_{k,n'} \Gamma_{k,i}^{n'} \left(\delta_{n'0} - \sum_{l} T_{i,k\to l}^{n'\to 0}\right) c_i^k P_i^k \Lambda_{ij}^k \delta_{n0}, \tag{4.120}$$

   where c_i^k is the charge-exchange fraction for the neutrals entering into region *i* from region *k*.

3. The n-th moment of external source neutrals

   The n-th external source moment is the contribution from the uniform external volumetric sources and their progenies. It will remain the same form as the original equation,

$$\Gamma_{i,j}^{n,ext} = S_{ext}^{i} P_i \Lambda_{ij} \delta_{n0}, \tag{4.121}$$

   where S_{ext}^{i} is the external volumetric source, and P_i and Λ_{ij} are the total and directional probabilities associated with a uniform and isotropic source in region *i*, which have same meaning as those defined in Chapters 2 and 3.

Combining the three contributions the final balance equation for the n-th moment current from region *i* to region *j* can be written as

$$\Gamma_{i,j}^{n} = \sum_{k,n'} T_{i,k\to j}^{n'\to n}\Gamma_{k,i}^{n'} + \sum_{k,n'} \Gamma_{k,i}^{n'} \left(\delta_{n'0} - \sum_{l} T_{i,k\to l}^{n'\to 0}\right) c_i^k P_i^k \Lambda_{ij}^k \delta_{n0} + S_{ext}^{i} P_i \Lambda_{ij} \delta_{n0}. \tag{4.122}$$

4.5 Linear representations of an angular flux at interface

The diffusion approximation and the finite element method have been exploited to evaluate total and directional escape probabilities in the previous section. These approximations allow us to take into account the fact that charge-exchanged sources are preferentially distributed near the incident surface for an optically thick region. The new approximations are expected to and should be more accurate than the original flat collision source approximation, and their improvements will be tested in the following sections. However, the representation functions defined in 3.35 are spatially independent, this implies that the neutral angular flux are uniformly distributed over each interface, while in the previous section it was assumed that the scalar flux within a region is piecewise linear. Errors introduced by the assumption of the uniform angular flux over interface had already been observed for an optically thick region with a purely absorbing media in section 3.7.2. The comparisons in the next section will also show this approximation leads to an over-prediction for regions where the neutral mean free path is much smaller than the characteristic dimension and with strong charge-exchanged sources.

To relax this limitation, a spatially linear function is added to the original representation functions. The orthogonal representation functions are

$$\psi^0_{i,j}(x_{ij}, \mathbf{\Omega}) = \frac{1}{\pi L_{ij}}, \tag{4.123a}$$

$$\psi^1_{i,j}(x_{ij}, \mathbf{\Omega}) = \frac{2\sqrt{3}}{\pi L^2_{ij}}(x_{ij} - 0.5L_{ij}), \tag{4.123b}$$

$$\psi^2_{i,j}(x_{ij}, \mathbf{\Omega}) = \frac{2}{\pi L_{ij}} \sin\theta_{ij} \sin\phi_{ij}, \tag{4.123c}$$

$$\psi^3_{i,j}(x_{ij}, \mathbf{\Omega}) = \frac{3\sqrt{2}}{\pi L_{ij}} \sin\theta_{ij} \cos\phi_{ij} - 2\sqrt{2}\psi^0_{i,j}(\mathbf{r}_{ij}, \mathbf{\Omega}), \tag{4.123d}$$

where L_{ij} is the length of the interface.

$\psi^0_{i,j}$ is a spatially-uniform and angularly-isotropic representation function (DP_0), $\psi^1_{i,j}$ is a spatially-linear and angularly-isotropic representation function (spatially-linear DP_0), $\psi^2_{i,j}$ and $\psi^3_{i,j}$ are spatially-uniform and angularly-linear representation functions (DP_1). Here

spatially-linear DP_1 representation functions are not taken into consideration because they can always be regarded as higher order approximations either for optically thick or thin regions. Apparently, for optically thin regions, all the spatially-linear terms can be neglected, while for optically thick region, it has been shown that all DP_1 terms can be safely ignored because of the randomization of charge-exchanged scattering events.

Substituting these representation functions into Eq. 3.13a and changing dummy variables, the four-dimensional integrations can be integrated analytically in the direction parallel to neutral trajectories and leads to two-dimensional numerical integrations, which can be evaluated using adaptive numerical integration techniques. Since some of the integrations are the same as those in Eqs. 3.31, here we just list the transmission probabilities associated with the spatially-linear representation function,

$$T_{i,k\to j}^{0\to 1} = \frac{4\sqrt{3}}{\pi L_{ki} L_{ij}} \int_0^{L_{ki}} dx_{ki} \int_{\varphi_{\min}}^{\varphi_{\max}} (x_{ij} - 0.5L_{ij}) \cos\varphi_{ki} \cdot Ki_3\left(\Sigma_t l(x_{ki}, \varphi_{ki})\right) d\varphi_{ki}, \tag{4.124a}$$

$$T_{i,k\to j}^{1\to 0} = \frac{4\sqrt{3}}{\pi L_{ki}^2} \int_0^{L_{ki}} dx_{ki} \int_{\varphi_{\min}}^{\varphi_{\max}} (x_{ki} - 0.5L_{ki}) \cos\varphi_{ki} \cdot Ki_3\left(\Sigma_t l(x_{ki}, \varphi_{ki})\right) d\varphi_{ki}, \tag{4.124b}$$

$$T_{i,k\to j}^{1\to 1} = \frac{24}{\pi L_{ki}^2 L_{ij}} \int_0^{L_{ki}} dx_{ki} \int_{\varphi_{\min}}^{\varphi_{\max}} (x_{ij} - 0.5L_{ij})(x_{ki} - 0.5L_{ki}) \tag{4.124c}$$

$$\cos\varphi_{ki} \cdot Ki_3\left(\Sigma_t l(x_{ki}, \varphi_{ki})\right) d\varphi_{ki},$$

$$T_{i,k\to j}^{1\to 2} = \frac{8\sqrt{3}}{\pi L_{ki}^2} \int_0^{L_{ki}} dx_{ki} \int_{\varphi_{\min}}^{\varphi_{\max}} (x_{ki} - 0.5L_{ki}) \tag{4.124d}$$

$$\sin\varphi_{ij} \cos\varphi_{ki} \cdot Ki_4\left(\Sigma_t l(x_{ki}, \varphi_{ki})\right) d\varphi_{ki},$$

$$T_{i,k\to j}^{1\to 3} = \frac{12\sqrt{6}}{\pi L_{ki}^2} \int_0^{L_{ki}} dx_{ki} \int_{\varphi_{\min}}^{\varphi_{\max}} (x_{ki} - 0.5L_{ki}) \tag{4.124e}$$

$$\cos\varphi_{ki} \cos\varphi_{ij} \cdot Ki_4\left(\Sigma_t l(x_{ki}, \varphi_{ki})\right) d\varphi_{ki} - 2\sqrt{2} T_{i,k\to j}^{0\to 0},$$

$$T_{i,k\to j}^{2\to 1} = \frac{8\sqrt{3}}{\pi L_{ki} L_{ij}} \int_0^{L_{ki}} dx_{ki} \int_{\varphi_{\min}}^{\varphi_{\max}} (x_{ij} - 0.5L_{ij}) \tag{4.124f}$$

$$\sin\varphi_{ki} \cos\varphi_{ki} \cdot Ki_4\left(\Sigma_t l(x_{ki}, \varphi_{ki})\right) d\varphi_{ki},$$

$$T_{i,k\to j}^{3\to 1} = \frac{12\sqrt{6}}{\pi L_{ki} L_{ij}} \int_0^{L_{ki}} dx_{ki} \int_{\varphi_{\min}}^{\varphi_{\max}} (x_{ij} - 0.5L_{ij}) \tag{4.124g}$$

$$\cos^2\varphi_{ki} \cdot Ki_4\left(\Sigma_t l(x_{ki}, \varphi_{ki})\right) d\varphi_{ki} - 2\sqrt{2} T_{i,k\to j}^{0\to 0}.$$

Notice that x_{ij} is the length from the starting point of interface ∂D_{ij} to point $\mathbf{r}_{ij}$ in the clockwise direction of ∂D_i, x_{ij} is not equal to x_{ji}, but always $x_{ij} - 0.5L_{ij} = -(x_{ji} - 0.5L_{ji})$.

The non-uniformity of uncollided fluxes is embodied in the above transmission probabilities. Obviously the flux at interfaces due to the contribution of charge-exchanged sources is also nonuniform for an optically thick region. To take the collided flux into account, the total and directional escape probabilities associated with the nonuniform representation functions must be evaluated and be embodied in the partial current balance equation. Though the higher order approximations can be easily extended, here only the lowest nonuniform order, spatially linear, approximation is made. To the lowest order the following two linear contributions for the collided flux at an interface of a given region must be considered: (1) the spatially-linear outgoing collided flux associated with a spatially-uniform flux entering into that region, where non-uniformity is driven by material attenuation; (2) the spatially-linear collided angular flux associated with a spatially-linear flux entering into that region, where non-uniformity is driven by the nonuniform incoming flux and material attenuation.

The finite element method to solve a diffusion equation with the first collision source associated with a spatially-uniform incoming flux has already been discussed in the previous sections. For the second case, we just need to replace the source term with the first collision source associated with spatially-linear incoming flux, which can be written as in the following form,

$$S^1_{j,i}(\mathbf{r}) = \frac{2\sqrt{3}\Sigma_{cx}(\mathbf{r})}{\pi L_{ji}} \int_{\varphi_{min}(\mathbf{r})}^{\varphi_{max}(\mathbf{r})} d\varphi Ki_2(\Sigma_t l(\mathbf{r},\varphi))(x_{ji} - 0.5L_{ji}). \tag{4.125}$$

Then, following the same steps we can solve the diffusion equation and calculate the outgoing current. As before the generalized total and directional escape probabilities are denoted as $P_i^{k,n'\to n}$ and $\Lambda_{ij}^{k,n'\to n}$ respectively, where i is the region of interest, k is the incident region, j is the exiting region, n' is the incoming partial current moment and n is the

outgoing partial current moment. These escape probabilities can be written in the form,

$$P_i^{k,n'\to n} = \frac{\sum\limits_l \int\limits_{\partial D_{il}} dS_i(\mathbf{n}_{il}\cdot \mathbf{J}^{n'}_{\mathbf{il}}(\mathbf{r}))\pi L_{il}\psi^n_{i,l}(x_{il})}{\int\limits_{D_i} S^{n'}_{k,i}(\mathbf{r})d\mathbf{r}}, \tag{4.126}$$

and

$$\Lambda_{ij}^{k,n'\to n} = \frac{\int\limits_{\partial D_{ij}} dS_{ij}(\mathbf{n}_{ij}\cdot \mathbf{J}^{n'}_{\mathbf{ij}}(\mathbf{r}))\pi L_{ij}\psi^n_{i,j}(x_{ij})}{\sum\limits_l \int\limits_{\partial D_{il}} dS_i(\mathbf{n}_{il}\cdot \mathbf{J}^{n'}_{\mathbf{il}}(\mathbf{r}))\pi L_{il}\psi^n_{i,l}(x_{il})}. \tag{4.127}$$

And accordingly, we can write the balance equation for the n-th total partial current from region i to region j as

$$\Gamma^n_{i,j} = \sum_{k,n'} T^{n'\to n}_{i,k\to j}\Gamma^{n'}_{k,i} + \sum_{k,n'}\Gamma^{n'}_{k,i}\left(\delta_{n'0} - \sum_l T^{n'\to 0}_{i,k\to l}\right)c_i^k P_i^k \Lambda_{ij}^{k,n'\to n} + S^i_{ext}P_i\Lambda_{ij}\delta_{n0}. \tag{4.128}$$

4.6 Comparisons and tests

In the previous section, the diffusion approximation and the finite element method had been employed to correct directional escape probabilities. In this section the validity of these approximations or assumptions will be tested. First the specially-designed problems with a linear or exponential volumetric source will be used to test the accuracy of directional escape probabilities. Then a nine-rectangular regions with different ranges of Δ/λ ratios will be used to explore the validity of the linear approximation of angular flux and the overall accuracy.

4.6.1 Test of escape probabilities

For optically thick regions, the scattered or charge-exchanged neutrals are preferentially located near the incident surface because of material attenuation. Even for optically thin regions, geometric attenuation, which is inversely proportional to the square of the distance between the point of interest and the source, leads to the nonuniform distribution of charge-exchanged sources. Consequently the probability that these charge-exchanged neutrals escape back across the incident interface is greater than the probability that the

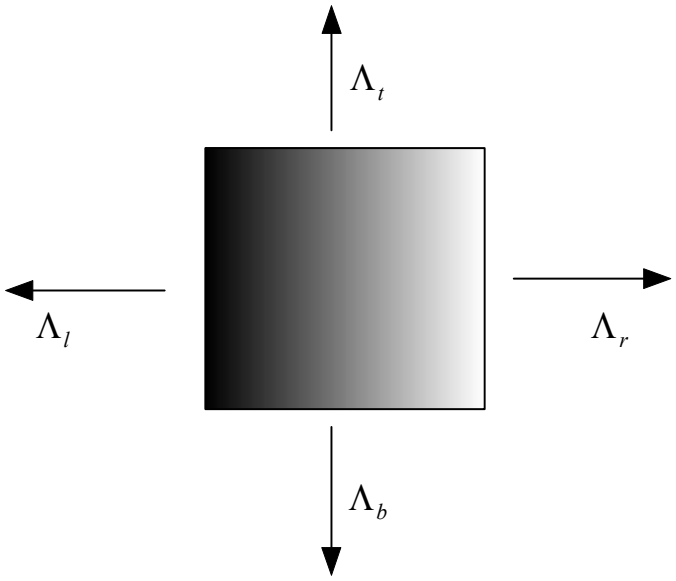

Figure 4.6. Computational model used to compute the total and directional escape probabilities

collided neutrals escape toward any other direction. The nonuniform collided sources can be easily taken into account by the diffusion approximation, which is based on the assumption that the neutral flux is linearly anisotropic. The purpose of this section is to assess, by comparison with Monte Carlo calculations, the accuracy of the total and directional escape probabilities predicted by the diffusion theory.

In order to verify the accuracy of total and directional escape probabilities predicted by the diffusion theory, a square region shown in Figure 4.6 is considered to investigate effects of non-uniform volumetric sources. With reference to Figure 4.6, Λ_l, Λ_r, Λ_t and Λ_b represent the directional escape probabilities that neutrals escape across the left, right, top and bottom interfaces, respectively. P is the total escape probability.

First, a spatially linear volumetric source with the highest strength at the left boundary and the lowest strength at the right boundary is taken into account. The study has been conducted for a variety of Δ/λ ratios and charge-exchange factions. For example, Table 4.1 shows the comparisons of escape probabilities calculated by the Monte Calor method and the diffusion theory in a square with $\Delta/\lambda = 3$ and $cx = 0.9$. For all the range of Δ/λ ratios and charge exchange fraction, the agreement between the two is very good, with an error

Table 4.1. Escape probabilities predicted by the Monte Carlo method and the diffusion theory in a square with a linear volumetric source, $\Delta/\lambda = 3$ **and** $cx = 0.9$

	Monte Carlo	Diffusion	Error(%)
Λ_l	0.3454	0.3401	-1.53
Λ_b	0.2494	0.25	0.24
Λ_r	0.1546	0.1599	3.43
Λ_t	0.2494	0.25	0.24
P	0.8549	0.8727	2.08

Table 4.2. Escape probabilities predicted by the Monte Carlo method and the diffusion theory in a square with a linear volumetric source, $\Delta/\lambda = 3$ **and** $cx = 0.6$

	Monte Carlo	Diffusion	Error(%)
Λ_l	0.3631	0.3589	-1.16
Λ_b	0.2499	0.25	0.04
Λ_r	0.1371	0.1411	2.92
Λ_t	0.2499	0.25	0.04
P	0.6015	0.6351	5.59

of less than 6%. It is clear that neutrals preferentially escape across the surface with the highest source, with contrast to the original non-directional assumption. It is also important to note that the shorter the mean free path, the more important the effects of a non-uniform volumetric source.

When the mean free path is smaller than the characteristic dimension of computational

Table 4.3. Escape probabilities predicted by the Monte Carlo method and the diffusion theory in a square with a linear volumetric source, $\Delta/\lambda = 1$ **and** $cx = 0.9$

	Monte Carlo	Diffusion	Error(%)
Λ_l	0.2758	0.2714	-1.60
Λ_b	0.2501	0.25	-0.04
Λ_r	0.2241	0.2286	2.01
Λ_t	0.25	0.25	0
P	0.9287	0.9417	1.40

Table 4.4. Escape probabilities predicted by the Monte Carlo method and the diffusion theory in a square with a linear volumetric source, $\Delta/\lambda = 1$ **and** $cx = 0.6$

	Monte Carlo	Diffusion	Error(%)
Λ_l	0.279	0.2741	-1.76
Λ_b	0.2499	0.25	0.04
Λ_r	0.2212	0.2259	2.12
Λ_t	0.2499	0.25	0.04
P	0.7666	0.8019	4.60

Table 4.5. Escape probabilities predicted by the Monte Carlo method and the diffusion theory in a square with a linear volumetric source, $\Delta/\lambda = 0.3$ **and** $cx = 0.9$

	Monte Carlo	Diffusion	Error(%)
Λ_l	0.2627	0.2558	-2.63
Λ_b	0.2494	0.25	0.24
Λ_r	0.2385	0.2442	2.39
Λ_t	0.2498	0.25	0.08
P	0.9786	0.9841	0.56

Table 4.6. Escape probabilities predicted by the Monte Carlo method and the diffusion theory in a square with a linear volumetric source, $\Delta/\lambda = 0.3$ **and** $cx = 0.6$

	Monte Carlo	Diffusion	Error(%)
Λ_l	0.2633	0.256	-2.77
Λ_b	0.2495	0.25	0.20
Λ_r	0.2379	0.244	2.56
Λ_t	0.2493	0.25	0.28
P	0.9201	0.9395	2.11

Table 4.7. Escape probabilities predicted by the Monte Carlo method and the diffusion theory in a square with an exponential volumetric source ($S0(x) = \exp(-\frac{x}{\lambda})$), $\Delta/\lambda = 3$ and $cx = 0.9$

	Monte Carlo	Diffusion	Error(%)
Λ_l	0.4083	0.4036	-1.15
Λ_b	0.2345	0.236	0.64
Λ_r	0.1226	0.1243	1.38
Λ_t	0.2346	0.236	0.59
P	0.7921	0.8097	2.22

Table 4.8. Escape probabilities predicted by the Monte Carlo method and the diffusion theory in a square with an exponential volumetric source ($S0(x) = \exp(-\frac{x}{\lambda})$), $\Delta/\lambda = 3$ and $cx = 0.6$

	Monte Carlo	Diffusion	Error(%)
Λ_l	0.4431	0.4419	-0.27
Λ_b	0.2293	0.2308	0.65
Λ_r	0.0983	0.0966	-1.72
Λ_t	0.2293	0.2308	0.65
P	0.5045	0.5309	5.23

regions, a linear model may not sufficiently represent the non-uniformity of the charge-exchanged neutrals. Since the first collision source exponentially decreases as it is away from the incident surface, it is necessary to verify the validity of the new approximation for problems with an exponentially non-uniform volumetric source. Tables 4.7-4.12 shows the results for the cases with an exponentially non-uniform source and different Δ/λ and charge exchange fractions. The results predicted by the diffusion theory agree very well with those calculated by Monte Carlo, with an error less than 5%. Is also evident that the directional escape is significant, with the preferable escape toward the surface near to the highest volumetric source, and that the directional escape effect increases as the mean free path decreases.

4.6.2 Test for 2D 9-region problems

In the previous section, the accuracy of total and directional escape probabilities was studied. In this section, the cumulative accuracy of the approaches to correct directionality on

Table 4.9. Escape probabilities predicted by the Monte Carlo method and the diffusion theory in a square with an exponential volumetric source ($S0(x) = \exp(-\frac{x}{\lambda})$), $\Delta/\lambda = 1$ and $cx = 0.9$

	Monte Carlo	Diffusion	Error(%)
Λ_l	0.29	0.2825	-2.58
Λ_b	0.2485	0.2492	0.28
Λ_r	0.213	0.2191	2.86
Λ_t	0.2485	0.2492	0.28
P	0.9295	0.9419	1.33

Table 4.10. Escape probabilities predicted by the Monte Carlo method and the diffusion theory in a square with an exponential volumetric source ($S0(x) = \exp(-\frac{x}{\lambda})$), $\Delta/\lambda = 1$ and $cx = 0.6$

	Monte Carlo	Diffusion	Error(%)
Λ_l	0.2946	0.2954	0.27
Λ_b	0.2482	0.2491	0.36
Λ_r	0.2089	0.2064	-1.12
Λ_t	0.2483	0.2491	0.32
P	0.7679	0.8025	4.50

Table 4.11. Escape probabilities predicted by the Monte Carlo method and the diffusion theory in a square with an exponential volumetric source ($S0(x) = \exp(-\frac{x}{\lambda})$), $\Delta/\lambda = 0.3$ and $cx = 0.9$

	Monte Carlo	Diffusion	Error(%)
Λ_l	0.2589	0.2544	-1.73
Λ_b	0.2499	0.25	0.04
Λ_r	0.2412	0.2456	1.82
Λ_t	0.25	0.25	0
P	0.9789	0.9841	0.53

Table 4.12. Escape probabilities predicted by the Monte Carlo method and the diffusion theory in a square with an exponential volumetric source ($S0(x) = \exp(-\frac{x}{\lambda})$), $\Delta/\lambda = 0.3$ and $cx = 0.6$

	Monte Carlo	Diffusion	Error(%)
Λ_l	0.2595	0.2545	-1.92
Λ_b	0.2499	0.25	0.04
Λ_r	0.2417	0.2455	1.57
Λ_t	0.2499	0.25	0.04
P	0.92	0.9395	2.11

a 9-region model will be evaluated.

The geometry of the problem is shown in Figure 3.22. The background plasma is assumed to be uniform. The plasma ion temperature is 10 eV. The vacuum boundary conditions are assumed on the four external surfaces. An isotropic and uniform neutral flux with the unit strength and the energy of 10 eV is injected on the left boundary of region 2. Charge exchange factions for all the regions are adjusted to 0.9. The same geometry, plasma properties and neutral parameters are used to run DEGAS and GTNEUT with the linear source expansion or diffusion approximation. The results for various Δ/λ ratios are shown in Figures 4.7-4.14.

For the problem with $\Delta/\lambda = 0.26$, in which the mean free path is much longer than the characteristic dimension of computational regions, the assumption of uniform charge-exchanged neutrals has no obvious effect on the calculations of neutral density for the following two reasons:(1) the charge-exchanged neutrals are almost uniformly distributed because of little attenuation; (2) the neutral transport is dominated by the uncollided neutrals. Consequently, there is no obvious improvement observed by the approach to correct escape probabilities via either the linear source expansion or the diffusion approximation as shown in Figures 4.7 and 4.8.

When the ratio Δ/λ increases to 1, the collided neutrals play a more important role on the neutral transport and the non-uniformity of collided sources is obvious. The assumption of non-directional escape results in an over-prediction of neutral densities for regions away from the external source, though this trend is compensated to some extent by under-estimations introduced by the DP_0 approximation. It is clear from Figures 4.9 and 4.10 that the correction to directional escape probabilities by the linear source expansion or the diffusion approximation significantly improves the agreement with the Monte Carlo simulations because the non-uniformity of collided sources is taken into account.

If the ratio Δ/λ increases to 3, the neutral flux is dominantly composed of the collided neutrals, which are almost isotropic and consequently result in no improvement by the DP_1

approximation. In addition to the preferential distribution of collided neutrals near to the incident surface, the non-uniformity of the angular flux across each interface has a very important effect on the neutral transport. For example, there exists a strong gradient of angular flux on the interface between regions 2 and 3, and thus the probability that the neutrals escape to the left boundary is larger than the probability that neutrals escape to region 6. Although the correction to directional escape probabilities by the two approaches improves the agreement with the Monte Carlo simulations, they still over-predict results for regions away from the incident source due to the failure of taking into account the non-uniformity of angular fluxes. It can be clearly seen from Figure 4.12 that the linear angular flux expansion, together with the diffusion theory, predicts neutral densities very well for all the regions.

When the ratio Δ/λ is extended to 5, the collided neutrals are highly located near to the incident surface. The calculations of the new approaches are shown in Figures 4.13 and 4.14. It is evident from Figure 4.13 that the linear source expansion breaks down because the linear approximation can not sufficiently represent the strong non-uniformity of charge-exchanged neutrals. It reveals that a quadratic or even higher order approximation is necessary. However, the calculations of the GTNEUT code with the correction to directional escape probabilities by solving the diffusion equation and the linear angular flux approximation are in an excellent agreement with those of the Monte Carlo code, DEGAS.

If the ratio Δ/λ is further extended to 10, the spatially linear approximation of angular fluxes would break down and results in negative fluxes, since the linear approximation cannot sufficiently represent the strong non-uniformity of the angular flux at each interface. This issue can be solved by the introduction of higher order approximations or subdivision of regions.

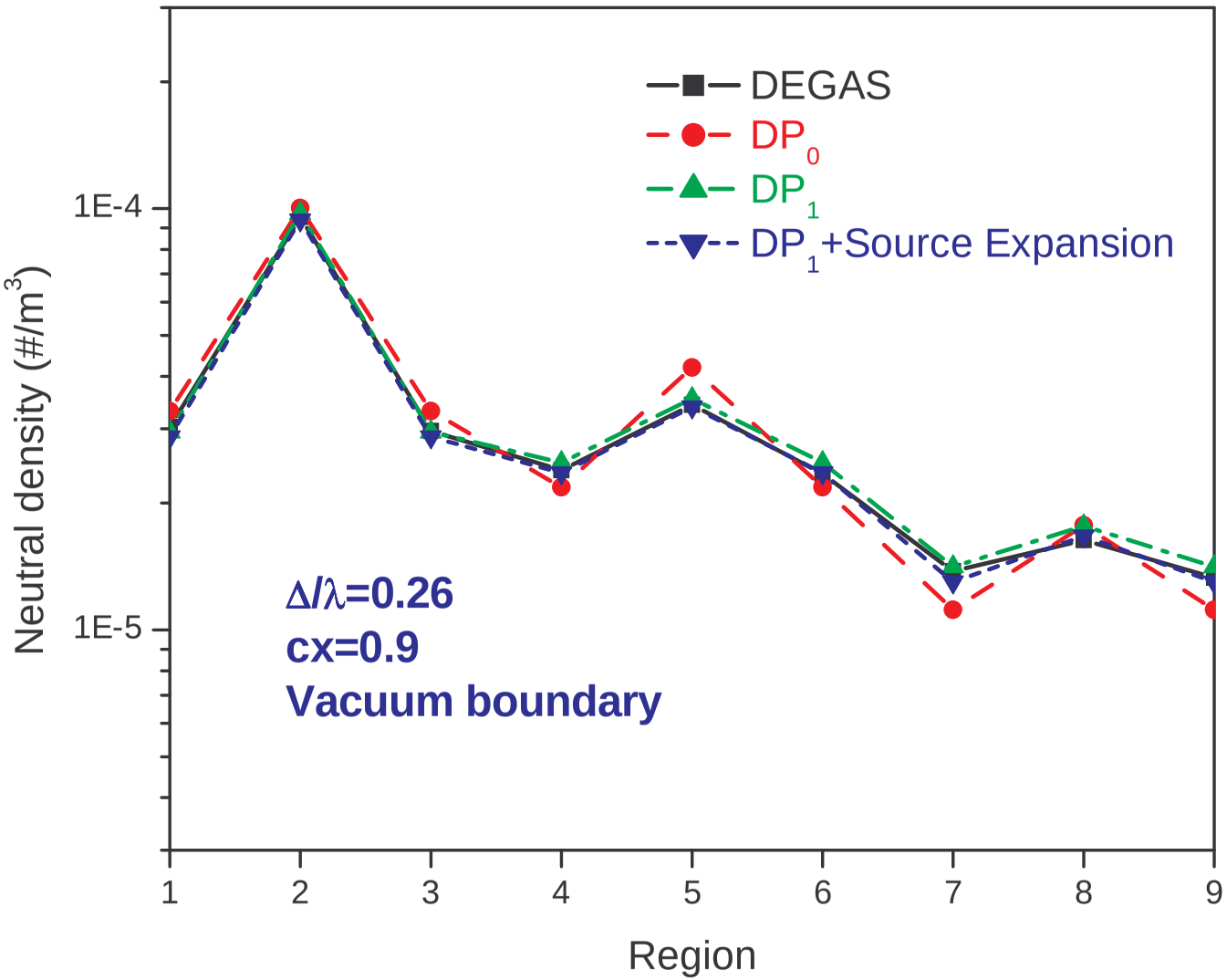

Figure 4.7. The effect of the linear source expansion on a nine-region model with c=0.9 and $\Delta/\lambda = 0.26$

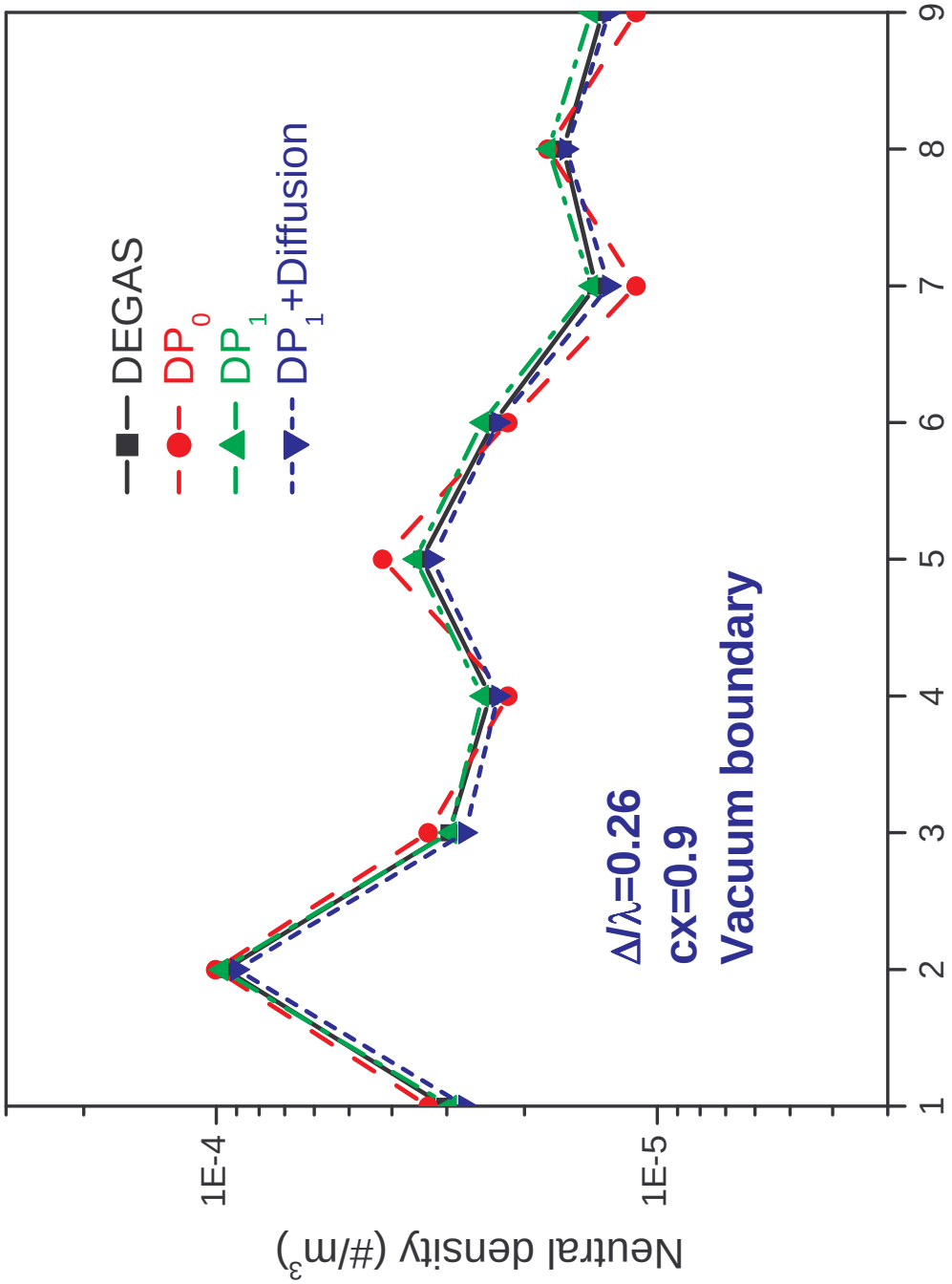

Figure 4.8. The effect of the diffusion approximation on a nine-region model with c=0.9 and $\Delta/\lambda = 0.26$

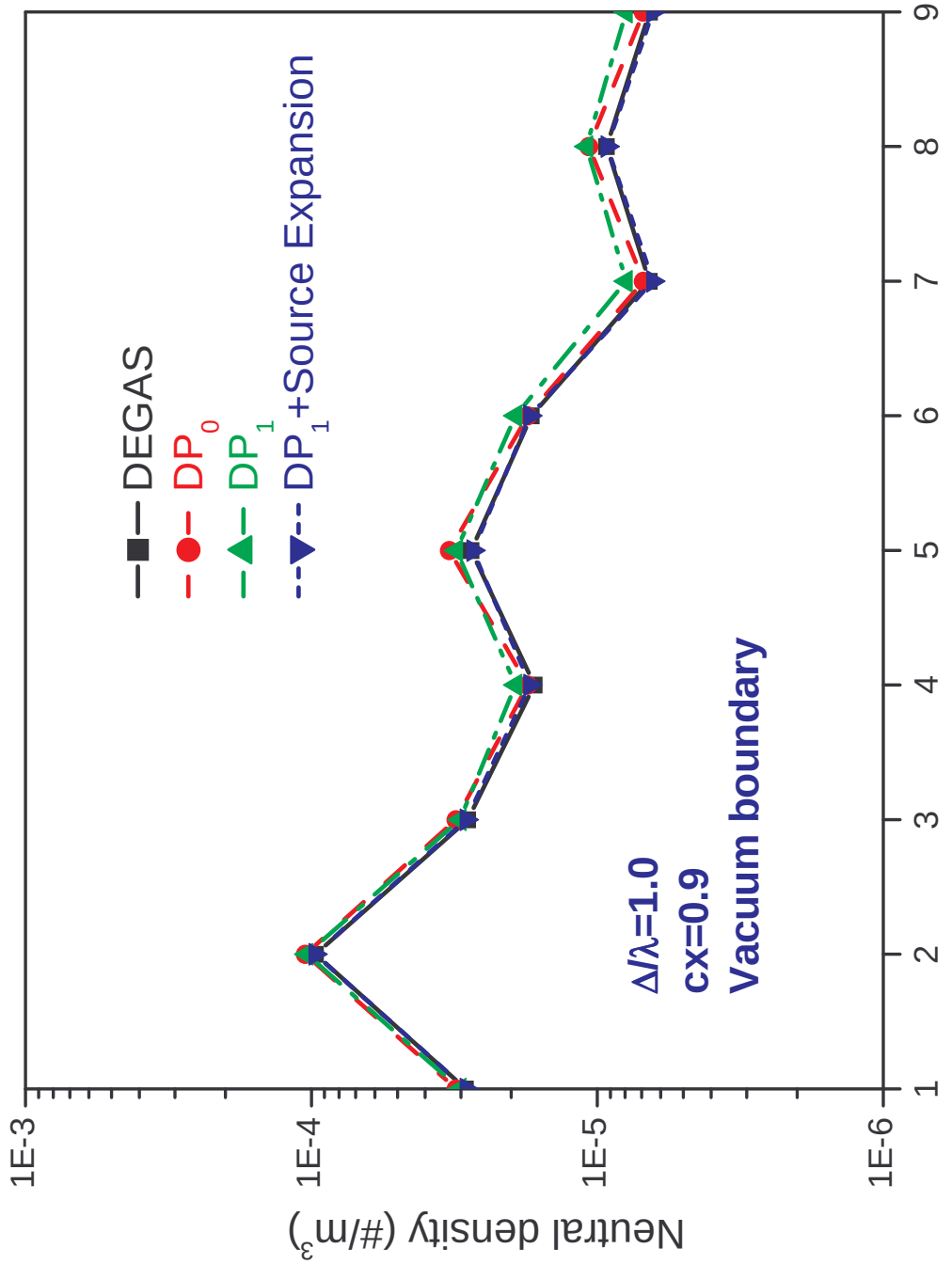

Figure 4.9. The effect of the linear source expansion on a nine-region model with c=0.9 and $\Delta/\lambda = 1$

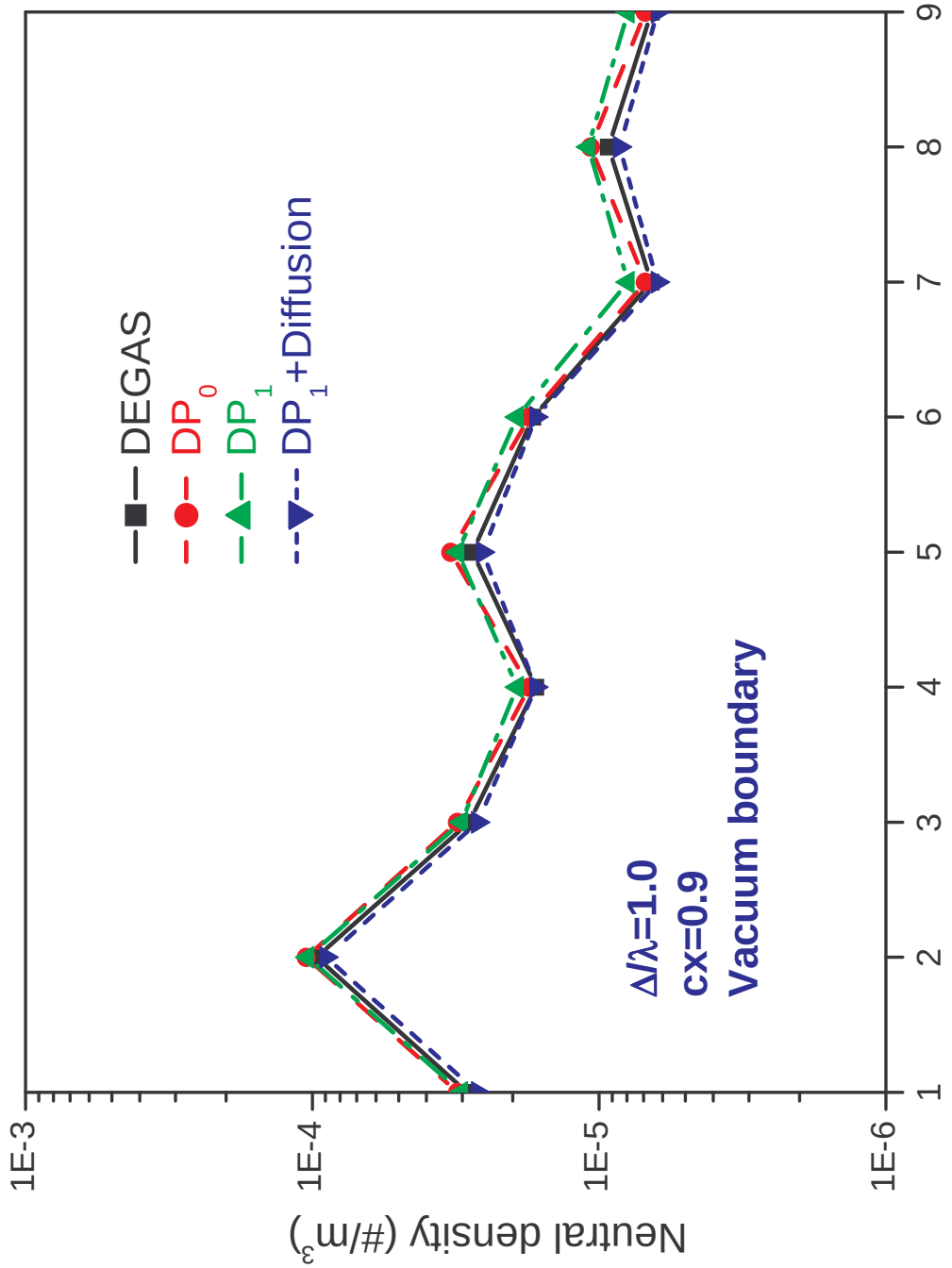

Figure 4.10. The effect of the diffusion approximation on a nine-region model with c=0.9 and $\Delta/\lambda = 1$

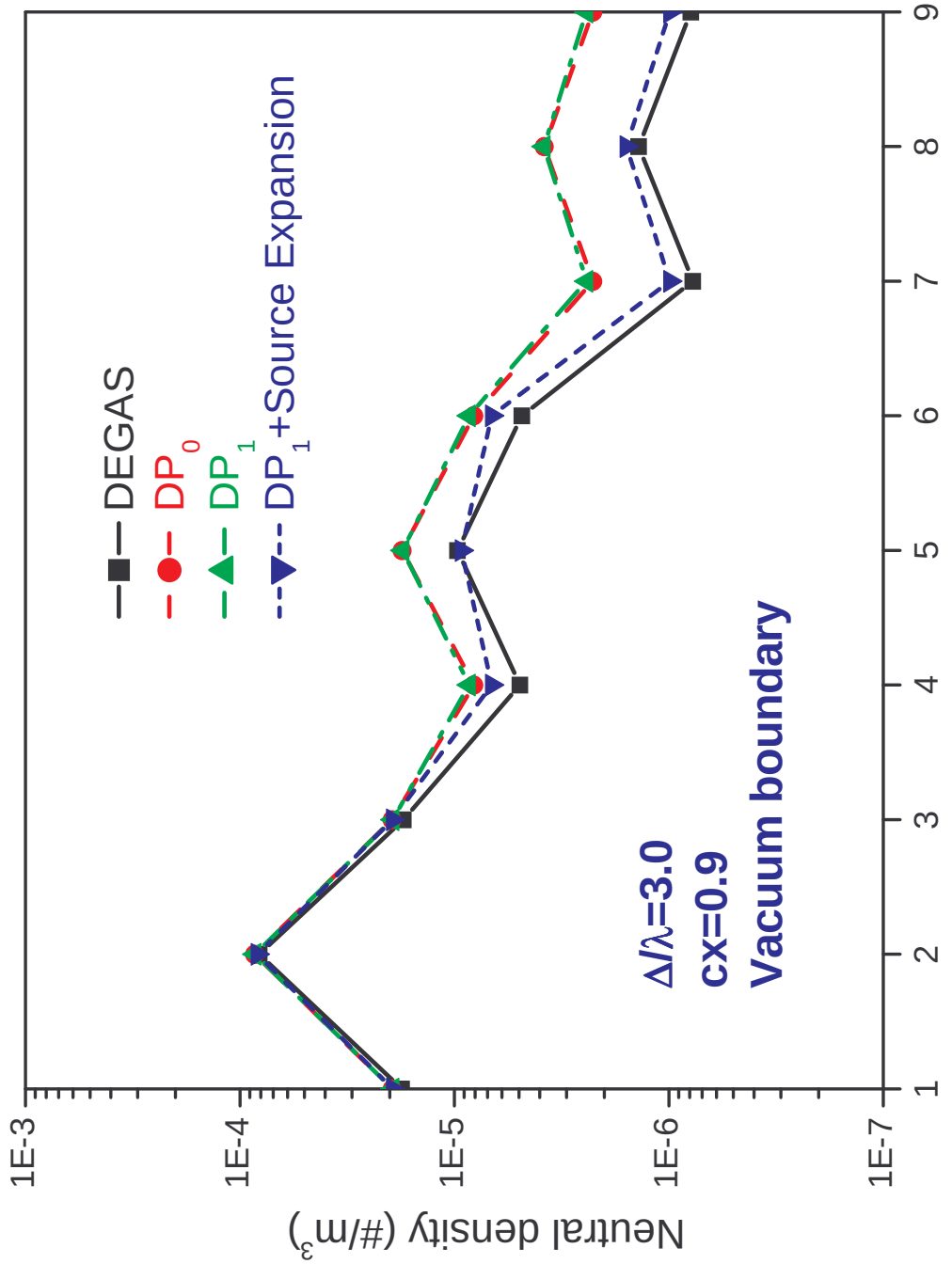

Figure 4.11. The effect of the linear source expansion on a nine-region model with c=0.9 and $\Delta/\lambda = 3$

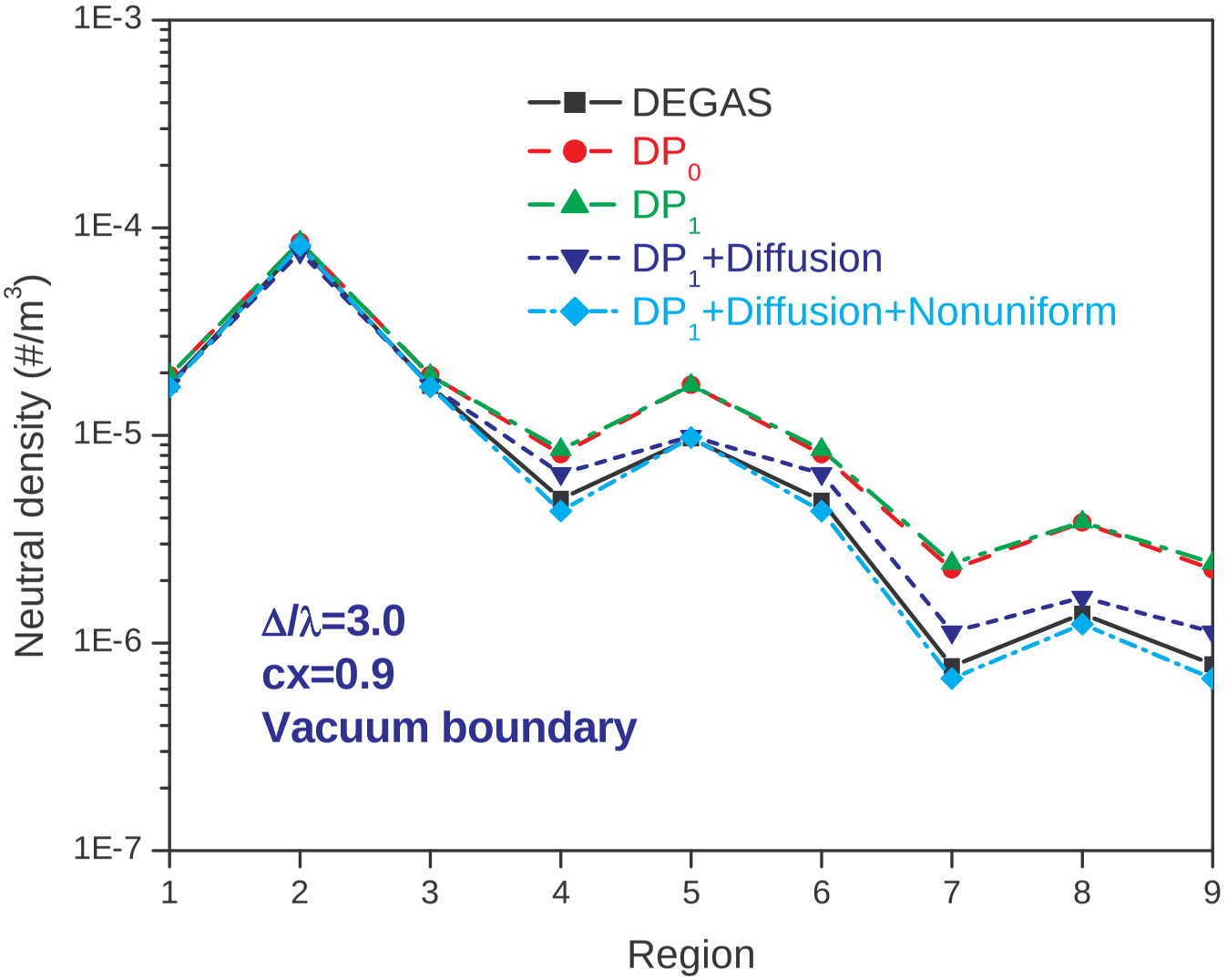

Figure 4.12. The effect of the diffusion approximation on a nine-region model with c=0.9 and $\Delta/\lambda = 3$

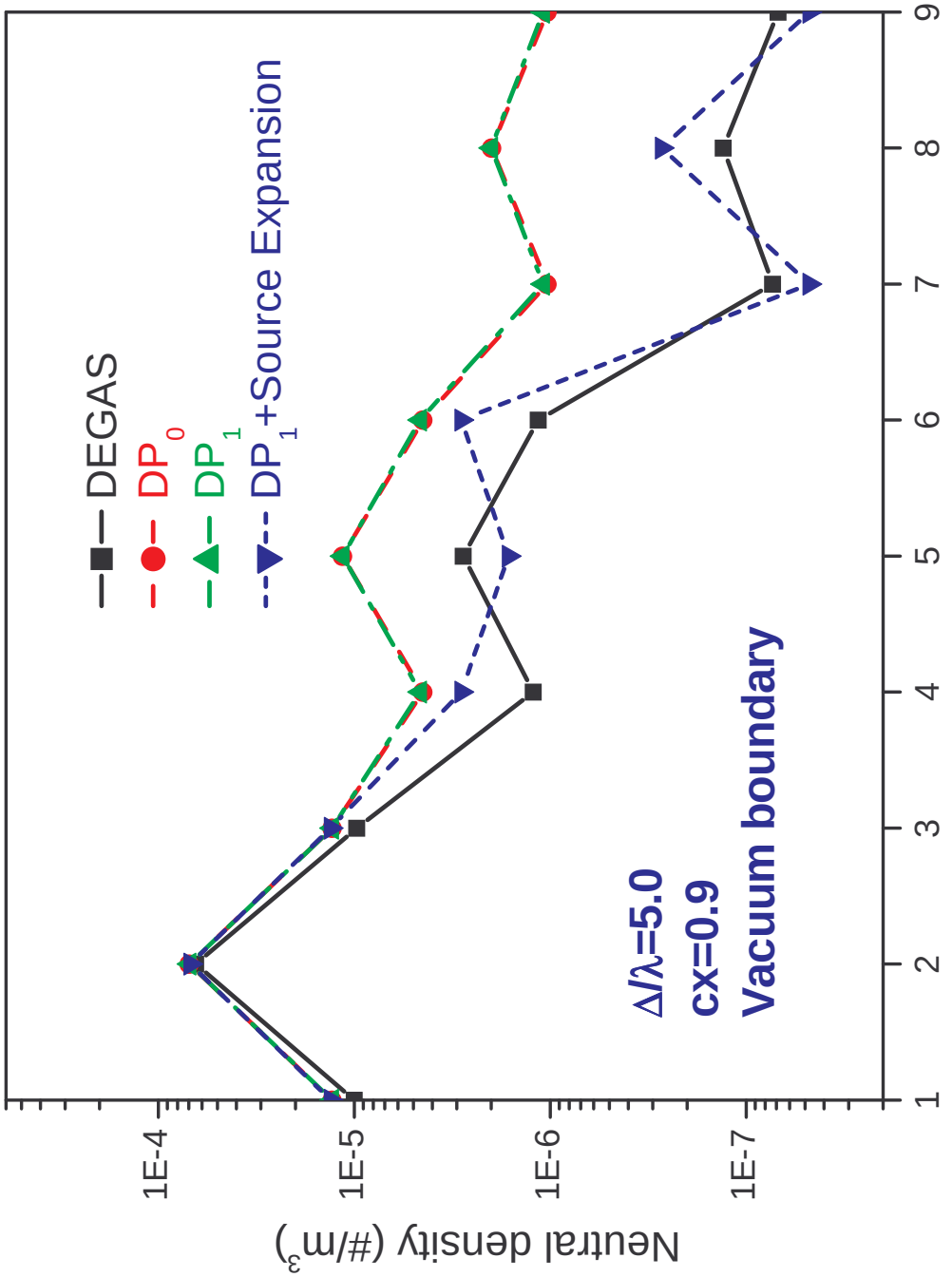

Figure 4.13. The effect of the linear source expansion on a nine-region model with c=0.9 and $\Delta/\lambda = 5$

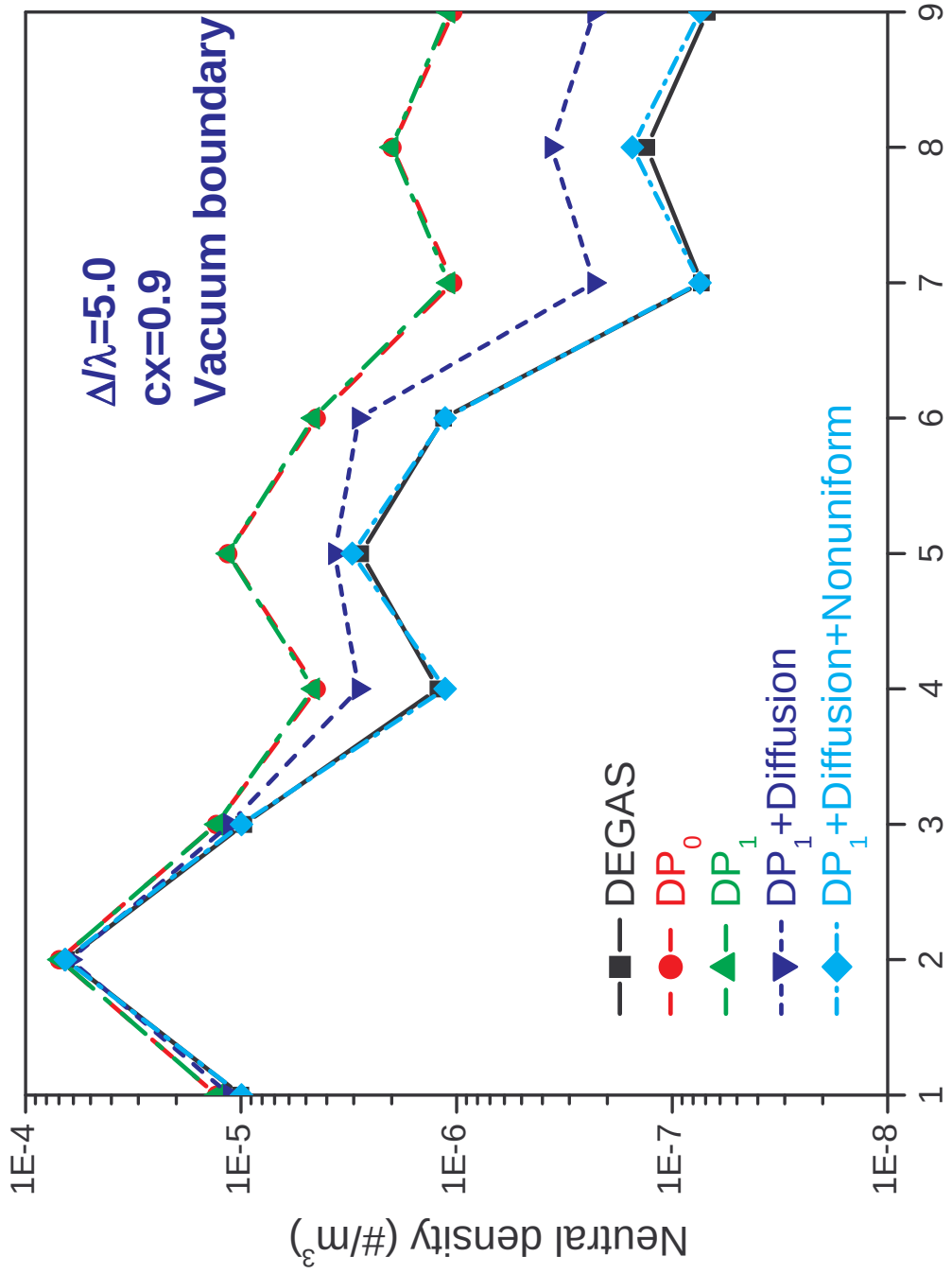

Figure 4.14. The effect of the diffusion approximation on a nine-region model with c=0.9 and $\Delta/\lambda = 5$

4.7 Conclusions

Three different approaches, subdivision of regions, collision source expansion and diffusion approximation, have been proposed and implemented to correct the directional escape probabilities associated with the non-uniformity of charge-exchanged neutrals in optically thick regions. Although the subdivision of regions is the easiest and most straightforward approach to implement and does not require to modify the original methodology, it results in large probabilities matrices, which increase requirements for the CPU time and computer memory. The collision source expansion does not require to further subdivide computational regions and has been shown to be accurate if $\Delta/\lambda < 3$. However, its accuracy deteriorates for very optically large ($\Delta/\lambda > 3$) regions, where the non-uniformity of collision source can not be sufficiently represented by linear expansion functions. Furthermore, because of very time-consuming region-region collision probabilities the collision source expansion are generally applied to periodic geometries, which are highly unlikely for fusion devices.

Assuming a neutral flux is expressed in terms of piecewise linear element functions, the diffusion equation is solved, by the finite element method, to calculate the total and directional escape probabilities for optically thick regions. In addition to the gradient of collision sources, the non-uniformity of the angular flux at an interface is taken into account by an introduction of spatially linear representation functions.

A number of calculations of the specially designed models have indicated that the directional error could be eliminated by solving the diffusion equation with a non-uniformly distributed first collision source. Its accuracy and computational efficiency have been demonstrated for all range of Δ/λ ratios. The study has also shown that a linear angular flux expansion significantly improves the accuracy of the TEP methodology for very optically large regions.

CHAPTER 5

NEUTRAL ENERGY TREATMENT

5.1 Introduction

The original TEP methodology is based on the local ion temperature (LIT) approximation, which assumes the energy of neutrals from each computational region is equal to the local ion temperature. If neutrals originate from boundaries, their energies are set by the corresponding boundary models (such as albedo, mirror or wall material boundaries). As mentioned in Chapter 2, the local ion temperature assumption would be reasonable if the most of the neutrals entering a region underwent one or more scattering or charge exchange collisions before leaving the region. However, if the neutral mean free path is much longer than the characteristic ion temperature gradient length L, defined as $L = 1/\frac{dlnT}{dx}$, the neutral flux from a region is primarily attributed to uncollided neutrals, which could have very different energy from the local charge-exchanged neutrals. Consequently, a significant error may be introduced by the local ion temperature assumption because the majority of neutrals are assigned the wrong energy. A two-group treatment of the energy dependence [26] has been already implemented in the GTNEUT code to treat the energy dependence of wall reflected neutrals, and very encouraging results have been obtained. In that approach, the neutral population is divided into two distinct energy groups: a slow energy group consisting of Franck-Condon atoms and externally injected neutrals with a few electron volts, and a fast energy group consisting of collided neutrals in thermal equilibrium with the local plasma ion populations. However, the two-group approximation may not be sufficient to represent the neutral energy dependence when background plasmas are characterized by strong gradients. Of course, this situation could be addressed by a full multi-group implementation which, however, would require time-consuming evaluation of probability matrices for each energy group. The average neutral energy approximation introduced in this thesis is intended to provide a more computationally efficient approximation.

5.2 Average neutral energy approximation (ANE)

In the average neutral energy approximation, all the neutrals crossing an interface are assumed to be monoenergetic and are assigned an average energy corresponding to the region from which they come. According to the particle balance equation, $\Gamma^n_{i,j}$, the n-th moment of the total partial current from region *i* to region *j*, can be written in the following expression,

$$\begin{aligned}\Gamma^n_{i,j} &= \Gamma^{uc,n}_{i,j} + \Gamma^{c,n}_{i,j} \\ &= \sum_{k,n'} T^{n'\to n}_{i,k\to j}\Gamma^{n'}_{k,i} + \Gamma^{c,n}_{i,j}.\end{aligned} \tag{5.1}$$

where $\Gamma^{uc,n}_{i,j}$ is the total uncollided partial current from region *i* to region *j*, $\Gamma^{c,n}_{i,j}$ is the total collided partial current from region *i* to region *j* and $T^{n'\to n}_{i,k\to j}$ is the transmission probability from region *k*, moment n' to region *j*, moment *n* through region *i*.

If the angular flux at the interface between regions i and j, $\psi(\mathbf{r}, E, \mathbf{\Omega})$, is assumed to be variable-separable, then it can be expressed as

$$\begin{aligned}\psi(\mathbf{r}, E, \mathbf{\Omega}) &= \sum_n \Gamma^n_{i,j}\psi^n_{i,j}(\mathbf{r}, \mathbf{\Omega}) f(E) \\ &= \sum_{k,n',n} T^{n'\to n}_{i,k\to j}\Gamma^{n'}_{k,i}\psi^n_{i,j}\delta(E - \overline{E}_{k,i}) + \sum_n \Gamma^{c,n}_{i,j}\psi^n_{i,j}\delta(E - T_i).\end{aligned} \tag{5.2}$$

where $f(E)$ is the neutral energy distribution function at the interface ∂D_{ij}, and $\psi^n_{i,j}(\mathbf{r}, \mathbf{\Omega})$ are angular flux representation functions. In addition, we assume that uncollided neutrals from region *k* to region *j* through region *i* are monoenergetic and have an energy of $\overline{E}_{k,i}$, and collided neutrals from region *i* have an energy of T_i, which is equal to the local ion temperature in region *i*.

We define the average energy of neutrals from region *i* to region *j* as

$$\begin{aligned}\overline{E}_{i,j} &= \frac{\int_{\partial D_{ij}} dS_{ij} \int_{\mathbf{\Omega}\cdot\mathbf{n}_{ij}>0} d\mathbf{\Omega} \int dE E\psi(\mathbf{r}, E, \mathbf{\Omega})(\mathbf{\Omega}\cdot\mathbf{n}_{ij})}{\int_{\partial D_{ij}} dS_{ij} \int_{\mathbf{\Omega}\cdot\mathbf{n}_{ij}>0} d\mathbf{\Omega} \int dE\psi(\mathbf{r}, E, \mathbf{\Omega})(\mathbf{\Omega}\cdot\mathbf{n}_{ij})} \\ &= \frac{\pi S_{ij} \int dE E \left\langle \psi^0_{i,j}(\mathbf{r}, \mathbf{\Omega}) \middle| \psi_{i,j}(\mathbf{r}, E, \mathbf{\Omega}) \right\rangle}{\Gamma^0_{i,j}},\end{aligned} \tag{5.3}$$

where $\mathbf{n}_{ij}$ is the outward normal at the interface ∂D_{ij}.

Substituting Eq. 5.2 into Eq. 5.3, the average neutral energy can be expressed as

$$
\begin{aligned}
E_{i,j} &= \frac{\pi S_{ij} \int dE E \left\langle \psi^0_{i,j}(\mathbf{r},\mathbf{\Omega}) \middle| \sum_n \Gamma^n_{i,j} \psi^n_{i,j}(\mathbf{r},\mathbf{\Omega}) f(E) \right\rangle}{\Gamma^0_{i,j}} \\
&= \frac{\sum_{k,n',n} T^{n' \to n}_{i,k \to j} \Gamma^{n'}_{k,i} \delta_{n0} \overline{E}_{k,i} + \sum_n \Gamma^{c,n}_{i,j} \delta_{n0} T_i}{\Gamma^0_{i,j}} \\
&= \frac{\sum_{k,n} T^{n \to 0}_{i,k \to j} \Gamma^0_{k,i} \overline{E}_{k,i} + \Gamma^{c,0}_{i,j} T_i}{\sum_{k,n} T^{n \to 0}_{i,k \to j} \Gamma^0_{k,i} + \Gamma^{c,0}_{i,j}}.
\end{aligned}
\tag{5.4}
$$

Since the average energy of the outgoing neutrals from a given interface is coupled to the average energy of the incoming neutrals through each interface bounding that region, the neutral transport equation can be solved by an iterative process as follows:

1. Assume $\overline{E}_{i,j} = T_i$ (the local ion temperature assumption);
2. Calculate the neutral mean free path, transmission and escape probabilities, then solve the linear system;
3. Calculate the collided and uncollided fluxes;
4. Use equation 5.4 to update the average neutral energy $\overline{E}_{i,j}$;
5. Repeat steps 2-4 until convergence;
6. Calculate the final neutral densities and the ionization rates.

5.3 Test of the average neutral energy approximation in a 9-region problem

In DEGAS code, a neutral remains its initial energy before a collision. The energy of a newly created neutral from a charge exchange scattering event at cell *i* is sampled from the

Maxwellian distribution with the temperature $T = T_i$, where T_i is the plasma ion temperature in cell i. Since DEGAS calculations are continuous in energy and more accurate, a 9-region problem with nonuniform background plasmas is used in both the GTNEUT and DEGAS codes to compare the accuracy of the local ion temperature and average neutral energy approximations. The geometric configuration and cell arrangement are illustrated in Figure 3.33. Vacuum boundary conditions are imposed on the four external surfaces. An isotropic, uniform and unit strength neutral flux with an energy of 10 eV is injected at the left boundary of cell 2.

In the first case, the ion temperature, electron temperature, ion density and electron density vary linearly from 10 eV, 6 eV, 1.7×10^{18} m^{-3} and 1.7×10^{18} m^{-3} in cells (Cells 1, 2 and 3) adjacent to the left boundary to 100 eV, 10 eV, 2.7×10^{18} m^{-3} and 2.7×10^{18} m^{-3} in cells (Cells 7, 8 and 9) adjacent to the right boundary, respectively. The resulting mean free path varies from 0.85 to 0.94 m, and the charge exchange faction c_i varies from 0.88 to 0.92. The results of the GTNEUT and DEGAS predictions are shown in Figure 5.1, in which the five curves correspond to calculations of the Monte Carlo (labeled as DEGAS), GTNEUT with the DP_0 and local ion temperature (LIT) approximations (labeled as DP_0+LIT), GTNEUT with the local ion temperature and DP_1 approximations, as well as corrections to the spatial non-uniformity of collided neutral sources and angular fluxes (labeled as DP_1+Diffusion+Nonuniform+LIT), GTNEUT with the DP_0 and average neutral energy approximations (labeled as DP_0+ANE), and GTNEUT with the average neutral energy and DP_1 approximations, as well as corrections to the spatial non-uniformity of collided neutral sources and angular fluxes (labeled as DP_1+Diffusion+Nonuniform+ANE).

Since the neutral mean free path is longer than the characteristic grid dimension, the DP_0 approximation, as before, over-estimates neutral densities in cells away from the source. Since the neutral mean free path is also much longer than the characteristic ion temperature gradient length L, the neutral flux exiting across an interface consists predominantly of the uncollided neutrals from the adjacent regions, and therefore, the local ion

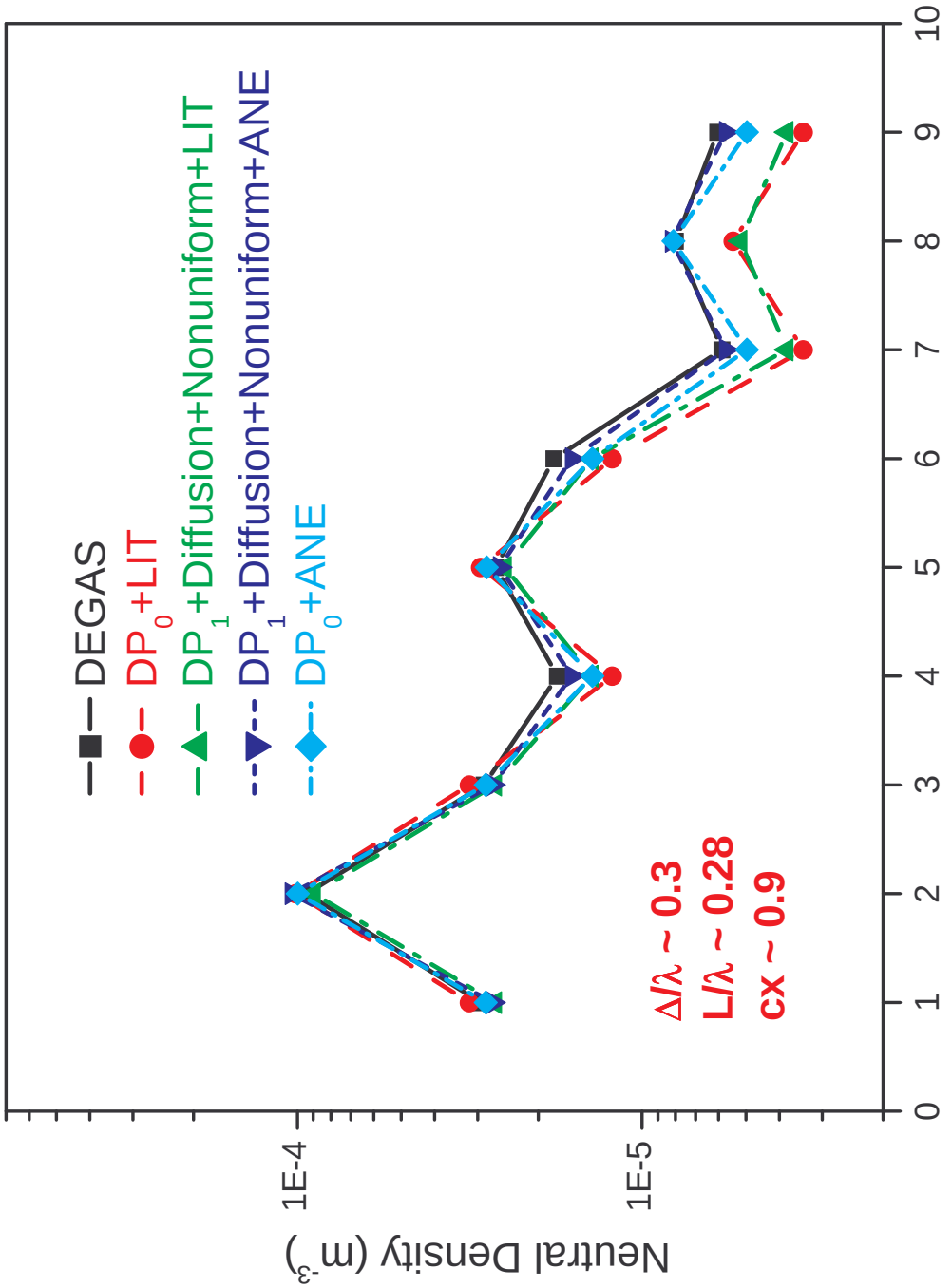

Figure 5.1. Effects of the neutral energy approximation in a 9-region problem with $cx \approx 0.88$ and $\Delta/\lambda \approx 0.33$

temperature approximation, by which the local ion temperature is assigned to uncollided neutrals, is a poor approximation. For instance, all neutrals from region 5 to region 8 are assigned 55 eV by the local ion temperature approximation, but in reality, most of neutrals are directly transmitted from region 2 with an energy of 10 eV. As a result, the local ion temperature approximation leads to a significant under-prediction of the neutral density in cell 8, since it over-estimates the neutral energy. The same thing is true for regions 7 and 9 as it can be easily seen from Figure 5.1. If the average neutral energy and the DP_1 approximations, as well as corrections to the non-uniformity of collided neutrals and angular fluxes, are made, the GTNEUT results agree very well with those predicted by Monte Carlo. By checking the results, it is found neutrals from region 5 to region 8 are assigned 25 eV, which is significantly lower than the local ion temperature in region 5. It also should be mentioned that the GTNEUT with the average neutral energy approximation converges after 2 or 3 iterations, where the convergence criterion is the maximum change of average neutral energies from the previous iteration is less than 1%.

In the second case, the ion temperature, electron temperature, ion density and electron density linearly vary from 10 eV, 6 eV, 1.7×10^{19} m^{-3} and 1.7×10^{19} m^{-3} in cells (Cells 1, 2 and 3) adjacent to the left boundary to 100 eV, 10 eV, 2.7×10^{19} m^{-3} and 2.7×10^{19} m^{-3} in cells (Cells 7, 8 and 9) adjacent to the right boundary, respectively. The resulting mean free path is about 0.09 m, and the charge exchange faction c_i is about 0.9. Figure 5.2 shows the comparison of results predicted by the DEGAS code and the GTNEUT code with the local ion temperature and average neutral energy approximations. Since the neutral mean free path is much shorter than the characteristic ion temperature gradient length, the local ion temperature assumption is found to be sufficient to represent the neutral energy dependence. It is clear that the calculations of GTNEUT with either the local ion temperature or average neutral energy approximation, in addition to the DP_1 approximation and corrections of directional escape probabilities, are in good agreement with the Monte Carlo simulations. GTNEUT with the average neutral energy approximation converges only after 1 iteration,

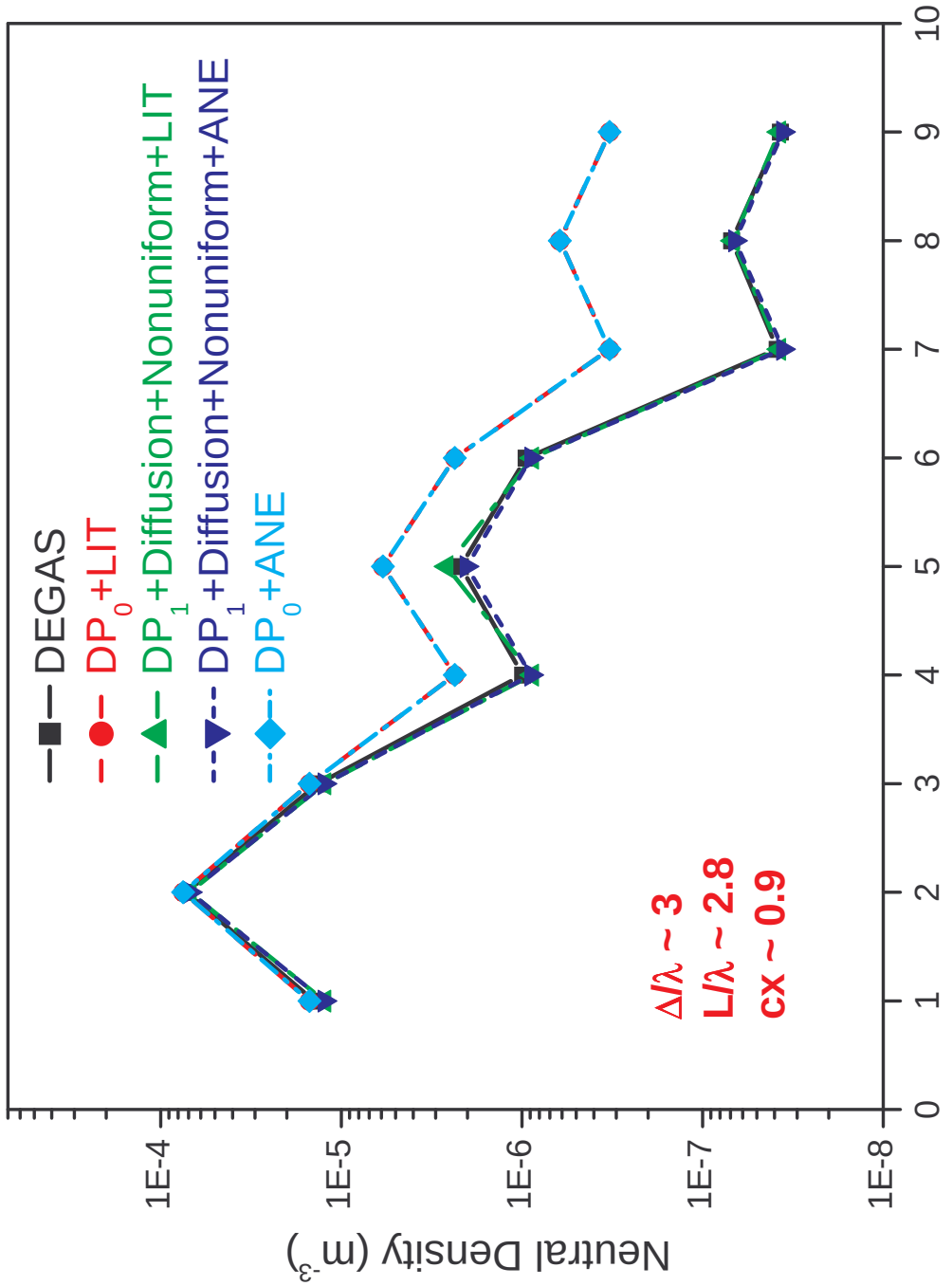

Figure 5.2. Effects of the neutral energy approximation in a 9-region problem with $cx \approx 0.9$ and $\Delta/\lambda \approx 3.0$

so it is essentially the same as the local ion temperature approximation.

In the next two cases, the ion temperature remains the same as in the previous two cases, and the other plasma properties are adjusted so that the charge exchange ratio varies from 0.52–0.72 and the ratio L/λ is equal to 0.28 and 1, respectively. The calculations of the DEGAS and GTNEUT codes are shown in Figures 5.3 and 5.4. As the previous two cases, if the neutral mean free path is longer than the characteristic ion temperature gradient length, big discrepancies between the DEGAS and GTNEUT predictions with the local ion temperature approximation are observed, but the average neutral energy approximation significantly improves the agreement with the Monte Carlo simulations. If the neutral mean free path is comparable with or shorter than the characteristic ion temperature gradient length, GTNEUT with either the local ion temperature or average neutral energy approximation agrees very well with DEGAS.

5.4 Transport in a 15×20 region model

In the previous section, a small 3×3 problem was used to test the accuracy of the average neutral energy approximation. To extend the test to large problems, the model considered in this section is a 2D rectangular problem, which extends from 0.0 to 0.9 m along the x direction and from 0.0 to 1.0 m along the y direction. The domain of interest is uniformly partitioned into 15×20 identical rectangular regions, in which the background plasma properties can be treated as constants. The cell arrangement is shown in Figure 5.5. Specular reflection boundaries are assumed at the four external interfaces. Two localized external neutral fluxes with a strength of 1×10^{22} s^{-1} is imposed at the right boundary of cells 290 and 291, respectively.

5.4.1 Problem with a uniform background plasma

In the first case considered, a uniform background plasma is assumed with $n_i = n_e = 6 \times 10^{19}$ m^{-3} and $T_i = T_e = 1000$ eV. The energy of the incident neutrals is also 1000 eV. As a result, the charge exchange fraction is 0.75 and the mean free path is 0.058 m, which

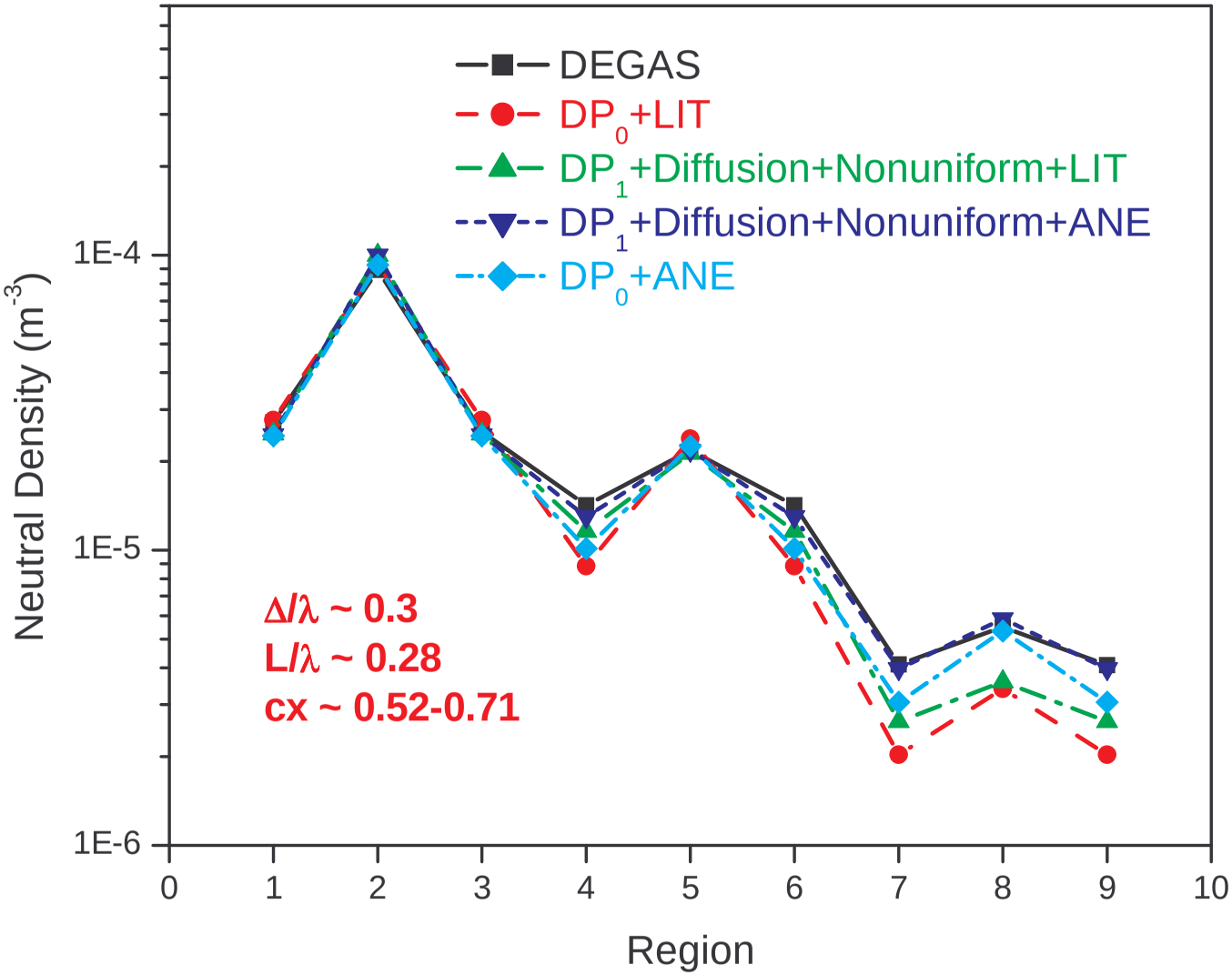

Figure 5.3. Effects of the neutral energy approximation in a 9-region problem with $cx \approx 0.52$ and $\Delta/\lambda \approx 0.33$

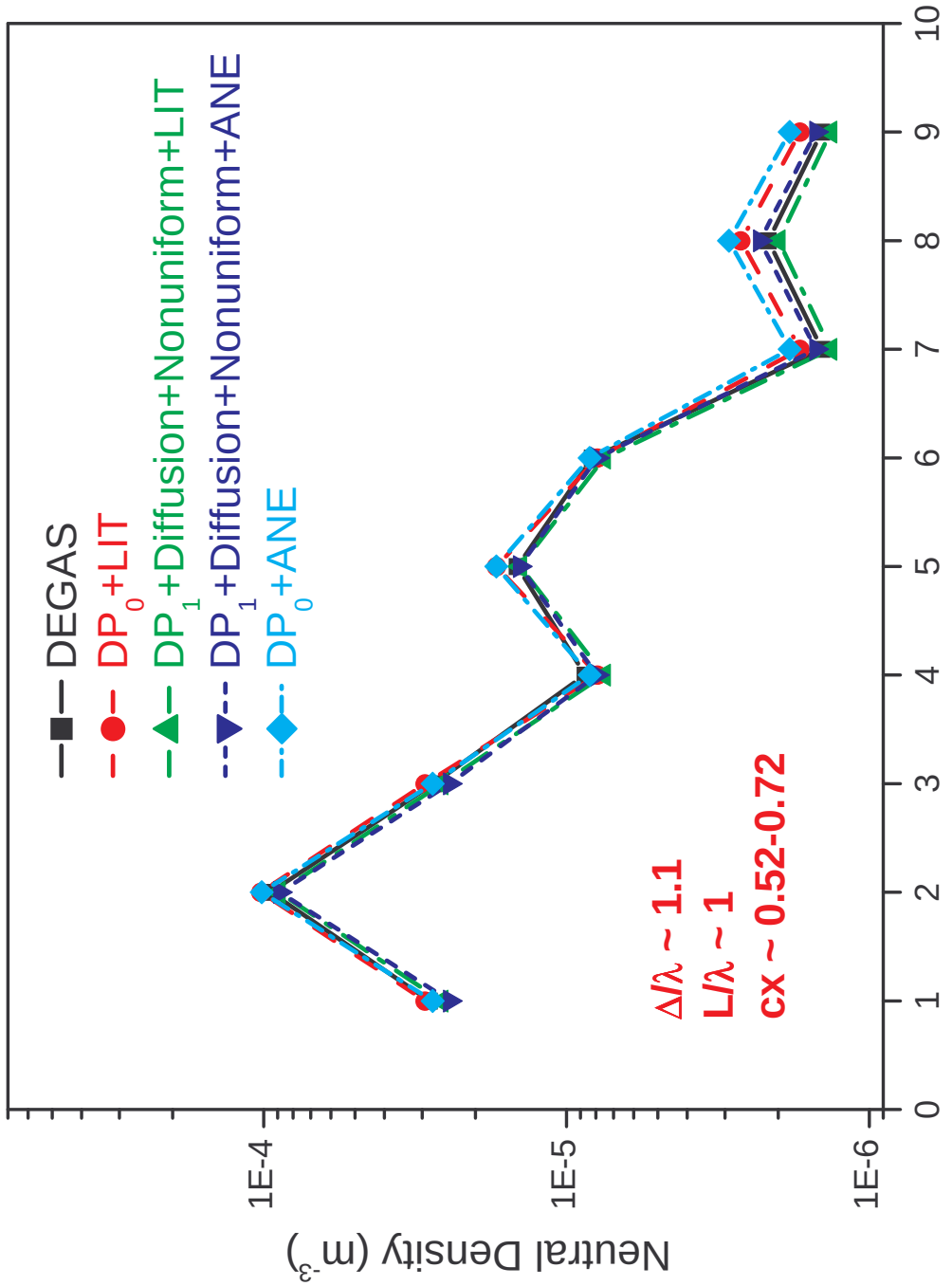

Figure 5.4. Effects of the neutral energy approximation in a 9-region problem with $cx = 0.52 - 0.72$ **and** $\Delta/\lambda \approx 3.0$

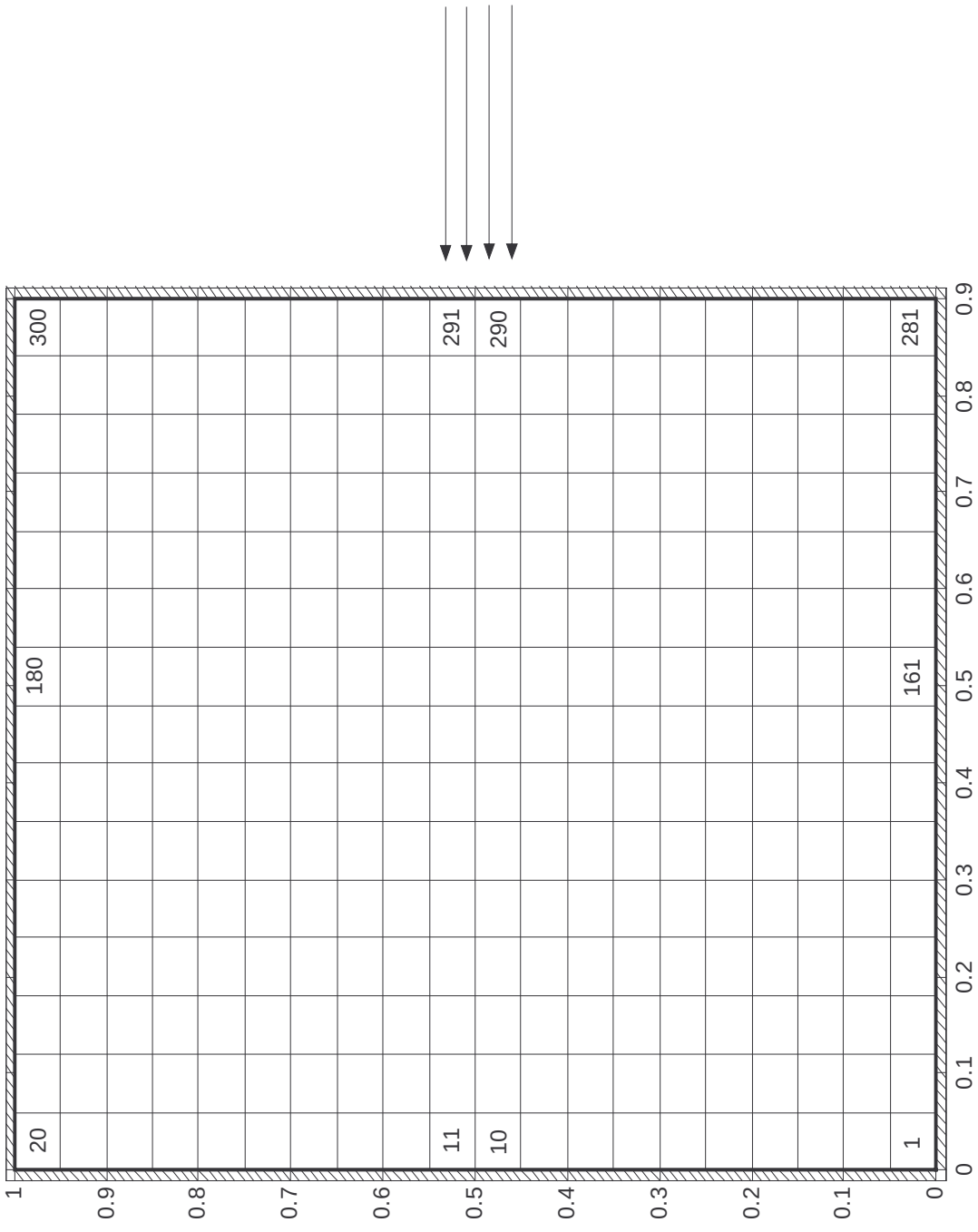

Figure 5.5. Geometry for the 15×20 **region model**

is comparable to the characteristic size of the computational regions. Since the background plasma is uniform (i.e. $L \rightarrow \infty$), the local ion temperature approximation is used in the GTNEUT code.

The contours of the neutral densities predicted by the Monte Carlo method and the TEP method with the different level approximations are shown in Figure 5.6. The DP_0 simulation (green dot) under-predicts neutral densities when we move away from the neutral sources, resulting from the underestimation of transmission probabilities introduced by the DP_0 assumption, though the trend is canceled to some extent by the over-estimation of directionalities introduced by the flat collision source approximation. The discrepancy between DP_0 and DEGAS increases as we move towards the left boundary. The DP_1 approximation takes into consideration the anisotropy of angular fluxes, leading to an error dominated by the over-prediction of directional escape probabilities. Therefore, it is expected that the DP_1 simulation (red dash) substantially over-predicts neutral densities for regions away from the sources. When the correction to directionalities is added, the GTNEUT simulation (cyan dot dash) still over-predicts results to some degrees, mainly because the non-uniformity of the angular flux at each interface is not taken into account. Finally when all the approximations (the DP_1 approximation, the correction to directionalities and the spatially linear approximation of angular fluxes) are turned on, the agreement between GTNEUT (blue short dash) and DEGAS (black solid) is excellent for the whole domain.

5.4.2 Problems with a non-uniform background plasma

In order to evaluate the two assumptions on the neutral energy dependence, three non-uniform 2D multi-region problems will be tested in this subsection. The geometric configuration shown in Figure 5.5 will be used by both the GTNEUT and DEGAS codes. Mirror boundary conditions are imposed on all the external surfaces. Two surface sources with the strength 1×10^{22} s^{-1} are located at the right boundary of cells 290 and 290, respectively. The details of the three non-uniform problems are listed as follows:

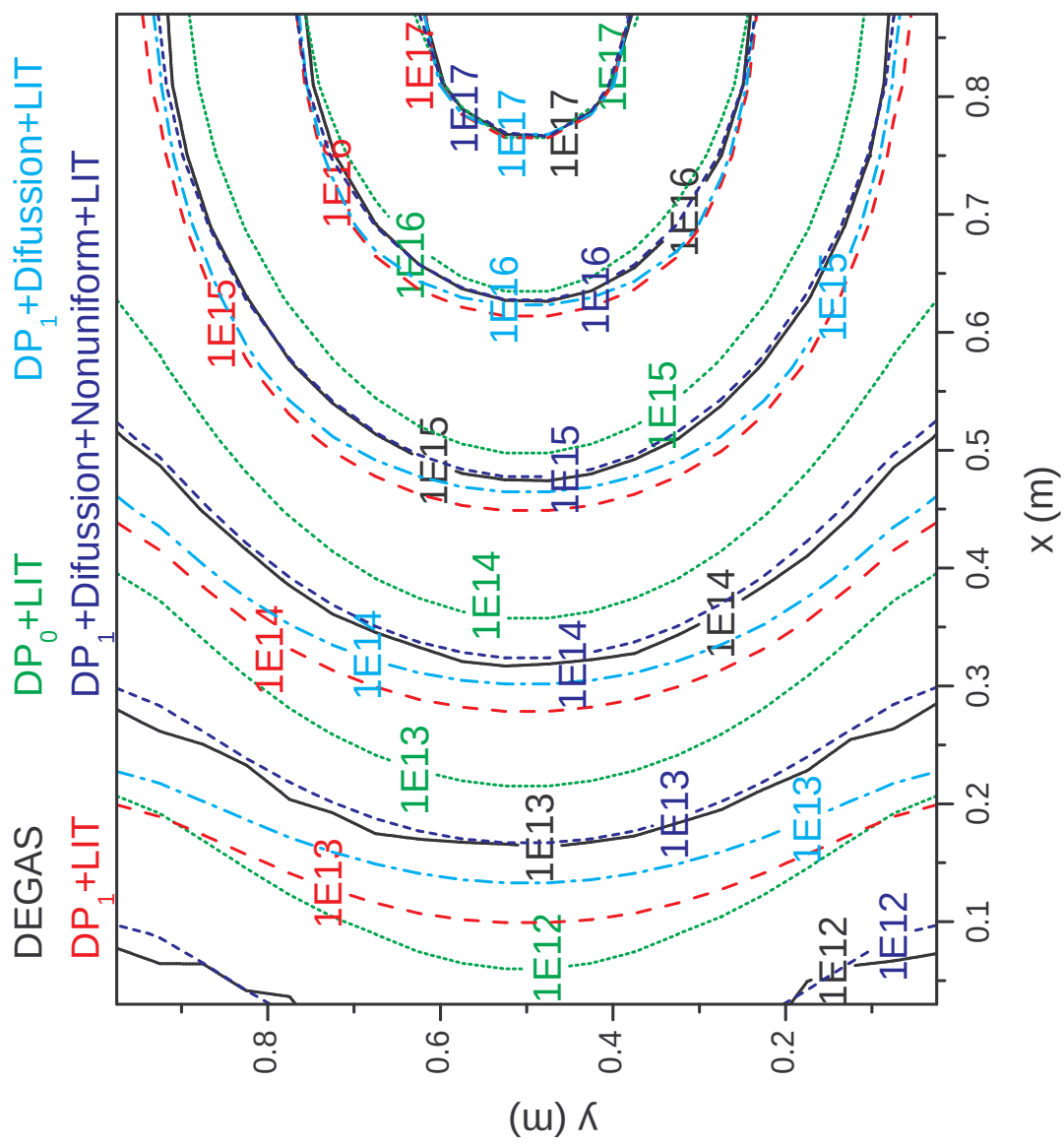

Figure 5.6. Contours of the neutral densities for the 15×20 region model with a uniform background plasma

1. In the first benchmark case, the plasma densities and temperatures are assume to vary as the following form,

$$n(x,y) = n_0 \exp\left[-\frac{(x-0.45)^2 + (y-0.5)^2}{r_0^2}\right], \tag{5.5}$$

$$T(x,y) = T_0 \exp\left[-\frac{(x-0.45)^2 + (y-0.5)^2}{r_0^2}\right], \tag{5.6}$$

where $n_0 = 10^{20}$ m^{-3}, $T_0 = 1$ keV and $r_0 = 0.5$ m.

The plasmas have the highest density and temperature at the center, and gradually decrease by about 60% when we move towards the boundaries, therefore, the neutral mean free path varies from 3.4 cm at the center to 9.2 cm at the four corners. The temperature of neutral sources is 493 eV.

2. In the second benchmark case, the background plasmas have a relatively strong gradient. Plasma densities and temperatures vary linearly as the following form,

$$T(i,j) = 100 + \frac{900}{14}(j-1) \quad \text{eV}, \tag{5.7}$$

$$n(i,j) = \left[1.0 + \frac{4}{14}(j-1)\right] \times 10^{19} \quad \text{m}^{-3}, \tag{5.8}$$

where i the row index from the bottom to the top, j is the column index from the left to the right.

The plasma temperatures vary linearly from 100 eV at the leftmost region, to 1000 eV on the rightmost region. The plasma densities have the lowest value 1×10^{19} m^{-3} at the left boundary, then linearly increase to 4×10^{19} m^{-3} at the right boundary. The neutral mean free path is in the range 7.8–14.3 cm, longer than the characteristic grid dimension. The energy of neutral sources is 1000 eV.

3. In the last case, the background plasmas have a very strong gradient. Plasma densities and temperatures vary exponentially as the following form,

$$T(i,j) = 400 \exp\left[-0.378(j-1)\right] \quad \text{eV}, \tag{5.9}$$

$$n(i, j) = 4.0 \exp\left[-0.099(j-1)\right] \times 10^{19} \quad \mathrm{m}^{-3}. \tag{5.10}$$

The plasma temperatures vary exponentially from 400 eV at the leftmost region, to 2 eV on the rightmost region. The plasma densities have the highest value 4×10^{19} m^{-3} at the left boundary, then exponentially decrease to 1×10^{19} m^{-3} at the right boundary. The neutral mean free path is in the range 5.0–14.1 cm, comparable or longer than the characteristic grid size.

To test the accuracy of various GTNEUT approximations, the above-described nonuniform problems are analyzed by the Monte Carlo code DEGAS, GTNEUT with the DP_0 approximation, the DP_1 approximation and the correction to the non-uniformity of collided neutral sources and neutral fluxes. The results of these simulations are shown in Figures 5.7–5.9.

Since in the first case the ion temperature varies slowly across the region, the results of the local ion temperature assumption with the corrections to the angular and spatial distribution of neutral fluxes and collision sources are in good agreement with the DEGAS calculations as shown in Figure 5.7. It is clear from Figure 5.7 that there is no obvious improvement to further implement the average neutral energy approximation and that the local ion temperature assumption is adequate for problems with a small gradient in the background ion temperature. However, the background plasmas in the last two cases are characterized by a strong gradient, large discrepancies between DEGAS and GTNEUT with the local ion temperature assumption are observed in Figures 5.8 and 5.9, since a wrong energy is assigned to uncollided neutrals. It can be seen from Figures 5.8 and 5.9 that the average neutral energy assumption significantly improves the agreement with DEGAS simulations, especially for optically thin regions with a background plasma characterized by steep gradients.

The CPU time required to carry out the simulations by the DEGAS code and the GTNEUT code with various approximations is illustrated in Figure 5.10, where all the calculations are performed on a SUN workstation (ULTRA-10, 360 MHz), and 5,000,000 particle

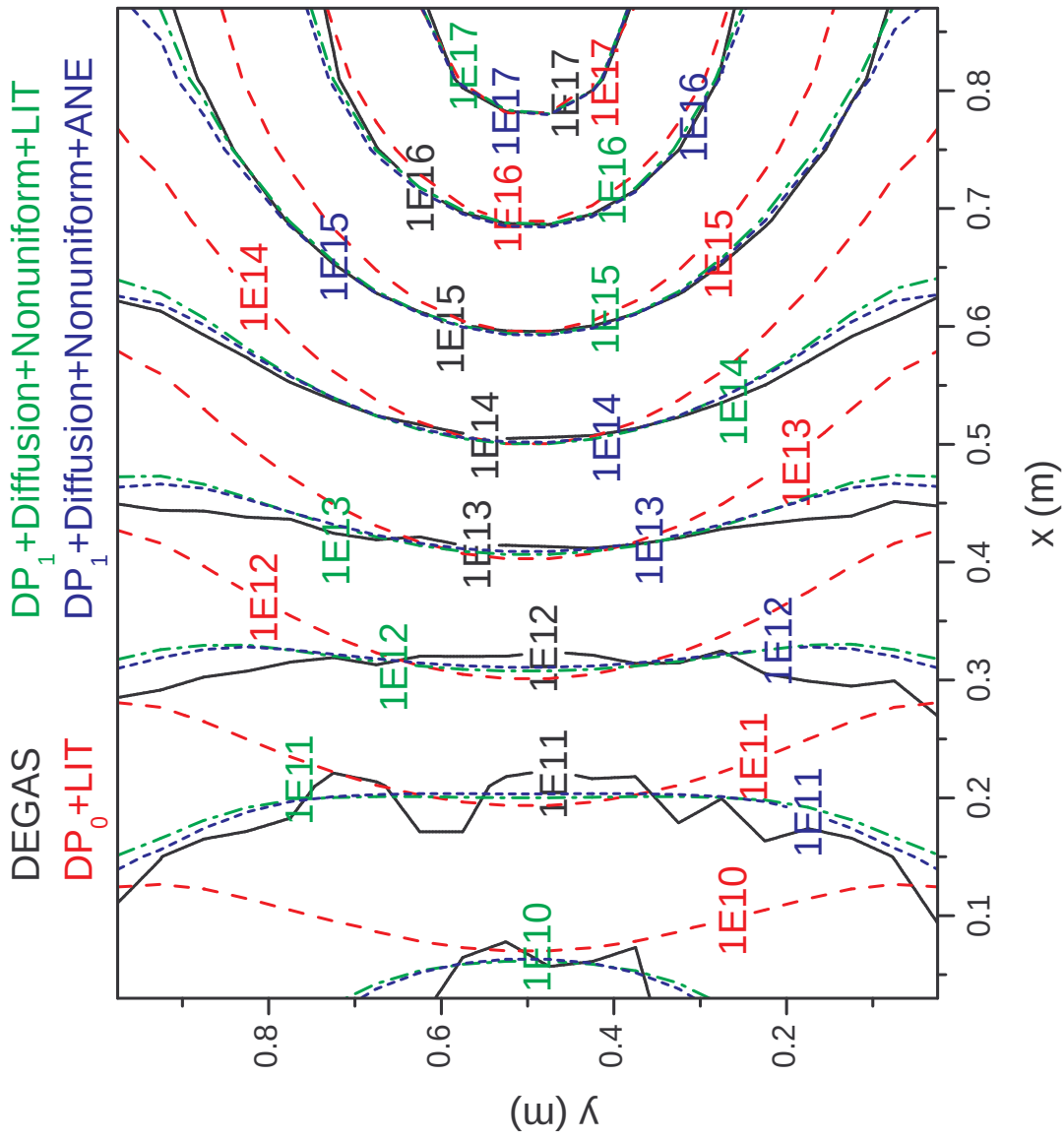

Figure 5.7. Contours of the neutral densities for the 15×20 region model with a gaussianly distributed background plasma

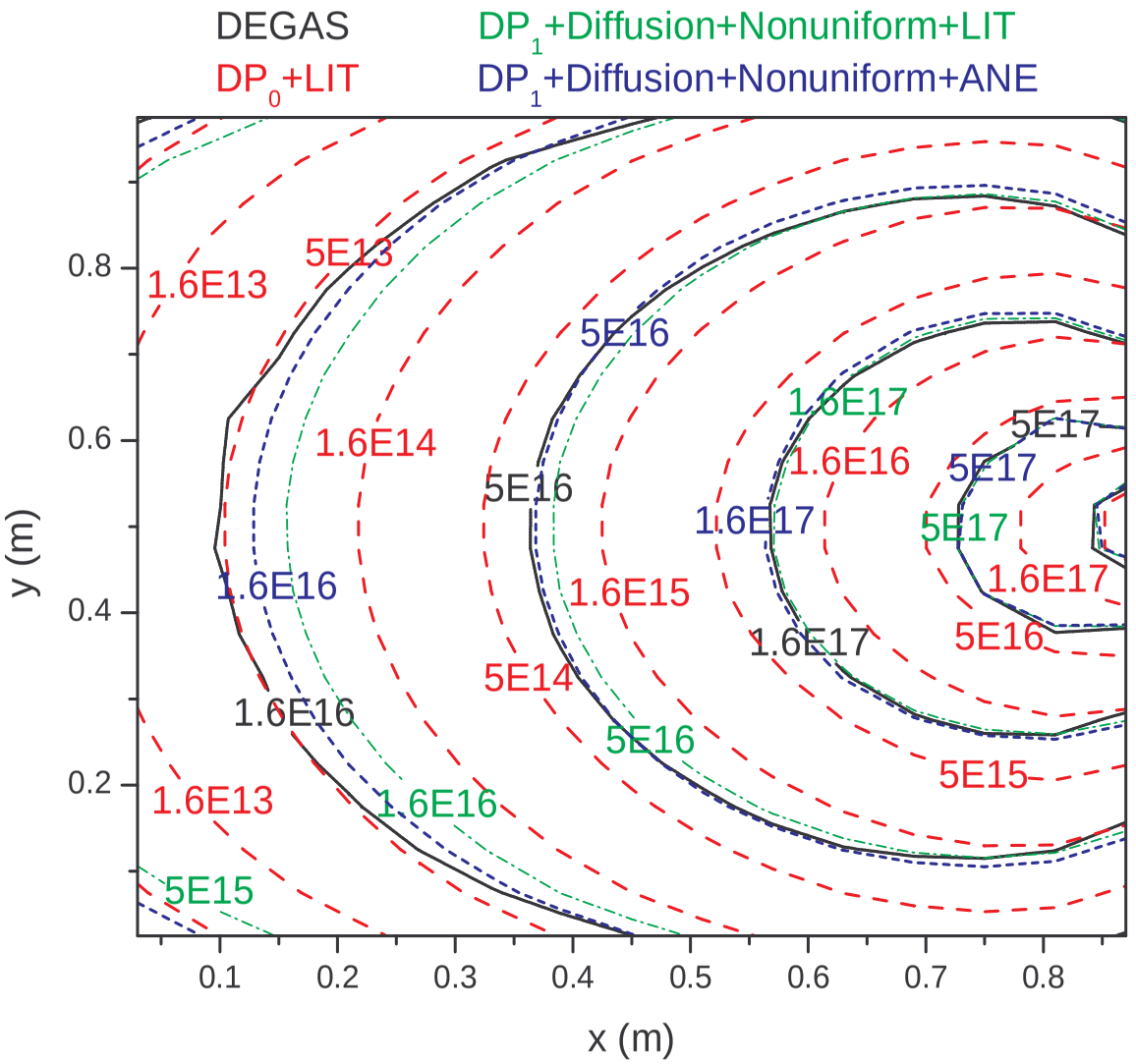

Figure 5.8. Contours of the neutral densities for the 15×20 **region model with a linearly distributed background plasma and long mean free path**

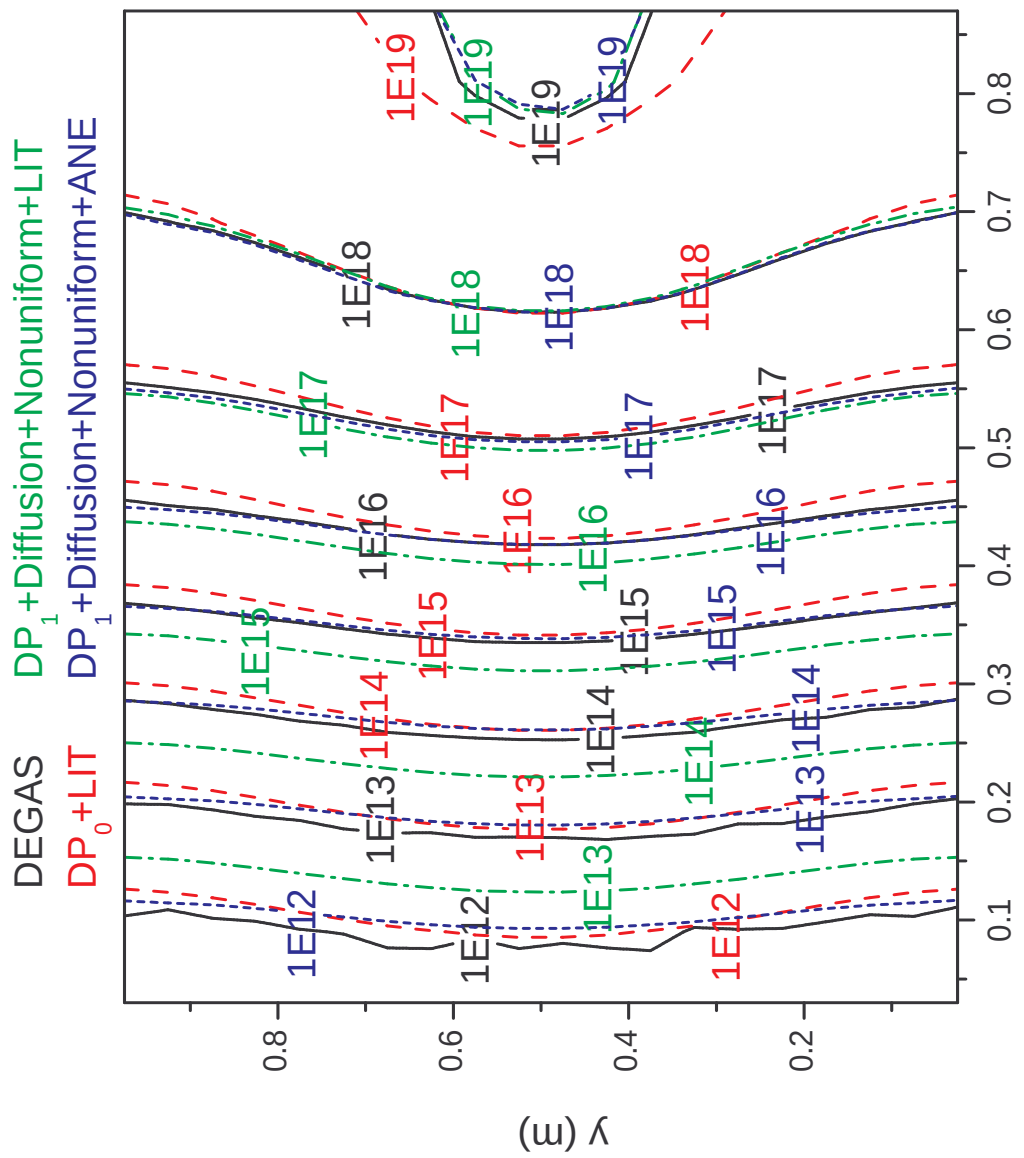

Figure 5.9. Contours of the neutral densities for the 15×20 region model with an exponentially distributed background plasma and short mean free path

histories were followed in DEGAS to reduce the maximum statistical error to less than 10 %. It is clear that GTNEUT with the DP_0 approximation is the fastest, and the DP_1 approximation will double the CPU time since more transmission probabilities are required to be numerically evaluated. The diffusion and spatially-linear angular flux approximations are computationally economic, therefore they will not obviously increase the CPU time. The average neutral approximation will triple the CPU time since three iterative steps are required to get converged results, but it is still three orders of magnitude faster than the Monte Carlo code DEGAS.

5.5 Conclusions

A more realistic approximation of the neutral energy dependence for optically thin regions, the average neutral energy approximation, has been developed and implemented into the GTNEUT code. Essentially, this approximation calculates the average energy of the neutrals in a region as a weighted average of the average energies of neutrals entering the region from contiguous regions and the average energies (the local ion temperature) of neutrals charge-exchanging in the region.

The Monte Carlo and GTNEUT comparisons have indicated that the average neutral energy approximation improves the accuracy of the TEP method significantly in optically thin regions when background plasmas are characterized by strong ion temperature gradients.

Finally, the tests have also shown the energy of neutrals can be sufficiently described by the local ion temperature approximation if the neutral mean free path is comparable with or shorter than the characteristic ion temperature gradient length.

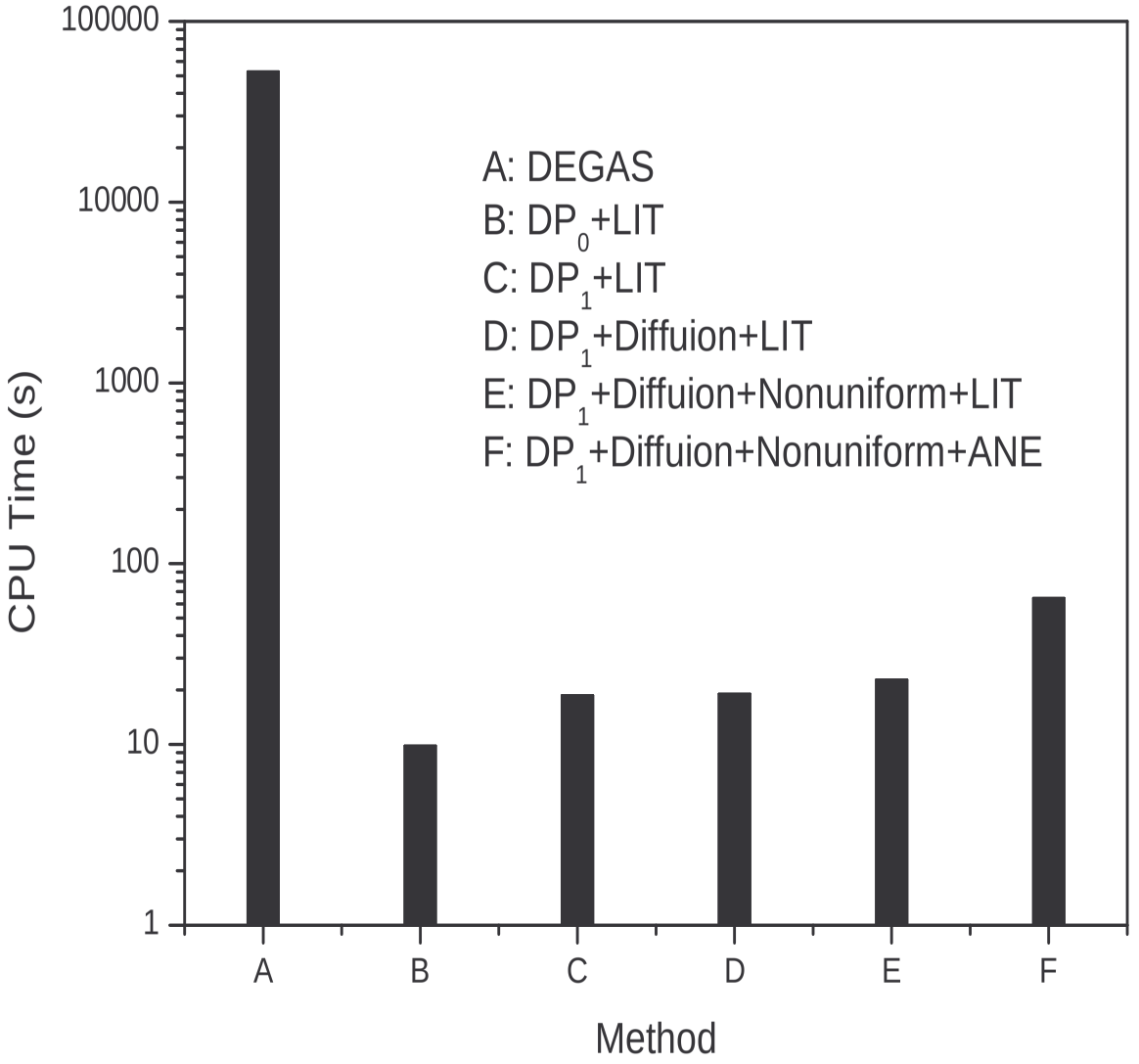

Figure 5.10. Comparison of the CPU time for the 15×20 region model with an exponentially distributed background plasma and short mean free path (unit: s)

CHAPTER 6

TEST OF THE IMPROVED TEP METHOD FOR REALISTIC DIII-D CONFIGURATIONS

6.1 Introduction

The accuracy of the improved TEP method has been studied in the previous chapter, where 2D multi-region problems with nonuniform background plasmas were used to carry out benchmark simulations with Monte Carlo. The objective of this chapter is to compare the calculations of the upgraded GTNEUT code with DEGAS predictions for realistic tokamak configurations, as well as with the experimental measurements of neutral densities.

The neutral densities in the divertor of the DIII-D tokamak have been measured in both L mode and H mode plasmas [35]. In the experiment, the D_α light emission from the lower divertor was recorded by a tangentially viewing charge injection device (CID) television camera. The plasma properties such as temperature and density near the X-point were measured by a divertor Thomson scattering system (DTS). Two photomultipliers (PMT) were used to calibrate the tangential TV system. The neutral densities were then obtain by the relation

$$I_{D_\alpha} = n_e n_0 \langle \sigma(T_e, n_e) v_e \rangle_{exc}. \tag{6.1}$$

where I_{D_α} is the intensity of the D_α light emission measured by the tangential TV, $\langle \sigma(T_e, n_e) v_e \rangle_{exc}$ is the electron excitation rate and n_e is the electron density measured by the DTS.

The comparison with the experimental measurements for the DIII-D L mode or H mode have been previously conducted by R. Rubilar et al [25] and J. Mandrekas et al [26]. In the former paper, the neutral densities of the DIII-D L mode discharge predicted by the GTNEUT code with mirror boundaries were in the good agreement with the calculations of the DEGAS code, as well as the experimental measurements in the vicinity of the X-point. The comparisons also identified several approximations in the original TEP methodology limiting the further improvement of the agreement with Monte Carlo simulations: 1) lack

of a realistic wall reflection model, 2) the local ion temperature assumption, 3) the DP_0 assumption, 4) the flat collision source assumption or the non-directional approximation. In the latter paper, a realistic wall reflection model and a two-group treatment of the neutral energy dependence were implemented to improve the accuracy of the TEP methodology. The calculated neutral densities were in excellent agreement with the DEGAS simulations for the DIII-D L mode discharge, but the agreement for the DIII-D H mode discharge was not good. The simulations also indicated that, in addition to the assumptions of the angular distribution at each interface and the spatial distribution of collision sources within each computational region , the treatment of the neutral energy dependence also plays a very important role in the accuracy of the TEP methodology.

In this chapter, the L mode and H mode discharges will be calculated by both the Monte carlo code and the GTNEUT code, taking into account the anisotropy of the angular flux, the non-uniformity of collision sources and a more reasonable treatment of the neutral energy dependence. The comparisons will be based on the same 2D geometry and the same atomic rate data.

6.2 DIII-D L mode

6.2.1 Problem description

The geometric model for the L mode DIII-D discharge 96740 at 2250 ms is shown in Figure 6.1. The X-point height above the divertor floor is 13.8 cm. The domain of interest is divided into 182 cells to match the local geometry. The shaded regions in Figure 6.1 represents the location where the neutral densities were measured, their heights from the divertor floor and region index are listed in Table 6.1. Cells 133–136 are located at the private flux region, Cells 61–63 and 124–125 are located above the X-point.

The problem is bounded by carbon walls, with no wall absorption. The background plasma data was computed by the fluid plasma code B2.5 [36]. Recycling neutral sources emerge at the bottom boundary of regions 1–10 and 172–181. Plasma densities and temperature vary from 3.1×10^{17} to 3.4×10^{19} m^{-3} and from 2.3 to 180 eV, respectively. The typical

Table 6.1. Region index and height off the divertor floor for the measurement locations in the L mode DIII-D discharge 97640 at 2250 ms

Regions	Height off the divertor floor (cm)
136	5.2
135	6.5
134	8.6
133	11.3
61, 124	17.4
62, 125	20.8
63	22.8

neutral mean free path and the charge exchange fraction are in the range of 0.035–4.5 m and 0.52–1, respectively.

6.2.2 Results and discussion

Since molecule transport is not included in the current version of the GTNEUT code, it is assumed that neutral molecules, released after the thermal equilibrium with wall materials, are immediately broken up as Frank-Condon atoms with an energy of a few electronvolts. DEGAS is aslo run without the molecule transport. The energy of puffing and desorbed neutral atoms is assumed to be 3 eV, same as the GTNEUT reflection model.

To investigate the impact of the nonuniform plasma temperature on the accuracy of the TEP method, GTNEUT will be run for the following three cases: 1) the DIII-D L mode with a uniform ion temperature, 2) the DIII-D L mode with the original nonuniform ion temperature and GTNEUT with the local ion temperature assumption, and 3) the DIII-D L mode with the original nonuniform ion temperature and GTNEUT with the average neutral temperature approximaiton.

6.2.2.1 DIII-D L mode with uniform ion temperature

In the first case, to exclude the error produced by the neutral energy treatment, it is assumed the plasma ion has a uniform temperature of 10 eV but the other plasma properties remain the same as the original background plasma. The neutral densities vs the height above the

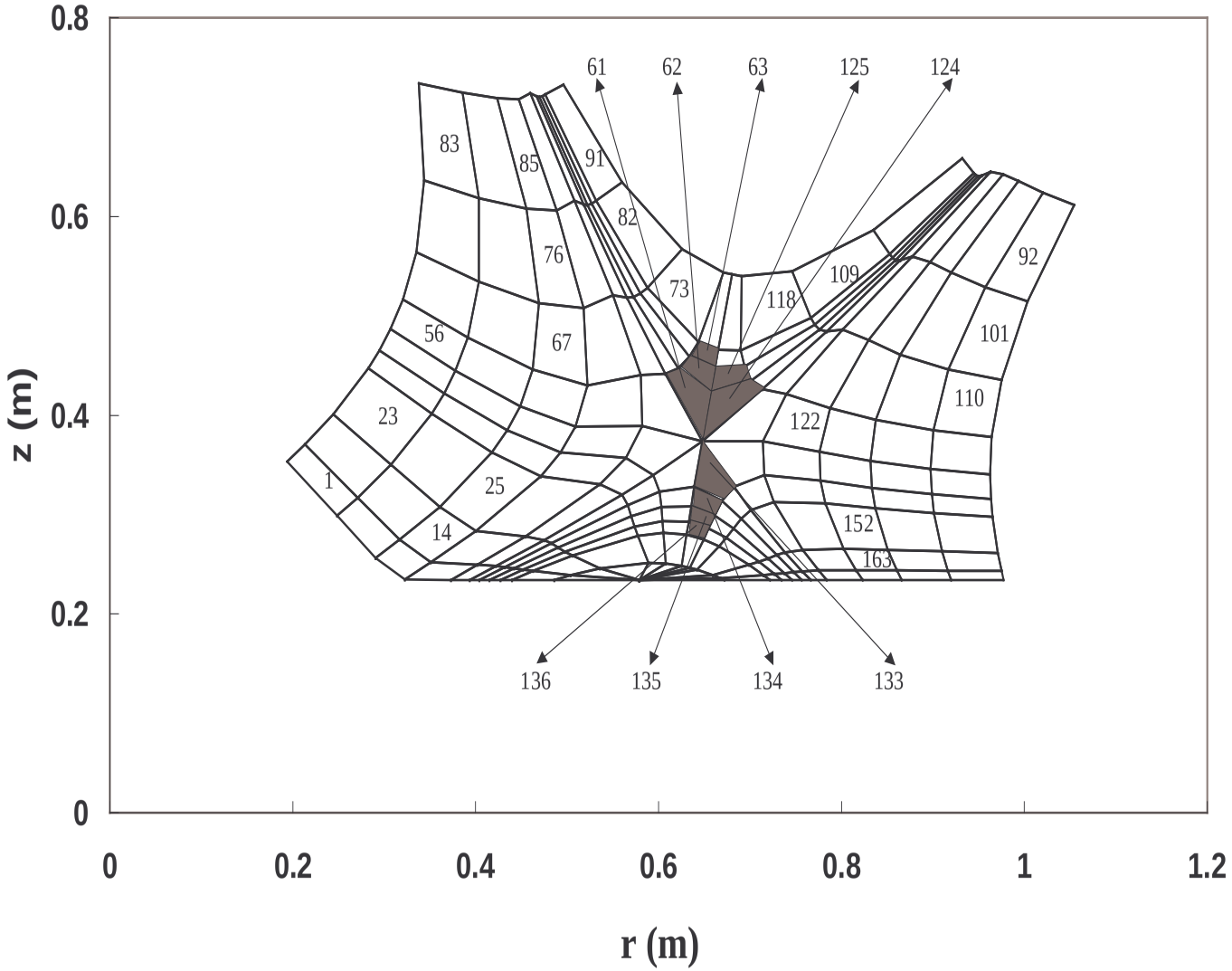

Figure 6.1. Geometric model for the analysis of the DIII-D L mode discharge 97640 at 2250 ms

divertor floor are shown in Figure 6.2, where the four curves corresponds to the calculations of DEGAS without molecules, GTNEUT with the DP_0 approximation, the DP_1 approximation and with both the DP_1 approximation and the diffusive correction to nonuniform collided neutral sources. It can be seen that the DP_0 approximation under-predicts neutral densities approximately by a factor of two. The difference is due to the under-estimation of the transmission of uncollided fluxes by the DP_0 approximation. Taking the anisotropy of angular fluxes into account, the DP_1 approximation agrees very well with DEGAS both above and below the X-point. However, the correction to the non-uniformity of collided neutrals makes no obvious difference for all the regions. This is expected since the neutral mean free path is much larger than the grid size for all the regions. Similar results are also observed if we vary the plasma ion temperature form 2 to 400 eV.

6.2.2.2 Calculations of GTNEUT with the local ion temperature assumption

In the second run, the original non-uniform background plasma properties are used by both DEGAS and GTNEUT. The local ion temperature assumption is made in the GTNEUT simulations. The neutral densities versus the heights above the divertor floor predicted by DEGAS and GTNEUT with various assumptions, as well as the experimental measurements with error bars, are shown in Figure 6.3.

A quick examination of Figure 6.3 indicates that the GTNEUT code with the DP_0 approximation agrees very well with the DEGAS simulations without molecule transport in the private flux region, but a up to 40% overestimation of neutral densities by the GTNEUT code with the DP_0 approximation is observed in the main plasma region. These calculations agree with the experimental measurements within error bars. On the contrary, the GTNEUT code with higher approximations (the DP_1 approximation or the correction of non-uniform collided neutral sources) under-predicts results by 30–300% compared to the Monte Carlo calculations, but there is no obvious difference between the calculations of GTNEUT with and without the correction to non-uniform charge-exchanged neutrals. The

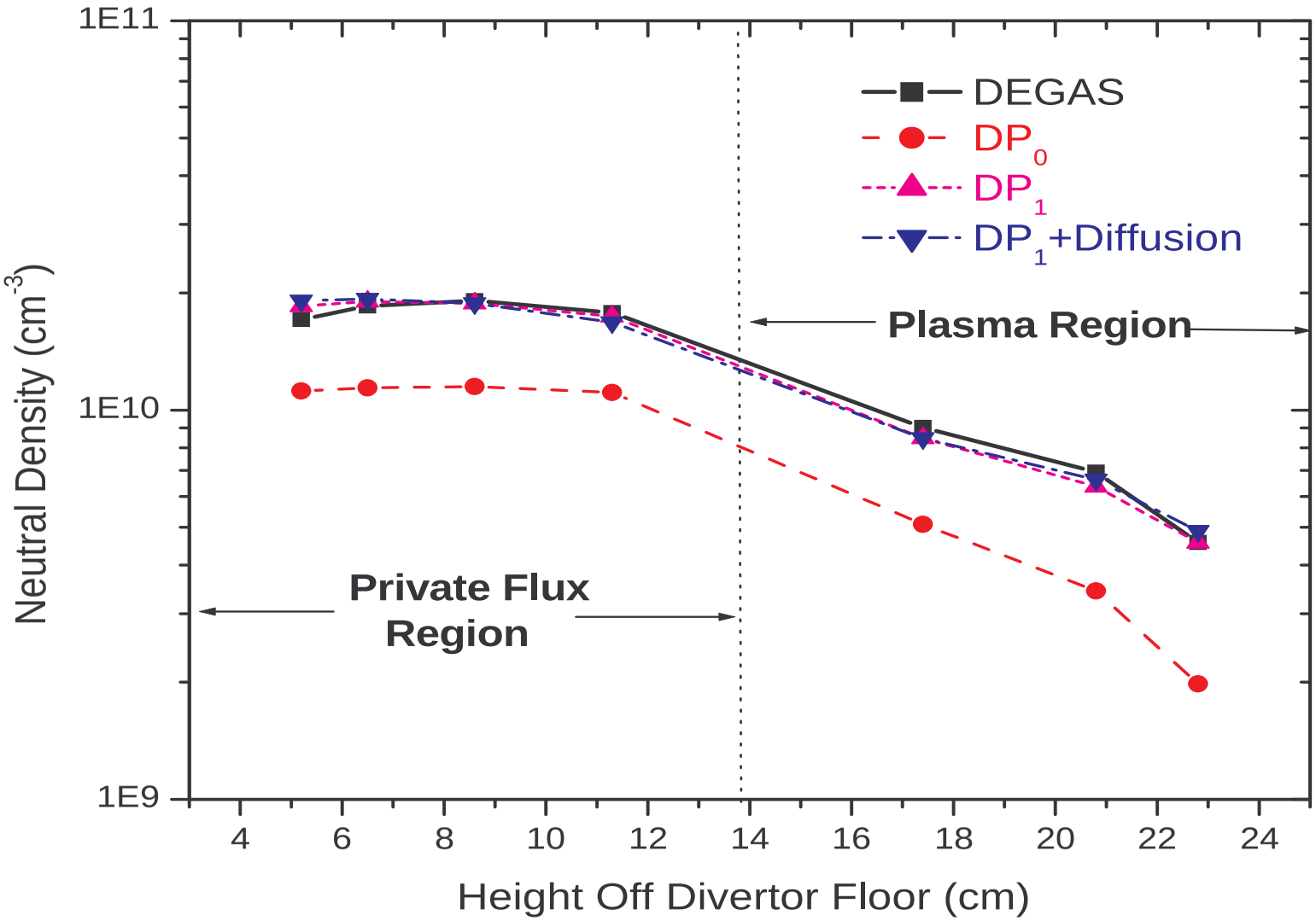

Figure 6.2. Comparison of GTNEUT and DEGAS simulations for the analysis of the DIII-D L mode discharge 97640 at 2250 ms with the uniform background ion temperature

disagreement of the GTNEUT predictions with the higher approximations is due to the local ion temperature approximation, which is not valid for optically thin regions. In such a situation the neutral mean free path is much larger than the characteristic dimension for each computational region, and it is also found that the uncollided flux is about an order of magnitude higher than the collided flux at each interface. As a result, a significant portion of neutrals in the shaded regions is directly transmitted from the divertor floor with an energy of a few electronvolts, while the energies of these particles are assumed to be the plasma ion temperatures in the contiguous regions, some of which are quite different from their real energies. Taking region 136 as an example, the neutrals entering from regions 53, 135, 137 and 147, based on the local ion temperature assumption, are assigned an energy of 3.6, 11.7, 2.3 and 15.5 eV, respectively. However, the majority of neutral population from regions 53, 135 and 147 is transmitted from the divertor with an energy of 2 eV. Consequently the local ion temperature assumption leads to a under-prediction of the neutral density by GTNEUT with the DP_1 approximation for region 136. The same thing is true for the other regions. If the DP_0 approximation is made, on the one hand, GTNEUT under-estimates the neutral fluxes from region 53 to region 136 and from region 247 to region 136 due to the under-prediction of transmission probabilities across a region; on the other hand, because DP_0 assumes more particles move in large angles, GTNEUT over-predicts the neutral flux entering from region 53, whose local ion temperature is very close to the real neutral energy. Consequently, the good agreement of the DP_0 results from a coincidental cancelation between the two errors. It should be pointed out that no obvious difference between GTNEUT with and without the correction to directionalities is expected for optically thin regions, where the non-uniformity of collided neutral sources can be safely ignored.

6.2.2.3 Calculations of GTNEUT with the average neutral energy assumption

In the last run, the original nonuniform background plasmas are used by both the DEGAS and GTNEUT codes. In order to take into account the neutral energy effects, the average

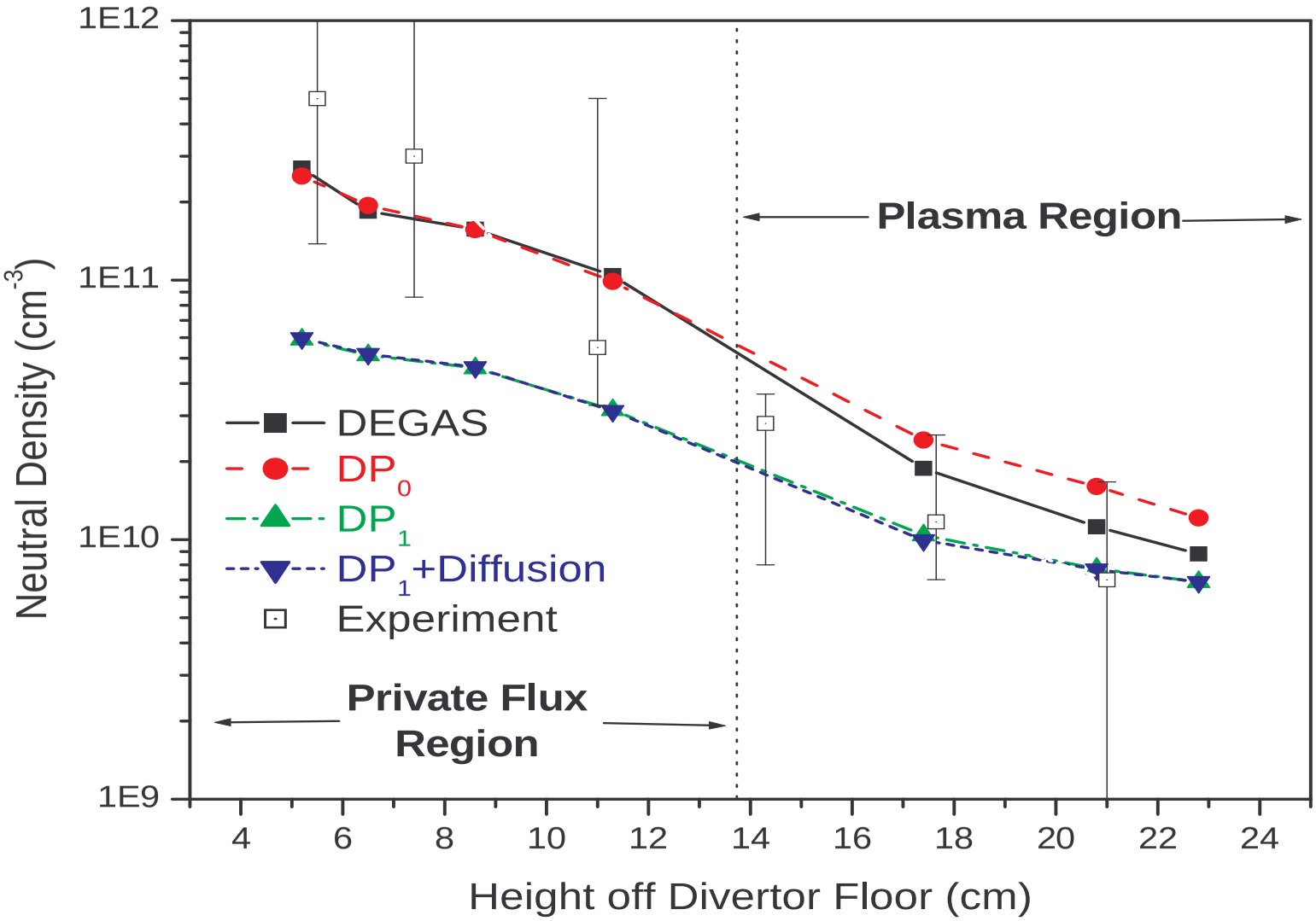

Figure 6.3. Comparison of GTNEUT with the local ion temperature assumption and DEGAS simulations for the analysis of the DIII-D L mode discharge 97640 at 2250 ms with the original nonuniform background ion temperature

Table 6.2. Comparison of the energy assigned to neutrals entering into region 136 by the two approximations for the L mode DIII-D discharge 97640 at 2250 ms (unit: eV)

Approximation	LIT	ANE
Region 53 to region 136	3.6	3.5
Region 135 to region 136	11.7	5.8
Region 137 to region 136	2.3	2.7
Region 147 to region 136	15.5	4.0

neutral energy assumption is made in GTNEUT. Since the neutral flux from an optically thin region predominately consists of uncollided neutrals, GTNEUT with the average neutral energy assumption generally converges in 2 or 3 iterations.

The results of DEGAS and GTNEUT with a variety of approximations, as well as the experimental measurements with error bars, are shown in Figure 6.4. DP_0 agrees very well with DEGAS without molecule effects in the private flux region, but it under-predicts results by 30–40% in the main plasma region. It can be seen that the agreement between the DP_1 approximation and DEGAS without molecule transport is excellent for the entire domain. As before there is no further advantage to correct directionalities for the fine-mesh DIII-D L mode discharge. The comparison of the energy assigned to neutrals entering into region 136 by the two assumptions is shown in Table 6.2, from which it can be seen that the local ion temperature assumption substantially overestimates the energy of neutrals from regions 135 and 147 to region 136. A more detailed comparison of the results predicted by DEGAS without molecule transport and GTNEUT with the DP_1 and average neutral energy approximations is presented in Figure 6.5. The comparison indicates the agreement between DEGAS and GTNEUT is very good in all but a few regions near the upper-left corner, where GTNEUT slightly over-predicts the neutral density. The discrepancy is mainly due to albedo boundaries assumed by GTNEUT, in contrast DEGAS treats these regions as a part of the SOL. The neutral density achieves its maximum value near the divertor floor, where neutral gases are recycled, then gradually decreases by several orders of magnitude when we move toward the main plasma region.

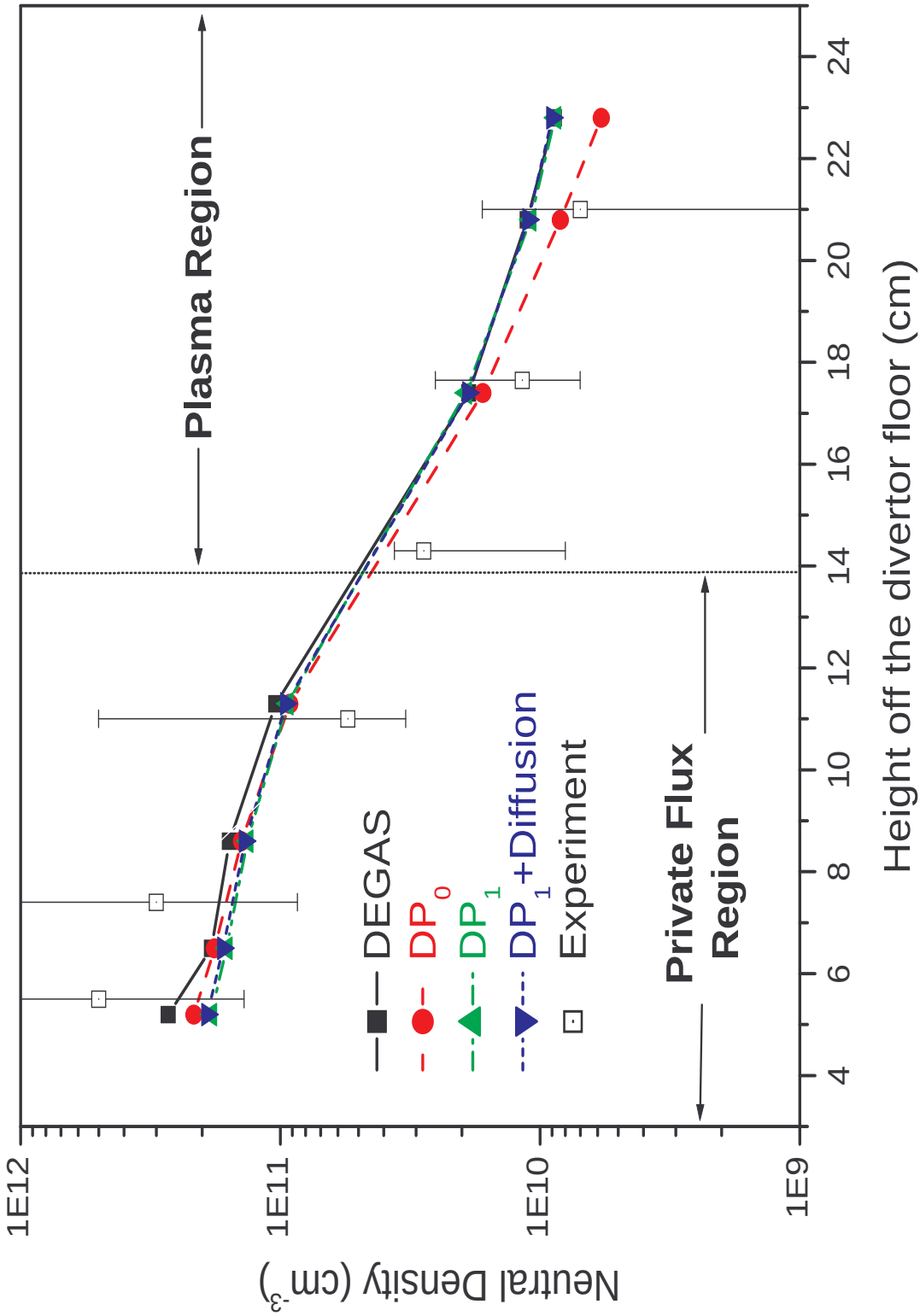

Figure 6.4. Comparison of GTNEUT with the average neutral energy assumption and DEGAS simulations for the analysis of the DIII-D L mode discharge 97640 at 2250 ms with the original nonuniform background ion temperature

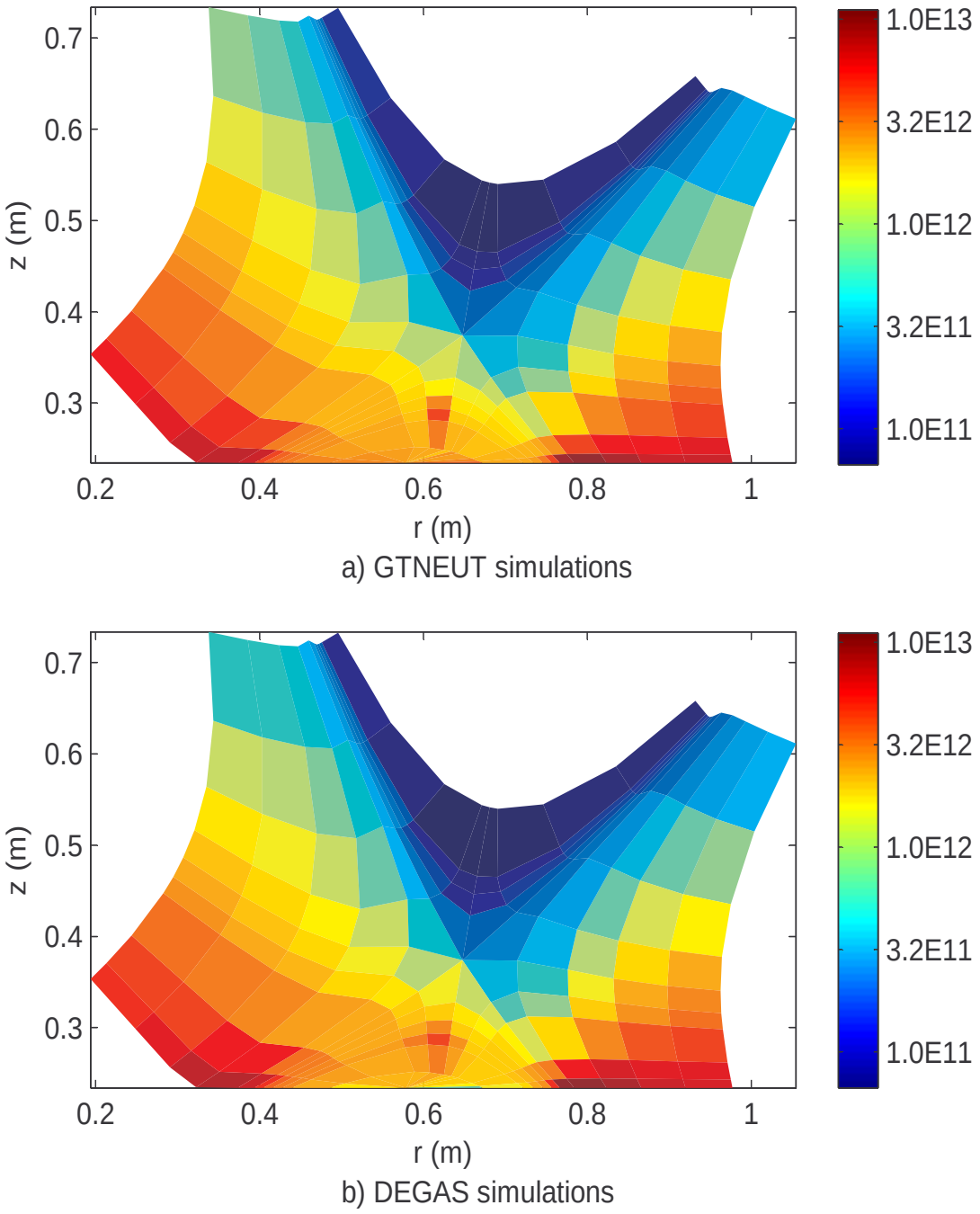

Figure 6.5. Comparison of GTNEUT with the average neutral energy assumption and DEGAS simulations for the analysis of the DIII-D L mode discharge 97640 at 2250 ms with the original nonuniform background ion temperature

Table 6.3. Region index and height off the divertor floor for the measurement locations in the H mode DIII-D discharge 96747 at 3940 ms

Regions	Height off the divertor floor (cm)
38,156	4.2
37,155	5.2
35,36,153,154	8.5
49,50,140,141	14.8
51, 142	18.9
52	21.9

6.3 DIII-D H mode

6.3.1 Problem description

The geometric model for the H mode DIII-D discharge 96747 at 3940 ms is shown in Figure 6.6. In this case the X-point is located 10.6 cm above the divertor floor. The problem consists of 188 regions. The shaded regions in Figure 6.6 represents the location where the neutral densities were measured, their heights from the divertor floor and region index are listed in Table 6.3. Cells 35–38 and 153–156 are located at the private flux region, Cells 49–52 and 140–142 are located above the X-point.

Carbon is assumed as the wall material. The external neutral sources emerge at the bottom boundary of regions 1–14 and 175–188. Both the background plasma densities and temperatures are higher than those in the L Mode discharge. For instance, the electron temperature varies from 3.8 to 59 eV in the private flux region and from 100 to 430 eV inside the separatrix, and ion temperature is in the range 57–218 eV in the private flux region and in the range 120–600 eV in the main plasma region, respectively. As a consequence, the neutral mean free path varies from 0.7 m to 26 m outside the separatrix and from 0.06 m to 0.5 m in the plasma region, much longer than the grid size for regions both outside and inside the separatrix.

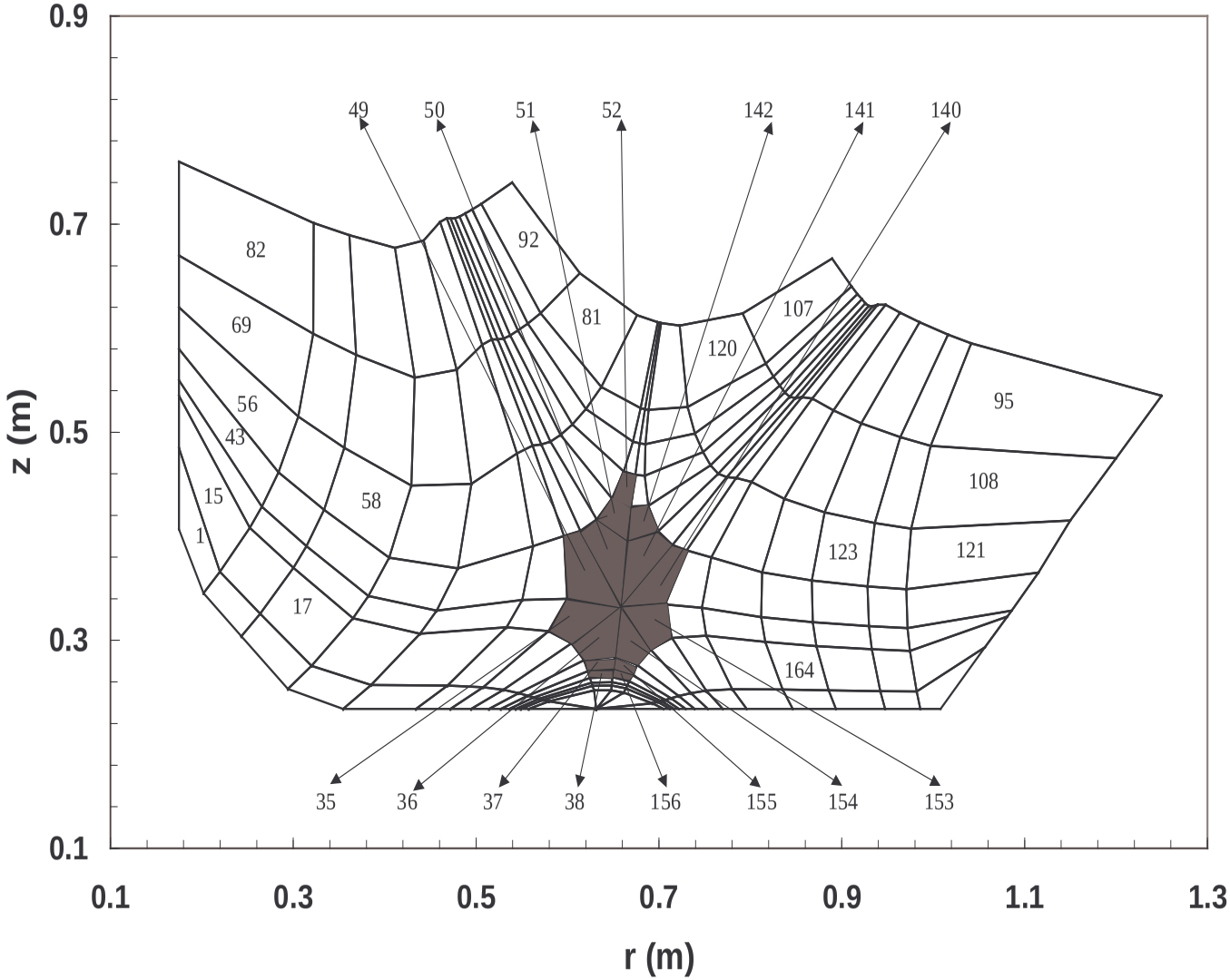

Figure 6.6. Geometric model for the analysis of the DIII-D H mode discharge 96747 at 3940 ms

6.3.2 Results and discussion

As in the L mode discharge, the DEGAS code is run without molecule transport. All the molecules recycled and desorbed from wall segments are assumed to be dissociated as Frank-Condon atoms with an energy 3 eV at the plasma-wall interface. Again, three cases of the energy dependence, a uniform plasma ion temperature, a nonuniform plasma ion temperature and GTNEUT with the local ion temperature or average neutral energy approximation, are investigated to compare the DEGAS and GTNEUT calculations.

In the first case, the background plasma is assumed to have a uniform ion temperature 10 eV, while other properties remain the same as the original plasma. Neutral densities calculated by DEGAS without molecule transport and GTNEUT with different level approximations are illustrated in Figure 6.7, from which it can be seen that the DP_0 approximation leads to the underestimation of neutral densities, especially in the main plasma region. The higher order angular approximation DP_1 either with or without the correction to directionalities significantly improves the agreement with the DEGAS simulations.

In the second run, the original nonuniform background plasmas are used by both the DEGAS and GTNEUT codes. The local ion temperature (LIT) approximation is assumed in GTNEUT. A series of comparisons of the various GTNEUT simulations with the DEGAS results are shown in Figure 6.8, where the experimental results are also presented. DEGAS with molecule transport under-predicts neutral densities in the private flux region, mainly due to the error of background plasma properties calculated in the B2.5 code. Our simulations have shown neutral densities in the private flux region are very sensitive to the background ion temperature. In reality, the local ion temperature approximation used by GTNEUT cannot correctly represent the neutral energy dependence in optically thin regions, since the approximation is based on the assumption that the majority of neutrals have at least one collision with the background ions in each computational region. This is the reason that a large discrepancy between DEGAS without molecule transport and GTNEUT with either the DP_0 or DP_1 approximation is observed in Figure 6.8.

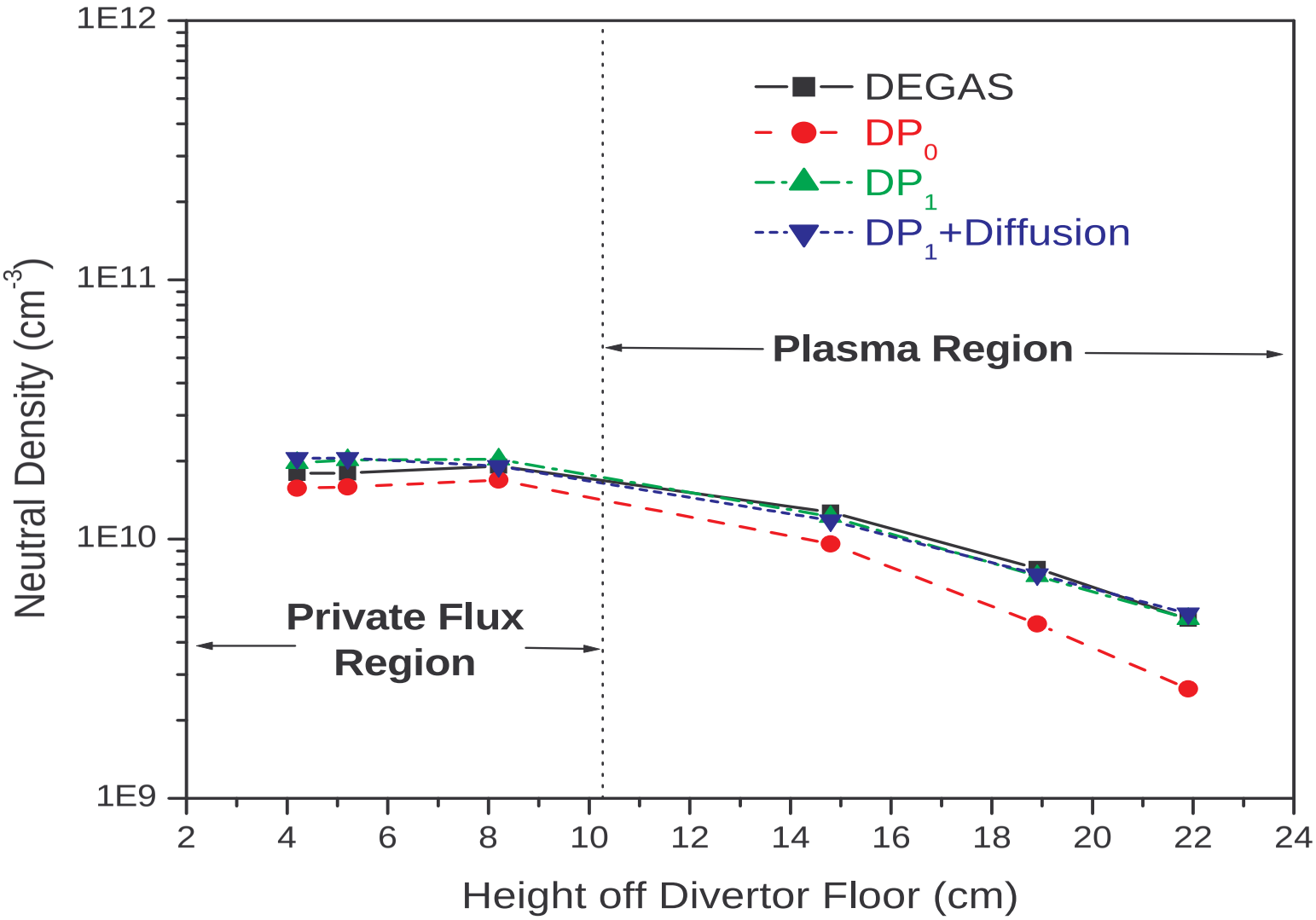

Figure 6.7. Comparison of GTNEUT and DEGAS simulations for the analysis of the DIII-D H mode discharge 96747 at 3940 ms with the uniform background ion temperature

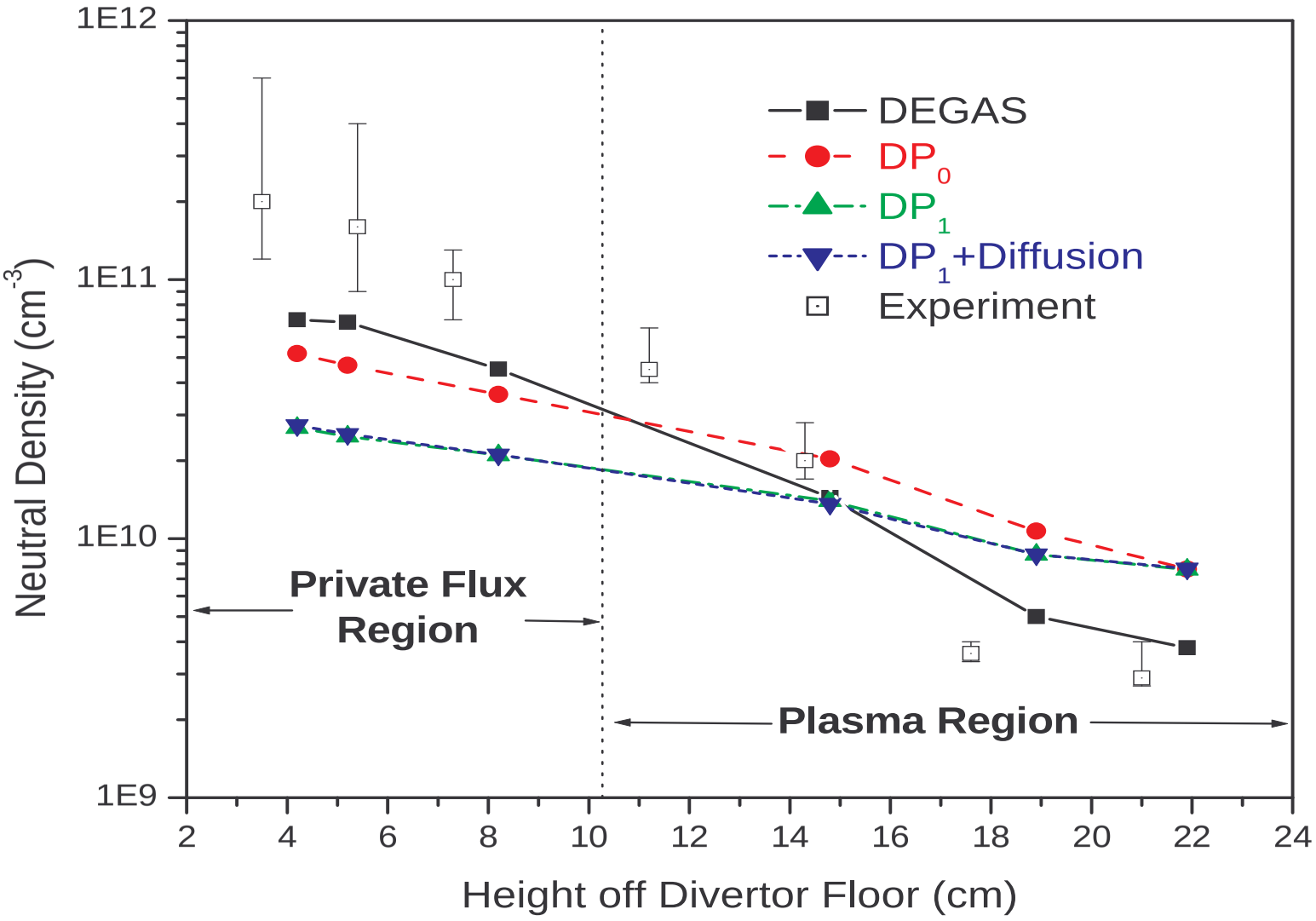

Figure 6.8. Comparison of GTNEUT with the local ion temperature assumption and DEGAS simulations for the analysis of the DIII-D H mode discharge 96747 at 3940 ms with the original nonuniform background ion temperature

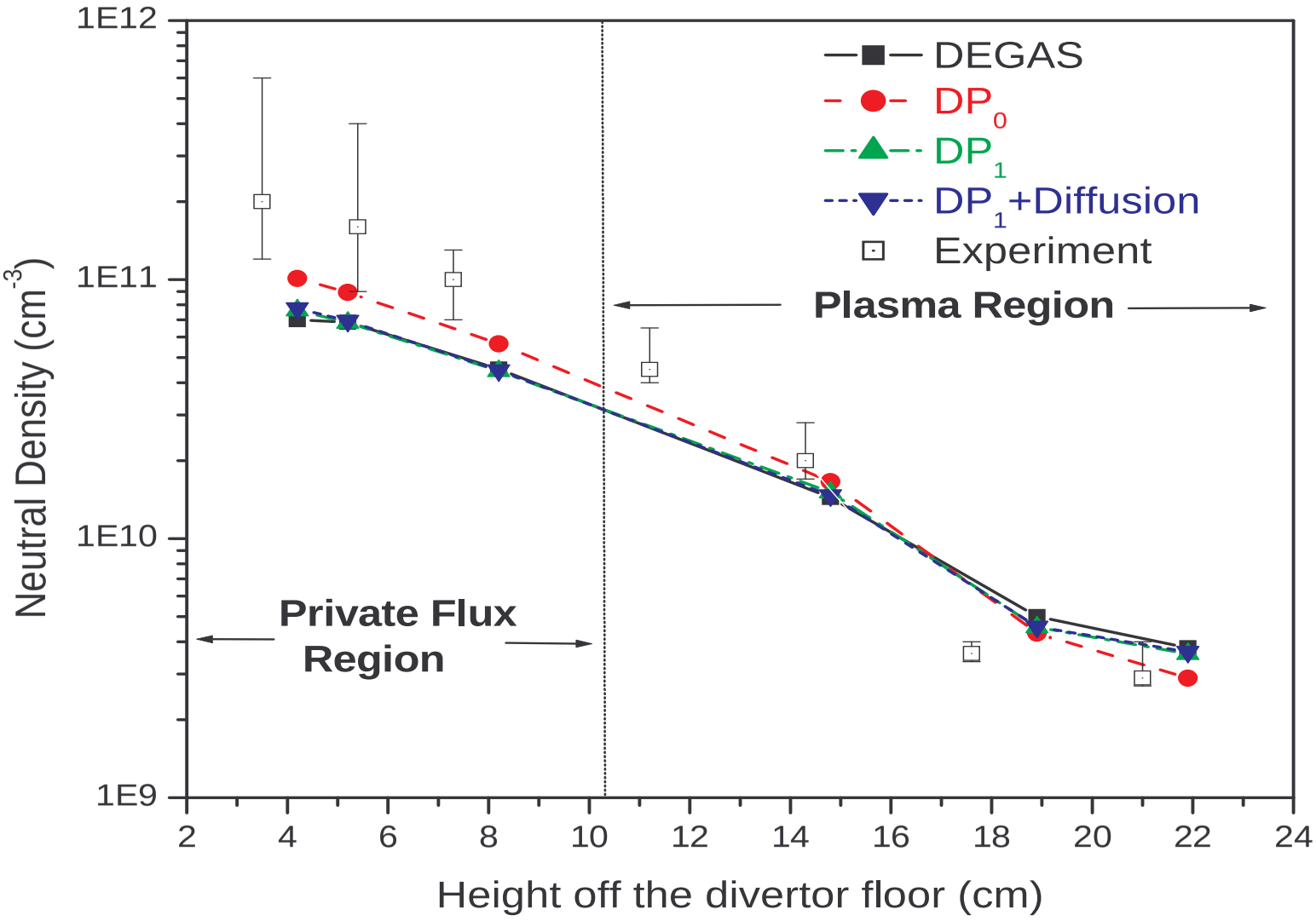

Figure 6.9. Comparison of GTNEUT with the average neutral energy assumption and DEGAS simulations for the analysis of the DIII-D H mode discharge 96747 at 3940 ms with the original nonuniform background ion temperature

Table 6.4. Comparison of the energy assigned to neutrals entering into region 136 by the two approximations for the H mode DIII-D discharge 96747 at 3940 ms (unit: eV)

Approximation	LIT	ANE
Region 24 to region 38	74.9	6.0
Region 37 to region 38	71.2	10.7
Region 39 to region 38	59	4.6
Region 156 to region 38	97.3	6.8

In the last run, the average neutral energy (ANE) approximation is used in GTNEUT to take into account the nonuniform background ion temperature. The comparison of DEGAS and GTNEUT calculations is presented in Figure 6.9. To show energy effects, the energies of neutrals entering into region 38 assigned by the two assumptions are listed in Table 6.4, from which it can be seen the average neutral energy is an order of magnitude lower than the local ion temperature. Figure 6.9 indicates that the average neutral energy approximation significantly improve the agreement between DEGAS and GTNEUT compared to the local ion temperature approximation. With reference to the DEGAS simulations without molecule effects, the DP_0 approximation over-predicts neutral densities in the private flux region and slightly over-predicts results in the deep plasma region. The DP_0 calculations are observed to be in better agreement with the experimental results, resulting from the coincident balance between errors introduced by the DP_0 approximation and the calculated background plasma parameters. The DP_1 calculations are in excellent agreement with the DEGAS simulations without molecule effects for the entire domain. As in the L mode case, there is no obvious advantage to correct directionalities for fine grid meshes. The detailed comparison of DEGAS without molecule transport and GTNEUT with the DP_1 approximation is shown in Figure 6.10.

6.4 Conclusions

Simulations of GTNEUT with a variety of approximations in DIII-D L and H mode discharges are performed. The agreement between the GTNEUT with the DP_1 and average

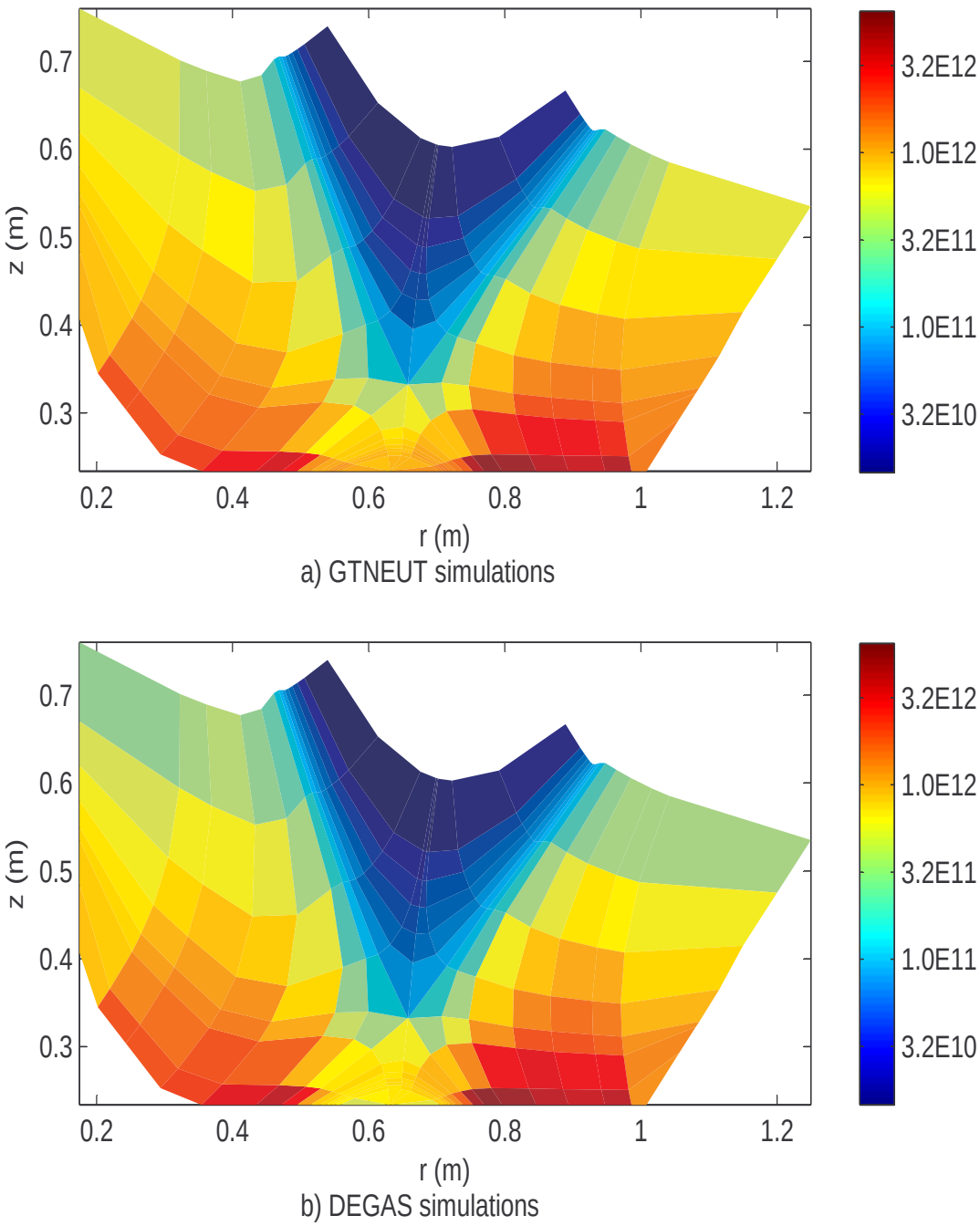

Figure 6.10. Comparison of GTNEUT with the average neutral energy assumption and DEGAS simulations for the analysis of the DIII-D H mode discharge 96747 at 3940 ms with the original nonuniform background ion temperature

neutral energy approximations and the DEGAS simulations without molecule transport is excellent for both the L mode and H mode discharges. Both the DEGAS and GTNEUT predictions are in good agreement with the experimental measurements.

The comparisons in both the discharges indicate the neutral energy dependence has an important impact on neutral transport in both the private flux region and the main plasma region. It has been shown the average neutral assumption is superior to the local ion temperature approximation, especially for regions with strong ion temperature gradients. Benchmarking calculations with DEGAS in realistic DIII-D configurations indicate the DP_1 approximation is significantly better than the original DP_0 approximation, but there is no advantage to correct directional escape probabilities for optically thin regions.

CHAPTER 7

CONCLUSIONS AND FUTURE WORK

7.1 Conclusions

Neutral particles can have important impacts on the performance of tokamak plasmas. An efficient and accurate method simulating neutral transport in diverted plasmas is indispensable to analyze experimental phenomena in the current fusion devices and to predict the performance of next generation fusion reactors.

In this dissertation, a number of refinements have been made in the TEP methodology and implemented into the original GTNEUT code. The accuracy of the upgraded code has been investigated by comparisons with the Monte Carlo code DEGAS. The major contributions of this work are summarized as follows:

1. The extension of the original DP_0 approximation to linearly (DP_1) or quadratically (DP_2) angular distributions has been made to take into account the anisotropy driven by the presence of sources, boundaries, vacuum regions, etc. Extensive comparisons with Monte Carlo have shown that the DP_1 approximation significantly improves the accuracy of the TEP method if anisotropic effects are important, while there is little further advantages to extend to the DP_2 approximation.

2. Three approaches, subdivision of regions, collision source expansion and diffusion approximation, have been proposed and implemented into the GTNEUT code to address the effect of non-uniformity of collided neutral sources on directional escape probabilities. Solving the diffusion equation via the finite element method has been shown to be computationally efficient and accurate for optically thick regions by comparisons with Monte Carlo simulations, has been shown to be the preferable approach.

3. To take into account spatial non-uniformities in the angular fluxes along interfaces,

a linear spatially dependent set of DP_N representation functions has been adopted. Benchmark simulations with Monte Carlo show that this approach significantly improves the accuracy of the simulations for optically thick reigons.

4. The average neutral energy (ANE) approximation, which assumes that the average neutral energy from a region is the weighted average of the energy of neutrals incident from contiguous regions and of the energy of neutrals resulting from charge-exchanged ions within the region, have been developed and implemented into the GTNEUT code. The average neutral energy approximation has been shown to be more accurate than the original local ion temperature assumption for optically thin regions, where neutral fluxes dominantly consists of uncollided neutrals.

5. Extensive benchmark simulations with the Monte Carlo code DEGAS have shown that the improved TEP methodology is accurate and computationally economic for a broader range of Δ/λ ratios than was the original TEP method.

6. Simulations with the refined GTNEUT code agree excellently with the DEGAS predictions of recent DIII-D L-mode and H-mode discharges, and the results of both the codes are in good agreement with the experimental measurements.

7.2 Recommendations

While the validity of the TEP method has been extended to extreme cases with a broader range of Δ/λ by the refinements in this work, the improvements in the following aspects could further enhance its computational efficiency and accuracy:

1. The present version of the GTNEUT code is two or three orders of magnitude faster than the DEGAS code, but its computational efficiency can be significantly improved by the adoption of fast integration algorithms for the evaluation of transmission probabilities. By the mean cord method [37] the original 2D numerical integration of transmission probabilities can be analytically reduced to 1D numerical integrations,

which are independent on the neutral mean free path. Furthermore, symmetric and conservation relations can be used to further reduce the time to compute transmission probabilities because of the independence on neutral mean free path.

2. Since in the TEP balance equations the exiting partial current moment from a given region is only coupled to all the incoming partial current moments from the contiguous regions, a large problem can be easily decomposed into a number of relatively independent small problems. This local nature of the TEP method makes it very suitable for parallel computing in a multi-processor computer.

3. The local ion temperature or average neutral energy assumption is sufficient for most cases, but under some special conditions the two assumptions may break down. For instance, if a problem is very sensitive to the charge-exchange fraction, a minor error of the charge-exchange fraction introduced by either of the two energy approximations could lead to a significant error in the calculated neutral densities or ionization rates. In addition, the energy distribution function may be needed to couple with a plasma fluid code. In order to remedy this issue, a full multi-group treatment of the energy dependence is recommended. The implementation of the multi-group methodology should be straightforward, and the number of energy groups is expected to be small since the reaction rates in fusion devices vary relatively smoothly in energy.

4. Molecule transport is not explicitly included in the current version of the GTNEUT code, which basically assumes all the desorbed molecules from material surfaces dissociate immediately as Franck-Condon neutral atoms. Since the dissociative ionization of molecules are ignored in the GTNEUT code, it over-predicts neutral densities in both the DIII-D L mode and H mode discharges. To remedy molecule effects, the implementation of molecule transport in GTNEUT is suggested. It is believed

that the implementation of molecule transport is not difficult conceptually. In principle, adding a molecular specie is the same as adding an extra energy group to the GTNEUT code.

5. It is assumed in the present TEP methodology that charge-exchanged neutrals are isotropically emitted in the laboratory system. This assumption is not valid for the case of a strong plasma flow. In such a situation the charge-exchanged neutrals are preferably emitted in the plasma flow direction. To take this effect into account, the preferential scattering of charge-exchanged neutrals in the plasma flow direction could be addressed by solving a extended diffusion equation with the $P3$ or higher order approximation via finite element methods.

6. The current version of the TEP method is based on 2D cylindrical configurations, but the GTNEUT code will most likely be used to model neutral transport in toroidal configurations. This is not an issue for most cases, where the neutral mean free path is shorter than the characteristic dimension in the toroidal direction. Benchmarking tests [25] with the DEGAS code in DIII-D configurations have shown that toroidal effects are not important. However, if the mean free path is longer than the characteristic dimension in the toroidal direction and, at the same time, fusion reactors have a very low aspect ratio configuration, the toroidal effects may not be ignored. In addition, a strongly localized external source may also break the symmetry in the toroidal direction. For these cases, an extension of the TEP method to 3D geometries is necessary.

REFERENCES

[1] M. Tendler and D. Heifetz, "Neutral particle kinetics in fusion devices," *Fusion Technology*, vol. 11, p. 289, 1987.

[2] T. Fülöp, P. J. Catto, and P. Helander, "Effect of neutral atoms on tokamak edge plasmas," *Physics of Plasmas*, vol. 8, p. 5214, 2001.

[3] K. Tsuchiya, H. Takenaga, T. Fukuda, S. Ishida, M. Sata, and T. Takizuka, "Effect of edge neutrals on the condition of the H-mode transition in TJ-60u," *Plasma Physics and Controlled Fusion*, vol. 38, p. 1295, 1996.

[4] M. Greenwald, "Density limits in toroidal plasmas," *Plasma Physics and Controlled Fusion*, vol. 44, p. R27, 2002.

[5] R. J. Groebner, M. Mahdavi, and A. L. et al, "Density limits in toroidal plasmas," *Plasma Physics and Controlled Fusion*, vol. A265, p. 44, 2002.

[6] R. L. Boivin, J. W. Hughes, B. LaBombard, D. Mossessian, and J. L. Terry, "High resolution measurements of neutral density and ionization rate in the Alcator C-Mod tokamak," *Review of Scientific Instruments*, vol. 72, p. 961, 2001.

[7] J. H. Marable and E. M. Oblow, "The application of neutron transport codes to the transport of neutrals in plasmas," *Nuclear Science and Engineering*, vol. 61, p. 90, 1976.

[8] R. D. M. Garcia, G. Pomaraning, and C. Siewert, "On the transport of neutral hydrogen atoms in a hydrogen plasma," *Plasma Physics*, vol. 24, p. 903, 1982.

[9] J. Spanier and E. M. Gelbard, *Monte Carlo Principles and Neutron Transport Problems*. Masschusetts: Addison-Wesley Publishing Company, 1969.

[10] D. Heifetz, D. Post, M. Petravic, J. Weisheit, and G. Bateman, "A Monte Carlo model of neutral-particle transport in diverted plasmas," *Journal of Computational Physics*, vol. 46, p. 309, 1982.

[11] D. Stotler, C. Karney, R. Kanzleiter, and S. Jaishnkar, "DEGAS2 manual." http://w3.pppl.gov/degas2/, Nov. 2001.

[12] D. Reiter, "The EIRENE code user manual." http://www.eirene.de/manuals/eirene.pdf, July 2003.

[13] J. Riemann, M. Borchardt, R. Schneider, A. Nutzke, T. D. Rognlien, and M. Umansky, "Navier-Stokes neutral and plasma fluid modeling in 3D," *Contributions to Plasmas Physics*, vol. 44, p. 35, 2004.

[14] J. J. Duderstadt and W. R. Martin, *Transport Theory*. New York: Wiley-Interscience, 1979.

[15] B. Davison, *Neutron Transport Theory*. Landon: Oxford University Press, 1971.

[16] G. I. Bell and S. Glasstone, *Nuclear Reactor Theory*. New York: Van Nostrand Reinhold, 1970.

[17] P. M. Valanju, "NUT: a fast three-dimensional neutral transport code," *Journal of Computational Physics*, vol. 88, p. 144, 1990.

[18] M. M. Anderson and H. C. Honeck, "An interface current technique for two-dimensional cell calculations," in *Proc. Conf. Mathematical Models and Computional Techniques for Analysis of Nuclear Systems*, no. 730414, (Ann Arbor, Michigan), p. 133, U.S. Atomic energy Commission, Apr. 1973.

[19] R. Sanchez, "Approximation solutions of the two-dimensional integral transport equation by collision probability methods," *Nuclear Science and Engineering*, vol. 64, p. 384, 1977.

[20] R. Sanchez, "A transport multicell method for two-dimensional lattices of hexagonal cells," *Nuclear Science and Engineering*, vol. 72, p. 9, 1979.

[21] R. Sanchez and N. J. McCormick, "A review of neutron transport approximations," *Nuclear Science and Engineering*, vol. 80, p. 481, 1982.

[22] W. M. Stacey and J. Mandrekas, "A transmission/escape probability model for neutral transport in the outer regions of a diverted tokamak," *Nuclear Fusion*, vol. 34, p. 1384, 1994.

[23] W. M. Stacey, E. W. Thomas, and J. Mandrekas, "Neutral atom transport," *Contributions to Plasma Physics*, vol. 36, p. 319, 1996.

[24] J. Mandrekas, "GTNEUT: A code for the calculation of neutral particle transport in plasmas based on the transmission and escape probability method," *Computer Physics Communications*, vol. 161, p. 36, 2004.

[25] R. Rubilar, W. M. Stacey, and J. Mandrekas, "Comparison of the TEP method for neutral particle transport in the plasma edge with Monte Carlo method," *Physics of Plasmas*, vol. 41, p. 1003, 2001.

[26] J. Mandrekas, R. J. Colchin, W. M. Stacey, D. Zhang, and L. W. Owen, "Neutral transport analysis of recent DIII-D neutral density experiments," *Nuclear Fusion*, vol. 43, p. 314, 2003.

[27] R. Rubilar, *Neutral Particle Transport in the Plasma Edge and Divertor Region*. PhD dissertation, Georgia Institute of Technology, School of Mechanical Engineering, June 2000.

[28] P. C. Stangeby, *The Plasma Boundary of Magnetic Fusion Devices*. Philadelphia, PA: Institute of Physics Publishing, second ed., 2000.

[29] W. Eckstein, "Physical sputtering and reflection processes in plasma-wall interactions," *Journal of Nuclear Materials*, vol. 248, p. 1, 1997.

[30] R. V. Meghreblian and D. K. Holmes, *Reactor Analysis*. New York: McGraw-Hill, 1960.

[31] P. Mohanakrishnan, "Choice of angular current approximations for solving neutron transport problems in 2-D by interface current approach," *Annual Nuclear Energy*, vol. 9, p. 261, 1982.

[32] D. Zhang, J. Mandrekas, and W. M. Stacey, "Extensions of the TEP neutral transport methodology," *Contributions to Plasma Physics*, vol. 44, p. 45, 2004.

[33] E. E. Lewis and W. Miller, *Computational Methods of Neutron Transport*. New York: John Wiley and Sons, 1984.

[34] R. T. Ackroyd, *Finite Element Methods for Particle Transport: Applications to Reactor and Radiation Physics*. England: Research Studies Press Ltd, 1997.

[35] R. J. Colchin, R. Maingi, and et al., "Measurement of neutral density near the X point in the DIII-D tokamak," *Nuclear Fusion*, vol. 40, p. 175, 2000.

[36] R. Maingi, J. Hogan, and et al., "Comparison of a simple recycling model and a complex recycling model in edge plasma transport calculations," *Nuclear Fusion*, vol. 34, p. 283, 1994.

[37] J. M. Sicillian and M. M. Anderson, "Mean-chord-length approximation in the interface-currents formulation of the collision-probabilities techniques," *Nuclear Science and Engineering*, vol. 57, p. 78, 1975.

VITA

Dingkang Zhang was born in Hubei, China in 1968. He received a Bachelor degree in Applied Physics from National University of Defense Technology (Changsha, China) in 1991.As an undergraduate he became involved in computational plasma physics. In 1994, he received a Master degree with emphasis in radiation detection from Northwest Institute of Nuclear Technology (Xi'an, China). As an engineer, Dingkang had worked on radiation detection, particle transport theories at NINT since 1995. In 2000, Dingkang conducted research on nuclear fusion at Georgia Institute of Technology as a visiting scholar. He completed the degree Doctor of Philosophy in Nuclear and Radiological Engineering from Georgia Institute of Technology in 2005.